Electronic structure of Titanates and layered Manganites probed by optical spectroscopy

Inaugural Dissertation

zur

Erlangung des Doktorgrades
der mathematisch-naturwissenschaftlichen Fakultät
der Universität zu Köln

vorgelegt von

Alexander Gößling

aus Bielefeld

Köln, 19. April 2007

Berichterstatter:	Prof. Dr. M. Grüninger Prof. Dr. J.A. Mydosh
Vorsitzender der Prüfungskommission:	Prof. Dr. L. Bohatý
Tag der mündlichen Prüfung:	15. Juni 2007

für Kerstin und Hannah-Marie

Contents

List of Figures

List of Tables

1 Introduction

The electronic structure is a crucial property of every solid. In semiconductors and conventional metals one has a very well established understanding in terms of electronic energy bands and can describe and predict material properties in quite a unique way. In materials with open d shells things become more complicated because the bands are very flat and electrons tend to localize. The theories working well for conventional materials break down. In general these unconventional materials are denoted as *correlated* electron systems, because one electron strongly influences the other ones.

In correlated materials a variety of interesting phenomena has been found. The most prominent examples are probably the high-temperature superconductivity and the colossal-magneto resistance [1].

In this study we are concerned with the electronic structure of titanates and single-layered manganites. They are prototypical examples where the conventional description in terms of energy bands breaks down: a metallic ground state is predicted for undoped titanates $RTiO_3$ (R-rare earth) and undoped (single-layered) manganites (e.g. $LaSrMnO_4$) but they are both found to be insulating. We will investigate their electronic structure by means of different optical techniques. In addition we are interested in the coupling of electronic degrees of freedom to additional degrees of freedom like the spin or the lattice. A competition of those is a generic property of a correlated electron system.

Optical spectroscopy has been proven to be a powerful tool for investigating the electronic structure. One measures excitations from the ground state of the system to the excited states. In a non-correlated system the optical spectra represent the folding of the unoccupied and occupied density of states. In correlated materials, electrons strongly influence each other which makes this folding procedure not uniquely applicable. Additionally optical spectroscopy can probe the coupling of the electronic structure to different degrees of freedom [1]. One can for example observe changes in the optical response at several eV ($\sim$ 12000 K) when the system changes its magnetic state on a meV scale ($\sim$ 12 K). The first (major) project in this thesis deals with the investigation of these *spin-controlled* bands [2], which are studied as function of temperature and polarization.

In a second project we investigated excitations below the optical gap by means of Raman spectroscopy[1]. Here, the goal is to get information on the nature of the underlying ground state, which has been discussed controversially in the literature [3–16].

This thesis is organized as follows: In the second chapter we will give a brief overview on correlated electron systems and introduce different models suitable for their description, e.g. the Hubbard model and extensions of it. In the second part we will discuss which

[1] in collaboration with C. Ulrich and B. Keimer from the Max-Planck Institute in Stuttgart

excitations are expected in a correlated material and how they can be detected by optical spectroscopies. In the third chapter we will present the experimental techniques used in this work: Fourier-transform spectroscopy, Raman spectroscopy and ellipsometry. Since the ellipsometer has been put into operation by my colleague C. Hilgers and myself we will focus on that topic. We are interested in properties down to liquid-He temperatures. Therefore, it was the major experimental issue to get the system running down to these temperatures. In chapter four the single-layered manganites are introduced, i.e. the system $La_{1-x}Sr_{1+x}MnO_4$ for $x = 0.0$, 0.13, and 0.5. We present the results from Fourier-transform spectroscopy and ellipsometry and give a detailed analysis of the electronic structure of this system in terms of multiplets. We focus on the undoped compound with $x = 0.0$ since this is the starting point for a deeper understanding of the whole series. In chapter five we first give the status of the field in the titanates, especially $YTiO_3$, $SmTiO_3$, and $LaTiO_3$, which have been investigated in this thesis. We proceed with the results from Raman spectroscopy, where we studied the orbital excitations on $LaTiO_3$ and $YTiO_3$. The last part of this chapter deals with the electronic structure of the three titanates mentioned above. The excitation spectrum is measured by spectroscopic ellipsometry. Here, we concentrate on $YTiO_3$ because we find evidence for an excitonic resonance (*Mott-Hubbard exciton*) in this compound. Again we will give an assignment of the peaks observed in terms of multiplets. We end with a final conclusion and some additional information, like sample preparation, etc. in the appendix.

2 Electronic structure of correlated systems and its observation in optics

Optical spectroscopy can cover a wide energy range with high resolution. In this thesis we use different techniques, in particular Raman, Fourier, and ellipsometric spectroscopy to investigate strongly correlated electron systems. More specifically, we will focus on the electronic structure of these systems and its relation to the magnetic, orbital and vibrational degrees of freedom.

This chapter is organized as follows: we will start with the onsite properties of a transition-metal ion. In the next section we will discuss different models applied to correlated materials, in particular the Hubbard model and different spin-orbital models. The chapter will end with a brief overview of the excitations in a correlated material and their observation by optical spectroscopy.

2.1 Onsite properties - lifting the orbital degeneracy

The knowledge of the onsite orbital properties is crucial for a proper understanding of a solid. Since we are dealing with transition-metal oxides, it is often sufficient to analyze the properties of the magnetic ions, in the case that the rare-earth ions as well as the oxygen ions have closed shells. Consider for example the compound $YTiO_3$ with Y^{3+} = [Kr]$4d^0$, Ti^{3+} = [Ar]$3d^1$, and O^{2-} = [He]$2s^2 6p^6$ or $LaSrMnO_4$ with La^{3+} = [Xe]$5d^0$, Sr^{2+} = [Kr]$5s^0$, Mn^{3+} = [Ar]$3d^4$, and O^{2-}=[He]$2s^2 6p^6$, where the magnetic ions with open shells are Ti^{3+} and Mn^{3+}. Moreover, the onsite orbital energy scale is often comparable to the intersite exchange interactions which gives rise to a competition. Additionally the orbital properties can be regarded as a kind of preselection for the formation of an electronic band: the band will have the same symmetry as the orbitals forming this band. Orbitals are therefore the basic building blocks of different bands, e.g. the "valence" and "conduction" band. There are three effects which can lift the onsite orbital degeneracy (exchange mechanisms will be discussed below): steric effects, the Jahn-Teller effect, and spin-orbit coupling. All of these effects can be described by crystal-field theory which will be discussed briefly.

In the perovskites, steric effects are caused by a mismatch of ionic sizes. This will lead to distortions and rotations (away from a cubic arrangement). The magnetic ion is surrounded by an electric field produced by the charges of the ligands which lifts the degeneracy of certain energy levels.

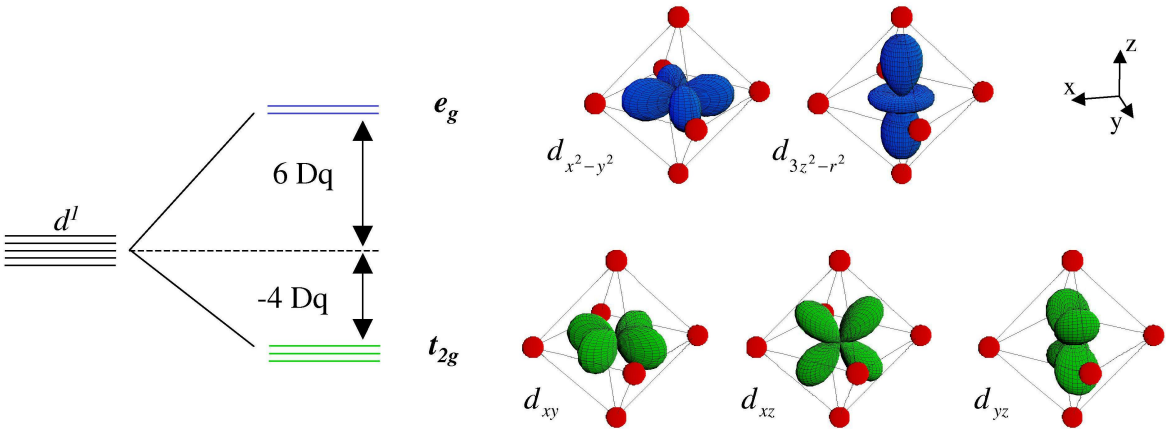

Figure 2.1: For an octahedral crystal field which can be produced for example by a ligand-oxygen cage the energy levels of a d^1 system are split into $t_{2g} \equiv (d_{xy}, d_{xz}, d_{yz})$ and $e_g \equiv (d_{x^2-y^2}, d_{3z^2-r^2})$ levels. The energy difference between these levels is $10\,Dq$.

In addition to simple steric effects a possible reason for the lifting of the degeneracy can be found in the Jahn-Teller effect. The theorem of Jahn and Teller states that "*any non-linear molecular system in a degenerate electronic state will be unstable and will undergo distortion to form a system of lower symmetry and lower energy thereby removing the degeneracy*" [17]. Presuming Hund's rules are not violated, a cubic d^3, d^5, and d^8 will not show a Jahn-Teller distortion, because for an e.g. d^5 system all d orbitals are occupied and thus no orbital degeneracy is present (the same is true for d^3 and d^8). If the Jahn-Teller effect is the dominating mechanism a strong coupling to the lattice is expected, i.e. a mixing of the orbital and lattice degrees of freedom.

A further source for lifting the degeneracy is the spin-orbit coupling. However, for $RTiO_3$ and $(La,Sr)_2MnO_4$ this is a rather small correction of the order of ~ 50 meV [8, 18]. One could say, that the orbital moment is almost quenched. The natural limit for the lifting of degeneracy is the Kramers degeneracy.

Crystal-field theory

In the so called *crystal-field theory* [19–21] the local properties of magnetic ions can be properly treated. The starting point, of course, is the central magnetic ion which is placed in the potential of all surrounding ligands. One may assume that the charge distribution on each ligand is point-like, e.g. for the case of $YTiO_3$ the Ti ion with charge $^{3+}$ will be placed in the origin. It will be surrounded by the O ions with charge $^{2-}$, the Y ions with charge $^{3+}$, and additional Ti ions. In order to obtain the Madelung potential at the origin, the summation of all Coulomb contributions is carried out here up to infinity, half in real, half in reciprocal space (Ewald summation)[1]. These calculations can be found in the appendix

[1]The parameters of the Madelung potential have been calculated with a program written by M. Haverkort [8].

for the materials discussed later on. Whether the lattice distortions are caused by steric effects or the Jahn-Teller effect can not be unraveled using crystal-field theory, since the observed crystal structure has to be used as an input. If necessary, one can treat spin-orbit coupling as a further perturbation on top of the electrostatic effects. As discussed above we will omit spin-orbit coupling due to its comparably small magnitude.

As an example, consider a d^1 electron in a cubic crystal field as indicated in Fig. 2.1. This cubic crystal field can e.g. be produced by an oxygen octahedron as found in the perovskite structure. The five d orbitals are split into t_{2g} and e_g orbitals. The energy difference is commonly denoted by $10Dq$. The lobes of the t_{2g} orbitals point towards the median line between two O ions, while those of the $d_{x^2-y^2}$ (e_g) orbital for example point directly onto the oxygen ions. Therefore, the t_{2g} orbitals are lower in energy because electrons can better avoid each other. For crystals with lower symmetries the degeneracy will be further reduced. For $LaSrMnO_4$ one finds tetragonal symmetry, while for $RTiO_3$ (R - rare earth) orthorhombic symmetry has been reported [7, 22, 23]. In the latter case the degeneracy of all d levels will be lifted. The corresponding level diagram will be shown in chapters 4 and 5.

Multiplets

So far, our discussion is only correct as long as only one electron is put into the crystal-field levels. For more than one electron, one has to consider the whole multiplet structure. Because of the antisymmetry of the fermionic wave function, the two-electron wavefunction is not simply a product of two single-electron wavefunctions. This is taken into account by using the Slater determinants. The new basis functions in the cubic case are superpositions of e_g and t_{2g} single-electron functions (configuration mixing) [20]. For a d^2 system there are 45 basis functions (10 possibilities for the first electron times 9 possibilities for the second electron - divided by two in order to tackle double counting), 120 basis states for d^3, 210 for a d^4 system, and so on. In addition to the crystal-field parameter Dq for the $t_{2g} - e_g$ splitting in the cubic case, one has to take the *Slater integrals* F^0, F^2, and F^4 into account [1, 19]:

$$F^k = e^2 \int_0^\infty r_1^2\, dr_1 \int_0^\infty r_2^2\, dr_2\, \frac{r_<^k}{r_>^{k+1}}\, R_{3d}(r_1)^2 R_{3d}(r_2)^2 \tag{2.1}$$

where R_{3d} represents the radial wavefunction and $r_<$ ($r_>$) the minimum (maximum) value of r_1 and r_2. This set of parameters describes the repulsion energy between two electrons which are placed on one ion. The definition of the full crystal-field Hamiltonian can be found e.g. in Refs. [18–20]. Alternatively to the Slater integrals F^0, F^2, and F^4, one can use either another set of Slater integrals F_0, F_2, and F_4 or the *Racah* parameters A, B, and C. The conversion rules are given in Tab. 2.1. Starting from the full multiplet, as presented above, there exist several simplifications which are commonly used in the literature. This is an important issue when comparing for instance values of Hubbard U from different publications. Different schemes lead to different values of U. Here a brief overview:

Table 2.1: Conversion of different multiplet schemes [18–20].

Slater integrals	$F_0 = F^0, \;\; F_2 = \frac{1}{49}F^2, \;\; F_4 = \frac{1}{441}F^4$
Racah parameters	$A = F^0 - \frac{49}{441}F^4, \;\; B = \frac{1}{49}F^2 - \frac{5}{441}F^4, \;\; C = \frac{35}{441}F^4$
Simple scheme	$U^{simple} = F^0, \;\; J_H^{simple} = \frac{1}{14}(F^2 + F^4)$
Kanamori scheme	$U^{Kanamori} = F^0 + \frac{4}{49}F^2 + \frac{36}{441}F^4, \;\; J_H^{Kanamori} = \frac{2.5}{49}F^2 + \frac{22.5}{441}F^4$
Multiplet average	$U^{av} = F^0 - \frac{14}{441}(F^2 + F^4)$

- *Simple scheme* - In the simple scheme two electrons always repel each other with an energy U^{simple} regardless in which orbital they reside. If the spins of these two electrons are parallel one gains an energy J_H^{simple}. The advantage of the simple scheme is that one can estimate the energy of a many-electron state just by counting the pairs. Every pair gets an energy U^{simple} in case of antiparallel spins and $U^{simple} - J_H^{simple}$ in case of parallel spins. Consider for example four electrons in a $S = 2$ state. One finds six pairs with parallel alignment, which results in an energy of $6U^{simple} - 6J_H^{simple}$ (for $Dq = 0$). The parameters of the simple scheme can be related to the Slater integrals as indicated in Tab. 2.1. The disadvantage of the simple scheme is that both multiplet energies and multiplicities differ sometimes significantly from the full multiplet calculation (see Ref. [18]). However, we will use the simple scheme occasionally in order to get rough estimates of multiplet energies.

- *Kanamori scheme* - The Kanamori scheme extends the simple scheme in the following way: the parameter $U^{Kanamori}$ measures the electron repulsion of electrons in the same orbital, while the repulsion is reduced to $U^{Kanamori} - 2J_H^{Kanamori}$ if electrons reside in different orbitals (regardless their spin). $U^{Kanamori}$ and $J_H^{Kanamori}$ have of course a different meaning when comparing to the simple scheme. Their relation to the Slater integrals can be read from Tab. 2.1. Consider again the above example of four electrons in an $S = 2$ state (for $Dq = 0$): the energy reads $6U^{Kanamori} - 18J_H^{Kanamori}$. The Kanamori scheme conserves more of the multiplet character than the simple scheme.

- *Multiplet average* - This is not a scheme. We just wanted to note that the value of Hubbard U is often given as an average U^{av} over all multiplets. The relation of U^{av} to the Slater integrals is also given in Tab. 2.1.

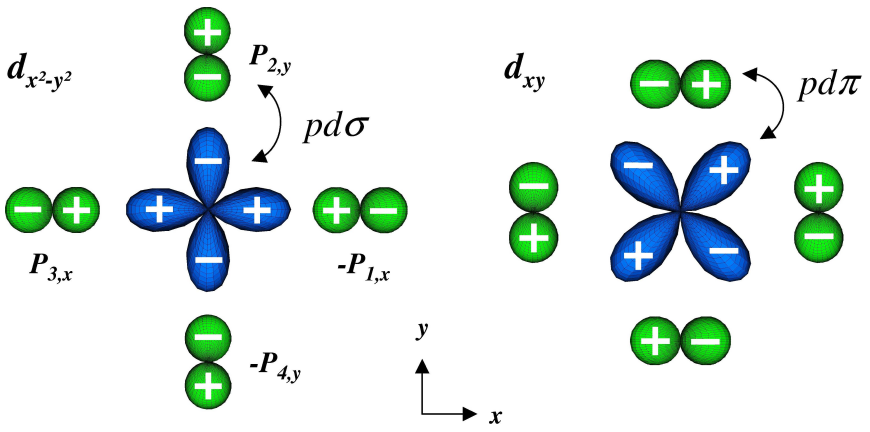

Figure 2.2: Sketch of the σ-bonding $d_{x^2-y^2}$ (left) and the π-bonding d_{xy} orbitals (right). For the anti-bonding configuration the phases of all oxygens have to be inverted.

Hybridization

A further improvement of the crystal-field theory is to allow for hopping from the central transition-metal ion to its ligands. In titanates and manganites these ligands are oxygens, i.e. one has to consider p orbitals. Depending on the overlap, there will be a sizable admixture of the p wavefunctions. This is commonly denoted by $\alpha_1|d^n\rangle + \alpha_2|d^{n+1}\rangle\underline{L}$ states where $|d^{n+1}\rangle\underline{L}$ is a ligand-hole state. However, the symmetry of the original $|d^n\rangle$ wavefunctions will not be changed. This can be seen in Fig. 2.2(left) for the case of the $|d^1\rangle = d_{x^2-y^2}$ orbital. This orbital can only hybridize with combinations of the ligands having the same symmetry, i.e. an orbital of the form $|d^2\rangle\underline{L} = \frac{1}{2}(-p_{1,x} + p_{3,x} + p_{2,y} - p_{4,y})$. The overlap between all kinds of orbitals is tabulated in Refs. [24, 25]. The energy levels obtained from a purely ionic picture will change when hybridization is switched on. As a rule of thumb the t_{2g}-e_g splitting is increased by a factor of two as shown for the titanates in Refs. [9, 26, 27]. This is quite obvious because the e_g orbitals point with their lobes towards the oxygen neighbors and will thus be more affected by hybridization than the t_{2g} orbitals. In chapter 5, we will show some results from configuration-interaction calculations, taking the hybridization to neighboring oxygen ions properly into account. For the manganites discussed in chapter 4 we carried out crystal-field calculations and used the crystal-field parameters in an effective manner. We did not use the results from an Ewald summation (see above) but assumed that the effective crystal-field parameters contain a covalent part. As mentioned above, this procedure is justified since the hybridization does not change the symmetry of the wavefunction considered. Due to the different screening the value of Hubbard U will depend on whether covalency is included or not. We will discuss this issue in more detail later on.

2.2 Intersite properties

2.2.1 Single-band Hubbard model

In the description of transition metals with open d shells, band theory (LDA[2]) fails in describing the electronic properties. At half filling these materials are metals within the LDA, although they are found to be insulators in experiments. The failure of LDA stems from the simplification to a *single-electron* picture. This approximation works pretty well in ordinary semiconductors, but is not justified in the case of correlated systems, where electrons strongly influence each other. The inclusion of the onsite electron-electron interaction can repair the discrepancy between theory and experiment. The most simple approach is the single-band Hubbard model [28]. The system Hamiltonian can be written as follows:

$$H = -t \sum_{\langle i,j\rangle,\sigma} (c^{\dagger}_{i\sigma} c_{j\sigma} + h.c.) + U \sum_{i} n_{i,\uparrow} n_{i,\downarrow} \tag{2.2}$$

Here, $n_{i\sigma} \equiv c^{\dagger}_{i\sigma} c_{i\sigma}$ is the number operator and $c^{\dagger}_{i\sigma}$ ($c_{i\sigma}$) creates (annihilates) an electron on lattice site i with an a spin $\sigma = \uparrow, \downarrow$. The summation is carried out over nearest neighbors $\langle i, j\rangle$. The first term of the Hamiltonian means that an electron can decrease its kinetic energy by changing its position with an energy gain t. The second term in the Hamiltonian represents the energy of a double occupancy which is denoted by U. At half filling the movement of an electron will of the one hand gain the energy t but on the other hand the electron is hindered by the repulsion U. The singly occupied sites will form the so-called lower Hubbard band (LHB), while the doubly occupied sites form the upper Hubbard band (UHB). The band width $W = 2zt$ is determined by the size of the hopping t and the coordination number z. In the limit $U/t \to 0$, the system is metallic because the LHB and UHB overlap and are half filled. In the other limit $U/t \to \infty$ it is an insulator because one finds only one electron per site. The energy cost for a double occupancy is very high, making the electrons immobile. This means LHB and UHB are far away from each other. Interestingly, one can drive a system from a metallic to an insulating state by changing the size of U/t. Regarding the magnetic properties, the insulating state ($t \ll U$) of the single-band Hubbard model favors antiferromagnetic arrangement of neighboring spins, because in this case electrons can gain the antiferromagnetic superexchange $J = 4t^2/U$, while in the ferromagnetic case the virtual hopping is blocked by Pauli's exclusion principle. The antiferromagnetic arrangement favored in the Hubbard model is described by the Goodenough-Kanamori-Anderson rule for 180°-superexchange. Formally the Hubbard model can be mapped on an effective spin model, which is known as the Heisenberg model

$$H = J \sum_{\langle i,j\rangle} \mathbf{S}_i \cdot \mathbf{S}_j \tag{2.3}$$

[2]Local Density Approximation.

Within this model, low-energy excitations ($\sim$ meV) such as spin waves can be described[3].

When simulating real materials with open d shells in more detail, the one-band Hubbard model may give erroneous results because "one-band" corresponds to a single orbital, strictly speaking to an s orbital. The model parameters t and U are of effective nature since real hopping paths have to be integrated out. Excited orbital states on each site are omitted within the single orbital picture and interesting phenomena which arise from *degenerate* orbitals are not captured. However, the character of the charge excitation gap can be reproduced quite well for lighter transition metals (Ti, V) but not for the heavier ones (Co, Ni, Cu) because the oxygen ligands are not included explicitly.

2.2.2 Mott-Hubbard and charge-transfer insulators

One extension to the single-band Hubbard model is the *pd* model [30]. It includes one or several oxygen orbital(s) in addition to the transition-metal orbital. This model is widely used for the description of the CuO_2 planes of high-T_c cuprate systems. For our purpose, the extension leads to a classification scheme for strongly correlated systems, known as the Zaanen-Sawatzky-Allen scheme [29]. In addition to the parameters t and U, the charge transfer energy Δ is taken into account: $\Delta = \epsilon_p - \epsilon_d$ where ϵ_d is the energy of the transition-metal d orbital and ϵ_p the energy of the oxygen p orbital. Two kinds of excitations are now possible: one electron can be transferred between two transition metals, or one electron can be transferred from an oxygen ion to a transition metal. Depending on which excitation is lower in energy, i.e. if U or Δ is larger, the insulator is called Mott-Hubbard insulator or charge-transfer insulator. The gap formed in this insulating state for an n-electron system is given by the many-body groundstate E_n and the ionic states given by E_{n+1} and E_{n-1}:

$$E_{gap} = E_{n+1} + E_{n-1} - 2E_n \tag{2.4}$$

As an example we will calculate E_{gap} for a Mott-insulating chain of N equal sites filled with n electrons. The one-electron energy is given by E_0. Thus the ground-state energy at one site is $E_n = nE_0 + n(n+1)/2\ U$. The term $n(n+1)/2\ U$ counts the onsite correlations for every electron pair. If one electron is added to one site, one obtains $E_{n+1} = (n+1)E_0 + (n+1)(n+2)/2\ U$. If one electron is removed one finds $E_{n-1} = (n-1)E_0 + (n-1)n/2\ U$. Substituting this into Eq. 2.4, the gap results in $E_{gap} = U$.

We will now discuss the ZSA scheme in more detail, see Fig. 2.3. Apart from the parameters U and Δ, one has to take a finite band width of the d and p bands into account. Roughly speaking, the diagram is split into two regions: for $\Delta < U$ the electronic structure is dominated by the oxygen band (charge-transfer type) and for $\Delta > U$ by the upper $3d$ band (UHB). In the first case (panel b) the gap is set by Δ, in the latter case (panel d) by U. Including a finite bandwidth an insulating state will not be formed under all circumstances but a metal can exist either in the charge-transfer or in the Mott-Hubbard region: if the band width of the d band W_d is larger than the onsite repulsion U, a d

[3]Transformation between Eqs. 2.2 and 2.3 [1]:
$S_i^+ = c_{i,\uparrow}^\dagger c_{i,\downarrow}$, $S_i^- = c_{i,\downarrow}^\dagger c_{i,\uparrow}$, and $S_i^z = \frac{1}{2}(n_{i\uparrow} - n_{i\downarrow})$

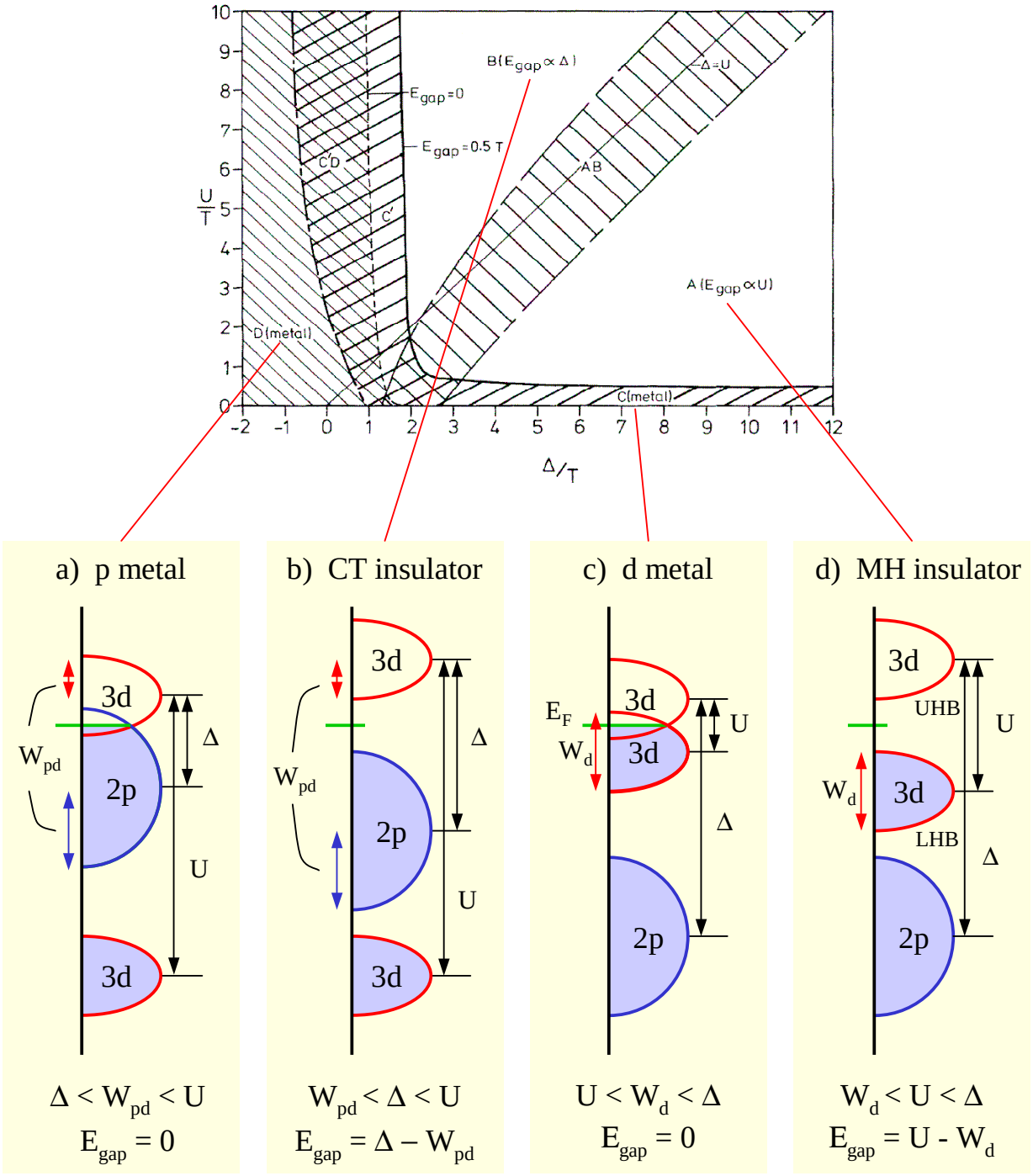

Figure 2.3: Zaanen-Sawatzky-Allen (ZSA) scheme. The interplay of the Coulomb repulsion U, the charge-transfer gap Δ, and the bandwidth W gives rise to different kinds of metallic and insulating states. Note, that $W_{pd} = \frac{1}{2}(W_p + W_d)$. The top panel is the original diagram from Ref. [29], while the cartoon illustrates the four main parts in a band-like picture. However in the cartoon representation the hybridization is neglected in order to be more illustrative.

metal is formed in the Mott region because LHB and UHB overlap (panel c). A similar argumentation leads to a p metal in the charge-transfer region (panel a). Additionally there are some intermediate regions in the ZSA scheme. For their discussion we refer to the original paper.

2.2.3 Multi-band Hubbard models

A generalization of the *pd* model is the multi-orbital Hubbard model, which allows for different (degenerate) orbitals on each site. The degenerate case is relevant for quasi-cubic systems because here the orbital degree of freedom is not fully quenched, contrary to systems with e.g. large crystal-field splitting [1, 31, 32]. The system Hamilton reads as

$$\begin{aligned} H &= \sum_{\substack{\langle i,j\rangle \\ \sigma,\alpha,\alpha'}} t_{ij}^{\alpha\alpha'}(c_{i\sigma\alpha}^{\dagger}c_{j\sigma\alpha'} + h.c.) + \sum_{\substack{i,\alpha,\alpha' \\ \sigma,\sigma'}} (1-\delta_{\alpha\alpha'}\delta_{\sigma\sigma'})U^{\alpha\alpha'}n_{i\sigma\alpha}n_{i\sigma'\alpha'} \\ &+ \sum_{\substack{\langle i,j\rangle \\ \alpha,\alpha',\sigma,\sigma'}} V_{ij}^{\alpha\alpha'}n_{i\sigma\alpha}n_{j\sigma'\alpha'} - \sum_{\substack{i,\alpha,\alpha' \\ \sigma,\sigma'}} J_H^{\alpha\alpha'}\mathbf{S_{i\alpha}}\cdot\mathbf{S_{i\alpha'}}(1-\delta_{\alpha\alpha'}) \end{aligned} \tag{2.5}$$

here spin operators are defined as:

$$\begin{aligned} S_{i\alpha}^{+} &= S_{i\alpha}^{x} + iS_{i\alpha}^{y} = c_{i\alpha\uparrow}^{\dagger}c_{i\alpha\downarrow} \\ S_{i\alpha}^{-} &= S_{i\alpha}^{x} - iS_{i\alpha}^{y} = c_{\alpha i\downarrow}^{\dagger}c_{i\alpha\uparrow} \\ S_{i\alpha}^{z} &= \frac{1}{2}(n_{i\alpha\uparrow} - n_{i\alpha\downarrow}) \end{aligned} \tag{2.6}$$

Again $n_{i\sigma} \equiv c_{i\sigma\alpha}^{\dagger}c_{i\sigma\alpha}$ is the number operator, $c_{i\sigma\alpha}^{\dagger}$ ($c_{j\sigma\alpha}$) creates (annihilates) an electron in the orbital α on site i with spin $\sigma =\uparrow,\downarrow$. The hopping $t_{ij}^{\alpha\alpha'}$ is now depending on the orbitals and the lattice sites, and also $U^{\alpha\alpha'}$ depends on the orbitals (this corresponds to the full multiplet, see Sect. 2.1). Additionally a nearest-neighbor interaction $V_{ij}^{\alpha\alpha'}$ is now included in order to capture charge-ordering phenomena. This interaction will be of relevance for the formation of *excitons* which will be discussed later on. Furthermore an intrasite exchange, the Hund's-rule coupling, $J_H^{\alpha\alpha'}$ is also incorporated. Electrons in two different orbitals with parallel spins are lower in energy than those with antiparallel spins due to Pauli's exclusion principle.

Due to the large number of possible states, these models require tremendous computational effort. The continually growing computer capabilities made it possible to study this kind of models for real systems exploiting e.g. LDA+DMFT[4] [10, 11, 33, 34].

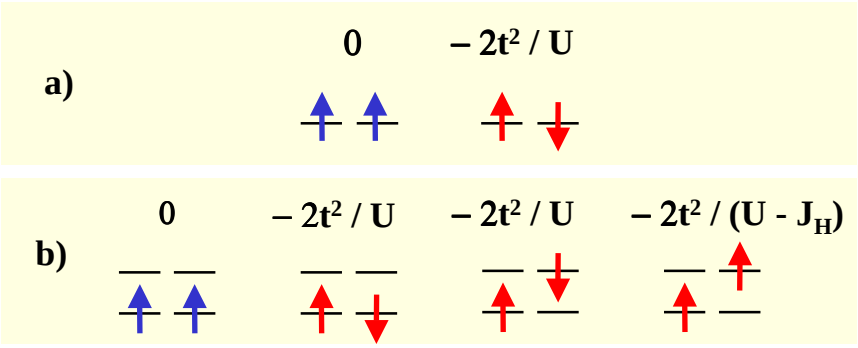

Figure 2.4: (a) For a degenerate spin-orbital model spins tend to align antiferromagnetically, while (b) in a two-fold orbital degenerate case they are aligned ferromagnetically. The figure is reproduced from Ref. [35].

2.2.4 Spin-orbital models

Kugel and Khomskii [31, 35] suggested that the degenerate Hubbard model can be mapped onto an effective spin-orbital model which is formally identical to the Heisenberg model. Within this model, orbital-ordering phenomena can be understood. Furthermore, this model shows that the orbital degeneracy of the onsite levels can be lifted by the superexchange interaction (in addition to steric effects, the Jahn-Teller effect, or spin-orbit coupling, see Sect. 2.1). This mechanism has been discussed earlier (1966) by Roth [36]. First, we will illustrate the interaction for two degenerate, perpendicular orbitals on each lattice site filled with one electron. We will make the following assumptions to simplify Eq. 2.5:

$$t_{ij}^{\alpha\alpha'} = t\delta_{\alpha\alpha'},\ U^{\alpha\alpha'} = U^{simple} = U,\ J_H^{\alpha\alpha'} = J_H^{simple} = J_H,\ V_{ij}^{\alpha\alpha'} = 0$$

The hopping between the two different orbitals is zero and between the same orbitals it has the magnitude t. For all orbitals the onsite repulsion and Hund's-rule coupling are assumed to be equal. The nearest-neighbor coupling V is neglected for a moment. The resulting spin-orbital Hamiltonian (in its general case known as *Kugel-Khomskii* Hamiltonian) reads in the strong coupling limit ($t \ll U$) in second-order perturbation theory as [1, 31, 32, 35]:

$$\begin{aligned} H &= \frac{2t^2}{U}(1 - \frac{J_H}{U}) \sum_{\langle i,j \rangle} \mathbf{S_i} \cdot \mathbf{S_j} + \frac{2t^2}{U}(1 + \frac{J_H}{U}) \sum_{\langle i,j \rangle} \mathbf{T_i} \cdot \mathbf{T_j} \\ &+ \frac{2t^2}{U}(1 + \frac{J_H}{U}) \sum_{\langle i,j \rangle} (\mathbf{S_i} \cdot \mathbf{S_j})(\mathbf{T_i} \cdot \mathbf{T_j}) \end{aligned} \tag{2.7}$$

[4] Dynamical mean-field theory.

Above the so called pseudo-spin operators $\mathbf{T_i}$ in addition to the spin operators have been used. More explicitly:

$$\begin{aligned} T_i^+ &= c_{i\alpha'\uparrow}^\dagger c_{i\alpha\uparrow} + c_{i\alpha'\downarrow}^\dagger c_{i\alpha\downarrow} \\ T_i^- &= c_{i\alpha\uparrow}^\dagger c_{i\alpha'\uparrow} + c_{i\alpha\downarrow}^\dagger c_{i\alpha'\downarrow} \\ T_i^z &= \frac{1}{2}(n_{i\alpha'\uparrow} + n_{i\alpha'\downarrow} - n_{i\alpha\uparrow} - n_{i\alpha\downarrow}) \end{aligned} \tag{2.8}$$

For example T_i^+ corresponds to an orbital flip on site i without flipping the spin. Formally the pseudo spin can be treated in the same manner as ordinary spins. But one has to keep in mind that this is a rough estimate since the orbitals do not have rotational invariance like the spins, i.e. there are no Goldstone modes in the orbital sector. The pseudo-spin spectrum is always gapped [37]. The different spin-orbital states are sketched in Fig. 2.4. For non-degenerate orbitals, the orbital sector is quenched and the system can lower its energy by an antiferromagnetic arrangement according to the Goodenough-Kanamori-Anderson rule. In contrast, for the two-fold degenerate orbitals, a ferromagnetic orientation is favored by Hund's-rule coupling. In that sense the Kugel-Khomskii model can be regarded as a generalization of the Goodenough-Kanamori-Anderson rule.

For realistic spin-orbital models, one has to take different hopping paths into account. The Hamiltonians become rather complicated already for the cubic case. Therefore we refer to Refs. [1, 31, 35, 38] for further reading. It has been shown that purely electronic interaction can stabilize orbital ordering in a cubic crystal with one electron or hole in a degenerate e_g orbital. The pattern consists of alternating $d_{x^2-z^2}/d_{y^2-z^2}$ orbitals. This pattern is indeed realized in the compound $KCuF_3$ [31].

Finally, we discuss the difference between e_g and t_{2g} electrons on one particular bond for the spin-orbital part of the above Hamiltonian. For simplicity we neglect Hund's coupling J_H, i.e. the above Hamiltonian for one bond reads:

$$H_{12} = \frac{2t^2}{U}(\mathbf{S_1}\cdot\mathbf{S_2})(\mathbf{T_1}\cdot\mathbf{T_2}) \tag{2.9}$$

(i) *degenerate e_g orbitals* - The e_g doublet in cubic symmetry is non-magnetic because it consist out of the spherical harmonics $Y_{l,m}$ of the form $Y_{2,0}$ ($d_{3z^2-r^2}$) and $1/\sqrt{2}(Y_{2,2}+Y_{2,-2})$ ($d_{x^2-y^2}$). This means that one cannot form singlet or triplet states out of the orbital channel. In the pseudo-spin language, one identifies e_g orbitals with $T = 1/2$ with $T^z = 1/2 \equiv d_{3z^2-r^2}$ and $T^z = -1/2 \equiv d_{x^2-y^2}$. We consider a bond along the z direction as shown in Fig. 2.5. There is finite hopping between two $T^z = 1/2$ orbitals (see Fig. 2.5(a)), zero hopping between $T^z = 1/2$ and $T^z = -1/2$ (see Fig. 2.5(b)), and small hopping between $T^z = -1/2$ orbitals (see Fig. 2.5(c))[5]. One can directly write down the pseudo-spin part of Eq. 2.9 for this bond. It is of $(T_1^z + 1/2)\,(T_2^z + 1/2)$ type, considering only exchange of type (a) in Fig. 2.5. The possibilities for the spin-orbital arrangement are fixed: the ferroorbital configuration combines with the spin singlet (see Fig. 2.5(a) and Fig. 2.4(b)).

[5]The effective hopping via an oxygen ion it is zero.

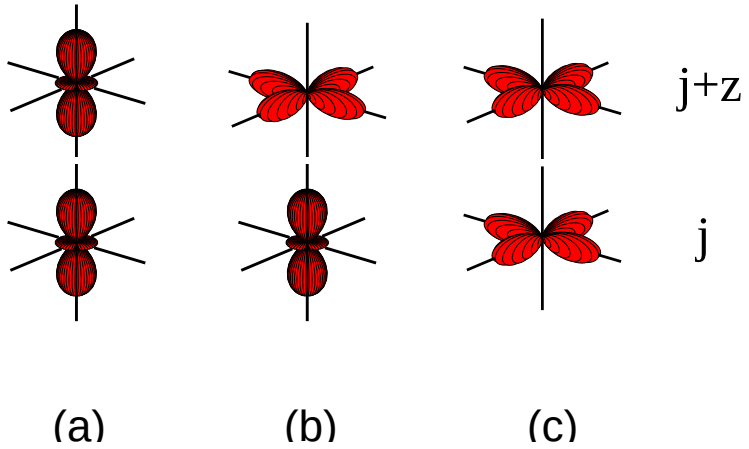

Figure 2.5: A bond of two e_g electrons along the z direction. Note that the overlap in (b) is zero. Figure taken from Ref. [39].

If one finds however the orbital configuration (b) of Fig. 2.5 the pseudo-spin part reads $(T_1^z - 1/2)\,(T_2^z + 1/2) + (T_1^z + 1/2)\,(T_2^z - 1/2)$ which can only be combined with the spin-triplet channel. One can show that the latter state becomes lower in energy for finite J_H [31, 40] (see Fig. 2.4(b)).

(ii) *degenerate t_{2g} orbitals* - In contrast to the e_g, orbitals the t_{2g} orbitals are magnetic. We again consider a bond in the z direction. The t_{2g} orbitals refer to $T = 1$ with $T^z = 1 \equiv d_{xz}$, $T^z = 0 \equiv d_{xy}$, and $T^z = -1 \equiv d_{yz}$. For the bond along z the $T^z = 0$ state has not to be considered because it can not take part in the hopping, as long as one takes the effective hopping via on oxygen into account. There are now no restrictions to the orbital channel and the Heisenberg-like form of the pseudo-spin Hamiltonian suggests the formation of orbital singlet and triplet states. Because the overall wavefunction has to be antisymmetric, the orbital triplet has to be combined with a spin singlet and vice versa. Interestingly, both states gain the *same* energy [37, 42]. Being a pure spin triplet, a ferromagnet will fluctuate in the orbital sector. A finite J_H will unbalance the ferromagnetic and antiferromagnetic contributions. The formation of this kind of orbital dimers has been suggested by G. Khaliullin for (quasi-)cubic systems. It is called in the literature *orbital liquid* [4, 37, 41–44]. For cubic symmetry, the orbital liquid is sketched in Fig. 2.6. The formation of dimers along all three cubic directions offers the possibility to lower the total energy. Two of three t_{2g} orbitals are involved in the superexchange in one particular direction. Since one t_{2g} orbital contributes in two of three directions, a fixed orbital pattern will not satisfy all bonds, but the kinetic energy can be lowered simultaneously in all three directions by orbital fluctuations (see Fig. 2.6). These fluctuations give rise to an isotropic orbital structure, which leads to an isotropic magnetic exchange coupling in all three directions. There are several predictions within the orbital-liquid picture for stabilizing different spin-orbital structures: for instance, for large J_H ferromagnetism should be stabilized together with a orbital ordering with principal axis [111]. This scenario has

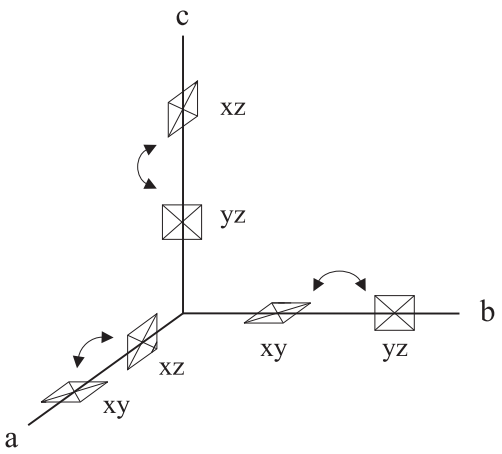

Figure 2.6: Two of three t_{2g} orbitals are involved in the superexchange in one particular direction, which may lead to a resonance. Figure taken from [41].

been suggested for $YTiO_3$ [43, 44]. Note that the applicability of the orbital-liquid picture to the titanates has been discussed controversially in the literature [7–11, 27, 45]. The majority of research groups favors the description of these systems in a rather conventional framework. We will come back to this issue in chapter 5. For further information on the orbital-liquid picture, we refer to a recent review article [37].

2.2.5 Lattice-mediated orbital interaction

There is a second mechanism which leads formally to the same kind of spin-orbital interaction, i.e. the Hamiltonian has the same form. It refers to a coupling via lattice vibrations. In the first section we discussed the Jahn-Teller effect as a source for lifting of the degeneracy on one particular transition-metal site which is surrounded by, e.g., an oxygen O_6 octahedron. In the pseudo-spin language, the Jahn-Teller Hamiltonian for an e_g electron on this transition-metal site reads [31, 39]:

$$H_{JT} = -gQ_3T^z + \frac{KQ_3^2}{2} \tag{2.10}$$

where g represents a coupling constant, T^z the pseudo-spin operator, K the elastic modulus, and Q_3 a $3z^2 - r^2$-like vibrational mode. If one considers now two neighboring transition-metal octahedra, an effective orbital interaction is induced, mediated by the vibrational mode [31, 39]. This is the *cooperative* Jahn-Teller effect

$$H_{i,i+1} = \frac{2g^2}{3K}T_i^zT_{i+1}^z \tag{2.11}$$

This Hamiltonian favors the antiferroorbital arrangement of the pseudo-spin, i.e. a $d_{3z^2-r^2}$-$d_{x^2-y^2}$ patterning along z. If the system is cubic a similar argumentation leads to a $d_{3x^2-r^2}$-

$d_{y^2-z^2}$ pattern along x[6]. If no direction is favored in the crystal this leads to an orbital frustration. In case of $LaMnO_3$, it has been nicely demonstrated that electronic as well as lattice-mediated orbital interactions are necessary [46]. The cooperative part of the Jahn-Teller effect is found to be the hidden driving force for the orbital ordering in $LaMnO_3$ [46].

So far we have only considered e_g-electron systems. For t_{2g} electrons the same considerations hold true. But things are more complicated because both, t_{2g} and e_g phonon modes, couple to t_{2g} electronic states. Also for t_{2g} systems there is formally no difference between the lattice-mediated orbital exchange and the spin-orbital superexchange [31, 44]. However, in the case of the lattice-mediated orbital interaction a term of the form of Eq. 2.10 will also enter the total system Hamiltonian, while it will not appear in a purely electronic spin-orbital system. This will lead to different ground and excited states.

2.3 On- and inter-site excitations and collective modes

In a semiconductor an optical transition can be expressed as the creation of an electron and a hole. Due to Blochs theorem electrons and holes are fully delocalized, i.e. one thinks in $\mathbf{k}$ space. Optical transitions can occur between electronic states which have equal $\mathbf{k}_e$, i.e. vertical excitations in an $E(\mathbf{k}_e)$ band diagram[7]. In other words, the total wavevector of the electron-hole pair has to be equal to zero $\mathbf{\Delta K} = \mathbf{k}_e + \mathbf{k}_h = 0$. We will give an illustrative picture for optical transitions in real space: one can think of an electron-hole pair, which is created on two arbitrary sites. Since all electron and all hole states belong equally to all sites, the electron-hole creation can be thought to be spread over all sites.

In the case of correlated materials the Bloch functions are no longer appropriate (with Bloch functions a metallic state is found at half filling). It is thus favorable to think in terms of real space, since the wavefunctions in the insulating ground state are expected to be rather localized. The optical excitations in a correlated material are sketched in Fig. 2.7 for the case of a ferromagnetic chain. An optical excitation creates an electron-hole pair. This can be done on the same site (onsite) or on neighboring sites (intersite). The onsite electron-hole creation as shown in Fig. 2.7(b) costs an energy of $\Delta_{orbital}$. When this excitation has a relatively small dispersion when compared to its excitation energy, it is commonly denoted as a crystal-field excitation or (onsite-)exciton. In contrast, if this excitation can move through the crystal, i.e. has a significant dispersion[8], it is sometimes termed as an orbital wave [47], in close analogy to spin waves.

The excitations across the conductivity gap are shown in Fig. 2.7(c). The hole refers to an empty site and the "electron" to a double occupancy. In this case, the double occupancy lives in the upper Hubbard band, thus this excitation is higher in energy than the onsite excitation ($\Delta_{orbital} \ll U$). Both, double occupancy and hole can freely move, i.e. they can

[6] This can be understood within the compass model [31, 39]. The pseudo-spin (T^z, T^x) plane is invariant under rotations of 120°.

[7] This is due to the large wavelength of visible light when comparing to the lattice spacing.

[8] The dispersion should be comparable to the excitation energy.

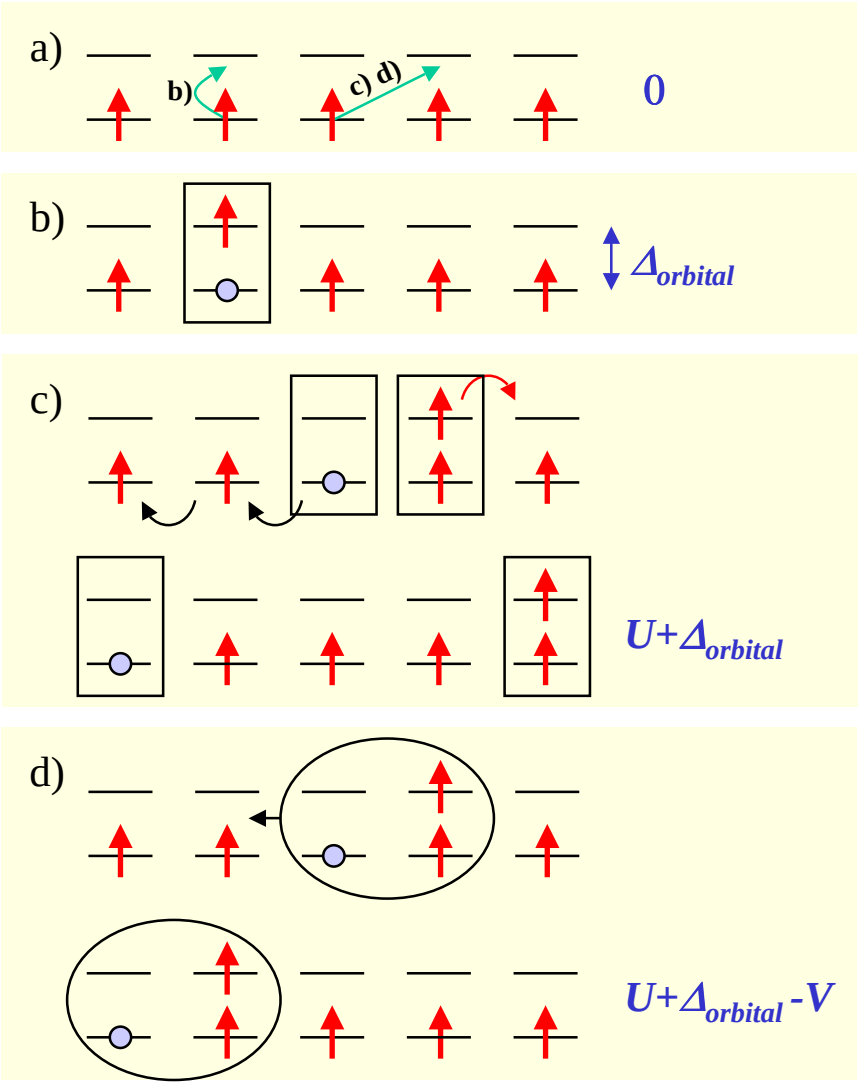

Figure 2.7: Sketch of possible optical excitations within a 1D chain: a) the ground state, b) onsite orbital excitation, c) inter-site excitation to an arbitrary site, i.e. the hole (empty site) and the "electron" (double occupancy) propagate independently, and d) inter-site excitation to a neighboring site (Mott-Hubbard exciton, bound electron-hole pair).

reside on any lattice site. Accordingly, the full bandwidth is observed in photoemission (PES, probing the single-hole states) and inverse photoemission (IPES, probing the states of one double occupancy). The conductivity gap corresponds to the difference of these two bands. It is the difference between the ionization energy E_I and the electron affinity E_A. Within our cartoon it corresponds to a transition between two sites which are far apart (so far that they no longer feel any interaction) as shown in Fig. 2.7(c). In our local cartoon the energy is thus $E_A - E_I = U + \Delta_{orbital}$. Things change when the double occupancy and the hole gain some additional attraction energy V. In this case, electron and hole may form a bound state and can disperse as only one object. This is also known as an exciton, but with a different size (see below). In the cartoon the transition energy is only $U - V + \Delta_{orbital}$ (see Fig. 2.7(d)). Taking into account the hopping t, it depends on the size of U, V and t whether the exciton is found as a truly bound state below the band gap or as a resonance inside the continuum [48]. In order to discriminate the excitons as found in semiconductors (Wannier and Frenkel [49]) we will denote the excitons in correlated materials as charge-transfer or Mott-Hubbard excitons [50]. It is important to note that optic is sensitive to both unbound electron-hole pairs and to excitons, whereas (I)PES do not allow for the direct observation of excitons.

2.3.1 Onsite excitations and collective modes

We start with excitations having no dispersion, i.e. crystal-field excitations within the d shell. We will call them onsite excitations, crystal-field excitations, or orbital excitations. Consider, e.g., the cubic structure in Fig. 2.1 where the electron resides in the lowest energy level. Now, a possible excitation is the transfer to a higher level. By analyzing the absorbed light of a white-light source the energy-level diagram can be measured. Putting this kind of excitations in the context of band-like solids, they can be regarded as onsite excitons. In semiconductors this kind of excitons is termed Frenkel exciton (see below). The bottleneck for the investigation of onsite excitations by optical spectroscopies is (i) the clear discrimination from other excitations which are simultaneously measured, (ii) in IR spectroscopy these excitations are parity forbidden and become only weakly allowed by the simultaneous excitations of a phonon. They can only be observed if they are located below the charge gap and above the phononic regime, otherwise they are masked by stronger excitations.

We will elaborate a bit on the first point. It might be that different degrees of freedom are intimately coupled to each other. In the case of a sizable electron-phonon coupling the orbital excitations are dressed by vibrational excitations. The combined vibrational-electronic excitation is called vibron. The underlying principle is the Franck-Condon principle [51, 52]. It is sketched in Fig. 2.8. Two parabolas are shown which represent the lattice potential of the ground state and the electronically excited state. The parabola of the excited state is shifted to the right due to the increased bond length. Since electronic transitions are usually much faster than motions of the nuclei (Born-Oppenheimer approximation), they are indicated as vertical lines, reflecting that the lattice can not change during the transition. As shown, the transition goes into a state at the side of

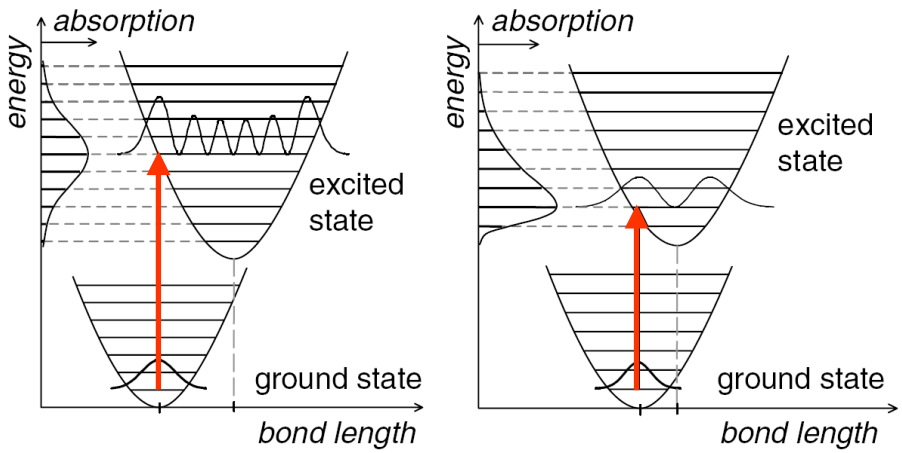

Figure 2.8: The Franck-Condon principle illustrates the occurrence of mixed vibrational and electronic states (vibronic states). The ground state and an electronically excited state of an ion are indicated by parabolas, where the minimum is shifted to larger bond lengths for the case of the excited state. Energetically equidistant horizonal lines represent the phonon levels of 1, 2, 3,.... phonons. Because electronic transitions are very fast when compared to the nuclear motions, they can be indicated as vertical arrows. The absorption is proportional to the overlap between the vibrational parts of the wave functions of ground and excited state (known as Franck-Condon factors). As indicated by two exemplary possibilities, e.g., in the left panel the maximum overlap does not occur between the minima of the two parabolas but from the ground state minimum to the side of the excited parabola, i.e. additionally to the electronic transition phonons are excited. The shape of the whole absorption band depends on the orbital and spin selection rules and on the difference in bond lengths between the ground state and the excited state. A larger difference results in a symmetric line shape (left), while a smaller difference leads to an asymmetric band (right). The figure has been taken from Ref. [26].

the parabola, i.e., a state where several phonons are excited. This leads to phononic side bands, in addition to the pure electronic transition in an absorption spectrum. In crystals several phonons (each with dispersion) may contribute to the Franck-Condon process, which makes the absorption band rather broad and structureless.

Things are "exciting" when the orbital excitations have a significant dispersion, i.e. they lose their local character. The excitations we would like to discuss here are those within the *degenerate* spin-orbital models. We will call these excitations orbitons or orbital waves. If a finite crystal field is switched on it will destroy the phenomena arising from degenerate orbitals when the energy gain due to the fluctuations of the orbitals is much lower than the size of the crystal field. Experimentally, the task is to find a compound in which the gain due to orbital fluctuations is larger than or at least comparable to the crystal-field splitting. However, also for a large crystal field the rather local excitations have a finite dispersion (Frenkel excitons), but for the low-energy properties the dispersion is only relevant if it is of the same order as the excitations energies.

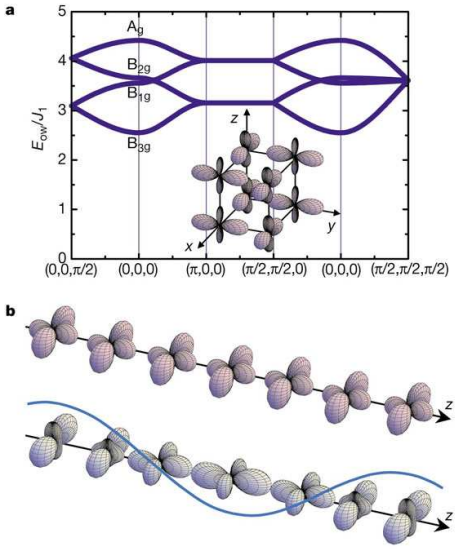

Figure 2.9: Orbital-wave dispersion as calculated for $LaMnO_3$ (top panel). Sketch of the propagation of an orbital wave for a ferroorbital chain (bottom panel). Picture taken from Ref. [47].

- *Orbital waves* - We start from an orbitally ordered ground state. Analogous to spin waves the excitations from this ground state are orbital waves, i.e. propagating orbital flips. This is shown in Fig. 2.9 for the case of a ferroorbitally ordered chain. The difference between spin waves and orbital waves lies in the symmetry properties of the spin and pseudo-spin operators: the spins are rotationally invariant while orbitals are restricted to certain axes (in cubic symmetry the cubic axes). It follows that orbital waves always have a gap [37]. Orbital waves have been suggested in the case of the orbitally ordered compound $LaMnO_3$ (e_g-orbital system) [47, 53] as well as for titanate and vanadate systems [47, 53–58] (see also chapter 5). However, a clear experimental evidence is still lacking, because the dispersion of the orbital waves has not been measured and because the orbital character of the observed excitations has not been demonstrated beyond any doubt. For instance in $LaMnO_3$, an alternative explanation in terms of multi-phonon absorption has been proposed [59]. Orbital waves show strongest dispersion when the coupling to the lattice is weak. The dispersion significantly reduces with increasing electron-phonon coupling [60, 61]. This might be the reason why so far no clear evidence for this dispersion has been reported in the literature. Experimentally, k-resolved spectroscopies like EELS[9] or RIXS[10] are best suited to track the dispersion. These techniques have been successfully used in order to determine the exciton dispersion in charge-transfer systems [62, 63].

[9]Electron energy loss spectroscopy.
[10]Resonant inelastic X-ray scattering.

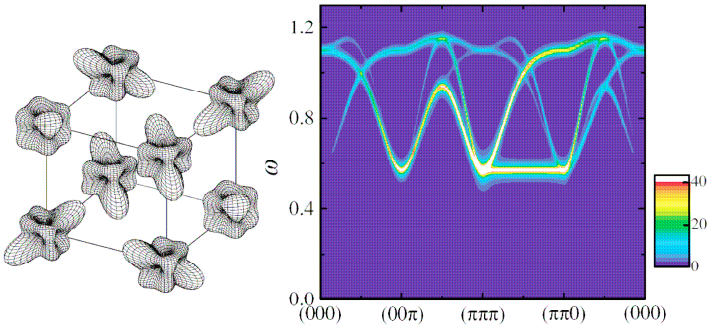

Figure 2.10: Orbiton dispersion as calculated for cubic $YTiO_3$ (right panel). Orbitally-ordered state, i.e. the electron density (left panel). Picture taken from Ref. [43].

- *Excitations from the orbital-liquid state (orbitons)* - Starting from an orbitally fluctuating ground state as discussed above, one finds also a dispersing excitation spectrum. It is shown for the case of cubic $YTiO_3$ in Fig. 2.10. Interestingly although the orbital ground state is fluctuating different spin orderings can be stabilized and orbital ordering can also survive (in the case of $YTiO_3$) [4, 37, 41–44]. Within the orbital-liquid picture a spin-orbital gap has been found and can be interpreted as the energy cost to break an orbital dimer. This behavior is similar to the gap formation in spin liquids such as two-leg ladders or dimerized spin-chains. Note, that orbital excitations always have a gap, in contrast to spin excitations (see above). Due to the striking similarity between spin and pseudo-spin Hamiltonians two-orbiton excitations [37, 64] in analogy to two-magnon excitations [65] have been proposed. Features in optical spectroscopy [26] and Raman scattering [57, 64] in $RTiO_3$ (R=Y, La) have been assigned to these kind of excitations (with an energy of roughly two times the spin-orbital gap) [37, 64]. We will comment on this issue in chapter 5.

2.3.2 Band-to-band transitions

In a semiconductor, band-to-band transitions occur with $\Delta\mathbf{K} = 0$. One can take a single electron with $\mathbf{k}_e$ from the valance band and put it into the conduction band at the same value of $\mathbf{k}_e$. This works only for non- or weakly interacting electrons. In a correlated insulator the interaction between electrons is strong. One can therefore not simply take one electron out without influencing the other electrons. Therefore we discuss the excitations in reals space as shown in Fig. 2.7. We will very briefly illustrate the two kinds of excitations: the Mott-Hubbard and the charge-transfer excitations. They are sketched in Fig. 2.11. Consider a Hubbard chain in the strong-coupling limit consisting of a transition-metal ion having only one orbital and one electron per site which can be either up or down spin. In between the transition metal ions we place an oxygen orbital which is filled with two electrons having antiparallel spins (a 1D two-band Hubbard model). We further assume that the system is antiferromagnetically ordered. The ground state is denoted by $d_i^1 d_j^1$.

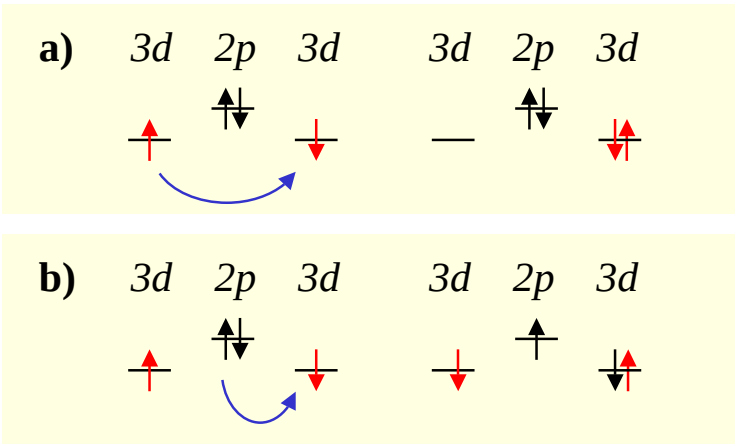

Figure 2.11: Sketch of Mott-Hubbard (a) and charge-transfer transitions (b) for the case of an antiferromagnetic chain.

For an intersite transition one has to remove one electron from one site i and place it on another site j. This can be done in two ways. Firstly, one can remove an electron from the transition-metal site and put it on the other transition-metal site. This state can be denoted as $d_i^0 d_j^2$. Secondly, one can remove one electron from the oxygen site, i.e., $d_i^1 d_j^2 \underline{L}$. This corresponds to two possible optical transitions: a Mott-Hubbard transition of the from $d_i^1 d_j^1 \rightarrow d_i^0 d_j^2$ with an energy $E(d^2) + E(d^0) - 2E(d^1) = U$, and a charge-transfer transition $d_i^1 d_j^1 \rightarrow d_i^1 d_j^2 \underline{L}$ with an energy $E(d^2\underline{L}) - E(d^1) = \Delta$. Depending on whether Δ or U is larger, the first observed intersite transition will be of Mott-Hubbard or charge-transfer type. Once identified one can determine the model parameters U and Δ from an optical spectrum. As one can see from Fig. 2.11, the oxygen can offer both, up and down spin, while the transition-metal site can only offer one spin channel in a magnetically ordered state. This fact makes it possible to disentangle[11] Mott-Hubbard and charge-transfer excitations. One expects changes of the spectral weight of a certain transition across the magnetic ordering temperature for a Mott-Hubbard insulator, while magnetism does not affect the charge-transfer transitions [69]. A lucid example for this behavior is given in Ref. [2] and will be discussed below and in chapter 4. Our above considerations hold only true if the oxygen band and the transition metal band are well separated and hybridization is low. There will be mixing of the two types, but one may still be able to determine the predominant character. In real materials things will become a bit more complicated because five-orbitals on the transition-metal site have to be considered for the case of a d-electron system. The onsite degeneracy will be lifted and the levels are split. The ground state and the final state will become rather complicated multiplets. The above considerations will not change in principle but one has to take many more possibilities of transitions into account. There will also be more model parameters, like

[11] Another possibility to differentiate between charge-transfer and Mott-Hubbard insulators are their different behavior upon electron and hole doping [66–68].

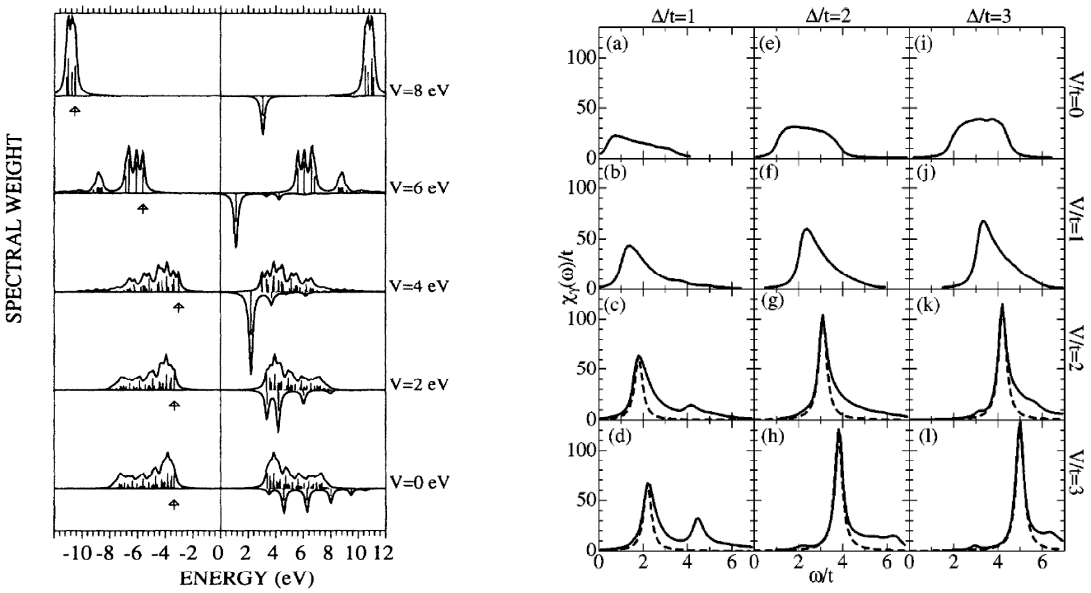

Figure 2.12: Excitons in a 1D extended Mott chain. Left: Mott-Hubbard exciton for a 14 site Mott-Hubbard ring with U=10 eV and t=1 eV for a one-band model for different values of V. The upper curves represent the electron removal and addition spectra as measured by PES and IPES, respectively. The lower curves represent the optical conductivity, where the arrows denote the zero of the energy, which for clarity is placed at the top of the lower Hubbard band. Figure taken from Ref. [48]. Right: charge-transfer exciton for a 129 site charge-transfer chain. Figure taken from Ref. [70].

J_H (or more generally speaking the Slater integrals) and the crystal-field parameters (see above). However, we will demonstrate that a determination of physically meaningful model parameters is possible from the experiment for the case of $LaSrMnO_4$ (see chapter 4) and for $YTiO_3$ (see chapter 5). A reference work for materials of Mott-Hubbard and charge-transfer type as well as their optical spectral can be found in Ref. [1].

2.3.3 Excitons

As already mentioned a bound electron-hole pair is termed an exciton. This pair propagates through the crystal as *one* particle with only one wave vector. The excitonic excitations are commonly found below the band gap of a semiconductor. One defines the binding energy of the excitons as the energetic distance to the electron-hole continuum. If the binding energy is low (meV), the exciton extends over many lattice spacings and is called *Wannier* exciton. Wannier excitons can be found e.g. in Cu_2O or GaAs [71, 72]. They can be very well described as hydrogen-like bound states, i.e. the energies are $E_n = E_g - R_x/n^2$, where E_g is the optical gap energy (the onset of the electron-hole continuum), R_x the renormalized Rhydberg constant of the exciton, and n the quantum number.

There are also excitons which have a binding energy of the order of eV. One can therefore conclude that the extension of the pair is very small, e.g. only one site. This kind of excitons is called Frenkel excitons. Typical examples are rare-gas crystals like Xe, Ne etc. or ionic crystals like LiF [71]. As discussed above, local *dd* excitations can also be regarded as Frenkel excitons (see Fig. 2.7(a)).

For correlated materials the observation of charge-transfer excitons has been reported. Their binding energies lie in between those of Frenkel and Wannier excitons. In the limit $t/V \to 0$ they extend over one TM-O bond (TM - transition-metal). The parameter V measures the nearest-neighbor binding energy but this is not the binding energy of the exciton [73]. Representative systems are e.g. high-T_c materials [62, 63, 74]. Theoretical spectra of a charge-transfer exciton are shown in Fig. 2.12.

In Mott-Hubbard insulators one expects *Mott-Hubbard* excitons because the charge-transfer band lies lower in energy [50]. Here we mean an exciton which extends over one TM-O-TM bond (in the limit $t/V \to 0$), i.e. the hole (empty site) and the "electron" (double occupancy) reside on neighboring TM sites. As pointed out by Essler *et al.* [75] the excitonic properties in a correlated system are somewhat different from ordinary Wannier excitons. This is due to the strong electron-electron coupling. Including nearest and next-nearest neighbor interactions V and V_2 in a model Hamiltonian for a 1D chain similar to Eq. 2.5 they found that the binding energy of the excitons does not change in a simple way with the nearest-neighbor interaction V. Including only nearest-neighbor interactions V the charge gap is not affected by a change of V as shown in Fig. 2.12. The class of Hamiltonians as e.g. used by Essler *et al.* is referred to as the extended Hubbard model [76]. As mentioned above the additional parameter to the single-band Hubbard model is the nearest-neighbor interaction V. The value of V can not be identified with the binding energy as defined above, because V has to exceed a critical value in order to yield a truly bound state. This means a Hubbard "exciton" can also be found as a resonance above the optical gap. This can be understood because the gap is very roughly speaking at $U - 2zt$ (see Fig. 2.3, z denotes the number of nearest neighbors) and the exciton is located at $U - V$. This means the binding energy is roughly $V - 2zt$ which can be positive ore negative. Such behavior is nicely shown in Fig. 2.12. One can clearly see that an excitonic resonance resides above the optical gap up to values of $V = 2t$ whereas a truly bound exciton is observed just below the gap for $V = 4t$. Note that in 1D our rough estimate of the binding energy $V - 2zt$ becomes positive for V>4t.

Another interesting aspect has been discussed by Wrobel and Eder [77]. In an antiferromagnetic background, the movement of a hole and/or double occupancy on separate tracks leaves back a number of misaligned spins. This track can be healed out by emitting magnons, which reduces the bandwidth from t to J. In an excitonic bound state the double occupancy "follows" the path of the hole, and these misaligned spins are healed out. This reduces the suppression of the bandwidth, thus the kinetic energy is reduced. This may contribute to the exciton binding energy. Excitonic binding due to the reduction of kinetic energy is obviously very different from the conventional mechanism, in which the potential energy is minimized. The similarity to the binding of electrons or holes in a two dimensional antiferromagnet (the Cooper-pair formation in the high-T_c materials) has

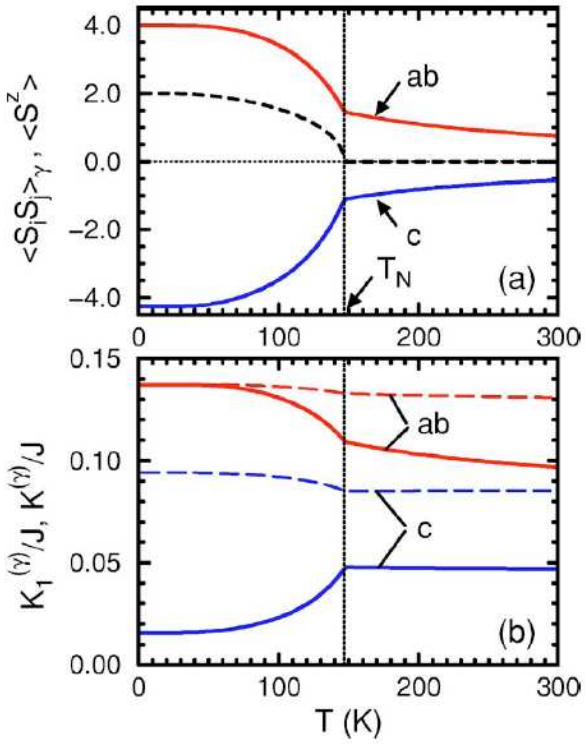

Figure 2.13: Top panel: nearest-neighbor spin-spin correlation function $\langle \mathbf{S}_i \cdot \mathbf{S}_j \rangle_\gamma$ ($\gamma = ab, c$) and the magnetic ordering parameter $\langle S^z \rangle$ as a function of temperature for $LaMnO_3$. Bottom panel: The evolution of kinetic energy K_γ/J per Mn-O-Mn bond according to superexchange interactions for all transitions within the e_g^2 manifold (dashed curves) and for the lowest transition into the e_g^2 high-spin state (solid curves). Taken from Ref. [83].

been pointed out [77]. We will refer to this study in chapter 5.

There are several theoretical studies dealing with excitons on one- and two-dimensional Hubbard models. To summarize the main features for a fixed Hubbard $U \gg V, t$: with increasing V optical weight is shifted to lower energies. In 1D above a critical value of V a bound state is formed below the optical gap. Upon a further increase of V the system enters a charge-density wave state by forming electron-hole droplets or exciton strings [48, 73, 75, 78–80]. In 2D the optical spectra look similar but in contrast to 1D not only one but many different eigenstates contribute to the bound state below or within the electron-hole continuum [81, 82].

2.3.4 The intensity of an optical transition

Optical selection rules will limit the number of observable final states. They can give valuable information about the spin and orbital states of the observed compound, because one can test the selection rules for a certain spin-orbital pattern and compare to the

measured transitions. However, this does not necessarily lead to clear answers. Additional information can be gained from the temperature dependence of a certain optical transition A. One has to monitor the integral over the optical conductivity (called the spectral weight) as a function of temperature:

$$SW(T) = \int_A \sigma_1(\omega) d\omega \tag{2.12}$$

For the following we will only consider electric dipole transitions since magnetic dipole and electric quadrupole transitions are weak. Relative to the electric dipole transitions their intensities are reduced by a factor $10^{-5} - 10^{-6}$ [72, 84].

When the electronic wave functions can be written as a product of spin, orbital, and lattice degrees of freedom[12], the selection rules and the temperature dependence of all contributions can be treated separately. However, especially in correlated materials all degrees of freedom may be coupled with each other and the above approximation breaks down. Nevertheless we will start from the most simple case, i.e. a decoupling of all degrees of freedom.

At first we discuss the vibrational degree of freedom. For parity-allowed transitions the intensity should be independent of temperature [21, 84]. However, thermal expansion and electron-phonon-coupling will give rise to a change of the interatomic distances with temperature, and thus will change the hybridization. Therefore one expects a change in intensity: if the lattice spacing increases with temperature one generally expects a loss of intensity in a certain channel of excitations.

For a parity-forbidden transition (e.g. onsite *dd* transitions) the latter argumentation remains valid. On top of that an increase of intensity according to the *coth*-rule is expected [21, 84, 85]:

$$I(T) = I_0 \sqrt{\coth\left(\frac{\hbar\Omega}{2k_B T}\right)} \tag{2.13}$$

The simultaneous excitation of an odd-parity phonon will lead to an admixture of odd-parity orbital states (p) to the even-parity electronic orbital wavefunctions (d). This admixture will scale with the thermal population of the phonons. The formally forbidden "even-even" transitions become more and more dipole allowed. The same argumentation holds true for indirect transitions in a band semiconductor.

The spin selection rule limits the number of final states that can be reached. If the orbital moment is quenched or the spin-orbit coupling is small (as assumed for our systems), then the total spin of the initial and final state have to be equal, i.e. $S_i^z = S_f^z$. The temperature dependence arising from the spin selection rule is related to the nearest-neighbor spin-spin correlation function. This correlation function gives a measure of short-range spin alignments as function of temperature. Although long-range order is lost at T_N or T_c, short-range "ordering" persists up to temperatures above the magnetic ordering temperature.

[12] There is also one part referring to the charge degree of freedom. This will not be discussed here because the major part of the work presented in this thesis deals with compounds which are insulation but not charge ordered.

In contrast also below T_N or T_c one will find a certain amount of "disordered" spins. In general one expects a redistribution of weight with temperature for the different spin channels. As an example we have chosen the system $LaMnO_3$, which is an $S = 2$ system [2, 83]. Since the orbital ordering temperature in $LaMnO_3$ is known to be located at 780 K (far above $T_N = 150$ K), one can assume that the orbitals are locked in their orbitally ordered pattern. It is sufficient to take only the spin degree of freedom into account. The spin-spin correlation function as derived by Oles *et al.* [83] is plotted in Fig. 2.13. At low temperatures $T \ll T_N$ the spin-spin correlation function $\langle \mathbf{S}_i \cdot \mathbf{S}_j \rangle_{ab} \rightarrow 4$, while at high temperatures $\langle \mathbf{S}_i \cdot \mathbf{S}_j \rangle_{ab} \rightarrow 0$. This can be understood since within the ab direction neighboring spins are parallel which yields in a classical treatment a value of four with $S = 2$. In the paramagnetic state the correlation function should be zero. Similar arguments yield $\langle \mathbf{S}_i \cdot \mathbf{S}_j \rangle_c \rightarrow -4$ since spins are ordered anti-parallel in this crystal direction. For the spectral weight in the ab direction this means the following: a transition which is allowed only for ferromagnetic spin alignment gets suppressed when the system becomes paramagnetic. In contrast a transition which is allowed only for an antiferromagnetic alignment becomes more allowed in the paramagnetic state. The precise evolution of the spin-spin correlation function with temperature shows that even at $2 \cdot T_N$ the correlation functions are still ± 0.5.

The orbital selection rule takes the overlap between different orbitals into account. There is for example no overlap between the d_{xy} and d_{xz} orbitals on neighboring sites in a cubic crystal (see Fig. 2.1). In cubic symmetry t_{2g} orbitals generally only have overlap with the same t_{2g} orbital, while all e_g orbitals overlap with each other. There is no overlap between t_{2g} and e_g orbitals. The temperature dependence arising from the orbital selection rule is related to the orbital-orbital correlation function. By introducing the pseudo-spin operators the problem can be dealt with in an analogue fashion as in the spin case. To be more illustrative: an orbital-ordering pattern can be destroyed by thermal fluctuations. For $LaMnO_3$ an orbital ordering of the form $|\pm\rangle = \cos(\frac{\theta}{2})|d_{3z^2-r^2}\rangle \pm \sin(\frac{\theta}{2})|d_{x^2-y^2}\rangle$ along the ab direction has been reported [87], whereas ferro-orbital ordering along the c direction has been proposed. The angle θ is the mixing angle of the two different e_g orbitals and has a value of approximately $\theta = 108°$ in $LaMnO_3$ [2, 87, 88]. Assuming analogous to the spins that the pseudo-spins are classical vectors, the correlation function along the ab direction reads for $T \ll T_{OO}$ $\langle \frac{1}{4} - \tau_i \cdot \tau_j \rangle_{ab} \rightarrow \frac{1}{4}(\frac{3}{4} + \sin^2\theta)$ [2, 83]. For the para-orbital phase for $T \gg T_{OO}$ one expects $\langle \frac{1}{4} - \tau_i \cdot \tau_j \rangle_{ab} \rightarrow \frac{1}{4}$. For the c axis one finds: $\langle \frac{1}{4} - \tau_i \cdot \tau_j \rangle_c \rightarrow \frac{1}{4}(\sin^2\theta)$ (for $T \ll T_{OO}$) and $\langle \frac{1}{4} - \tau_i \cdot \tau_j \rangle_c \rightarrow \frac{1}{4}$ (for $T \gg T_{OO}$). A sizable orbital-lattice coupling will destroy the spin-orbital correlations because the orbitals will be pinned to the lattice.

In general all different degrees of freedom are not necessarily decoupled. In case of titanate and vanadate systems the importance of a coupled spin-orbital correlation function has been pointed out [37, 42, 83, 86]. This leads to corrections in the evolution of spectral weight with temperature. As an example we plot these corrections as calculated for the d^2 system $LaVO_3$ in Fig. 2.14. In the upper panel one can see that the inclusion of the spin-orbital nearest-neighbor correlations leads to a further decrease of spectral weight ($\equiv$ kinetic energy).

To give a brief conclusion: the temperature dependence of the spectral weight measures

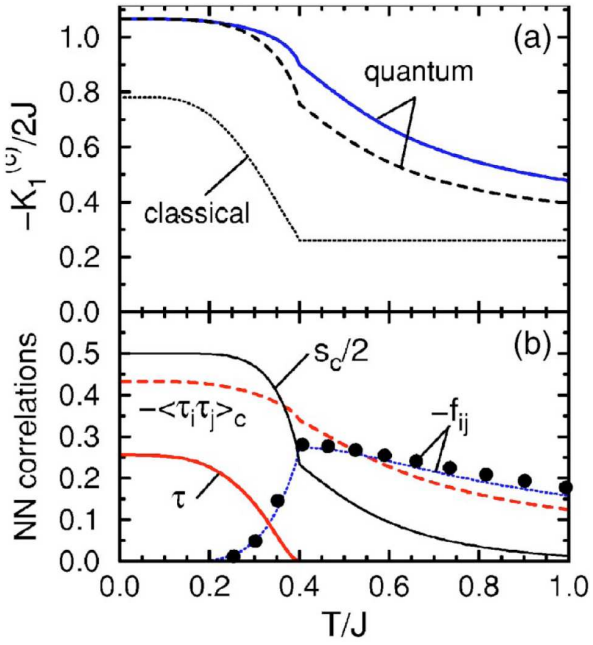

Figure 2.14: Top panel: Kinetic energy (≡ spectral weight) of a high-spin excitation in a d^2 system (here $LaVO_3$) within a classical model and two quantum models with (solid) and without (dashed) joined spin-orbital correlations. Bottom panel: nearest-neighbor correlation functions, namely the spin $s_c = \langle \mathbf{S}_i \cdot \mathbf{S}_j \rangle$, the orbital $\tau_c = \langle \tau_i \cdot \tau_j \rangle$, and the joined spin-orbital correlation function $f_{ij} = \langle \delta(\mathbf{S}_i \cdot \mathbf{S}_j)\delta(\tau_i \cdot \tau_j) \rangle$. Additionally the orbital order parameter τ is plotted. Taken from Ref. [86].

the contributions of all different degrees of freedom, spin, orbital, (charge,) and lattice contributions. In the simplest case these contributions can be treated separately. In the manganite systems this approach is frequently applied because orbital ordering and magnetic ordering temperatures are very different. It depends strongly on the nearest-neighbor spin-orbital arrangement whether the intensity decreases or increases with temperature. We will analyze our spectra under the assumption that decoupling of all degrees of freedom is possible and will see to what extend the data can be understood within this framework.

3 Spectroscopic techniques

Optical spectroscopy and Raman scattering are widely used techniques in solid state physics. A large number of excitations, e.g. phonons, magnons, excitons, orbital excitations, etc. can be monitored. Furthermore, optical spectroscopy gives information about the band structure of solids and the magnitude of the electronic gap.

The quantity of interest in optical spectroscopy is the complex refractive index

$$N = n + ik. \tag{3.1}$$

The real part of N quantifies the ability of a material to change the direction of a light wave following Snell's law. The extinction k describes the damping of a light wave in a material. Via Fermi's golden rule it is directly related to the transition probabilities for the excitations mentioned above. Being interested in the microscopic properties and excitations of a solid, it is the goal to determine k for different frequencies.

The corresponding quantity in Raman spectroscopy is the scattering cross section. It quantifies the probability, that an incoming light wave is inelastically scattered by an elementary excitation. For crystals with inversion symmetry, Raman scattering is complementary to optical spectroscopy, because it probes even-parity excitations, in contrary to optical spectroscopy, which is sensitive to odd-parity excitations.

The typical energy range of excitations probed by optical spectroscopy and Raman scattering is meV-eV. Often the energy is given in wavenumbers, sometimes called Kayser:

$$1 \text{ cm}^{-1} = 0.12398 \text{ meV} = 29.979 \text{ GHz} \tag{3.2}$$

The wavenumber will be denoted by ω.

The data presented in this thesis were obtained by three different optical techniques. The following sections give a brief introduction into these. In the first part, the basics of optical spectroscopy are summarized. The second part introduces briefly the Fourier transform spectroscopy. Detailed information about this technique can be obtained from previous theses [89, 90]. The third part elucidates ellipsometry. In 2004 a Woollam ellipsometer type VASE has been purchased by the Institute of Physics II of the University of Cologne and has been put into operation by my colleague C. Hilgers and myself. Therefore, we place emphasis on the latter section. An exemplary data analysis is shown for the case of $YTiO_3$. The last part deals with Raman scattering[1].

[1]The Raman measurements were carried out at the MPI Suttgart in collaboration with C. Ulrich and B. Keimer. I heartily thank for this fruitful collaboration.

3.1 Linear response functions and optical constants

An electromagnetic field **E** evokes a response in a solid. For a homogeneous medium the *linear part* of the response can be expressed in terms of the displacement field **D**, the current **J**, or the polarization **P** of the form:

$$\begin{aligned} \mathbf{D}(\mathbf{k},\omega) &= \epsilon_0\,\epsilon(\mathbf{k},\omega)\,\mathbf{E}(\mathbf{k},\omega), \\ \mathbf{J}(\mathbf{k},\omega) &= \sigma(\mathbf{k},\omega)\,\mathbf{E}(\mathbf{k},\omega), \\ \mathbf{P}(\mathbf{k},\omega) &= \epsilon_0\,\chi(\mathbf{k},\omega)\,\mathbf{E}(\mathbf{k},\omega) \end{aligned} \tag{3.3}$$

where $\mathbf{k}$ and ω are the momentum and the frequency. The optical constants ϵ, σ, and χ are called dielectric permittivity or dielectric constant, optical conductivity, and electric susceptibility tensors. They are complex second rank tensors, which have to satisfy the crystal symmetry. The relation to the index of refraction will be given below. In the further discussion the following limitations are made, adapted to our case:

1. The solid is a homogeneous medium.

2. Since in optical spectroscopy the wave vectors are close to zero we assume $\mathbf{k} = 0$ and use $\epsilon(0,\omega) \equiv \epsilon(\omega)$, $\sigma(0,\omega) \equiv \sigma(\omega)$, and $\chi(0,\omega)_e \equiv \chi_e(\omega)$.

3. For optical frequencies it is sufficient to set the real part of the permeability $\mu_1 = 1$ and its imaginary part $\mu_2 = 0$ [91].

4. We will follow the semiclassical approximation, i.e. the electronic states of the solid are treated quantum mechanically, while the electromagnetic radiation is treated classically.

5. The interaction of light with matter (for a one-electron system) can be described by the following Hamiltonian.

$$\mathbf{H} = \mathbf{H}_0 + \frac{e}{m}\mathbf{A}\cdot\mathbf{p} + \cancel{\frac{e^2}{2m}\mathbf{A}^2} \tag{3.4}$$

The system $\mathbf{H}_0 = \frac{\mathbf{p}^2}{2m} + \mathbf{V}(\mathbf{r})$ will be perturbed by $\frac{e}{m}\mathbf{A}\cdot\mathbf{p}$, with $\mathbf{A}$ and $\mathbf{p}$ being the vector potential and the momentum operator. Note, that we assume the Coloumb gauge $\nabla\cdot\mathbf{A} = 0$. The term proportional to $\mathbf{A}^2$ is omitted since we will focus on the linear response. For the vector potential a plane wave $\mathbf{A} = \mathbf{A_0}\left(\mathrm{e}^{i(\mathbf{k}\cdot\mathbf{r}-\omega t)} + \mathrm{e}^{-i(\mathbf{k}\cdot\mathbf{r}-\omega t)}\right)$ is assumed. Our experiments are carried out in an energy range of approximately 0.1-6.0 eV which means $\mathbf{k}\cdot\mathbf{r} \sim 10^{-3}..10^{-5}$ if one assumes a dimension of $|\mathbf{k}| \sim 10^{-10}$ m. Therefore one can assume $\mathrm{e}^{i\mathbf{k}\cdot\mathbf{r}} \simeq 1$ which is called dipole approximation. Equation (3.4) reduces with $\mathbf{E} = -\frac{\partial\mathbf{A}}{\partial t}$ and $[\mathbf{H}_0, \mathbf{r}] = \frac{i\hbar}{m}\,\mathbf{p}$ to

$$\mathbf{H} = \mathbf{H}_0 - e\,\mathbf{E}\cdot\mathbf{r}. \tag{3.5}$$

6. The symmetry of the systems investigated within this thesis is orthorhombic or higher. Therefore the tensor of the optical constants will be diagonal:

$$\begin{aligned}
\epsilon &= \begin{pmatrix} \epsilon_{xx} & 0 & 0 \\ 0 & \epsilon_{yy} & 0 \\ 0 & 0 & \epsilon_{zz} \end{pmatrix}, \\
\sigma &= \begin{pmatrix} \sigma_{xx} & 0 & 0 \\ 0 & \sigma_{yy} & 0 \\ 0 & 0 & \sigma_{zz} \end{pmatrix}, \\
\chi &= \begin{pmatrix} \chi_{xx} & 0 & 0 \\ 0 & \chi_{yy} & 0 \\ 0 & 0 & \chi_{zz} \end{pmatrix}. \qquad (3.6)
\end{aligned}$$

   Note, that the tensor axes of ϵ_{jj}, σ_{jj}, and χ_{jj} coincide with the crystallographic axes. For lower crystal symmetry than orthorhombic this is not the case.

Under the latter assumptions the optical constants

$$\begin{aligned}
\epsilon &= \epsilon_1 + i\,\epsilon_2, \\
\sigma &= \sigma_1 + i\,\sigma_2, \\
\chi &= \chi_1 + i\,\chi_2, \\
N &= n + i\,k \qquad (3.7)
\end{aligned}$$

can be converted into each other following table (3.1). As a consequence of the law of causality, it can be shown that real and imaginary part of each optical constant are not independent of each other. The relationship is called Kramers-Kronig relation. For the optical constants n and k it has the form [93]:

$$\begin{aligned}
n(\omega) &= 1 + \frac{2}{\pi}\mathcal{P}\int_0^\infty \frac{\omega' k(\omega')}{\omega'^2 - \omega^2} d\omega' \\
k(\omega) &= -\frac{2}{\pi\,\omega}\mathcal{P}\int_0^\infty \frac{\omega'^2 (n(\omega') - 1)}{\omega'^2 - \omega^2} d\omega' \qquad (3.8)
\end{aligned}$$

with $\mathcal{P}$ being the Cauchy principal value of the integral. The relationship gives additional input for the determination of the optical constants from experiments. On the one hand the knowledge of e.g. the real part of an optical constant over a large energy range is sufficient in order to get its imaginary part. This is the common procedure for the determination of

Table 3.1: Conversion table between optical constants ϵ, σ, χ, and N in SI units [92]. While ϵ, χ, and N are dimensionless, σ is given in $[\sigma] = \Omega^{-1}\mathrm{cm}^{-1}$. The permittivity of the vacuum is $\epsilon_0 = 8.85 \cdot 10^{-14}$ $\mathrm{s}\Omega^{-1}\mathrm{cm}^{-1}$. Note, that $\tilde{\omega} = 2\pi\nu$ is the angular frequency in s^{-1} and ν being the frequency in Hz. In this thesis we will use ω in wavenumbers instead of $\tilde{\omega}$. These two quantities can be translated into each other using equation (3.2): $\tilde{\omega}[\mathrm{s}^{-1}] = 2\pi \cdot 29.97 \cdot 10^9\ \omega[\mathrm{cm}^{-1}]$.

	ϵ	σ	χ	N
ϵ	1	$\epsilon_1 = 1 - \frac{\sigma_2}{\epsilon_0\tilde{\omega}}$ $\epsilon_2 = \frac{\sigma_1}{\epsilon_0\tilde{\omega}}$	$\epsilon_1 = \chi_1 + 1$ $\epsilon_2 = \chi_2$	$\epsilon_1 = n^2 - k^2$ $\epsilon_2 = 2nk$
σ	$\sigma_1 = \epsilon_0\tilde{\omega}\epsilon_2$ $\sigma_2 = \epsilon_0\tilde{\omega}(1 - \epsilon_1)$	1	$\sigma_1 = \epsilon_0\tilde{\omega}\chi_2$ $\sigma_2 = -\epsilon_0\tilde{\omega}\chi_1$	$\sigma_1 = 2\epsilon_0\tilde{\omega}nk$ $\sigma_2 = \epsilon_0\tilde{\omega}(1 - n^2 + k^2)$
χ	$\chi_1 = \epsilon_1 - 1$ $\chi_2 = \epsilon_2$	$\chi_1 = -\frac{\sigma_2}{\epsilon_0\tilde{\omega}}$ $\chi_2 = \frac{\sigma_1}{\epsilon_0\tilde{\omega}}$	1	$\chi_1 = n^2 - k^2 - 1$ $\chi_2 = 2nk$
N	$n = \sqrt{\frac{\epsilon_1 + \lvert\epsilon\rvert}{2}}$ $k = \sqrt{\frac{-\epsilon_1 + \lvert\epsilon\rvert}{2}}$	$n = \sqrt{\frac{1 - \frac{\sigma_2}{\epsilon_0\tilde{\omega}} + \sqrt{(\frac{\sigma_1}{\epsilon_0\tilde{\omega}})^2 + (1 - \frac{\sigma_2}{\epsilon_0\tilde{\omega}})^2}}{2}}$ $k = \sqrt{\frac{-1 + \frac{\sigma_2}{\epsilon_0\tilde{\omega}} + \sqrt{(\frac{\sigma_1}{\epsilon_0\tilde{\omega}})^2 + (1 - \frac{\sigma_2}{\epsilon_0\tilde{\omega}})^2}}{2}}$	$n = \sqrt{\frac{1 + \chi_1 + \sqrt{(1+\chi_1)^2 + (\chi_2)^2}}{2}}$ $k = \sqrt{\frac{-1 - \chi_1 + \sqrt{(1+\chi_1)^2 + (\chi_2)^2}}{2}}$	1

the optical constants from reflectivity measurements alone (see below). On the other hand, if both the real and imaginary part of an optical constant are determined independently, the Kramers-Kronig relation can be used as a consistency check of the results. This is done in the case of ellipsometric measurements (see below).

3.2 Fourier-transform spectroscopy

Fourier-transform spectroscopy is a linear optical spectroscopy, which can be used to determine the reflectivity and the transmittance of a sample[2]. For the transmittance measurements the samples have to be sufficiently transparent. In practice these two quantities are obtained by two intensity measurements:

$$T(\omega) = \frac{I_T(\omega)}{I_0(\omega)}, \quad R(\omega) = \frac{I_R(\omega)}{I_{Au}(\omega)} \tag{3.9}$$

The intensity I_T (I_R) represents the measured intensity when the sample is placed into the light path, while for the reference intensity I_0 (I_{Au}) the transmitted (reflected) light without a crystal (on an Au mirror) is measured.

In order to obtain the optical constants n and k one should measure on two different samples of the same batch: one thin sample, which is sufficiently transparent to have a measurable transmittance, and one semi-infinite sample, where the reflectivity is determined by a single-interface reflection. In order to probe orbital or spin excitations below the Mott gap in correlated insulators the thickness has to be of the order of 10-300 μm, in order to measure a sizable transmittance up to 1 eV. By using the Fresnel equations as well as the Lambert-Beer absorption law, one gets the following relations between reflectivity, transmittance and the optical constants n and k [89, 92] [3].

$$\begin{aligned} R &= \frac{(n-1)^2 + k^2}{(n+1)^2 + k^2} \\ T &= \frac{(1-R)^2\Phi}{1-(R\Phi)^2} \\ \Phi &= e^{-(4\pi\, k\, d\, \omega)/10^4} \end{aligned} \tag{3.10}$$

[2]The discussion is restricted to a Michelson type spectrometer. Other types like e.g. Mach-Zener can also measure the phase.

[3]The equation given here follows from the equation given in Ref. [92] for $n \gg k$. If k is too large the sample would not be transparent.

From their inversion the optical constants can be obtained:

$$\begin{aligned} k &= \frac{10^4}{4\pi\, d\, \omega} \ln \frac{-2R^2T}{(1-R)^2 - \sqrt{(1-R)^4 + 4R^2T^2}} \\ n &= \frac{1 + R + \sqrt{4R - k^2(R-1)^2}}{1-R} \end{aligned} \tag{3.11}$$

where d denotes the thickness of the sample in μm for the transmittance measurement and ω the frequency in cm^{-1}. The results of Eq. 3.11 can be converted in every pair of optical constants using Tab. 3.1.

The transmittance in Eq. 3.10 is obtained by superposing intensities of multiply-reflected waves up to infinity, interference between these waves is neglected. In practise Fabry-Perot fringes might be observed for the case of almost parallel back- and front surfaces. If these fringes are averaged out, Eq. 3.10 can be used again. The observation of fringes with a frequency distance of $\Delta\omega$ has the advantage, that the thickness d can be determined by

$$d = \frac{1}{2n\Delta\omega}, \quad [d] \text{ in cm.} \tag{3.12}$$

For non-transparent samples, e.g. metals or insulators above their gap, the extinction is large. This makes a transmission measurement impossible, because the transmission becomes smaller than the noise levels for a thickness of the order of μm. But one can also obtain the two optical constants from the reflectivity measurement alone by considering not only the intensity R and but also phase ϕ_r. This can be directly seen in the general expression for the reflection coefficient r, and its relation to Eq. 3.10:

$$\begin{aligned} r &= \frac{(n-1)+ik}{(n+1)+ik} = \sqrt{R}\, e^{i\phi_r} \text{ or } \ln r = \ln\sqrt{R} + i\phi_r \\ R &= |r|^2 = r\, r^* \end{aligned} \tag{3.13}$$

The phase can either be measured or it can be calculated making use of the Kramers-Kronig relation [92]:

$$\phi_r(\omega) = -\frac{\omega}{\pi} \int_0^\infty \frac{\ln\sqrt{R(\omega')} - \ln\sqrt{R(\omega)}}{\omega'^2 - \omega^2} d\omega' \tag{3.14}$$

Please note, that for an accurate determination of ϕ_r the reflectivity has to be measured over a very broad energy range (strictly speaking 0 to ∞ cm^{-1}). For the determination of rather strong absorption features, arising e.g. from phonons, this technique gives reliable results. However, weak absorption peaks of a few Ω^{-1}cm^{-1} arising from combined excitations, like bimagnon-plus-phonon [94, 95] or orbiton-plus-phonon [26], can not be resolved. The optical constants presented in this thesis are not based on reflectivity measurements alone, but on ellipsometry or combined R and T measurements, as discussed above.

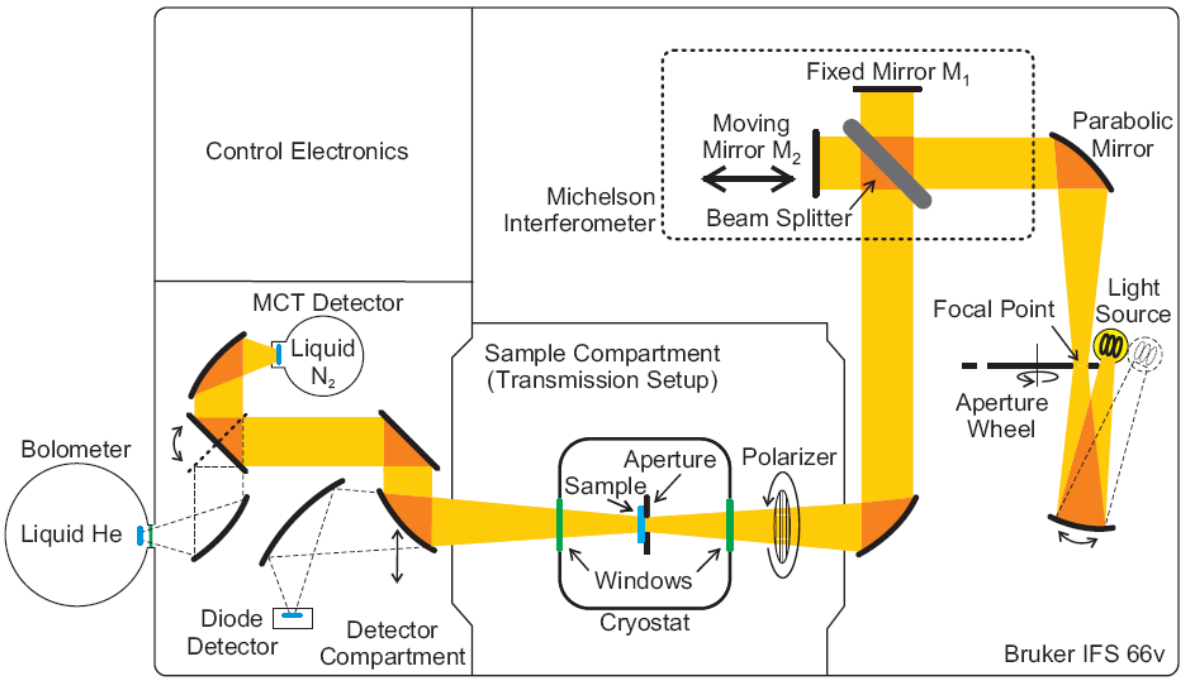

Figure 3.1: Sketch of the Fourier-transform spectrometer in transmittance configuration (Bruker IFS 66v). Picture taken from Ref. [89].

3.2.1 Experimental setup

Within a standard setup consisting out of a white-light source and a monochromator the quantities R and T are determined frequency-wise. In contrast, Fourier-transform (FT) spectroscopy measures a whole frequency band at once. In the infrared range this has the great advantage that the intensity at the detector is large, which greatly improves the signal-to-noise ratio (SNR) and makes this technique extremely fast. Furthermore the SNR is improved by the large *throughput* of a FT spectrometer in comparison to a monochromator, because circular apertures (mm) can be used without losing resolution. In a monochromator the entrance slits determine the resolution of the measurement and therefore they usually have to be quite narrow (few hundred μm).

The setup of the FT spectrometer in Cologne (Bruker IFS 66v) is shown in Fig. 3.1. The light of a broad-band lamp is focussed onto an aperture wheel. A parabolic mirror makes the light parallel before it passes through the heart of the FT spectrometer, the Michelson interferometer (see below). From the interferometer the light moves through a polarizer and is focussed onto the sample, which is located in a He-cooled cryostat. Temperatures from 4.2-780 K can be achieved. Behind the sample the transmitted light is focused by several mirrors onto the detector. Depending on the energy range, the corresponding set of detector, polarizer, cryostat windows, beam splitter and lamp has

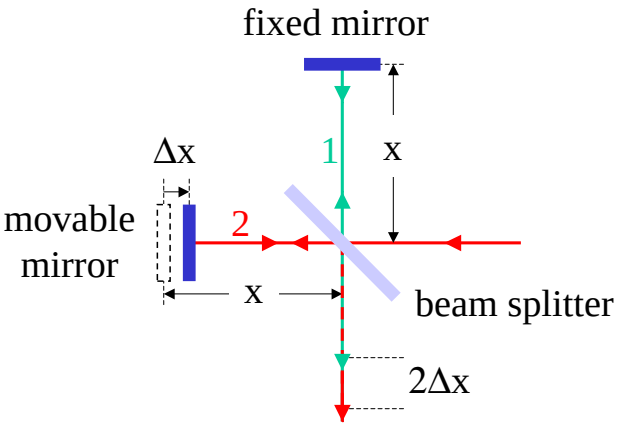

Figure 3.2: Sketch of a Michelson interferometer.

to be adapted. To cover the full energy range of the spectrometer of 10-55000 cm^{-1} (1.2 meV-6.8 eV), at least five different combinations are needed. For the reflectivity measurements (not shown) an additional unit containing four mirrors has to be placed into the spectrometer. The measurements can be carried out under quasi-normal incidence (11°). The reflectance/transmittance measurements presented in this thesis were performed in the mid- and near-infrared regime, i.e. from 650-12000 cm^{-1} (0.08 eV-1.49 eV). We used a nitrogen-cooled Mercury Cadium Telluride detector (MCT), a BaF_2 polarizer[4], KBr cryostat windows, a Ge/KBr beam splitter and two different lamps (Globar/Tungsten).

The functionality of the Michelson interferometer is sketched in Fig. 3.2: it consists of a beam splitter and two mirrors, of which one can move back an forth. If the movable mirror has the same distance x from the beam splitter as the fixed mirror (symmetric position), there will be no retardation between the two light paths 1 and 2. Regardless of the wavelength, constructive interference will occur (this position of the mirror is called white-light position). If the movable mirror is shifted Δx away from its symmetric position there will be a retardation $2\Delta x$ between the two light paths 1 and 2. One expects constructive interference only for the positions $2\Delta x = n\lambda$ with $n = 1, 2, ...$ Therefore the measured (time averaged) intensity for one wavelength λ at the detector will depend on the mirror position, which results in an intensity distribution [92] $I(\Delta x) = \frac{I_0}{2}(1+\cos(4\pi\Delta x/\lambda))$. The function $I(\Delta x)$ is called interferogram. A generalization for a whole spectrum yields

$$I(\Delta x) = \frac{1}{2}\int_0^\infty I(\omega)\big(1+\cos(4\pi\Delta x\,\omega)\big)d\omega \tag{3.15}$$

where the cosine integrand is the Fourier transform of $I(\Delta x)$ while $\frac{1}{2}\int_0^\infty I(\omega)d\omega$ gives the averaged intensity $I_0/2$. Thus, the inverse Fourier transform of $I(\Delta x)$ yields the frequency-resolved intensity spectrum $I(\omega)$. The latter procedure is exactly applied in FT spectrometry. The remaining problem is the determination of the mirror position Δx. It can be very

[4]The small polarizer leakage is corrected as described in Ref. [89].

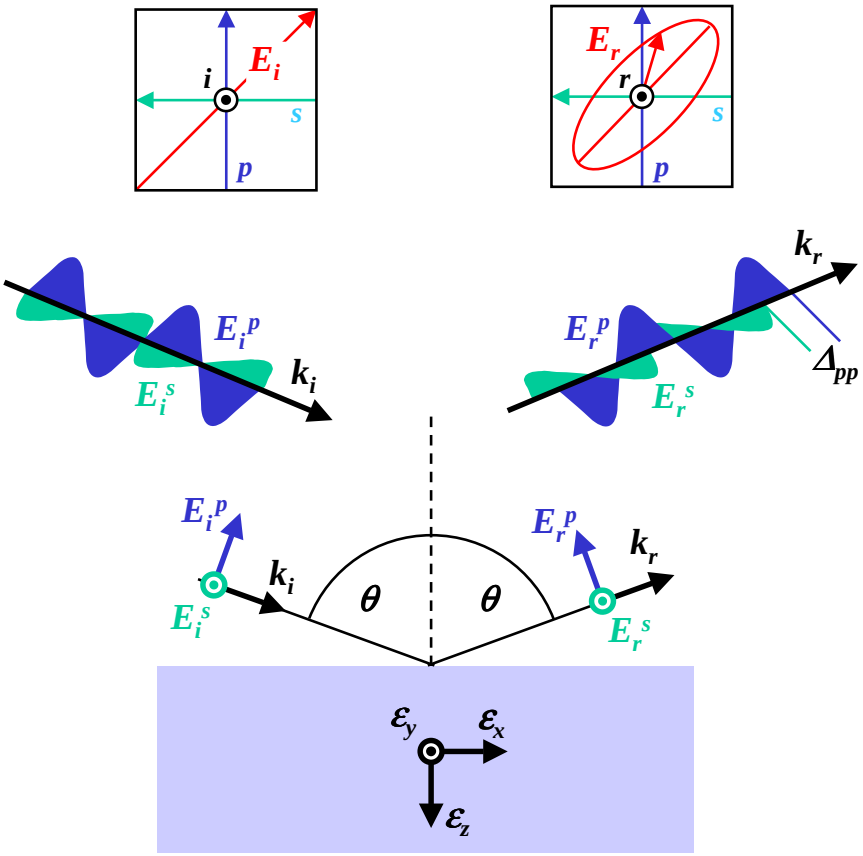

Figure 3.3: The basic geometry of an ellipsometric measurement.

accurately measured using a He-Ne laser, which also passes the Michelson interferometer. The resolution of a FT spectrometer is limited by the finite moving path of the mirror. As a result the interferogram of a monochromatic light wave is not a δ-function, but has a $\sin(\Delta x)/\Delta x$-like form. As a rule of thumb the resolution is given by $\Delta\omega \sim \Delta x_{max}^{-1}$. Another problem is induced by the sharp cut off at the turning points of the moving mirror, which yields a step in the interferogram. This leads to broad artifacts in the spectrum. A way out is the so called *apodization*, in which the interferogram is multiplied by an appropriate function, which strongly fades out the side bands of the interferogram [96]. For our spectrometer the best resulting resolution is approximately $\Delta\omega \sim 0.1$ cm^{-1}. For practical purpose in the mid-infrared region a resolution of 2-5 cm^{-1} is sufficient. Further details of the data processing and problems to take care of can be found in former PhD theses [89, 90].

3.3 Ellipsometry

Ellipsometry is a very sensitive and widely used technique to study optical properties. It goes back to Paul Drude [97]. The technique is sensitive to sub-nm thick surfaces and therefore often used in thin-film characterization. For bulk measurements however, some care has to be taken, because thin cover layers due to oxides or contaminations may be present on the sample surface. If there are indications for the presence of a cover layer it should be included into the data analysis. The main advantage of ellipsometry compared to standard reflectivity measurements is that it directly measures two independent quantities. Firstly the ratio of two intensities from the reflected light under two different polarizations and secondly the relative phase shift between these two reflected waves. Therefore one need not rely on the Kramers-Kronig analysis, as described in the previous chapter.

In the following the very basics of ellipsometry will be recalled. In Fig. 3.3 a standard ellipsometric measurement configuration is sketched. An incoming linearly polarized plane wave $\mathbf{E}_i$ with a wave vector $\mathbf{k}_i$ and frequency ω_i meets a surface. This results in a reflected wave $\mathbf{E}_r$ with wave vector $\mathbf{k}_r = -\mathbf{k}_i$ and frequency $\omega_r = \omega_i$. In order to characterize the polarization state of the waves the electric field vector can be split into two components, one parallel the plane of incidence ($E^p_{i,r}$) and one perpendicular to it ($E^s_{i,r}$) [98]:

$$\mathbf{E}_{i,r} = \begin{pmatrix} E^p_{i,r} \\ E^s_{i,r} \end{pmatrix} = \begin{pmatrix} |E^p_{i,r}| e^{i\delta^{i,r}_p} \\ |E^s_{i,r}| e^{i\delta^{i,r}_s} \end{pmatrix} e^{-i(kz-\omega t)} = \tilde{\mathbf{J}}_{i,r} e^{-i(kz-\omega t)}. \tag{3.16}$$

The normalized vector $\mathbf{J}_{i,r} = \tilde{\mathbf{J}}_{i,r}/|\tilde{\mathbf{J}}_{i,r}|$ is known as the *Jones vector*. It characterizes the polarization state of a light wave, e.g.

$$\begin{pmatrix} 0 \\ 1 \end{pmatrix}, \begin{pmatrix} 1 \\ 0 \end{pmatrix} \text{ or } \frac{1}{\sqrt{2}} \begin{pmatrix} 1 \\ i \end{pmatrix}, \frac{1}{\sqrt{2}} \begin{pmatrix} 1 \\ -i \end{pmatrix}$$

represent a linearly polarized wave (s and p-polarized) or circularly polarized wave (clockwise and counter-clockwise), respectively. In general the reflected light wave $\mathbf{E}_r$ is elliptically polarized. Its field vector can be calculated by multiplying the incident Jones vector with the matrix of the optical system (in this case the sample) [98]:

$$\mathbf{E}_r = \begin{pmatrix} E^p_r \\ E^s_r \end{pmatrix} = \begin{pmatrix} r_{pp} & r_{ps} \\ r_{sp} & r_{ss} \end{pmatrix} \begin{pmatrix} E^p_i \\ E^s_i \end{pmatrix} \text{ or } \mathbf{J}_r = \mathcal{J}\mathbf{J}_i. \tag{3.17}$$

The matrix accounting for the change in polarization is the *Jones matrix* $\mathcal{J}$. The Jones matrix is related to the components of the dielectric tensor in Eq. 3.6 via the Fresnel equations. In order to get simple formulas we assume a non-depolarizing material with orthorhombic symmetry[5], which is oriented such that the optical constants are parallel to

[5] For monoclinic or even lower symmetric materials there will be off-diagonal elements in the Jones matrix. Note, that a depolarizing and anisotropic sample can not be properly described by the Jones matrix formalism, because both effects lead to non-diagonal matrix elements and can not be discriminated. An extended approach is the Müller-matrix formalism, in which these effects can be distinguished.

the laboratory system for normal incidence (e.g. $p \parallel \epsilon_x$, see Fig. 3.3). This has the great advantage that the off-diagonal components of the Jones matrix vanish. An additional in-plane rotation of the laboratory coordinate system yields much more complicated relations [98, page 355]. The Fresnel equations for the geometry shown in Fig. 3.3 read [98–100]:

$$\begin{aligned} r_{pp} &= \frac{E_r^p}{E_i^p} = \frac{\sqrt{\epsilon_{zz} - \sin^2\theta} - \sqrt{\epsilon_{xx}\epsilon_{zz}}\cos\theta}{\sqrt{\epsilon_{zz} - \sin^2\theta} + \sqrt{\epsilon_{xx}\epsilon_{zz}}\cos\theta} \\ r_{ss} &= \frac{E_r^s}{E_i^s} = \frac{\cos\theta - \sqrt{\epsilon_{yy} - \sin^2\theta}}{\cos\theta + \sqrt{\epsilon_{yy} + \sin^2\theta}} \\ r_{ps} &= \frac{E_r^p}{E_i^s} = 0 \\ r_{sp} &= \frac{E_r^s}{E_i^p} = 0 \end{aligned} \tag{3.18}$$

For an isotropic material at normal incidence the well known Eq. 3.10 is recovered. In general, the measured quantities are the ratios

$$\begin{aligned} \rho_{pp} &= \frac{r_{pp}}{r_{ss}} = \tan\psi_{pp}\, e^{i\Delta_{pp}} \\ \rho_{ps} &= \frac{r_{ps}}{r_{pp}} = \tan\psi_{ps}\, e^{i\Delta_{ps}}\big(=0\big) \\ \rho_{sp} &= \frac{r_{sp}}{r_{ss}} = \tan\psi_{sp}\, e^{i\Delta_{sp}}\big(=0\big). \end{aligned} \tag{3.19}$$

In an orthorhombic sample the ratios depend on the sample orientation. One already can recognize that in order to extract six unknown variables (the real and imaginary parts of ϵ_{xx}, ϵ_{yy}, ϵ_{zz}), at least three different linearly independent sample orientations have to be measured. The optical constants can be obtained by inserting Eq. 3.18 into Eq. 3.19 and by inverting the resulting equations. This can not be done analytically anymore in orthorhombic symmetry. The software WVASE32 of the ellipsometer (J.A. Woollam, VASE) performs a least-square fit based on the latter two equations making use of the Levenberg-Marquard algorithm. For the isotropic case an analytic relation between the dielectric constant ϵ and the ellipsometric parameters ψ_{pp} and $\Delta_p p$ can be found [98, 99]. This is often called pseudo-dielectric function:

$$\epsilon = \epsilon_{xx} = \epsilon_{yy} = \epsilon_{zz} = \sin^2\theta + \sin^2\theta\, \tan^2\theta \left(\frac{1-\rho_{pp}}{1+\rho_{pp}}\right) \tag{3.20}$$

Aspnes [99] has extended Eq. 3.20 to the case of biaxial samples, i.e. $\epsilon_{xx} \neq \epsilon_{yy} \neq \epsilon_{zz}$. He assumed that the optical anisotropies $\Delta\epsilon_{x,y,z}$ are small variations around a suitable mean

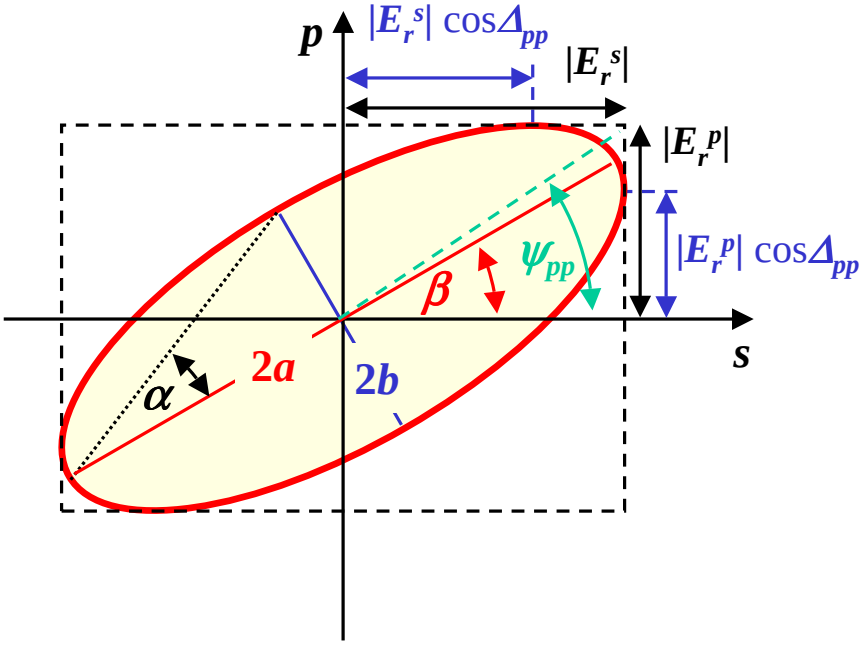

Figure 3.4: Connection between the measured quantities ψ_{pp} an Δ_{pp} and geometrical properties of the polarization ellipse. The ellipse is fully characterized by its ellipticity α (with $\tan\alpha = b/a$) and its position angle β.

value ϵ_{av}. It turns out that for large angles of incidence (70°) and moderately large values of $|\epsilon_{av}| = 10$ the pseudo-dielectric function is dominated by only one of the three anisotropies. The other two contributions cancel out approximately. In other words a measurement in a configuration as drawn in Fig. 3.3 is sensitive only to ϵ_{xx} under the assumptions mentioned above.

From the parameters ψ_{pp} and Δ_{pp} the polarization ellipse can be constructed as shown in Fig. 3.4. The parameters of the ellipse, namely the principal axes a and b and the position angle β, can be obtained using the following relations [101, page 21]:

$$\begin{aligned} \tan 2\beta &= \tan 2\psi_{pp} \cdot \cos\Delta_{pp} \\ \tan 2\alpha &= \pm \sin 2\psi_{pp} \cdot \sin\Delta_{pp} \end{aligned} \tag{3.21}$$

The ellipticity α is directly related to the ratio of the principal axes by $\tan\alpha = b/a$. Note, that $\tan\psi_{pp} = |E_r^p|/|E_r^s| = |r_{pp}|/|r_{ss}|$. As an example choose a retardation $\Delta_{pp} = 0, \pm\pi$ which yields an ellipticity of zero. This means the reflected light is linearly polarized. For another example consider a retardation $\Delta_{pp} = \pm\pi/2$ and $\tan\psi_{pp} = 1$, which produces an ellipticity of one, i.e. the reflected light is circularly polarized.

3.3.1 From Jones-matrix to Müller-matrix formalism

The most general case for describing an optical system is the *Müller-matrix* formalism [98, 102]. In contrast to the Jones-matrix formalism, the Müller-matrix formalism can handle depolarizing, anisotropic samples, since the incident beam is fully polarized [98]. Another advantage of this approach is that it describes the transfer of intensities through an optical system. The determination of the conjugate complex numbers as necessary in the Jones-matrix formalism can be omitted. Instead of the Jones vectors the Müller-matrix formalism uses a four-component vector, the *Stokes vector*. The vector is defined as

$$\mathbf{S} = \begin{pmatrix} S_0 \\ S_1 \\ S_2 \\ S_3 \end{pmatrix} = \begin{pmatrix} I_0 \\ I_p - I_s \\ I_{45^\circ} - I_{-45^\circ} \\ I_{\sigma^+} - I_{\sigma^-} \end{pmatrix} \tag{3.22}$$

where the intensity I can be obtained by four different measurements, namely (i) an unpolarized measurement determining $I_0 = I_p + I_s = I_{45^\circ} + I_{-45^\circ} = I_{\sigma^+} + I_{\sigma^-}$, (ii) a measurement with a linear polarizer in p or s polarization determining I_p or I_s, (iii) a measurement with a linear polarizer 45° away from the s or p polarization determining I_{45° or I_{-45°, and (iv) a measurement with a linear polarizer such as in (iii) and a $\lambda/4$ retarder, to create circularly polarized light determining I_{σ^+} or I_{σ^-}. As an example we will consider the Stokes vectors for linearly (p, s) and circularly (σ^+, σ^-) polarized light:

$$\begin{pmatrix} 1 \\ 1 \\ 0 \\ 0 \end{pmatrix}, \begin{pmatrix} 1 \\ -1 \\ 0 \\ 0 \end{pmatrix}, \text{ and } \begin{pmatrix} 1 \\ 0 \\ 0 \\ 1 \end{pmatrix}, \begin{pmatrix} 1 \\ 0 \\ 0 \\ -1 \end{pmatrix}$$

The degree of polarization can directly be read from the Stokes vector. It is the ratio of the polarized part of the light divided by the total intensity, which reads as $\sqrt{S_1^2 + S_2^2 + S_3^2}/S_0$. The analogue to the Jones matrix is the *Müller matrix* $\mathcal{M}$, but it has 16 entries.

$$\mathcal{M} = \begin{pmatrix} M_{11} & M_{12} & M_{13} & M_{14} \\ M_{21} & M_{22} & M_{23} & M_{24} \\ M_{31} & M_{32} & M_{33} & M_{34} \\ M_{41} & M_{42} & M_{43} & M_{44} \end{pmatrix} \tag{3.23}$$

We will briefly illustrate, how a Müller matrix in our case might look like. We will transform the Jones matrix given in Eq. 3.17 to its corresponding Müller matrix. We will follow the procedure described in Ref. [98]. In general for a given Jones matrix $\mathcal{J}$ the appropriate Müller matrix $\mathcal{M}$ can be derived by

$$\mathcal{M} = \mathcal{T} \cdot (\mathcal{J} \otimes \mathcal{J}^*) \cdot \mathcal{T}^{-1} \tag{3.24}$$

This description is valid for every Jones matrix. The matrix $\mathcal{T}$ transforms the coherency vector into the Stokes vector. The symbol represent $\otimes$ the direct product of two matrices[6]. The coherency vector is not explicitly needed for the further discussion; we refer to Ref. [98, page 62] for its definition. The matrix $\mathcal{T}$ for the transformation is given by

$$\mathcal{T} = \begin{pmatrix} 1 & 0 & 0 & 1 \\ 1 & 0 & 0 & -1 \\ 0 & 1 & 1 & 0 \\ 0 & i & -i & 0 \end{pmatrix}. \tag{3.25}$$

As mentioned above, assume a reflectivity Jones matrix for a non-depolarizing surface of a uniaxial crystal (tetragonal symmetry) with complex reflectivity coefficients r_{pp} and r_{ss}. The crystallographic axis should be oriented parallel to the laboratory system. In this case the Jones matrix has only diagonal entries.

$$\mathcal{J}_{tet} = \begin{pmatrix} r_{pp} & 0 \\ 0 & r_{ss} \end{pmatrix}. \tag{3.26}$$

Using the transformation (3.24) and normalizing to the reflected intensity of unpolarized light $M_{11} = \frac{1}{2}(|r_{pp}|^2 + |r_{ss}|^2)$ one obtains:

$$\mathcal{M}^{tet} = \begin{pmatrix} 1 & m_{12} & 0 & 0 \\ m_{21} & 1 & 0 & 0 \\ 0 & 0 & m_{33} & m_{34} \\ 0 & 0 & m_{43} & m_{44} \end{pmatrix} \tag{3.27a}$$

$$m_{12} = m_{21} = \frac{|r_{pp}|^2 - |r_{ss}|^2}{|r_{pp}|^2 + |r_{ss}|^2} \tag{3.27b}$$

$$m_{33} = m_{44} = 2\frac{\mathrm{Re}[r_{pp}]\mathrm{Re}[r_{ss}] + \mathrm{Im}[r_{pp}]\mathrm{Im}[r_{ss}]}{|r_{pp}|^2 + |r_{ss}|^2} \tag{3.27c}$$

$$m_{34} = -m_{43} = 2\frac{\mathrm{Re}[r_{pp}]\mathrm{Im}[r_{ss}] - \mathrm{Im}[r_{pp}]\mathrm{Re}[r_{ss}]}{|r_{pp}|^2 + |r_{ss}|^2} \tag{3.27d}$$

[6] If $\mathcal{J}_{ij}$ and $\mathcal{J}^*_{kl}$ are the matrix elements of the two Jones matrices the matrix element the direct product is defined as $(\mathcal{J} \otimes \mathcal{J}^*)_{\alpha\beta} = \mathcal{J}_{ij} \cdot \mathcal{J}^*_{kl}$ with $\alpha = 2(i-1) + k$ and $\beta = 2(j-1) + l$.

From the ellipsometric ratio in Eq. 3.19 one can evaluate:

$$\frac{|r_{pp}|}{|r_{ss}|} = \tan(\psi_{pp}) \tag{3.28a}$$

$$\mathrm{Re}\left[\frac{r_{pp}}{r_{ss}}\right] = \tan(\psi_{pp})\cos(\Delta_{pp}) \tag{3.28b}$$

$$\mathrm{Im}\left[\frac{r_{pp}}{r_{ss}}\right] = \tan(\psi_{pp})\sin(\Delta_{pp}) \tag{3.28c}$$

In terms of the ellipsometric parameters the normalized Müller matrix $\mathcal{M}^{tet}$ from Eq. 3.27 reads:

$$\mathcal{M}^{tet} = \begin{pmatrix} 1 & -\cos(2\psi_{pp}) & 0 & 0 \\ -\cos(2\psi_{pp}) & 1 & 0 & 0 \\ 0 & 0 & \cos(\Delta_{pp})\sin(2\psi_{pp}) & \sin(\Delta_{pp})\sin(2\psi_{pp}) \\ 0 & 0 & -\sin(\Delta_{pp})\sin(2\psi_{pp}) & \cos(\Delta_{pp})\sin(2\psi_{pp}) \end{pmatrix} \tag{3.29}$$

Only six matrix elements carry information in case of an isotropic or properly oriented anisotropic sample. Deviations from zero or one in the remaining 10 matrix elements indicate that (i) the sample surface depolarizes or (ii) the sample is anisotropic and its crystallographic axes are not parallel to the laboratory system. This matrix in Eq. 3.29 can be decomposed into a linear retarder with the retardation Δ_{pp} and a partial linear polarizer with relative attenuation $\sqrt{A_{min}/A_{max}} = \tan(\psi_{pp})$ [98, page 491]. Once the Müller matrix has been determined for different orientations, the Fresnel equations (see Eq. 3.18) can again be used for relating the matrix elements to the optical constants.

3.3.2 How to measure the Müller matrix?

All measurements are carried out using a Rotating Analyzer Ellipsometer (RAE). We will briefly show what a RAE can do in order to measure the Müller matrix of an unknown sample. The details of our setup will be discussed in the next section. For simplicity we will assume in the following discussion that all optical components are ideal, e.g. there is no leakage of the polarizers, etc. Simply speaking the RAE consists of the following components, see Fig. 3.5: the light source emits unpolarized light which becomes linearly polarized. Furthermore, a retarder of arbitrary angle can be inserted. As shown in Fig. 3.5 this leads to a non-vanishing fourth component of the Stokes vector, i.e. for the creation of circularly polarized light. After being reflected off the sample surface, the light passes a rotating analyzer. For the analysis the intensity at the detector is measured versus time, i.e. only the first component of the Stokes vector. It contains the components S_0^r, S_1^r, and S_2^r, i.e. information about the first three rows of the Müller matrix (see caption of Fig. 3.5).

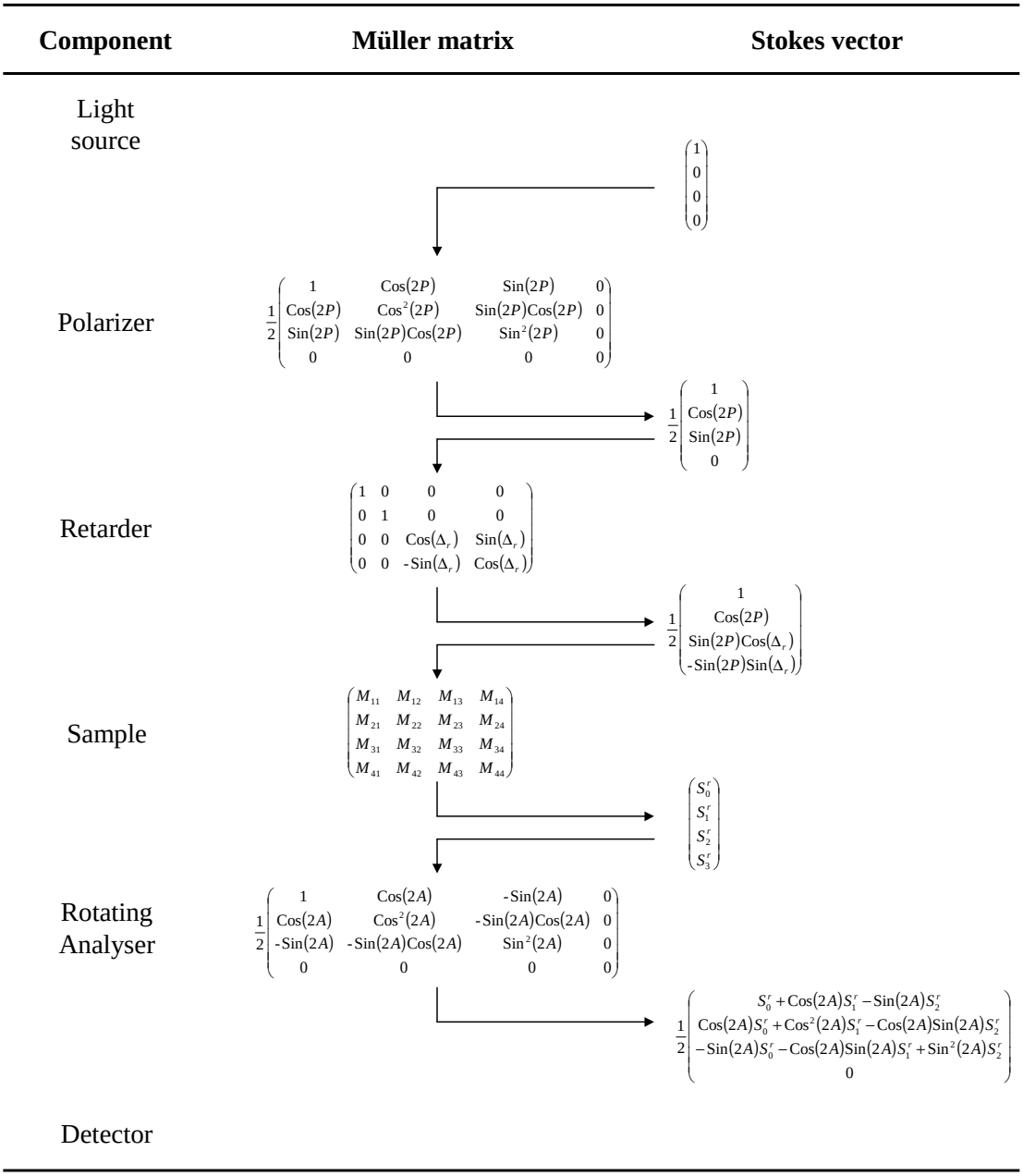

Figure 3.5: Principal optical path of a RAE in terms of the Müller matrix formalism. The Stokes vector at the detector position can be obtained by multiplying the Stokes vector associated with the light source, which is assumed to be fully unpolarized, by the Müller matrices of each module of the optical system. After reflection off the sample surface the components of the Stokes vector read: $S_0^r = \frac{1}{2}\big(M_{11} + M_{12}\cos 2P + (M_{13}\cos\Delta_r - M_{14}\sin\Delta_r)\sin 2P\big)$, $S_1^r = \frac{1}{2}\big(M_{21} + M_{22}\cos 2P + (M_{23}\cos\Delta_r - M_{24}\sin\Delta_r)\sin 2P\big)$, $S_2^r = \frac{1}{2}\big(M_{31} + M_{32}\cos 2P + (M_{33}\cos\Delta_r - M_{34}\sin\Delta_r)\sin 2P\big)$, and $S_3^r = \frac{1}{2}\big(M_{41} + M_{42}\cos 2P + (M_{43}\cos\Delta_r - M_{44}\sin\Delta_r)\sin 2P\big)$. We used the following parameters: the polarizer angle P, the retarder angle Δ_r, and the analyzer angle A.

This means that the last row of the Müller matrix is not accessible by RAE. A reason for this the missing of a retarder placed between sample and analyzer. The inclusion of the latter one would make the last row assessable.

This whole setup can be translated into one Müller matrix. One has to multiply the Müller matrices of all optical components. The resulting Müller matrix can be applied to the Stokes vector of the incoming light. The result gives the Stokes vector at the detector position. Mathematically speaking this reads as

$$\mathbf{S}^{Detector} = \left[\mathcal{M}_{Analyzer}\mathcal{M}_{Sample}\mathcal{M}_{Retarder}\mathcal{M}_{Polarizer}\right]\mathbf{S}^{i}. \tag{3.30}$$

We assume that p polarized light corresponds to a polarizer angle of zero degree. The polarizer angle will be denoted with P, the retarder angle with Δ_r, and the analyzer angle with A. As an example we consider the Müller matrix from Eq. 3.29. We further assume that $\Delta_r = 0°$. The detector measures only the total intensity $S_0^{Detector}$, i.e. the first entry of the Stokes vector. Because the analyzer is continuously in rotation, one can extract the Fourier components f_1 and f_2 from the measured intensity $S_0^{Detector}(t) = S_0^{Detector,0}(1 + f_1 \cos 2A(t) + f_2 \sin 2A(t))$. These have to be determined at least for six different configurations of P and Δ_r, in order to extract all 12 measurable matrix elements. The RAE ellipsometer used within this PhD project measures more than six configurations of P and Δ_r and determines the Müller matrix elements by regression. Using our example from Eq. 3.29 the intensity at the detector can be written as a function of the parameters ψ_{pp} and Δ_{pp}, which leads to:

$$\begin{aligned}\mathbf{S}^{Detector} = \frac{1}{4}(1 - \cos 2\psi_{pp}\cos 2P)\Big(1 \;&+\; \frac{\cos 2P - \cos 2\psi_{pp}}{1 - \cos 2\psi_{pp}\cos 2P}\cos 2A(t) \\ &+\; \frac{\cos\Delta_{pp}\sin 2\psi_{pp}\sin 2P}{1 - \cos 2\psi_{pp}\cos 2P}\sin 2A(t)\Big)\end{aligned} \tag{3.31}$$

One can directly read off the measured Fourier components f_1 and f_2:

$$\begin{aligned} f_1 &= \frac{\cos 2P - \cos 2\psi_{pp}}{1 - \cos 2\psi_{pp}\cos 2P} \\ f_2 &= \frac{\cos\Delta_{pp}\sin 2\psi_{pp}\sin 2P}{1 - \cos 2\psi_{pp}\cos 2P} \end{aligned} \tag{3.32}$$

From these, one can directly extract the ellipsometric parameters:

$$\begin{aligned} \cos 2\psi_{pp} &= \frac{\cos 2P - f_1}{1 - f_1\cos 2P} \\ \cos\Delta_{pp} &= \frac{f_2}{\sqrt{1 - f_1^2}}\cdot\frac{\sin 2P}{|\sin 2P|} \end{aligned} \tag{3.33}$$

For one particular orientation of an aligned (with respect to the laboratory system), non-depolarizing crystal the Müller matrix has now been fully determined via Eq. 3.29. The

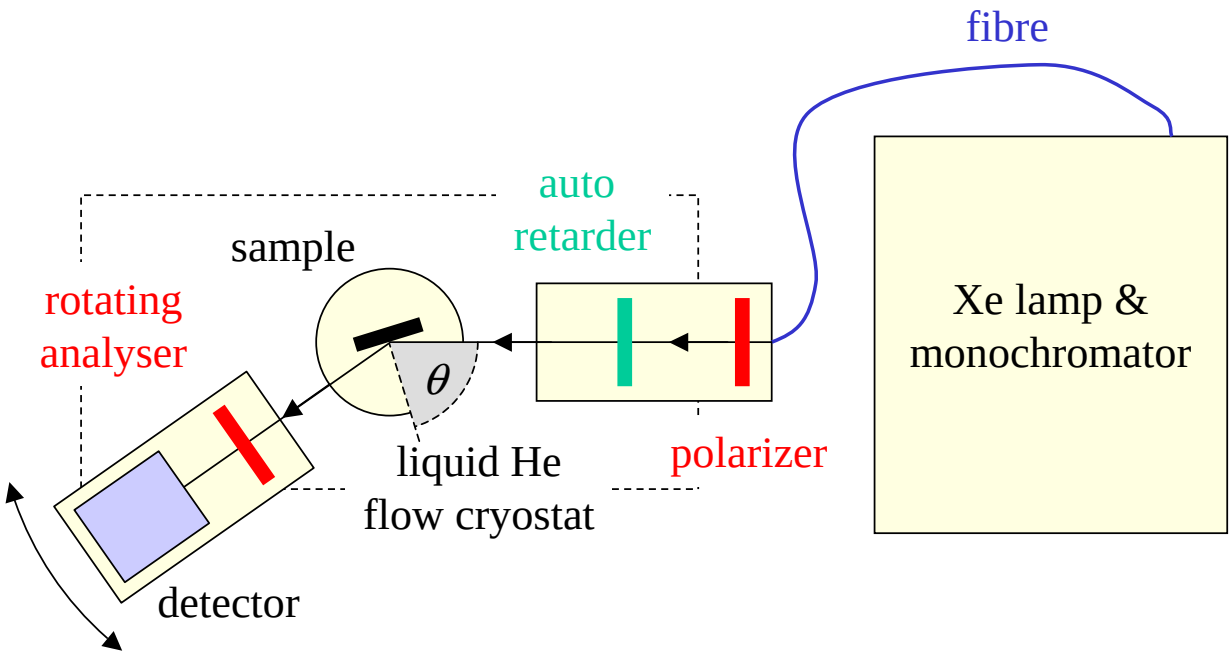

Figure 3.6: Sketch of the ellipsometer (J.A. Woollam, VASE).

determination of the dielectric constants require another additional measurement, i.e. a second Müller matrix, in case of a tetragonal crystal. With the use of Eqs. 3.18 and 3.19 one can relate Ψ_{pp} and Δ_{pp} to ϵ_{xx} and ϵ_{yy}. These equations have do be inverted and one can determine ϵ_{xx} and ϵ_{yy}. For an orthorhombic the determination of the full dielectric tensor requires three independent measurements.

3.3.3 Experimental setup

The principal setup of the ellipsometer used is given in Fig. 3.6. It consists of a commercial ellipsometer (VASE, J.A. Woollam) and a liquid-He flow cryostat (KONTI cryostat, CryoVac). A broad-band Xe lamp (190 nm - 2000 nm) serves as a light source. The light is dispersed by a double-grating monochromator and coupled into an optical fibre We used a thickness of 200 μm. The fibre is not transparent in the region 1340-1450 nm (0.86-0.93 eV); no data is acquired in this energy region. Before entering the fibre, the light is chopped, in order to make measurements in an illuminated room possible. This is done by making use of a synchronous detection. Behind the fibre the light passes through a linear polarizer. The polarizing angle is fixed for each measurement, but it can be varied. Behind the polarizer an auto-retarder is placed, which imposes a variable retardation between 0-90° on the light wave. This element consists of a MgF_2 Berek waveplate. The auto-retarder increases the accuracy of the measurement because the precision in measuring linearly po-

larized light, i.e. Δ_{pp} close to 0 or 180°, is poor[7]. Furthermore, the inclusion of a retarder makes it possible to differentiate between $\Delta_{pp} = \delta$ and $\Delta_{pp} = 360° - \delta$ which is necessary since Δ in Eq. 3.19 has this definition range. On top of that, the intensity is small for an analyzer angle perpendicular to the direction of the nearly linear polarization. Afterwards, the light shines onto the sample which is situated into the cryostat under a fixed angle of 70° (using two other windows also 55° and 50° are also possible, these configurations have not been used). Outside the cryostat variable angles between $20 - 90°$ can be used. Behind the sample the light passes a continually rotating analyzer. The intensity signal $I(t)$ is measured by a stacked detector consisting of Si (185-1100 nm) and InGaAs (800-1700 nm); the detector switches automatically. All components are fully computer-controlled using the software WVASE32 (J.A. Woollam). The software is used for modeling the optical constants as well. This will be shown exemplarily for the case of Si and $YTiO_3$.

3.3.4 Cryostat and bake-out

A crucial issue in ellipsometry is its surface sensitivity. Since our samples are prepared ex situ we have no chance to avoid surface contaminations. The samples have been prepared following the recipe described in the appendix. Directly after lift off the sample is glued on a Cu plate using silver paint. After a drying time of approximately 15 minutes the plate is mounted on the cold finger of the cryostat. Next to the sample, a piece of a Si wafer is placed on the cold finger as well. This wafer is used for the calibration routine (see below). The cryostat is evacuated afterwards until the pressure is below $< 10^{-7}$ mbar. It turned out that this pressure is not low enough in order to achieve reproducible results when varying the temperature. The main problem arises from H_2O vapor which leads to a permanently growing, detectable ice layer below 130-135 K depending on the pressure. Therefore we applied a bake-out procedure. We started by heating the whole system for 100 h at 400 K. But we found that 50 h heating at 400 K plus 24 h for cooling down are sufficient to reach an end pressure of approximately $5 \cdot 10^{-10}$ mbar at room temperature. Up from now no growing (ice-)layers have been observed.

3.3.5 Calibration procedure and data acquisition

After the bake-out procedure, one can start with the calibration routine. For every measurement, including the calibration routine, the sample has to be properly aligned with respect to the incoming beam and the detector.

First, the Si wafer is aligned. A measurement of ψ ($= \psi_{pp}$) and Δ ($= \Delta_{pp}$) at several wavelengths is used in order to determine the polarizer azimuth angles and the in-plane and out-of plane window effects[8]. This is done by simultaneously fitting the latter effects together with the parameters of an appropriate model for the Si wafer. This model has been obtained before by characterizing the wafer outside the cryostat (see below). It consists

[7] The Fourier component $f_2 \propto \cos \Delta_{pp}$. Thus, small variations away from 0 or 180° do not change f_2 much. In that sense the sensitivity is poor and a retardation of 90° should be used.

[8] The windows slightly modify the polarization state of the incoming and reflected light.

of a bulk Si substrate and a thin cover layer of SiO_2 connected by an interlayer. Only the thickness of the SiO_2 layer is adapted in the calibration routine. The results for the thickness can be compared to the values determined outside the cryostat as a consistency check.

Afterwards, the sample is aligned. The first three rows of the Müller matrix can be measured for a certain sample orientation. This procedure is fully automated.

The sample holder can nominally be cooled down to a temperature of 5 K, but a measurement with an additional thermometer close to the sample shows that this temperature can not be reached at the sample position, the lowest sample temperature corresponds to approximately 15 K [9]. A temperature calibration for the case of $YTiO_3$ is shown in the appendix. We will use this calibration for all measurements.

3.3.6 The standard Si wafer

As a first example, we will briefly show the results of a measurement on the Si (111) wafer mentioned above. Since Si has isotropic optical properties, we could in principle directly convert the measured quantities into the optical constants. However, Si forms a natural surface oxide SiO_2. This oxide must be taken into account for an accurate description. In Fig. 3.7, the measured data and results for three different models are shown (purely Si; Si/SiO_2; and Si/interlayer/SiO_2). The optical constants for Si, SiO_2, and the interlayer are taken from Ref. [103] and have been kept constant, while for the last two models the thickness of the SiO_2 has been fitted to the measured data. The interlayer thickness has been kept constant. The analysis shows that, in order to be consistent with literature data of Si, the inclusion of a SiO_2 cover layer is a must for an accurate description of the data. We used the Si/interlayer/SiO_2 model for the calibration routine inside the cryostat since the results give a slightly better mean squared error (MSE) than the Si/SiO_2 model. We fixed the thickness of the interlayer, because we wanted to keep the number of parameters as low as possible. An interlayer is physically meaningful, since the optical constants of two layers, here Si and SiO_2 will not change abruptly at their interface. It is a reasonable approach to average the optical constants of the two layers in a certain region. This is done in case of the interlayer.

3.3.7 Exemplary data processing for $YTiO_3$

As a second example, we will discuss the determination of an unknown set of optical constants. The principal procedure for the data processing in this case is indicated in the flowchart in Fig. 3.8. After the measurement of the Müller-matrix entries, the data is compared to an appropriate model. One starts from the simplest model, i.e. a model without any additional assumptions. The optical constants of the model are fitted to the measured quantities. If one has over-determined the problem, some refinements like surface

[9] The reason for is the absence of a complete radiation shielding, because we need holes for the incident and reflected light.

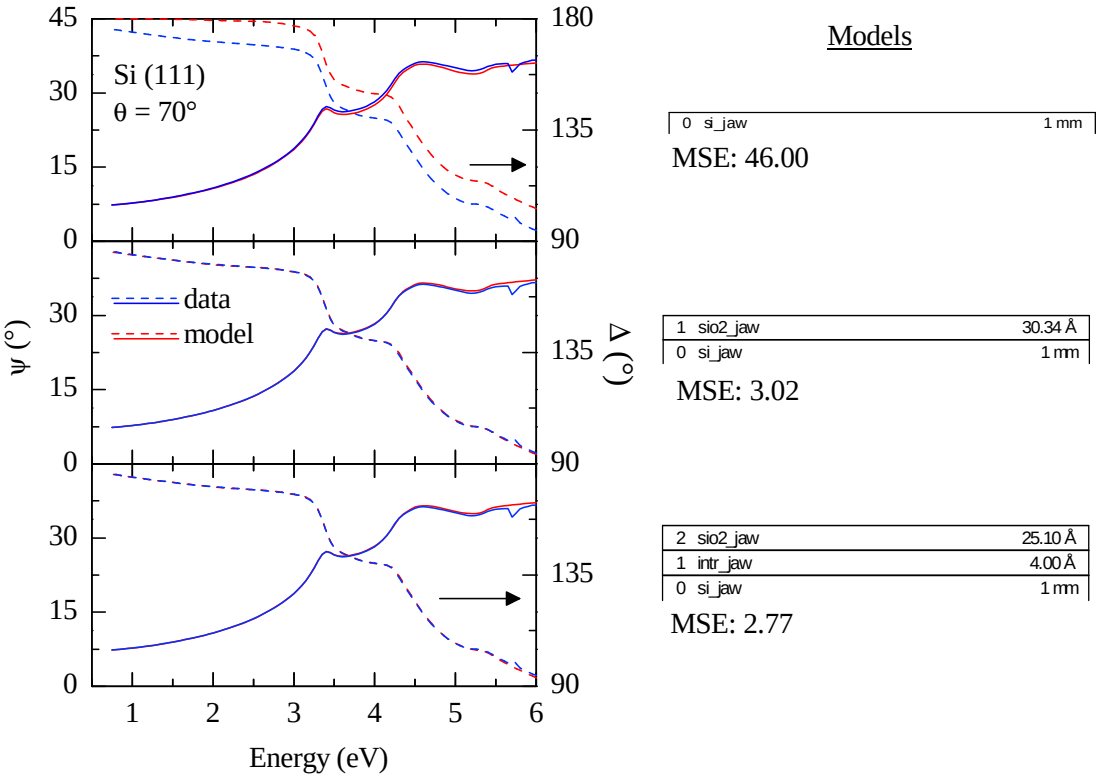

Figure 3.7: Ellipsometric measurement of the Si standard. The data is fitted by three different models: pure Si (top panel), Si/SiO_2 (middle panel), and Si/interlayer/SiO_2 (bottom panel). For the modeling we used the optical constants for Si (si_jaw), $SiOO_2$ (sio2_jaw), and for the interlayer (intr_jaw) from literature [103]. The means squared errors (MSE) are also given for each model.

roughness, cover layers, etc., can be incorporated in the model. These refinements should improve the quality of the fit, which is given by the mean squared error (MSE, proportional to χ^2), but at the same time should be based on realistic, physical assumptions. Finally one obtains the results: optical constants, thicknesses of cover layers, surface roughness, etc.. One can check the optical constants for Kramers-Kronig consistency.

We consider $YTiO_3$ for illustrating the latter procedure. The optical constants of this compound are not accurately known from the literature, especially not at low temperatures. Also the different components of the conductivity tensor have not been resolved yet. The goal of this work is to determine all entries of the conductivity tensor as function of temperature. We will compare those with data from literature.

Since $YTiO_3$ has orthorhombic symmetry, only the diagonal elements $\sigma^a = \sigma^{xx}$, $\sigma^b = \sigma^{yy}$ and $\sigma^c = \sigma^{zz}$ of the complex optical conductivity tensor $\sigma(\omega) = \sigma_1 + i\sigma_2$ are finite. We have determined $\sigma(\omega)$ from measurements with 4 different orientations, namely with s-polarized light parallel to the crystallographic a and b (a^* and c) axes on the ab (a^*c) surface, where $a^* = (110)$ within the $Pbnm$ space group. It turned out that a non-absorbing cover layer ($d \leq 2\,\mathrm{nm}$) has to be assumed in order to achieve a consistent description of the data of

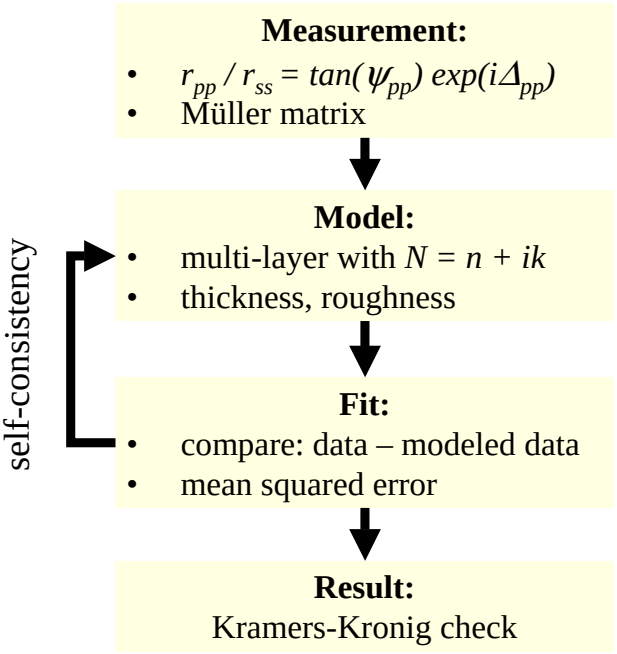

Figure 3.8: Data processing in ellipsometry.

the two distinct surfaces.

In Figs. 3.9-3.12 the *raw data* are shown, namely the Müller matrix elements and the model fits at 15 K for the four configurations mentioned above. For the analysis we simultaneously fit σ^a, σ^b, and σ^c to the measured data. Please note, that we only used the elements m_{12}, m_{21}, m_{33}, and m_{34} (which are normalized with respect to M_{11}, i.e. $m_{ij} = M_{ij}/M_{11}$) for the determination of $\sigma(\omega)$. These elements contain the main information, if the sample is oriented along its crystallographic axes (see above) and is non-depolarizing. The deviations in the other matrix elements from zero or one in Figs. 3.9-3.12 arise from the cryostat windows. Misalignment of the sample with respect to the laboratory system of a few degrees has basically no effect on the spectra.

In order to check the reproducibility of our data we tried the same measurement with new sample preparation several times. It turned out that the spectra did not always look the same, although always the same recipe of sample preparation has been used. An extreme example is shown in Fig. 3.13 for the matrix element m_{34}. This is a serious problem because the temperature dependence of the spectral weight in $YTiO_3$ is rather small when comparing to e.g. $LaSrMnO_4$ (see chapter 4). Therefore we developed the following strategy in order to obtain a self-consistent description for all measured data sets, opening the possibility to a detailed analysis of small changes of the spectral weight with temperature:

- In order to achieve a self-consistent multi-sample fit a thin cover layer can be included into the data analysis. Physically this cover layer can take surface roughness, surface

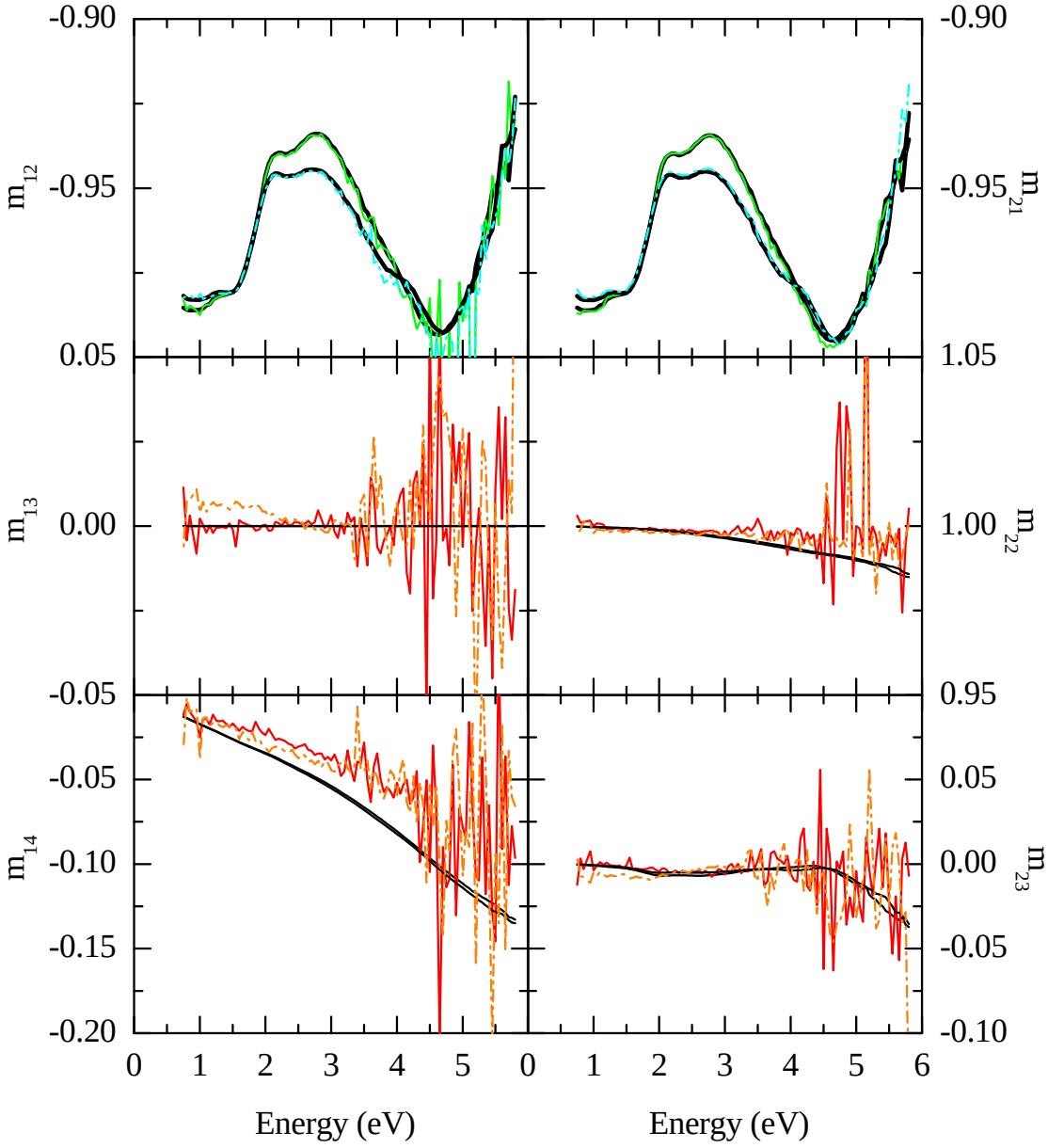

Figure 3.9: Measured Müller matrix elements of $YTiO_3$ at 15 K (*ab* surface). The elements are normalized with respect to the M_{11} element. The model consists of a Cauchy layer with a thickness of 0 nm (see text) and a biaxial medium with three different dielectric constants. Data set 1 (green and red curves, solid) denotes the sample orientation with $E_s||a$, while for data set 2 (cyan and orange curves, dashed) the sample has been rotated by 90°, i.e. $E_s||b$. Only the matrix elements m_{12}, m_{21}, m_{33}, and m_{34} are used for the determination of the optical constants (green and cyan curves). See also Fig. 3.10. The deviations of m_{13}, m_{14}, m_{22}, m_{23}, m_{24}, m_{31}, and m_{32} are entirely due to the window effects. The orientation of the sample with respect to the laboratory system is also given in terms of three Euler angles (ϕ, θ, ψ). The laboratory system has to be rotated around the (z, x', z') axis. These rotations have to be carried out in the sequence from left to right.

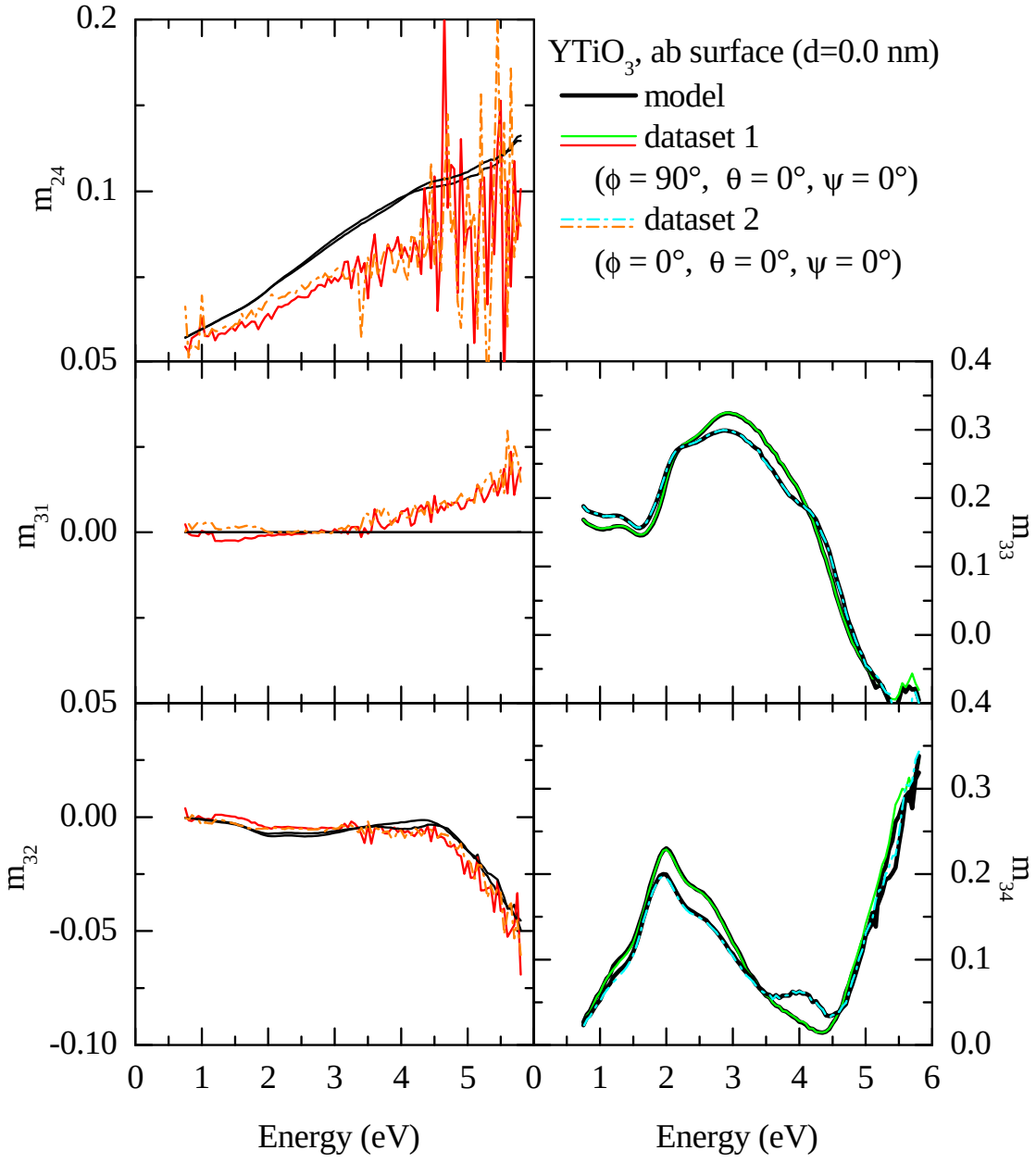

Figure 3.10: Measured Müller matrix elements of $YTiO_3$ at 15 K (*ab* surface). See also Fig. 3.9.

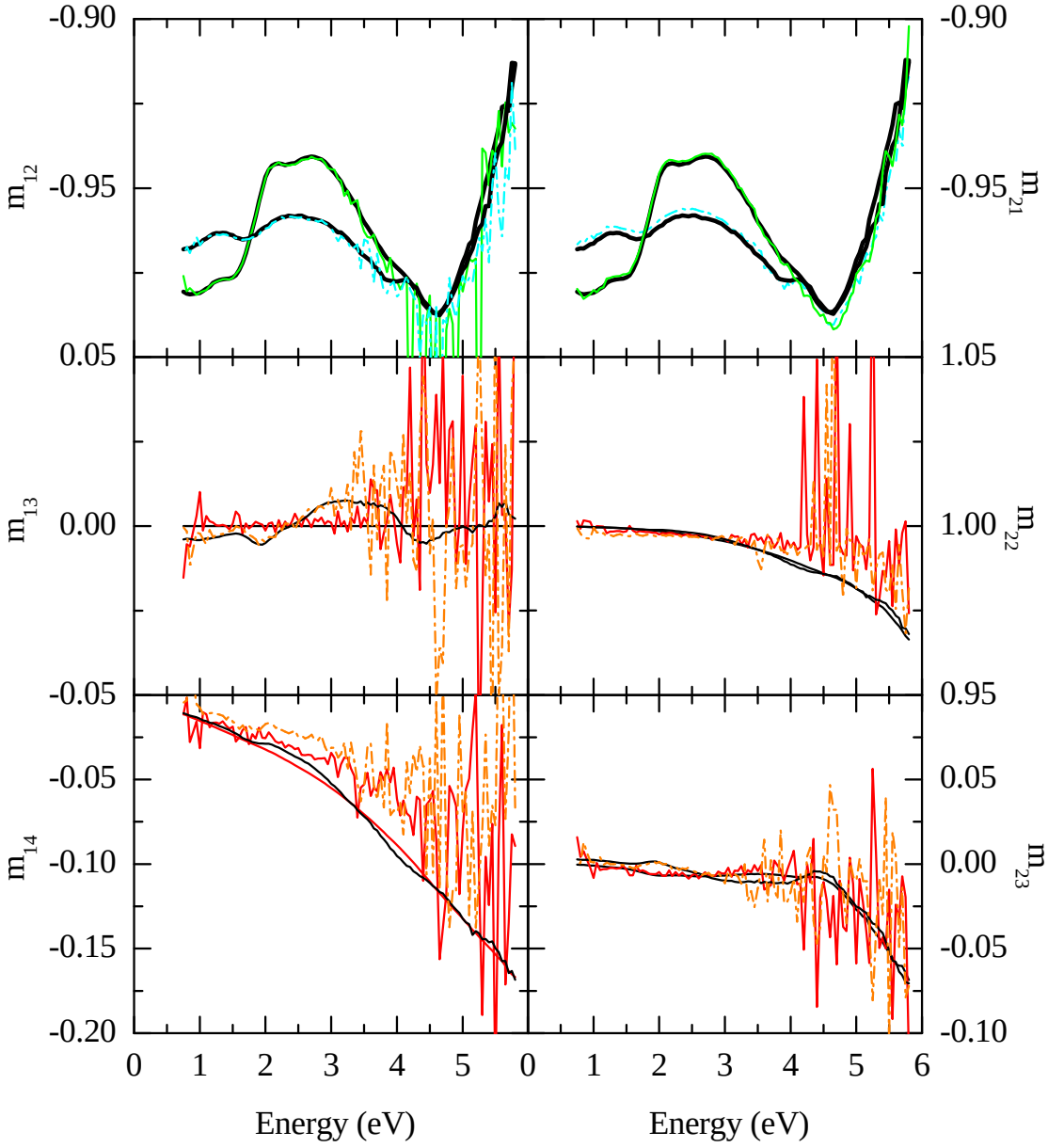

Figure 3.11: Measured Müller matrix elements of $YTiO_3$ at 15 K (a^*c surface). The elements are normalized with respect to the M_{11} element. The model consists of a Cauchy layer with a thickness of 2.2 nm (see text) and a biaxial medium with three different dielectric constants. Data set 1 (green and red curves, solid) denotes the sample orientation with $E_s||a^*$, while for data set 2 (cyan an orange curves, dashed) the sample has been rotated by 90°, i.e. $E_s||c$. Only the matrix elements m_{12}, m_{21}, m_{33}, and m_{34} are used for the determination of the optical constants (green and cyan curves). See also Fig. 3.12. The deviations of m_{13}, m_{14}, m_{22}, m_{23}, m_{24}, m_{31}, and m_{32} are entirely due to the window effects. The orientation of the sample with respect to the laboratory system is also given in terms of three Euler angles (ϕ, θ, ψ). The laboratory system has to be rotated around the (z, x', z') axes. These rotations have to be carried out in the sequence from left to right.

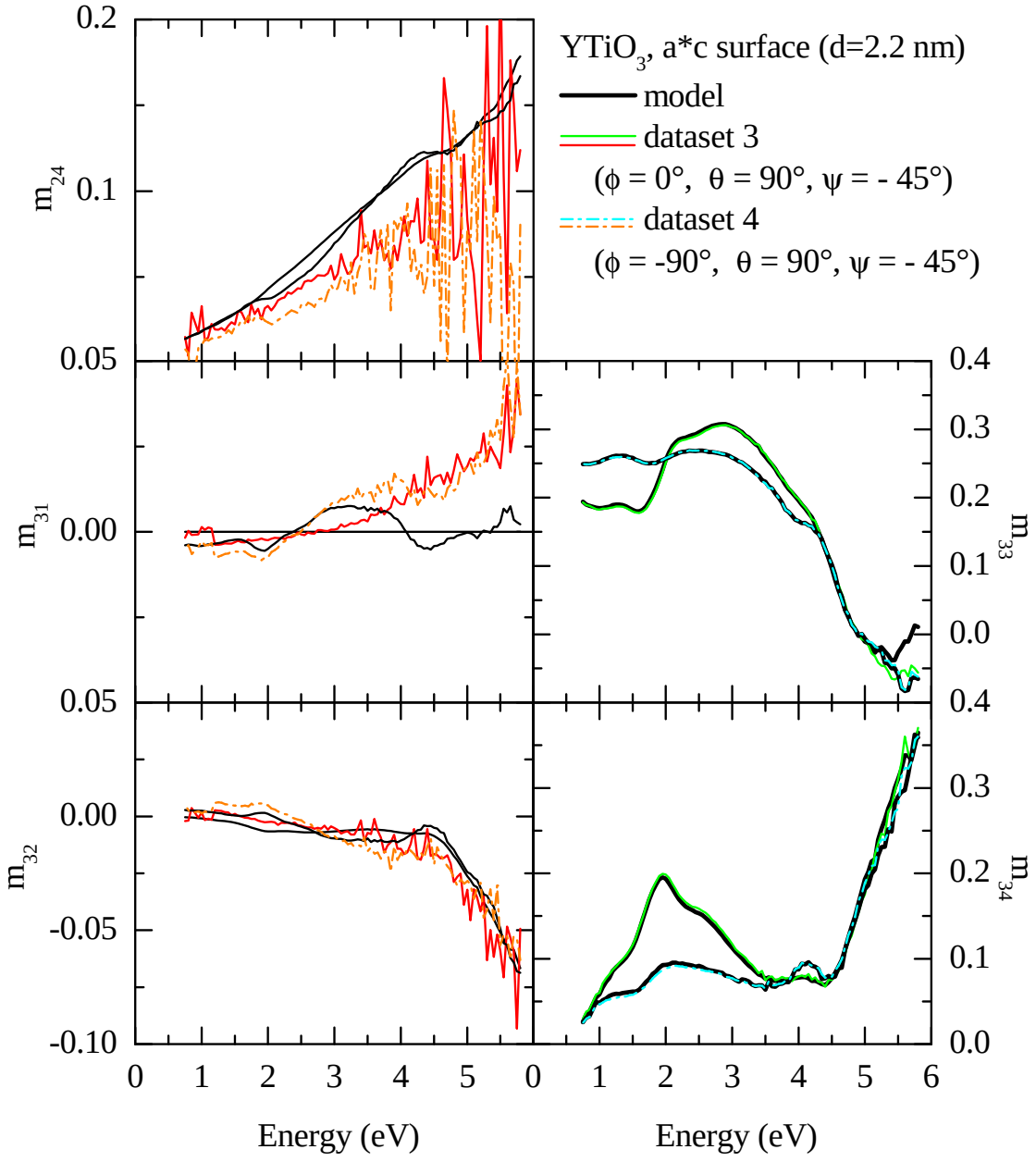

Figure 3.12: Measured Müller matrix elements of $YTiO_3$ at 15 K (a^*c surface). See also Fig. 3.11.

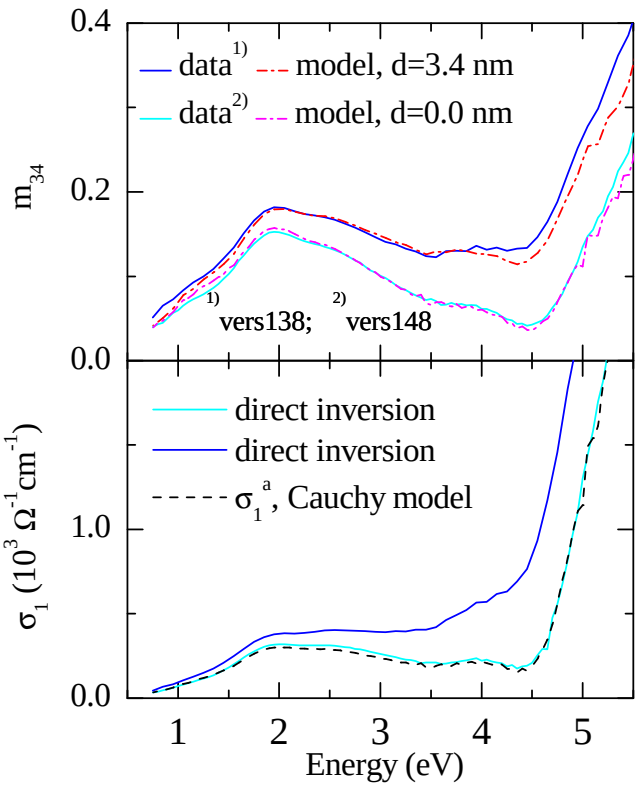

Figure 3.13: *Top panel:* Comparison of two different spectra (Müller matrix element m_{34}) measured on freshly prepared surfaces in the same geometry. The raw data show significant differences but both data sets can be modeled with the same optical constants assuming different thicknesses of the cover layers. *Bottom panel:* direct inversion (determination of the pseudo dielectric function, see Sect. 3.3 and Eq. 3.20) of the raw data from the top panel (without any covers layers). The large differences in the matrix element m_{34} directly translates into large differences in σ_1. Additionally σ_1^a from the full analysis is displayed leading basically to the same results as the direct inversion. This shows that to a good approximation we only detect the effect of one component of the dielectric tensor in one particular measurement geometry as suggest by Aspnes [99].

oxidation, or surface contamination from the surface preparation into account. We tried the following three cover layers:

(i) a surface-roughness layer which consists of a 50% mixture of the material constants and the vacuum optical constants. Only the thickness is fitted for each surface. This approach is called *effective-medium approximation (EMA).*

(ii) a layer with normal but fixed dispersion and no absorption. We have chosen SiO_2 as an example (this is suggested in the Woollam user handbook for the case of unknown cover layers.). Again only the thickness is varied.

(iii) a so-called *Cauchy layer* with normal dispersion and no absorption:

$$n(\lambda) = A + \frac{B}{\lambda^2}, \quad k(\lambda) = 0 \tag{3.34}$$

The thickness and the parameters A and B are varied.

As shown in Fig. 3.14 for the case of the 15 K data, all three cover layers lead to very similar results for the optical conductivity. Although the absolute values are slightly different the evolution with temperature stays almost unaffected. The deviations are

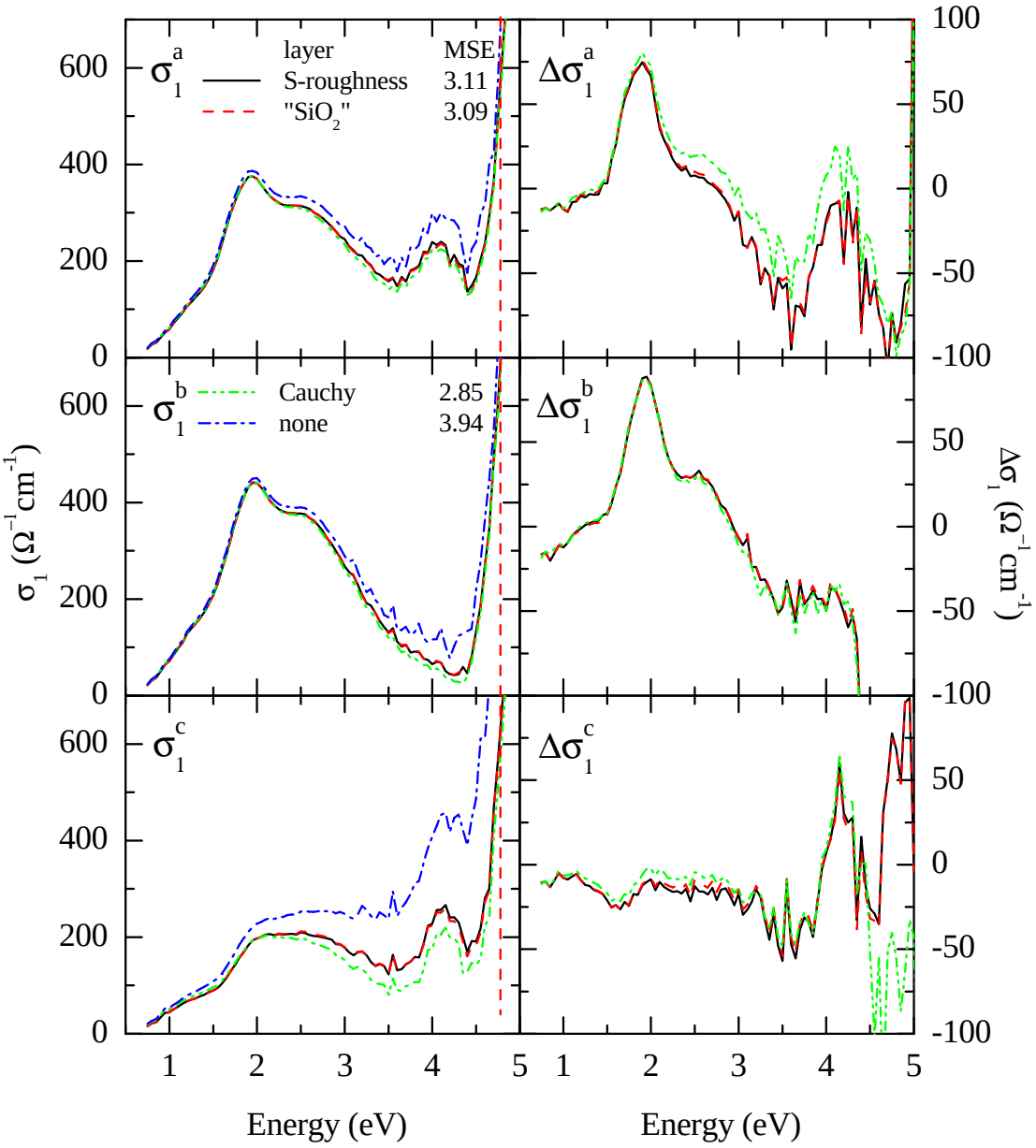

Figure 3.14: *Left column:* Optical conductivity of $YTiO_3$ at 15 K extracted from the measured Müller matrix elements using the three different cover layers: Surface-roughness layer (black), "SiO_2" (red), Cauchy layer (green). For comparison an analysis without any cover layers is shown (blue). Additionally the mean squared error (MSE) is listed in the plot. *Right column:* $\Delta\sigma_1 = \Delta\sigma_1(15K) - \Delta\sigma_1(295K)$ for the three different cover layers.

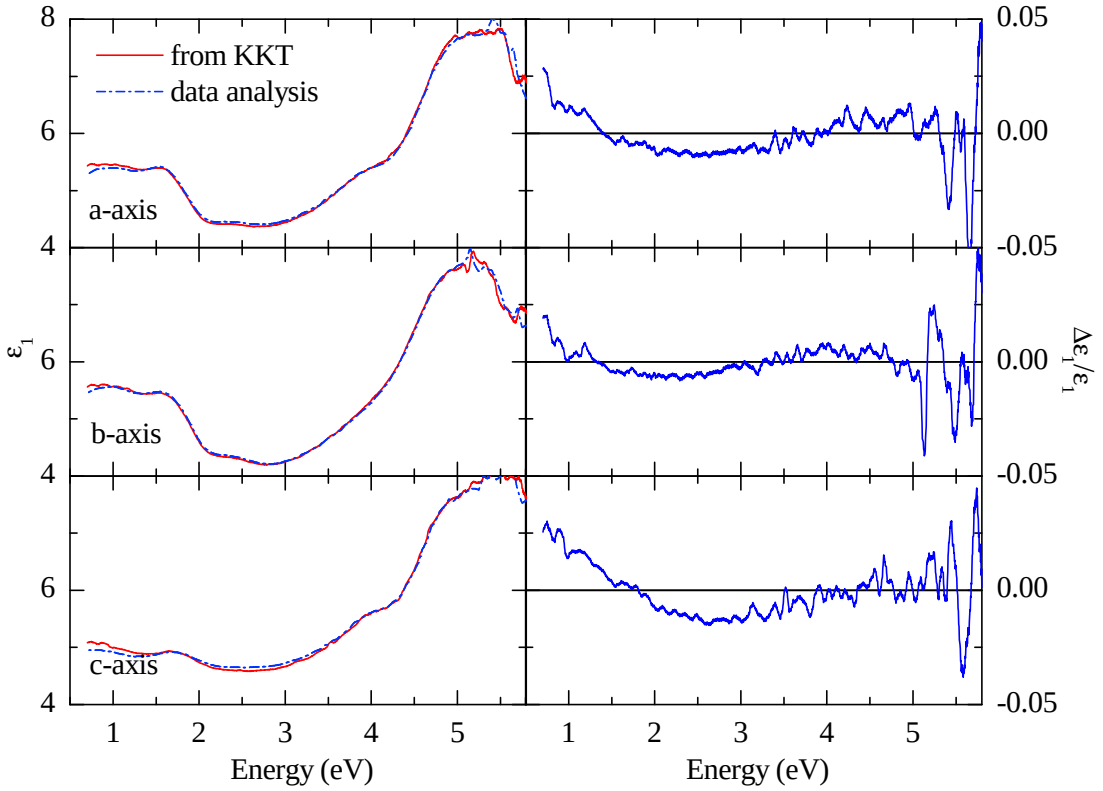

Figure 3.15: *Left column:* the dielectric function ϵ_1 as obtained by the data analysis on $YTiO_3$ at 15 K (blue, dashed) and from a Kramers-Kronig transformation on ϵ_2 (red, solid). Two poles have been used in order to mimic ϵ_2 outside the measured region. *Right column:* The relative error between the two values for ϵ_1

largest in $\Delta\sigma_a$, but still the curves exhibit the same characteristics. The analysis for all temperatures is only performed for the Cauchy layer (iii). The parameters A and B and the layer thickness d have been determined by a simultaneous fit of the lowest and the highest temperature data ($A = 1.010$, $B = 0.069$) and have afterwards been kept constant for intermediate temperatures. We also have incorporated an analysis without any additional cover layers. Its mean squared error (MSE) is 25% larger without a cover layer than for all models including cover layers. The steep increase at approximately 4.8 eV in the a and b direction is shifted to 4.5 eV in the c direction. However, the raw data suggests that for all directions the increase sets in at the same energy (see discussion below). We conclude that the inclusion of a proper cover layer greatly improves the description of many data sets with one set of optical constants.

- The imaginary part of the dielectric tensor or equivalently the optical conductivity σ_1 has to be positive: $\epsilon_2 > 0$. This is an important limitation. For the data analysis on the ab surface, we assumed a thickness of the cover layer of d_1=0 nm, while the

fits for the a^*c surface end up with d_2=2.2 nm. This result is not unique. If one assumes a larger thickness d_1 the fit will increase the thickness d_2, giving results of similar MSE and slightly different optical constants. However, if d_1 becomes larger than 0.2 nm the dielectric constant ϵ_2 gets negative which is an unphysical result.

- The measurements on $YTiO_3$ have been carried out on two different surfaces. The raw data in Figs. 3.9 and 3.10 suggest that for the ab surface all spectra above 4.5 eV should be equal, especially $E_s \parallel a, b, a^*$. This leads to the conclusion that $\epsilon_2^a = \epsilon_2^b = \epsilon_2^{a*}$ in this energy region. For the a^*c surface (see Figs. 3.11 and 3.12) a similar argumentation applies which results in $\epsilon_2^{a*} = \epsilon_2^c$. Putting this together $\epsilon_2(\omega > 4.5\,\mathrm{eV})$ should be isotropic in all three directions. Physically this means that the excitation causing the steep increase at 4.8 eV (charge-transfer band) should be almost isotropic. The raw data is in contrary to the expectation anisotropic in this region. The increase at approximately 4.8 eV is at slightly different energies. We believe that this discrepancy has to be repaired by assuming different thicknesses of cover layers for the two different surfaces. As one can see in Fig. 3.14, the data without a cover layer are not isotropic above 4.5 eV, while the inclusion of a proper cover layer makes ϵ isotropic in the high-energy region.

As a check for our model, we analyzed several data sets (the sample has always been lapped and polished again). All data sets can be described by the model by varying only the thickness of the Cauchy layer (see Fig. 3.14 and appendix). As a further cross check, the optical constant ϵ_2 from the data analysis has been compared to the result obtained from a Kramers-Kronig analysis on the values of ϵ_1 (the software WVASE32 has incorporated a model layer for doing this calculation). This is necessary since the fit is a point by point analysis, which has not to be necessarily Kramers-Kronig consistent[10]. The results are shown in Fig. 3.15. The overall agreement is always better than 5% (see right panel of Fig. 3.15).

Comparison to literature

As indicated in Fig. 3.16, the measured data are in excellent agreement with the infrared transmittance and reflectivity results by Rückamp *et al.* [26] which revealed an onset of interband excitations at about 0.6 eV. These measurements have been carried out on the same batch of samples. Moreover, the spectra are consistent with unpolarized room-temperature data of Refs. [104–106] for the energies $E < 2.5$ eV. There are deviations to the data of Okimoto *et al.* [107] and in general to all data for $E > 2.5$ eV. The optical conductivity from Refs. [104–107] has been obtained from reflectivity measurements at room temperature using the Kramers-Kronig transformation. The discrepancy can be explained either by errors in our measurement or analysis (due to low signal intensity of our lamp in the UV range or an improper handling of the thin cover layers in our model, see discussion

[10] We started our analysis with Drude-Lorentz functions, which are Kramers-Kronig consistent, and used the point by point analysis (*Normal fit*) only for the fine tuning.

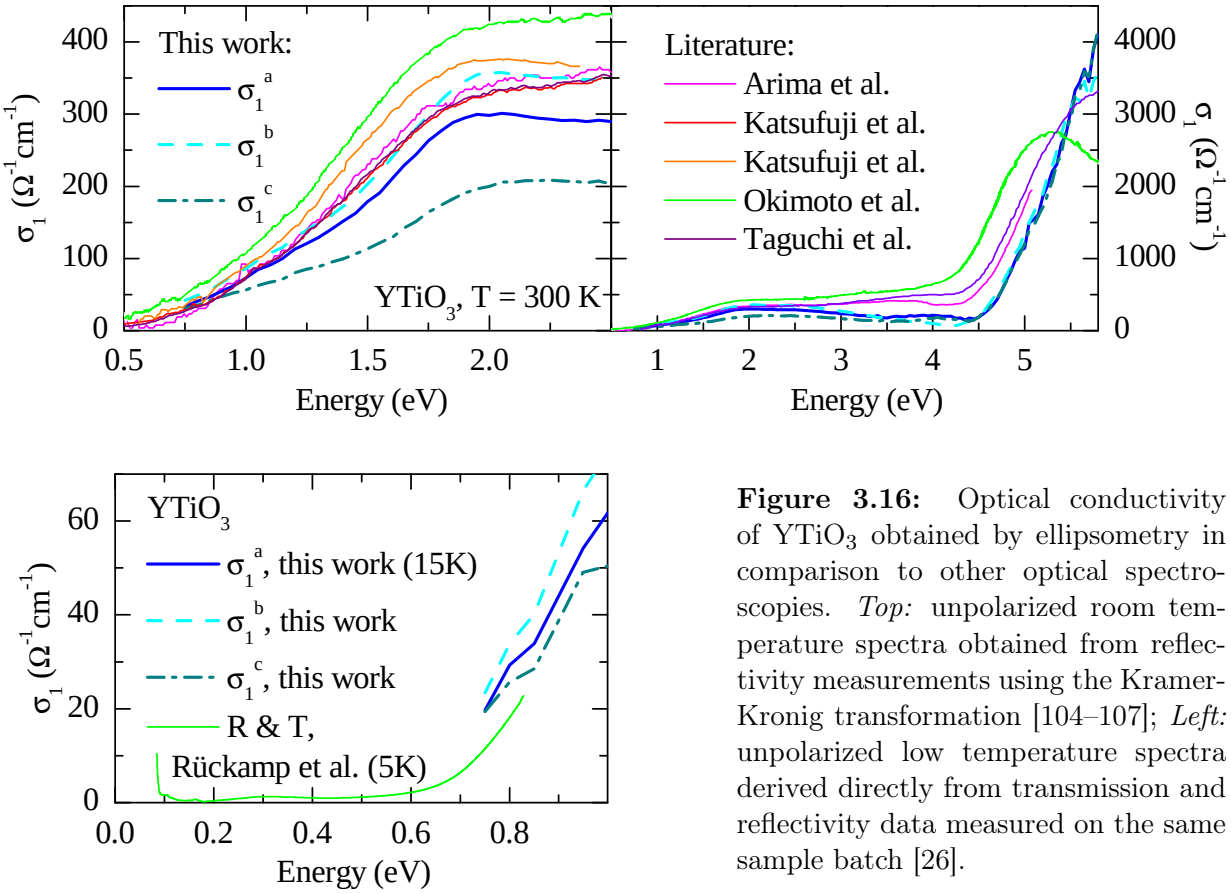

Figure 3.16: Optical conductivity of $YTiO_3$ obtained by ellipsometry in comparison to other optical spectroscopies. *Top:* unpolarized room temperature spectra obtained from reflectivity measurements using the Kramer-Kronig transformation [104–107]; *Left:* unpolarized low temperature spectra derived directly from transmission and reflectivity data measured on the same sample batch [26].

above), or by errors in the reflectivity measurement or in the extrapolations of the Kramers-Kronig transformation. Also a difference in the intrinsic sample properties (e.g. oxygen stoichiometry) may account for the discrepancy. Our samples are high-quality single crystals and their properties, such as the Curie temperature, are comparable to those reported in the literature [108]. As seen in the inset of Fig. 3.17 the reflectivity data from literature [105, 107] show striking differences above 5 eV, which of course explains the difference in conductivity reported by Okimoto *et al.* [107] and Taguchi *et al.* [105]. In the energy range of 0.8 eV $< E <$ 5.8 eV we derived the normal incidence reflectivity from our dielectric constants and compare it to the literature data, see Fig. 3.17. Up to 4 eV there is good agreement especially to the data of Taguchi *et al.* [105]. However, above 4 eV the derived reflectivity data significantly deviate from the measured reflectivity. The discrepancy vanishes if one assumes a thin cover layer (Cauchy layer, see discussion above) present on the samples measured in Refs. [105, 107]. We simulate the normal incidence reflectivity spectra for thicknesses of the cover layer of 0, 2, 4, and 6 nm for all polarization directions (*three top panels*) and for an unpolarized measurement (*bottom panel*). The reflectivity data of Taguchi *et al.* and Okimoto *et al.* can very well be reproduced by our optical constants if one assumes a thickness of 2-4 nm and 6 nm, respectively. On the other hand we note, that

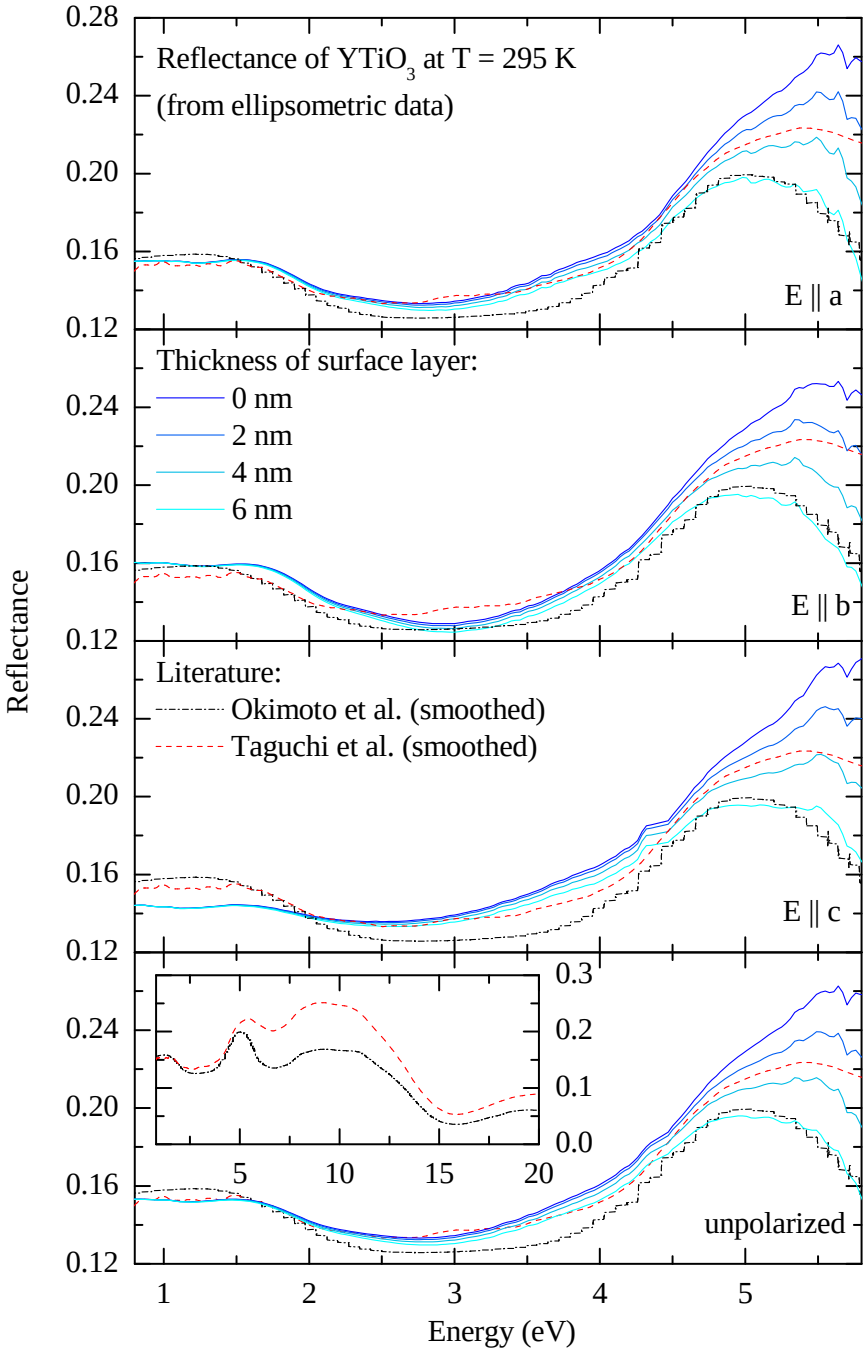

Figure 3.17: Comparison of measured unpolarized room-temperature reflectance data from literature [105, 107] and calculated spectra using the results from ellipsometry for $0.8 - 5.8$ eV. *From top to bottom:* $E||a$, $E||b$, $E||c$, and E unpolarized (average of a, b, and c) for different thicknesses of the cover layer (see text); *inset:* reflectance data from literature [105, 107] over a wide energy range.

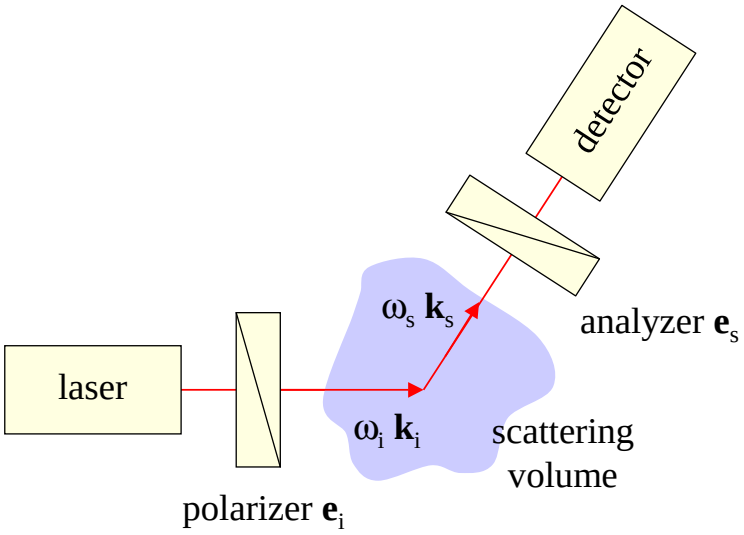

Figure 3.18: Schematic scattering experiment.

it is not possible to describe our ellipsometric data with the same quality over the entire energy range using the optical constants reported for $YTiO_3$ in the literature, because the reflectivity does not provide information about a possible cover layer. Our experimental analysis and the comparison to literature indicate that cover layers, when present, affect not only ellipsometry but also reflectivity measurements in the UV range. This can lead to errors in the extracted optical conductivity.

3.4 Raman scattering

Raman scattering is an inelastic light-scattering technique which was named after its inventor C.V. Raman [109]. He observed satellite peaks below and above the elastically scattered photons (Rayleigh scattering). For his exploration he received the Nobel prize in 1930. The basics of Raman scattering can be understood by regarding a schematic scattering experiment, see Fig. 3.18. An incoming light wave $\mathbf{E}_i$ with wave vector $\mathbf{k}_i$ (with $|\mathbf{k}_i| = \frac{2\pi}{\lambda_i} = \frac{2\pi n_s}{\lambda_{i,0}} = \frac{n_{i,s}\omega_i}{c_0}$, n_s - real part of the refractive index of the scattering volume) and frequency ω_i gets linearly polarized in the direction $\mathbf{e}_i$ and evokes a polarization $\mathbf{P}$ inside the scattering volume (crystal):

$$P^{\mu}(\mathbf{r},t) = \epsilon_0 \sum_{\nu} \chi^{\mu\nu}(\mathbf{r},t) E_i^{\nu}(\mathbf{r},t) \tag{3.35}$$

Here $\chi^{\mu\nu}$ represents the components of the electric susceptibility tensor and ϵ_0 is the permittivity of the vacuum. Following Maxwells's equations, $\mathbf{P}$ produces a scattered light wave $\mathbf{E}_s$ with $\mathbf{k}_s$ and ω_s, which can be measured with a detector. The so-called *Porto notation* serves as a brief description of the scattering geometry: $\mathbf{k}_i(\mathbf{e}_i\mathbf{e}_s)\mathbf{k}_s$.

Being an inelastic experiment, incoming and scattered frequency are not equal in Raman scattering, i.e. $\omega_i \neq \omega_s$. The incoming photon can either create an elementary excitation (called Stokes scattering) or annihilate an elementary excitation (called Anti-Stokes) in the scattering volume. The energy of this elementary excitation ω_e can be obtained using energy conservation:

$$\omega_e = |\omega_i - \omega_s| \tag{3.36}$$

In practice, ω_i is the laser frequency and therefore a known parameter. The scattered frequency ω_s is measured using a dispersive system, e.g. a monochromator. With Eq. 3.36 the frequency of the elementary excitation can be obtained.

The observability of elementary excitations in Raman scattering is limited by certain conservation laws, which will be briefly discussed for the case of Stokes scattering:

- *Spin conservation:* When linearly polarized light is used in the experiment, it follows from spin conservation $S_i = S_s + S_e$ that the elementary excitation can only be a $S_e = 0$ excitation. However, this does not mean that excitations with $S_e > 0$ can not be detected. For example a simultaneous excitation of two $S_e^{1,2} = 1$ excitations can be combined to $S_e = S_e^1 - S_e^2 = 0$. An example for the observation of a combined two-particle $S_e^i = 1$ excitation is two-magnon light scattering [65, 110–112].

- $\mathbf{k}$ *conservation:* As a result of the conservation of $\mathbf{k}$, namely $\mathbf{k}_i = \mathbf{k}_s + \mathbf{k}_e$, one can only probe (one-particle) excitations very close to the Brioullin-zone center, i.e. with $\mathbf{k}_e \sim 0$. This follows from the fact that visible light for the incident and scattered light wave have wave vectors of $|k_{i,s}| = \frac{2\pi}{\lambda_{i,s}} = \frac{2\pi n_s}{\lambda_{0,i,s}} \sim 10^7$ m^{-1}. This is rather small compared to an excitation from the center to the edge of a Brioullin-zone, which needs approximately $|k_e| = \frac{\pi}{a} \sim 10^{10}$ m^{-1}, where a denotes the lattice constant.

An effective Raman Hamiltonian, which describes the interaction between the scattered electromagnetic wave $\mathbf{E_s}$ and the polarization $\mathbf{P}$ can be written as:

$$H_{Raman} = \sum_{\mu\nu} E_s^\mu \chi^{\mu\nu}(\mathbf{r}, t) E_i^\nu \tag{3.37}$$

It arises from second-order perturbation of the $\mathbf{A} \cdot \mathbf{p}$ term and from first-order perturbation of the $\mathbf{A}^2$ term in the interaction Hamiltonian of matter and light, see Eq. 3.4 [113].

The observable in Raman scattering is the differential cross section[11] $\frac{d^2\sigma}{d\Omega d\omega}$ (not to be confused with the optical conductivity which is also denoted by σ). It measures the flux of scattered photons in a certain frequency interval $(\omega_s, \omega_s + d\omega)$ into a spatial angle $d\Omega$ with respect to the flux of incoming photons. For our purpose, it is sufficient to know that

$$\frac{d^2\sigma}{d\Omega d\omega} \propto \omega_s^3 \omega_i V |\sum_{\mu\nu} e_s^\mu \mathcal{R}^{\mu\nu} e_i^\nu|^2, \tag{3.38}$$

[11] A quantum-mechanical derivation of the cross section can be found e.g. in Refs. [72, 114], while an approach based on correlation functions can be found in Refs. [110, 115].

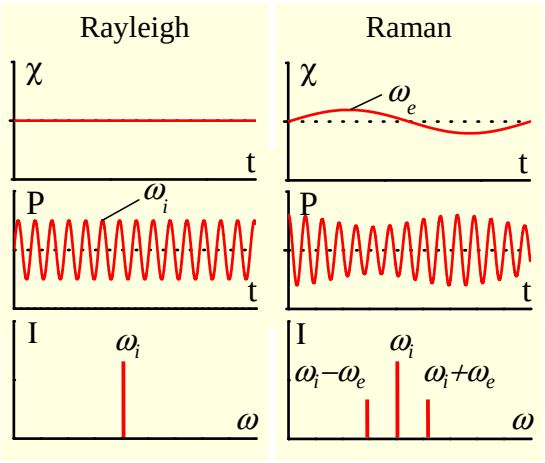

Figure 3.19: The susceptibility, polarization and the corresponding light-scattering spectra for Rayleigh and Raman scattering. The Stokes and Anti-Stokes satellites in the Raman spectra arise from a modulation of the electric susceptibility χ.

where $\omega_{i,s}$ are again the frequency of the incident and scattered light, V is the scattering volume, and $\mathcal{R}$ the so called *Raman tensor* [115]. This tensor reflects the symmetry of the excitation and can be evaluated from the susceptibility tensor, which will briefly be discussed below for the case of phonons. The Raman tensors for every symmetry are tabulated for instance in Refs. [115, 116].

Let us refer again to the polarization in Eq. 3.35 which depends on the incident wave and on the susceptibility. The creation of an elementary excitation gives rise to a time dependent χ. This is sketched in Fig. 3.19: if χ is constant in time then the polarization has the same frequency as the incident light wave (Rayleigh scattering). The spectrum shows a single peak at ω_i. On the other hand if χ becomes dependent on time, $\mathbf{P}$ gets modulated in frequency. This yields two satellite peaks at $\omega_i \pm \omega_e$. Because the modulation amplitude can be assumed to be small compared to the exciting amplitude, the susceptibility can be developed into a Taylor series in suitable coordinates around the time-independent susceptibility. For the case of phonons these coordinates are the normal coordinates $\mathbf{Q}$ (in the case of magnons the spin operators [110]), which results in $\chi^{\mu\nu}(\mathbf{Q},t) = \chi_0^{\mu\nu}(\mathbf{Q}) + \frac{\partial\chi^{\mu\nu}(\mathbf{Q})}{\partial\mathbf{Q}} \cdot \mathbf{Q} + ...$ The polarization from Eq. 3.35 in the harmonic approximation, namely $\mathbf{Q} = \mathbf{Q}_0 \cos(\omega_e t)$ and $\mathbf{E}_i = \mathbf{E}_0 \cos(\omega_i t)$, reads as:

$$P^\mu = \epsilon_0 \sum_\nu \chi_0^{\mu\nu} E_0^\nu \cos(\omega_i t) + \frac{\epsilon_0}{2} \sum_\nu \frac{\partial\chi^{\mu\nu}(\mathbf{Q})}{\partial\mathbf{Q}} \cdot \mathbf{Q}_0 \, E_0^\nu \cos((\omega_i \pm \omega_e)t) + ... \qquad (3.39)$$

The first term oscillates with ω_i and thus represents Rayleigh scattering, while the second term oscillates with $\omega_i \pm \omega_e$ and describes the inelastic scattering in Raman spectra, see

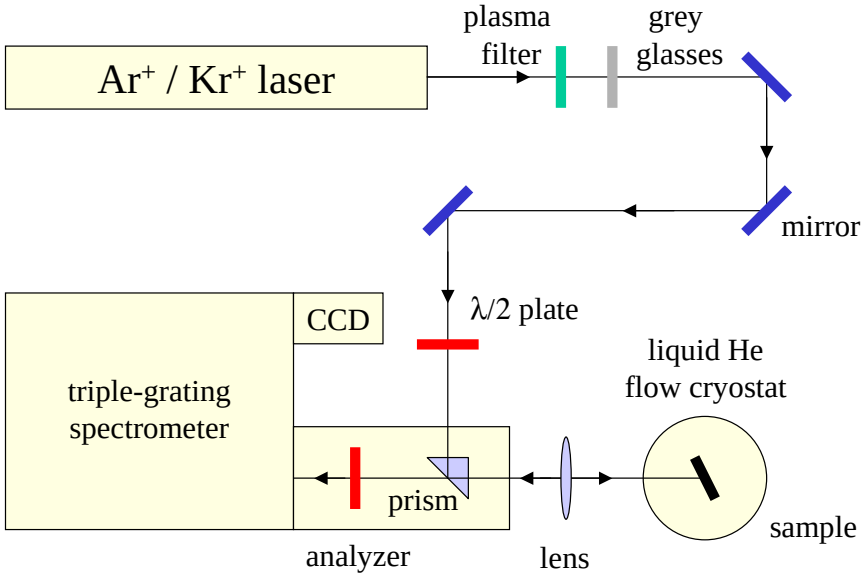

Figure 3.20: Schematic Raman-scattering setup (Dilor XY, MPI Stuttgart).

Fig. 3.19. The cross section for phononic scattering can be derived with some effort [115]:

$$\frac{d^2\sigma_{Stokes}}{d\Omega d\omega} \propto \omega_i \omega_s^3 V |\sum_{\mu\nu} e_s^\mu \frac{d\chi^{\mu\nu}}{d\mathbf{Q}} \cdot \mathbf{Q_0}\, e_i^\nu|^2 \frac{\hbar}{2\omega_e}(n+1) \tag{3.40}$$

$$\frac{d^2\sigma_{Anti-Stokes}}{d\Omega d\omega} \propto \omega_i \omega_s^3 V |\sum_{\mu\nu} e_s^\mu \frac{d\chi^{\mu\nu}}{d\mathbf{Q}} \cdot \mathbf{Q_0}\, e_i^\nu|^2 \frac{\hbar}{2\omega_e} n \tag{3.41}$$

where the factor $n = (e^{\hbar\omega_e/(k_B T)} - 1)^{-1}$ reflects the Bose-Einstein statistics. One can directly read that for a non-vanishing Raman signal $\frac{\partial\chi^{\mu\nu}(\mathbf{Q})}{\partial\mathbf{Q}} \neq 0$ has to be fulfilled. The derivative depends on the symmetry of the excitation and therefore on the underlying crystal symmetry. Knowing the point-group symmetry of the crystal and the site symmetries of the atoms, one can directly evaluate the selection rules for the observation of a certain phonon in a Raman experiment. The corresponding analysis is called *factor-group analysis* [117].

3.4.1 Experimental setup

The Raman measurements on $LaTiO_3$ and $YTiO_3$ were carried out at the Max-Planck institute for solid state research in Stuttgart[12]. The Raman setup, a Dilor 800 XY, is schematically shown in Fig. 3.20. The power of the incident laser light of an Ar^+/Kr^+ ion mixed-gas laser is reduced by grey glasses to 20 mW, which corresponds to a power below 10 mW at the sample position. The light passes a plasma-line filter and then a $\lambda/2$ plate in

[12] in close collaboration with C. Ulrich and B. Keimer

order to control the polarization state of the incident, linearly polarized light. The beam is reflected at a prism and focussed by a lens onto the sample. This is either placed inside a flow cryostat for the low-temperature measurements or on a sample rotator outside the cryostat. The scattered light is collected in quasi-backscattering ($\mathbf{k}_i = -\mathbf{k}_s$) geometry with a misalignment below 10°. The slight deviation of the angle of incidence from the sample normal strongly reduces the stray light since the directly reflected light from the sample surface does not meet the lens anymore. The polarization state of the scattered light is fixed by an analyzer to the direction of highest sensitivity of the spectrometer. The scattered light is analyzed by a triple-grating spectrometer system in the subtractive mode, i.e. a double monochromator suppresses the stray light by several orders of magnitude, and the third monochromator (1200 lines/mm) disperses the light. The detection takes place at a nitrogen-cooled back-illuminated CCD camera. Typically, recording times of 300 seconds have been used (typically 10-12 iterations). The measured intensities have been corrected for the spectrometer response using a calibrated white-light source (Ulbricht sphere); the measured energies have been checked by a standard Ar-lamp.

4 Ellipsometry and Fourier spectroscopy on $La_{1-x}Sr_{1+x}MnO_4$ (x=0, 1/8, 1/2)

In this chapter the optical studies on single-layer manganites are presented. It is organized as follows: in the first section a very brief introduction to the physics of manganites is given. Using a few examples of optical studies made on these systems in the past we will show how powerful this technique is in order to study correlation effects. We proceed with further details on the layered compounds which are necessary for the interpretation of our data. After that we will review the experimental findings, which are discussed and analyzed in the following sections. Here the focus is placed on the compound $LaSrMnO_4$, because it is the undoped d^4 mother compound which we wanted to understand in detail before increasing the complexity. For this compound we performed a multiplet calculation which we directly compare to our measured data. We also discuss the temperature dependence of the optical properties. In the last section we compare the doped compounds with the undoped one.

4.1 Physics of manganites

The physics of manganites became famous due to the discovery of the colossal magneto resistance (CMR), i.e. an extremely large drop of the resistance when a magnetic field is applied (see e.g. Refs. [118–121] for an overview). Qualitatively this behavior can be understood in terms of the double-exchange mechanism between Mn^{3+} and Mn^{4+} ions. The motion of an electron is greatly favored by a ferromagnetic alignment of the spins of adjacent manganese ions. It turned out that the pure double-exchange model is not sufficient to explain the magnitude of the CMR effect [119]. One extension of this model is the inclusion of Jahn-Teller distortions which leads to the formation of lattice polarons [122]. When an electron moves it now has to "pay" the Jahn-Teller distortion energy (Mn^{3+} is a Jahn-Teller ion, while Mn^{4+} is not). This effect greatly enhances the effective mass of the electron (polaron) and thus the magnitude of the double-exchange effect. However, the polaronic picture cannot capture the observed phase separation [119, 121]. Thus a deeper and complete understanding is still lacking. This discussion shows that the inclusion of lattice and charge degrees of freedom leads to an improved understanding. One might draw the conclusion that a fundamental study of the coupling between different degrees of freedom will give further insights to CMR and other phenomena of high complexity.

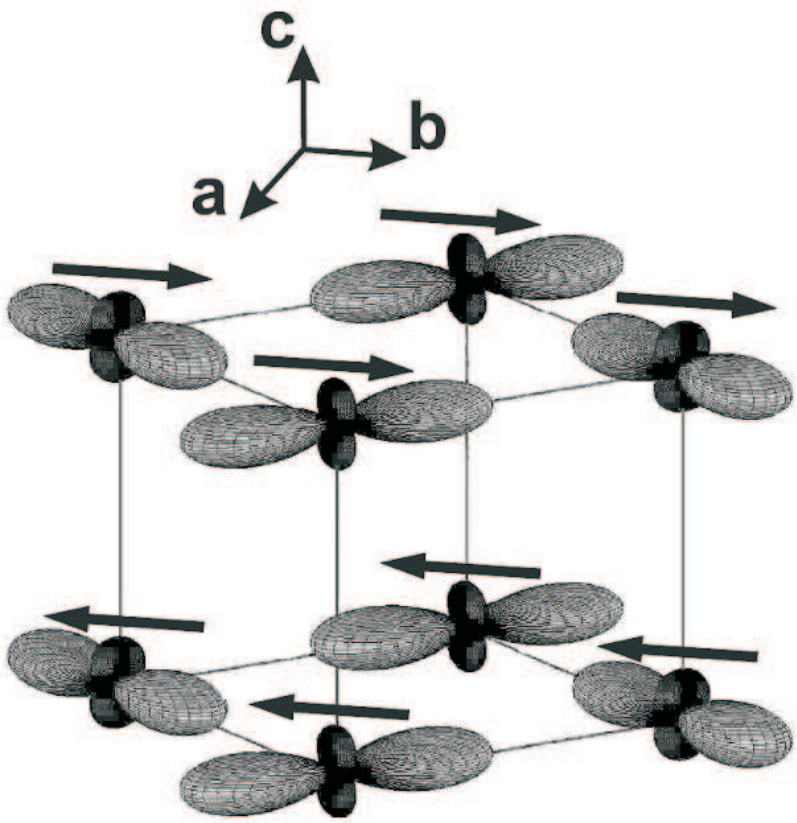

Figure 4.1: The spin-orbital structure of $LaMnO_3$. It is found to be ferromagnetically spin and antiferro-orbitally ordered within the *ab* planes, while it is antiferromagnetically/ferro-orbitally ordered between the planes (A-type antiferromagnet, C-type orbital order). Taken from Ref. [2].

Being the mother compound of CMR, $LaMnO_3$ has attracted much interest in the context of concurring spin, orbital and lattice degrees of freedom. The charge degree of freedom is quenched here, since only Mn^{3+} ions are present. $LaMnO_3$ shows A-type antiferromagnetic order below 140 K and is orbitally ordered below approximately 780 K [87, 123]. The spin-orbital structure of $LaMnO_3$ is shown in Fig. 4.1. The electronic properties of $LaMnO_3$ have been discussed for a long time in terms of a charge-transfer insulator [1, 69, 104, 124]. In more recent studies it has been claimed that a description as a Mott-Hubbard insulator is more favorable, since the lowest electronic transition arises from intersite $d_i d_j$-excitations [2, 125, 126]. We will discuss this below.

The orbital degree of freedom in $LaMnO_3$ has also attracted a lot of interest during the last years due to the prediction of orbital waves [60], sometimes termed orbitons. These excitations differ from local crystal-field excitations because they show a significant dispersion. Up to now no clear evidence of orbital waves, which means the direct observation of their dispersion, has been found in any compound. Features observed in $LaMnO_3$ by

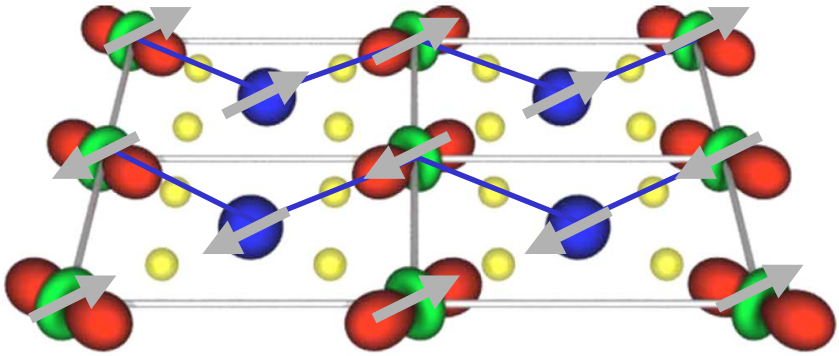

Figure 4.2: Sketch of the charge-exchange (CE) phase, as observed e.g. in $La_{0.5}Sr_{1.5}MnO_4$. It consists of alternating $3y^2 - r^2/3x^2 - r^2$ orbitals at the Mn^{3+} and holes at the Mn^{4+} sites (large blue spheres). The spin structure forms ferromagnetic zig-zag chains. This charge/spin/orbital structure is compatible with super-structure reflections as observed in neutron scattering and by X-ray diffraction techniques [22, 128–130]. Nore that another orbital pattern, namely x^2-z^2/y^2-z^2, has been suggested giving rise to the same superstructure reflections [131–134]. Also for the charge pattern an alternative model has been proposed: the charge is not ordered on the manganese sites but is distributed on the whole Mn-O-Mn bond, forming a Zener polaron [135]. The figure has been taken from Ref. [134] and has been extended by the spin structure.

Raman spectroscopy were discussed in terms of orbital waves [47] but turned out to be multi-phonon excitations [26, 59]. Very recently several authors reported on the observation of orbital waves in $YTiO_3$ and YVO_3 by means of Raman spectroscopy [55–58]. For further general information about the 113 manganites[1] we refer to Refs. [1, 127].

Another interesting class of manganites is composed of Mn-O layers[2], for example $La_{1-x}Sr_{1+x}MnO_4$. They offer rich physics with respect to all degrees of freedoms. The fundamentals of, e.g. double exchange, orbital-ordering phenomena, charge ordering, etc. can be studied within this class of compounds as well. The major number of publications deals with the doped compound with $x = 0.5$. Here one can formally assume that the crystal contains Mn^{3+} and Mn^{4+} in a ratio[3] of 1:1. Besides antiferromagnetism below approximately $T_N = 110$ K, charge ordering at $T_{CO} = 220$ K has been detected by neutron scattering and X-ray diffraction [128, 129], and in addition orbital ordering at the charge-ordering temperature $T_{CO} = T_{CO} = 220$ K [129–134]. The combined charge/orbital/spin structure is known as the charge-exchange[4] (CE) phase [136]. It is sketched in Fig. 4.2 and discussed in more detail in the figure caption. The CE phase is a generic feature of half-doped manganites since it has been also observed in half-doped 113 manganites [136].

[1] This abbreviation refers to the class of quasicubic compounds such as $R_1Mn_1O_3$ (R-rare earth).
[2] The class of bilayer compounds $La_{2-x}Sr_{1+2x}Mn_2O_7$ will not be discussed.
[3] In general: $Mn^{4+}/Mn^{3+} = x/(1-x)$.
[4] Strictly speaking the abbreviation CE refers only the magnetic part of the charge/orbital/spin structure.

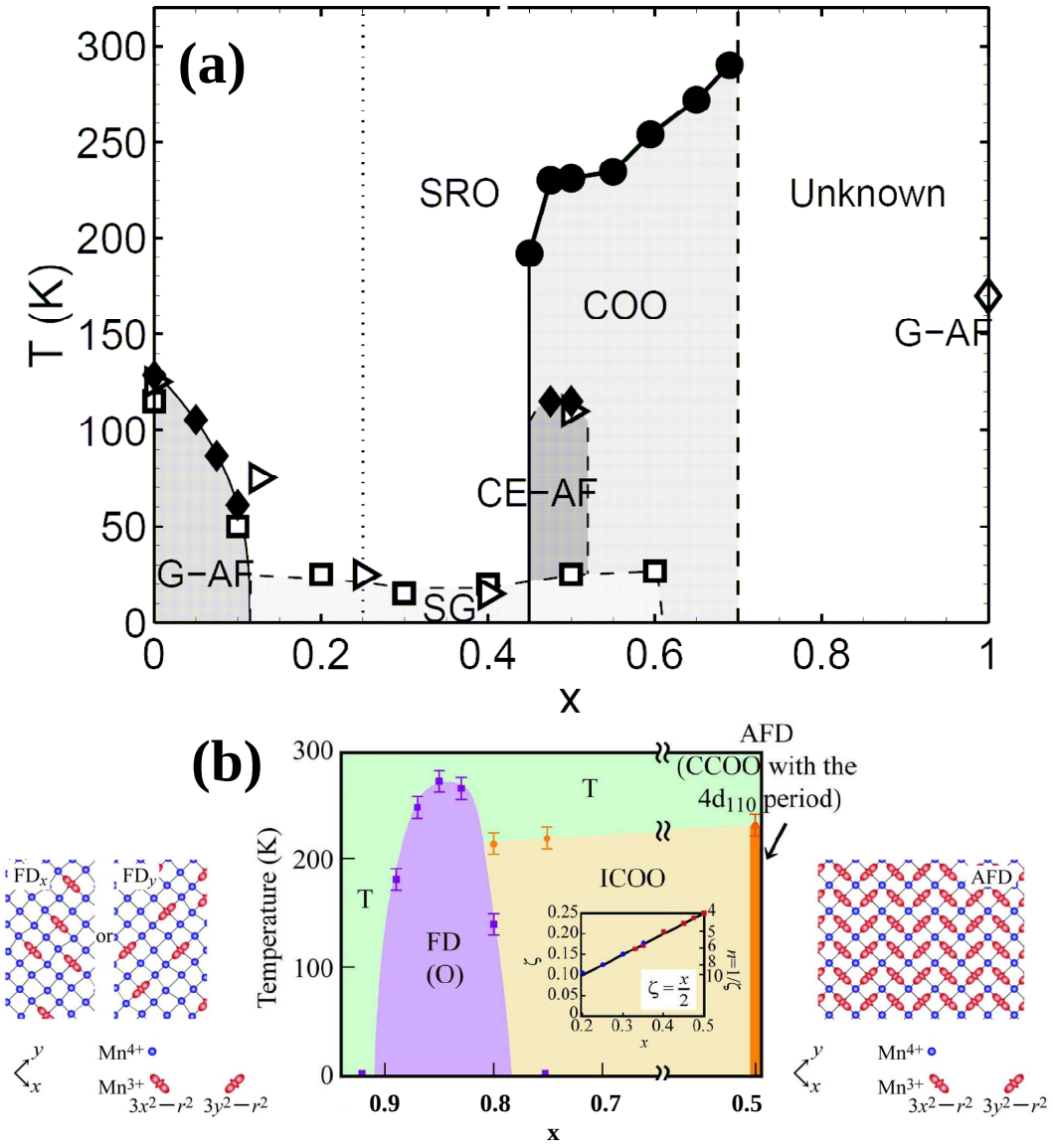

Figure 4.3: Phase diagrams of $La_{1-x}Sr_{1+x}MnO_4$. (a) $x = 0.0-1.0$ region: from X-ray scattering (• [137]), neutron scattering (⧫ [137] and ◊ [138]), magnetometry (□ [139]) and muon spin rotation (▷ [140]) measurements. G-AF: G-type antiferromagnet, CE-AF: CE-type antiferromagnet, SG: spin glass, COO: charge/orbital order phase, SRO: short-range charge and orbital order. Picture taken from Ref. [137]. (b) $x = 0.5-1.0$ region: from transmission microscopy [141]. T: tetragonal, FD: ferro-distortive, AFD: antiferro-distortive, ICOO: incommensurate charge and orbital order. The latter three phases have lower symmetry than tetragonal. Since the original graph in Ref. [141] is based on the formula $La_{\tilde{x}}Sr_{2-\tilde{x}}MnO_4$ we changed the axis by $\tilde{x} \mapsto 1-x$ in order to be consistent with the nomenclature used in (a). Diagram taken from Ref. [141]. In contrast to the phase diagram shown, the SG phase is already present at $x = 0$ [142, 143].

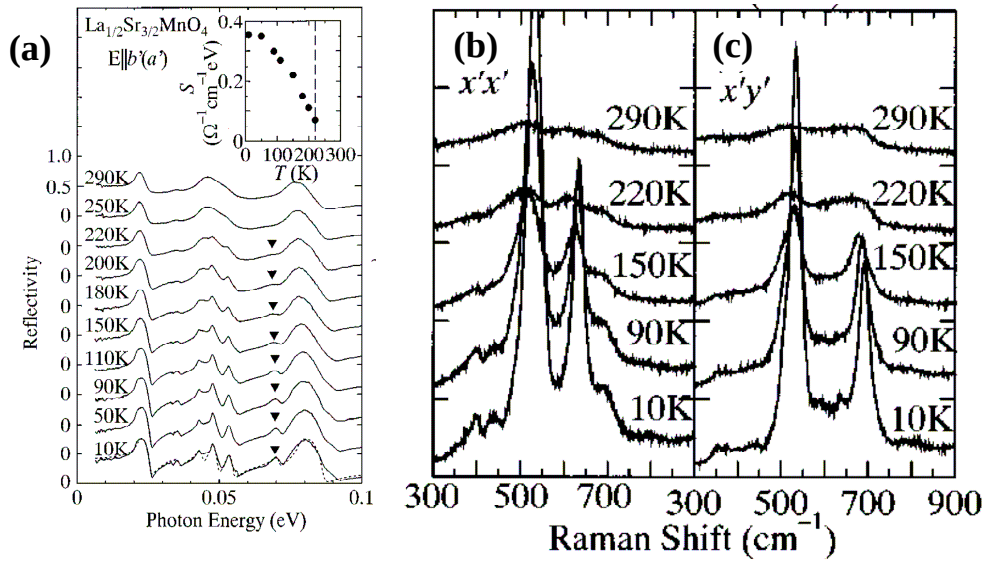

Figure 4.4: Phonon spectra of $La_{0.5}Sr_{1.5}MnO_4$ as a function of temperature. (a) Reflectivity data [144] and (b), (c) Raman data [145]. Both data sets show a strong loss of intensity (disappearance) of phonon modes across the charge-ordering temperature.

Very recently several studies investigated the layered manganites $La_{1-x}Sr_{1+x}MnO_4$ as function of x [23, 137, 139, 146–149]. The results are summarized in a phase diagram as shown in Fig. 4.3. For $x = 0$ one finds a G-type antiferromagnet (AF) below 130 K. Furthermore soft X-ray linear dichroism experiments at 90 K [150] identified orbital ordering with $3z^2 - r^2$ symmetry. This type of ordering is compatible with the observation of a strongly elongated MnO_6 octahedra along the c axis [148]. With increasing x antiferromagnetism is suppressed and transformed into a spin-glass (SG) phase below 30 K at $x = 0.13$ which extends up to $x = 0.6$. In contrast to the phase diagram shown, the SG phase is already present at $x = 0$ according to Refs. [142, 143]. In the region $0.45 < x < 0.7$ the charge- and orbitally-ordered (COO) phase has been found below approximately 250 K. Very recently it has been shown that this region extends up to $x = 0.85$, but with an incommensurate wave vector. The commensurability is recovered at around $x = 0.9$ [141], see Fig. 4.3(b). The symmetry in this phase is no longer tetragonal but orthorhombic, as deduced from an optical phonon-mode analysis, X-ray and neutron studies [137, 141, 145–147, 151]. For $0.45 < x < 0.5$ the CE phase has been found below 130 K (see discussion above). Outside the COO dome short-range charge and orbital order (SRO) has been suggested.

Manganites have been intensively studied by optical spectroscopy. We would like to give three short examples showing how powerful optical spectroscopy can be: (a) optical spectroscopy and charge/orbital ordering, (b) optical spectroscopy and metal-insulator transitions, and (c) optical spectroscopy and the kinetic energy of the Mott-phase. Note, that all studies assumed randomly distributed La ions Sr on one crystallographic site.

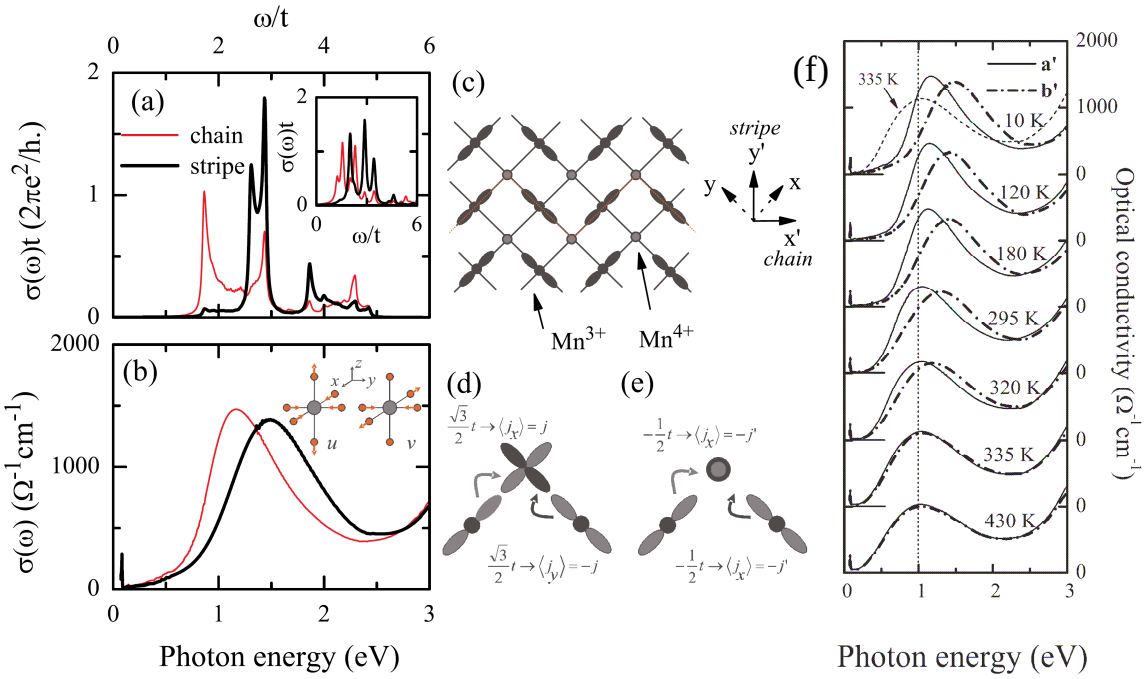

Figure 4.5: Optical conductivity of $Eu_{0.5}Ca_{1.5}MnO_4$ as function of temperature. Data and sketches taken from Ref. [152]: (a) calculated optical conductivity using the Hartree-Fock method (b) measured anisotropy between zig-zag chains (x') and the perpendicular direction (stripes, y') (c) CE phase pattern (d),(e) local hopping between adjacent electron-rich (Mn^{3+}) and electron-poor (Mn^{4+}) sites. There are two hopping paths, one via the $d_{x^2-y^2}$ orbital (d) and another one via the $d_{3z^2-r^2}$ orbital (e). Since the current operators[5] read $J_{x'} = (J_x - J_y)/\sqrt{2}$ and $J_{y'} = (J_x + J_y)/\sqrt{2}$ the contribution of (d) is suppressed in the y' direction while those of (e) get suppressed in the x' direction. Since the state (d) is lower in energy, more weight should be observed in the x' direction at lower energies, in accordance with the experiment. (f) Evolution of the anisotropy between the x' and y' directions as function of temperature.

(a) *Optical spectroscopy and charge/orbital ordering* - Optical spectroscopy is highly sensitive to the reduction of symmetry (much more sensitive than X-rays). This can be exploited in several ways, namely by the study of phonons and electronic transitions. The study of temperature-dependent phonon spectra offers the possibility to determine the number of optical phonon modes. As the number changes across a certain temperature this give evidence for a phase transition. The number of modes and their polarization dependence can be compared to the expectations from group theory (factor-group analysis [117]). As an example we have chosen the orbital/charge-ordering transition in $La_{0.5}Sr_{1.5}MnO_4$ as depicted in Fig.4.4. In reflectivity data a mode at 0.07 eV disappears at approximately the charge-ordering temperature of $\sim$ 220 K, while in the Raman spectra two modes at

[5]There is in our opinion a mistake in the paper, either in the coordinate system of Fig. 4.5 or in the definition of the current operator.

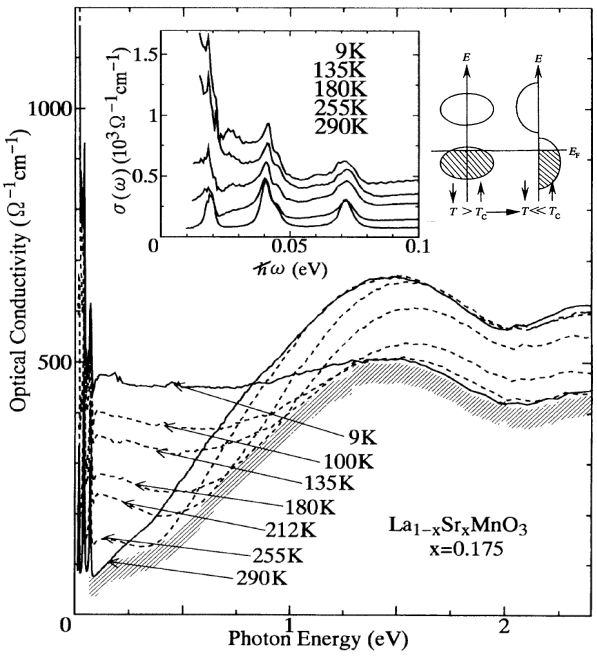

Figure 4.6: Optical conductivity spectra of $La_{1-x}Sr_xMnO_3$ for $x = 0.175$ [154]. The ferromagnetic transition temperature is T_c=240 K.

500 and 700 cm^{-1} are reduced in intensity towards this temperature. The same effects are also found by Jung *et al.* [151], showing further that the evolution of the optical gap with temperature can be equivalently used in order to visualize the breakdown of charge/orbital ordering as well as of the spin ordering [153]. Spin transitions can be observed in optics due to the magneto-elastic or electron-phonon coupling, i.e. via a slight modification of the bond length at the transition temperature. This modifies the hopping strength and thus the optical conductivity.

Optical spectroscopy is also highly sensitive to anisotropies arising from orbital ordering. In the CE phase the orbital pattern along and perpendicular to the zig-zag chains are very different, see Fig. 4.2. Therefore, one expects a reduction of symmetry at a temperature $T = T_{CO}, T_{OO}$. Due to the rearrangement of the orbitals the lattice will form an anisotropy between $x' = x - y$ and $y' = x + y$ directions. This corresponds to a reduction of symmetry from tetragonal to orthorhombic. The new axes in the orthorhombic space group are rotated by 45° around z with respect to the tetragonal axis. This anisotropy will lead to a different optical response in the x' and y' direction. This behavior is nicely shown in a very recent paper on $Eu_{0.5}Ca_{1.5}MnO_4$, see Fig. 4.5. Similar behavior has been reported for $La_{0.5}Sr_{1.5}MnO_4$ [144]. In both studies the optical feature at 1.0-1.5 eV have been explained in terms of Mn-intersite $d_i d_j$ transitions.

In another interesting study the impact of orbital rotations and mixing on the optical properties on $RMnO_3$ (R=La, Pr, Nd, Gd, Tb) was investigated [88]. Kim *et al.* found

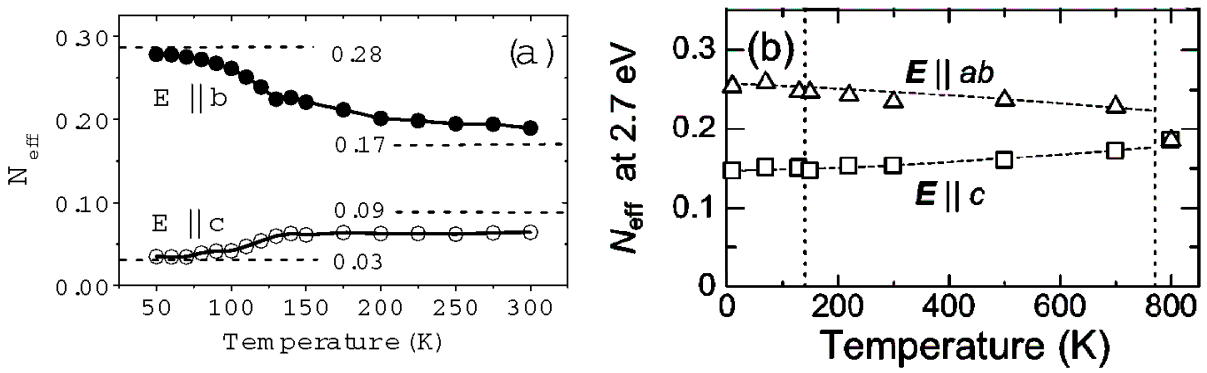

Figure 4.7: Effective carrier concentration (N_{eff}) of the first electronic transition in $LaMnO_3$ derived from (a) an oscillator fit to $\epsilon_{1,2}$ measured with ellipsometry [2] and (b) an integral over σ_1 up to 2.7 eV obtained from reflectivity measurements [69].

that the spectral weight of the first intersite Mn-Mn transition is increased with increasing Mn-O-Mn bond angle ϕ. However, it turned out that this effect alone is not sufficient to explain the reduction of spectral weight from La (large ionic radius, $\phi = 155°$) to Tb (small ionic radius, $\phi = 145°$). They concluded that the orbital mixing angle θ between $d_{x^2-y^2}$ and $d_{3z^2-r^2}$ is increased upon decreasing the ionic radius. This example shows again the high sensitivity of optical studies on the orbital arrangements.

(b) *Metal insulator transitions* - Especially in the 113 manganites optical spectroscopy has been used in order to study metal-insulator transitions. As an example we show the temperature-dependent optical conductivity of $La_{1-x}Sr_xMnO_3$ for $x = 0.175$ [154], see Fig. 4.6. With decreasing temperature a Drude peak develops, a clear signature of a metallic state. This behavior has been explained by the double-exchange mechanism. Further information about this topic can be found in Refs. [1, 155].

(c) *Optical spectroscopy and the kinetic energy of the Mott phase* - The optical conductivity has been used as a direct measure of the kinetic energy K related to an electronic transition. For that purpose one defines the effective carrier concentration N_{eff} by the following relation:

$$N_{eff}(\omega_c) = \frac{ma_0^2}{\hbar^2} \cdot K = \frac{2m}{\pi e^2 N} \int_0^{\omega_c} \sigma_1(\omega) d\omega \tag{4.1}$$

Here m, a_0, N, and ω_c represent the electron mass, the ion-ion distance, the density of ions, and the cut-off frequency. In Fig. 4.7 N_{eff} for the lowest electronic excitation around 2 eV has been plotted from two different studies on $LaMnO_3$. The first one determines N_{eff} from reflectivity measurements [69] while the second exploits spectroscopic ellipsometry [2]. Tobe *et al.* [69] argued that the lowest excitation at 2 eV can be assigned to a transition between an oxygen and manganese site because no change of N_{eff} has been observed across the magnetic ordering temperature of approximately 140 K. A charge-transfer transition

between oxygen and manganese (pd) should not be affected by the spin, because the oxygen can provide both up and down spins. Their conclusion is that $LaMnO_3$ is a charge-transfer insulator. In a later study Kovaleva *et al.* [2] argued that the opposite is true. They show in a detailed analysis that there is well a redistribution of weight across the magnetic ordering temperature. The magnitude of the spectral weight is in excellent agreement with the expectations from the spin-spin correlation function in an orbitally-ordered background [2, 83]. On the basis of their data they concluded that the lowest transition corresponds to a high-spin intersite $d_i d_j$ excitation and not a $p_i d_j$ transition. Finally they end up with the conclusion that $LaMnO_3$ is of Mott-Hubbard type.

The discrepancy in the presented data may result from a lack of accuracy in the reflectivity measurement R. For determining σ_1 one has to rely only on R and use the Kramers-Kronig transformation for calculating the phase. In ellipsometry one measures two independent quantities (see chapter 3). The consistency of the data can be *checked* by the Kramers-Kronig transformation. Additionally no standard is necessary for the measurement (for the reflectivity one usually takes Au as a reference material). Therefore we suggest to trust the data of Kovaleva *et al.*.

4.2 Details on layered manganites

We will give the details on the layered manganites $La_{1-x}Sr_{1+x}MnO_4$ for the compositions $x = 0.0$, $x = 0.13$, and $x = 0.5$, which have been measured in this thesis. The focus is laid upon the weak doping regime.

4.2.1 Crystal structure

The crystal structure of $La_{1-x}Sr_{1+x}MnO_4$ is shown in Fig. 4.8. For small x it crystallizes in a tetragonal structure with space group $I4/mmmm$ [148, 149]. As stated above, the crystal structure is orthorhombic for $x = 0.5$ in the CE-phase [144, 146, 147], but a determination of the space group is still missing. For the following discussion we will assume that all compounds are tetragonal. The manganese ions are surrounded by oxygen octahedra, which are elongated along the c axis; the Mn-O bonds coincide with the crystallographic axes. The nominal valence of the manganese changes with x as $Mn^{+(3+x)}$. The lattice parameters are summarized in Tab. 4.1. With increasing x the distortion of the octahedra is strongly reduced: for $x = 0.0$ the ratio $d_{\mathrm{Mn-O(1)}}/d_{\mathrm{Mn-O(2)}}$ is approximately 0.82 while it increases up to 0.97 for $x = 0.5$ [148]. As shown in Fig. 4.8 O(1) represents the basal and the O(2) the apical oxygens in the unit cell.

All crystals measured for this thesis are high-quality single crystals. They have been grown by M. Benomar ($x = 0.0$, $x = 0.5$) [143] and P. Reutler ($x = 0.13$) [156] using a mirror furnace. The samples have been characterized by resistivity, magnetic susceptibility, specific heat and thermal expansion measurements as well as X-ray and neutron scattering [157]. The details of growth and characterization can be found in their PhD theses [143, 156, 157].

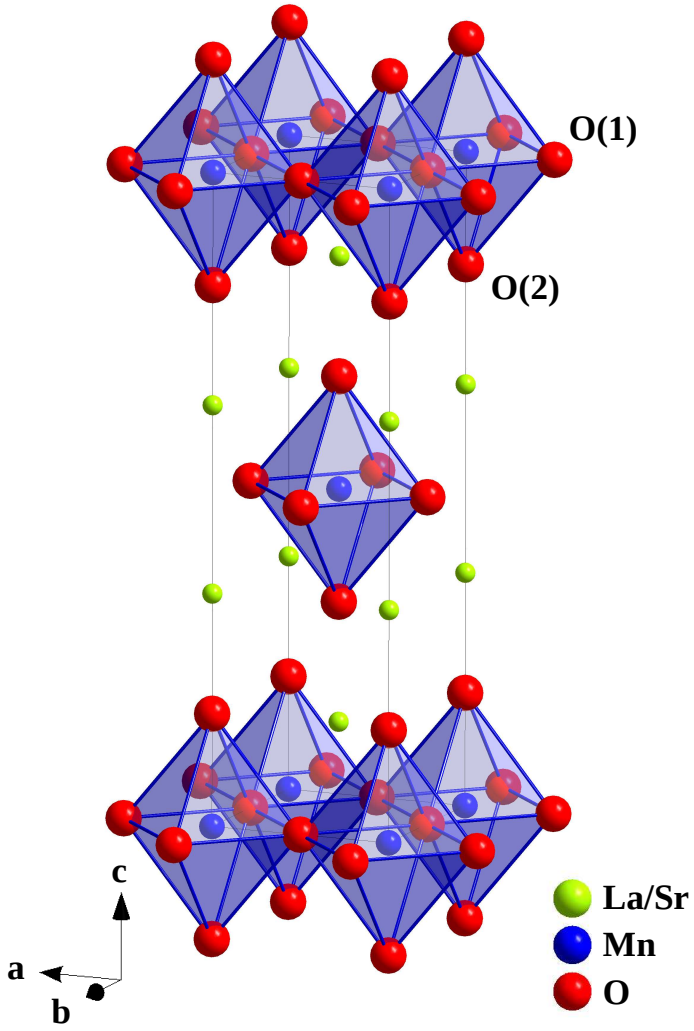

Figure 4.8: The unit cell of $La_{1-x}Sr_{1+x}MnO_4$ (space group $I4/mmmm$). It consists of MnO_6 octahedra, forming MnO_2 layers in the ab plane.

Table 4.1: Results of the single-crystal and powder neutron-diffraction experiments on $La_{1-x}Sr_{1+x}MnO_4$ for room temperature (RT) and for low temperature (LT) $\sim$ 20 K. The Mn site is at (0,0,0), the O(1) site is at (0,0.5,0), and O(2) and La/Sr are at $(0, 0, z)$. The data are reproduced from Ref. [148]. They are comparable to those in Ref. [23]. U_{iso} and U_{ii} represent the Debye-Waller factors (thermal displacements of the corresponding atoms)

			$x = 0.0^a$	$x = 0.125^b$	$x = 0.5^a$
a (Å)		RT	3.786	3.814	3.863
		LT	3.768	3.794	3.855
c (Å)		RT	13.163	12.938	12.421
		LT	13.195	12.985	12.397
V (Å^3)		RT	188.676	188.204	185.356
		LT	187.348	186.879	184.257
Mn	U_{iso} (10^{-4}Å^2)	RT	13(3)/68(3)^c	15(6)	19(2)/30(3)^c
		LT	9(3)/30(5)^c	5(4)	5(3)/ 5(3)^c
La/Sr	z	RT	0.35598(2)	0.35688(8)	0.35816(3)
		LT	0.35564(2)	0.35699(8)	0.35814(4)
	U_{iso} (10^{-4}Å^2)	RT	46(8)/38(8)^c	34(3)	40(1)/30(1)^c
		LT	19(1)/17(2)^c	18(3)	5(3)/ 5(3)^c
O(1)	U_{11} (10^{-4}Å^2)	RT	31(1)	46(8)	62(2)
		LT	27(2)	63(8)	36(3)
	U_{22} (10^{-4}Å^2)	RT	71(1)	46(7)	69(2)
		LT	45(2)	24(8)	68(3)
	U_{33} (10^{-4}Å^2)	RT	100(2)	74(8)	67(2)
		LT	58(3)	62(8)	27(4)
O(2)	z	RT	0.17221(3)	0.16900(11)	0.16106(8)
		LT	0.17270(4)	0.17023(11)	0.16138(10)
	U_{11} (10^{-4}Å^2)	RT	179(2)	191(7)	117(2)
		LT	131(2)	86(6)	70(2)
	U_{33} (10^{-4}Å^2)	RT	74(2)	163(9)	68(2)
		LT	51(3)	180(9)	52(3)
Bond length	$d_{Mn-O(1)}$ (Å)	RT	1.89335(1)	1.90714(3)	1.93164(3)
		LT	1.88403(8)	1.89684(4)	1.92763(6)
	$d_{Mn-O(2)}$ (Å)	RT	2.2668(4)	2.1873(14)	2.0005(9)
		LT	2.2788(5)	2.2104(14)	2.0006(13)

[a] Refinement of single-crystal data.

[b] Refinement of powder-crystal data.

[c] The single-crystal data refinement allows one to determine anisotropic thermal parameters on the Mn and La/Sr sites, U_{11}=U_{22} and U_{33}.

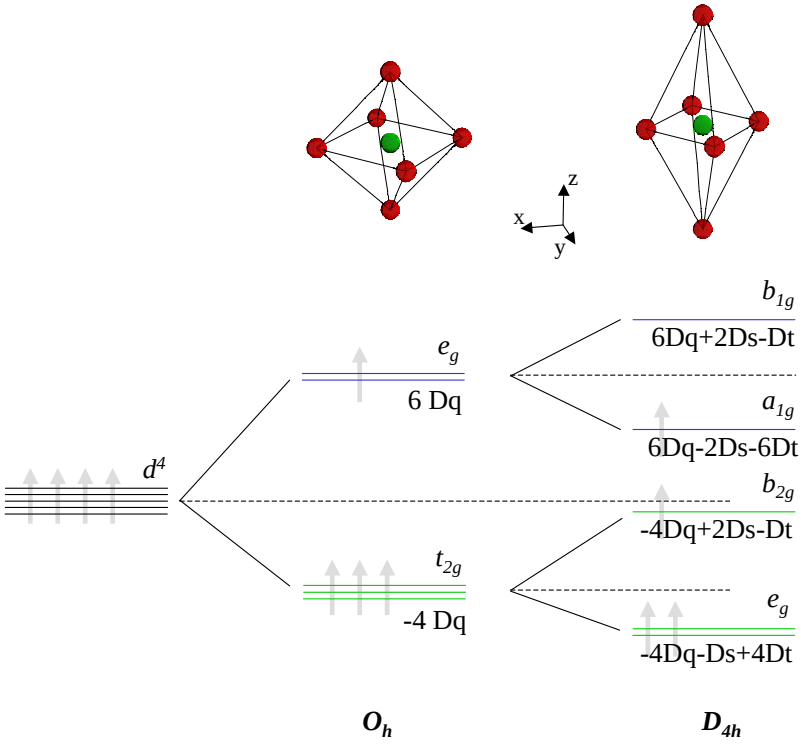

Figure 4.9: Manganese ion in a tetragonal crystal field: Mn^{3+} has four valence electrons. In the presence of a cubic crystal field, the degeneracy of the $3d$ levels is lifted and the energy levels are split into $t_{2g} \equiv d_{xy}, d_{xz}, d_{yz}$ and $e_g \equiv d_{x^2-y^2}, d_{3z^2-r^2}$ levels. Starting from cubic symmetry, an additional tetragonal elongation of the oxygen octahedra along the z axis lifts the degeneracy within the t_{2g} and e_g levels, respectively. The representations in D_{4h} are $b_{1g} \equiv d_{x^2-y^2}$, $a_{1g} \equiv d_{3z^2-r^2}$, $b_{2g} \equiv d_{xy}$, $e_g \equiv d_{xz}, d_{yz}$.

4.2.2 Manganese ion in a tetragonal crystal field

In a tetragonal crystal field, as present in $LaSrMnO_4$, the energy levels of the Mn^{3+} ion are split into four different levels. The crystal field can be characterized by using three parameters Dq, Ds and Dt [18], describing the cubic and tetragonal contributions of the crystal field. The levels are shown in Fig. 4.9. If four electrons are filled into these levels according to Hund's rules, the highest filled orbital is the $d_{3z^2-r^2}$ orbital while the first unoccupied one is $d_{x^2-y^2}$. Some care has to be taken especially when regarding excited d^4 states because configuration mixing has to be taken into account [20]. The crystal-field picture can already account for the increase of the ratio $d_{Mn-O(1)}/d_{Mn-O(2)}$ with increasing x. Enlarging x increases the number of Mn^{4+} ions. Mn^{4+} is a d^3 system and not Jahn-Teller active, i.e. the lattice relaxes. This can be seen for example when comparing the lattice constants of the Jahn-Teller compound $LaSrMnO_4$ (d^4) with those of a non-Jahn-Teller compound, e.g. Cr in $LaSrCrO_4$ (d^3). The latter materials shows a ratio of $c/a = 3.2$ while the former one has roughly 3.55 [158].

4.2.3 Thermal expansion

We show the thermal expansion for the compositions $x = 0.0$ and $x = 0.13$ as published in Ref. [148] in Fig. 4.10. For $x = 0.0$ the c axis shrinks up to 600 K. Several anomalies can be observed: one at approximately the Neél temperature of 130 K, one at approximately 220 K, and another one at 600 K. The a axis shows an almost linear increase starting from 100 K. Increasing the doping to $x = 0.13$ leads to a reduction of the magnetic ordering temperature to approximately 65 K. The thermal evolution of the lattice constants shows similar behavior, but the inflection point of the c axis observed at 600 K for $x = 0.0$ can now already be seen below 200 K. Both compositions also show a similar behavior in the thermal expansion coefficients (bottom panel of Fig. 4.10). The ordering temperatures of the two compounds can be directly read off: $T_N = 130$ K for $x = 0.0$ and $T_N = 65$ K for $x = 0.13$. These results coincide with the temperature dependence of the antiferromagnetic superstructure reflections.

In order to understand the anomalous contraction of the c axis as well as the x dependency of the lattice parameters, Senff *et al.* [148] suggested that the orbital mixing angle θ might change or fluctuate upon doping and temperature. The mixing angle determines the ground-state wave function of the highest e_g electron by $|\theta\rangle = \cos(\theta/2)|3z^2 - x^2\rangle + \sin(\theta/2)|x^2 - y^2\rangle$. These authors mentioned that this ground state requires a lower symmetry than tetragonal (for angles $\theta \neq n \cdot 120°$). A reduction of symmetry has not been observed. In a theoretical study of an orbital t-J model adapted to the layered manganites Daghofer *et al.* [159, 160] found indeed that the occupation of the in-plane orbitals is increased with increasing x, at the cost of the occupation of the out-of plane orbitals as suggested by Senff *et al.*A similar reorientation has been found Daghofer *et al.* [160] for $x = 0.0$ with increasing temperature. We note again that this reorientation must be accompanied by a structural phase transition which has not been observed for $x < 0.4$. Daghofer *et al.* assumed a static crystal field splitting E_z between the two e_g states of the order of $E_z = 0.5t = 0.25$ eV, where t is the Mn intersite hopping which is of the order of 0.5 eV [38]. For the temperature-dependent study an even lower value $E_z = 0.2t = 0.1$ eV has been used. From the experiments as presented in this chapter it is evident that E_z must be at least 0.2-0.5 eV ($\sim 1600 - 4000$ K) for the compound with $x = 0.0$. This makes the interpretation of a thermal occupation of a static crystal field level unlikely. However, the inclusion of phonons would change the picture. If we assume for a moment that the electron-phonon coupling is strong in this compound, then the orbitals are locked to the lattice. If one now thermally excites a phonon of A_{1g} symmetry then the electron-phonon coupling will force electrons into the $d_{x^2-y^2}$ orbital, because this is energetically favorable. In that sense the $d_{x^2-y^2}$ orbital gets thermally populated with increasing temperature, because more A_{1g} phonons get excited. This is physically fundamentally different to the approach of Daghofer *et al.* [160], where only a static crystal field has been considered and phonons have not been included. For the optical experiments a strong electron-phonon coupling will lead to Frank-Condon like transitions [161].

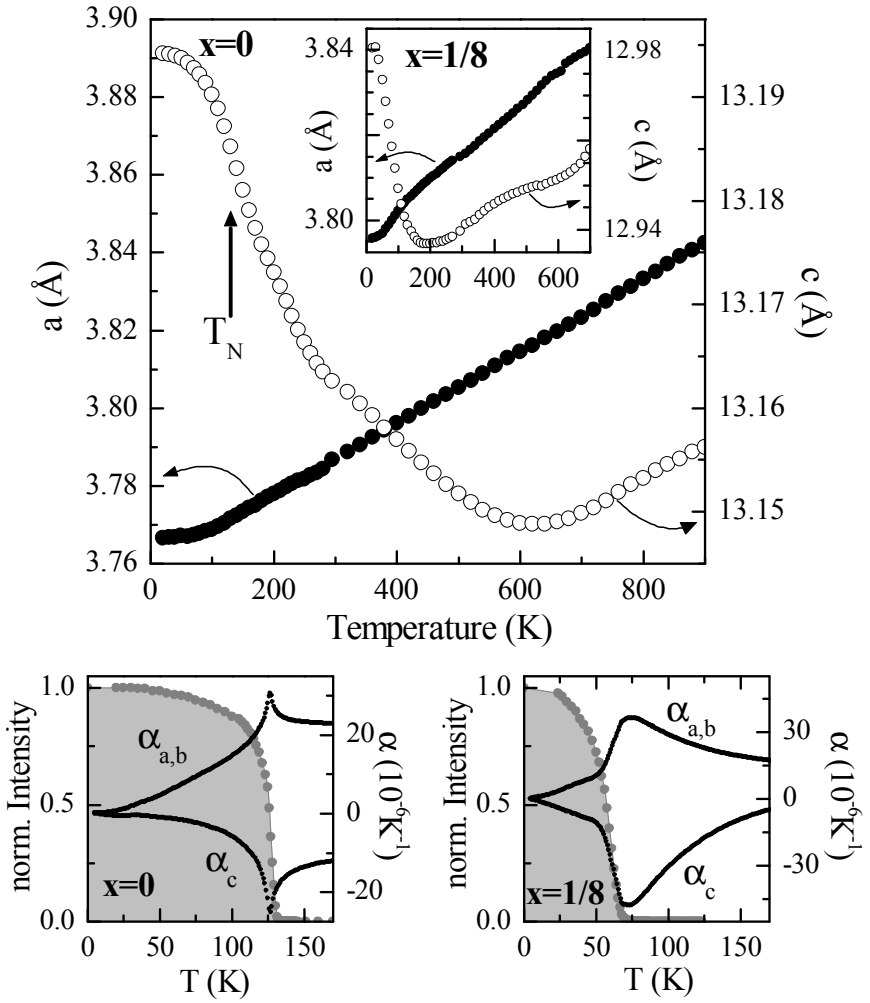

Figure 4.10: *Top panel:* temperature dependence of the lattice constants a and c of $La_{1-x}Sr_{1+x}MnO_4$ for $x = 0.0$ and $x = 0.13$ (inset). *Bottom panels:* thermal-expansion coefficients and the intensity of an antiferromagnetic superstructure reflection from neutron-scattering experiments at (0.5,0.5,0.0). Figure taken from Ref. [148].

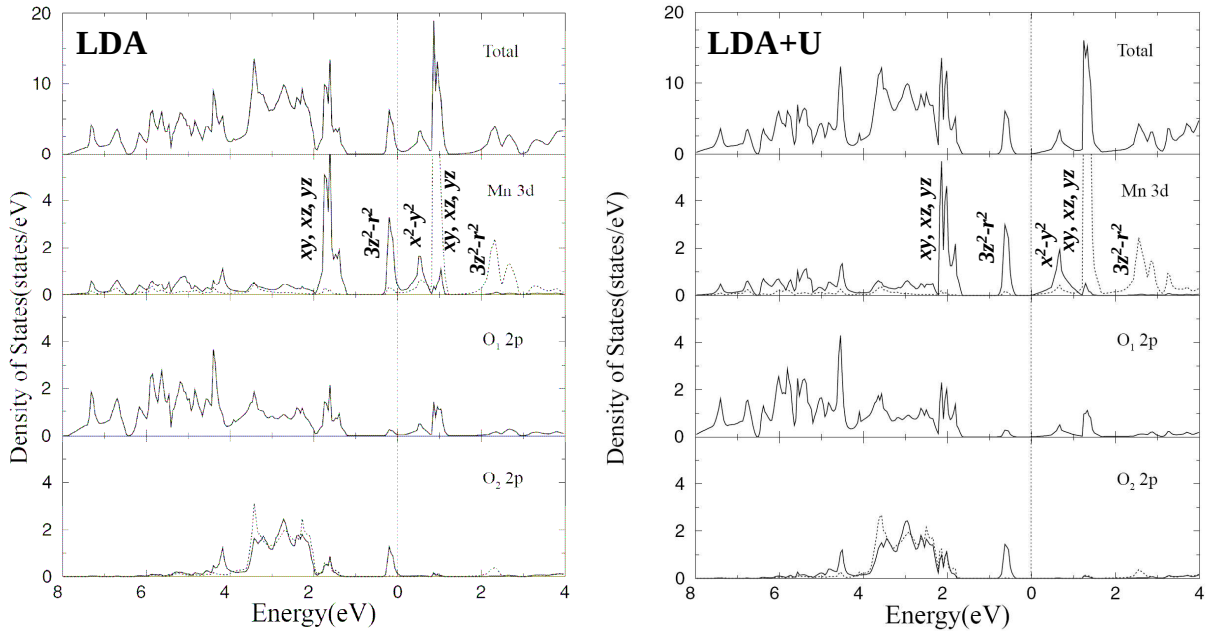

Figure 4.11: *Left:* LDA calculation of $LaSrMnO_4$ (spin up: solid; spin down dashed). *Right:* LDA+U_{eff} calculation with $U_{eff} = U - J = 2$ eV. The results are taken from Ref. [162]. We included the caption of the Mn band symmetries by comparing to a calculation by H. Wu. In Ref. [162] a precise assignment is only given for the two bands near the fermi edge.

4.2.4 Electronic structure

The major difference between layered manganites and the CMR compounds is that the layered compounds stay insulating upon doping while the latter ones become metallic (see above). In order to understand e.g. these difference one has to investigate the electronic structure. We give in this section a brief overview of results on the layered compounds. The focus is on the low-doping regime.

We will start with the undoped compound with a doping level of $x = 0.0$. Band structure calculations (LSDA) yield a metallic state [162], in contradiction to the insulating ground state found in experiments. However, LSDA shows that the antiferromagnetic solution is lower in total energy than the ferromagnetic one[6]. The wrong prediction of a metallic ground state points towards correlation effects in this compound. Indeed, the inclusion of an onsite repulsion U [150, 162] opens a gap in $LaSrMnO_4$, see Fig. 4.11.

One might address the following questions: If the system is a correlated insulator, is it of Mott-Hubbard or charge-transfer type? This is a crucial issue for the understanding of the doping dependence because the doped carriers reside either in a Mn $3d$ band or in an O $2p$ band [66]. Which orbitals are occupied and what is their occupation? Which are the

[6]Calculation carried out by H. Wu.

excited states? In how far can LDA+U explain the experimental findings? Is it possible to switch to a localized description?

From the experimental side different X-ray studies measured the occupied and unoccupied bands [23, 149, 150, 163–165]. The studies of Kuepper *et al.* [164, 165] are concerned with the compound $x = 0.0$. They determined the valence band by X-ray photo electron spectroscopy (XPS) and found a small peak at -0.7 eV and a stronger band centered at -4 eV with a width of 2 eV. By using (resonant) X-ray emission spectroscopy ((R)XES) they were able to determine the projected density of states for the Mn and O site. The Mn site shows its prominent contribution at -2 eV and a small shoulder at approximately -0.7 eV, while the O site has a maximum at -3 eV. They compared their data to the density of states obtained from LDA+U_{eff}[7] calculations with $U_{eff} = 2$ eV and 8 eV [150, 162]. Their data are in agreement with the calculation of Park [162] with $U_{eff} = 2$ eV. Their results suggest that $LaSrMnO_4$ is of the Mott-Hubbard type, because the lower Hubbard band is located above the oxygen band. By comparing to the LDA+U calculation one can read that the lower Hubbard band has $d_{3z^2-r^2}$ symmetry. Support comes from soft X-ray linear-dichroism data [132, 150]. The agreement with simulated spectra on the basis of a multiplet calculation with occupied $d_{3z^2-r^2}$ orbitals gives evidence for an orbital ordering [132, 150].

The unoccupied bands of the $x = 0.0$ compound have been studied by X-ray absorption spectroscopy by different groups [23, 132, 149, 150, 163, 165]. In the study of Ref. [165] no polarization-dependent spectra have been recorded. Thus, we will not discuss this study in further detail. Note that there exist large differences in the raw data especially between Ref. [163] and Refs. [23, 132, 149, 150]. We will only refer to the latter studies since they find similar results. From the anisotropy of the absorption along a and c a $d_{x^2-y^2}$ character of the lowest unoccupied orbital has been deduced [132, 150]. From near-edge X-ray absorption fine structure (NEXAFS) data Merz *et al.* [23, 149] suggested that the occupation of the $d_{x^2-y^2}$ orbital is not zero but 15% (and the occupation of the $d_{3z^2-r^2}$ orbital 85%). Furthermore they argued that $LaSrMnO_4$ shows typical charge-transfer behavior because the "*...UHB (upper Hubbard band) is continuously reduced and the VB (valence band) increases, indicating that holes are created in in-plane and out-of plane states and that spectral weight is transferred from the UHB to the VB*". This argumentation is not clear to us, since the first peak can also be regarded as a transition into the upper Hubbard band. This assignment has been done by Wu *et al.* [150]. Higher lying peaks are interpretable as higher-lying Hubbard bands.

Optical spectroscopy probes the transitions from the lower to the upper Hubbard band and from the oxygen band to the upper Hubbard band. For the low-doping regime optical studies have only been carried out at room temperature for $x = 0.0$ in comparison to other layered compounds of the series $LaSrMO_4$ (M=Cr, Mn, Fe, and Co) [158]. The authors of Ref. [158] analyzed all spectral features of $LaSrMnO_4$ in terms of charge-transfer excitations. The optical gap has been found at 0.5 eV in agreement with estimates for the charge-transfer energy from an ionic model.

[7]The effective onsite Coulomb repulsion is $U_{eff} = U^{simple} - J_H^{simple}$.

For low doping Merz *et al.* found a large redistribution of weight with increasing x [23, 149] in NEXAFS (see above) spectra. They suggest that with increasing x electrons are moved from the $d_{3z^2-r^2}$ orbitals into the $d_{3x^2-r^2}/d_{3y^2-r^2}$ orbitals, i.e. the orbitals are locally arranged in the CE-type pattern, see Fig. 4.2 and its caption. Note, that this breaks the tetragonal symmetry, which has not been observed in X-ray studies of the structure [148, 149].

The half-doped compound with $x = 0.5$ has already been discussed in the introductory section. Optical spectra have been analyzed in terms of the double-exchange model. The lowest excitation is observed at approximately 1 eV and has been assigned to intersite $d_i d_j$ transitions between the bonding and non-bonding bands of the Mn^{3+} and Mn^{4+} sites [153] (see also Fig. 4.5 and its caption). Similar features have been observed in the doped 113 manganites and attributed to the same origin [126].

To summarize: $LaSrMnO_4$ is a correlated insulator. In a one-electron language the lowest unoccupied orbital has predominantly $d_{x^2-y^2}$ symmetry and the highest occupied orbital $d_{3z^2-r^2}$ character. LDA+U seems to give a reliable description of the spectroscopic findings so far. Similar to the discussion in $LaMnO_3$ there is no consensus in literature that $LaSrMnO_4$ is of the Mott-Hubbard type. Since there have been no temperature- and polarization-dependent optical studies on $LaSrMnO_4$ we fully determined the optical conductivity tensor as function of temperature. As we will show in this chapter our results give further experimental evidence for the Mott-Hubbard character of the undoped compound.

4.3 Experimental results

In this section we would like to give an overview of the results obtained on $(La,Sr)_2MnO_4$. We only present the ϵ_1, ϵ_2, and σ_1 values obtained from the measured Müller matrix elements by means of ellipsometry. The spectra have been derived in the same way as described in chapter 3 for $YTiO_3$. We did not include any cover layers in the analysis because the surface of the manganites seems to be robust with respect to oxidation etc. (e.g. we measured the sample again after some time without a new preparation of the surface and the spectra are simialr and our data are in satisfactory agreement to room temperature data of Moritomo *et al.* (see below) for the $x = 0.0$ compound [158].

4.3.1 $LaSrMnO_4$

We start with the compound with $x = 0.0$. The dielectric function and optical conductivity are plotted in Fig. 4.12 in the range from 0.75 to 5.8 eV. We focus the discussion on ϵ_2 (or σ_1) because it is a measure of the absorption. It shows a striking polarization dependence between the a and c direction. In particular there is only one strong peak at 5.6 eV in the c direction, while a multi-peak structure is visible in the a direction (peaks at $\sim$ 2, 3.5, 4.5, 4.9, and 5.5 eV). All peak intensities show a strong temperature dependence, e.g. the structure $\sim$ 22 eV in the a direction gain weight with increasing temperature, while the peaks at 4.5 and 4.9 eV clearly loose weight. We monitor the transfer of spectral weight

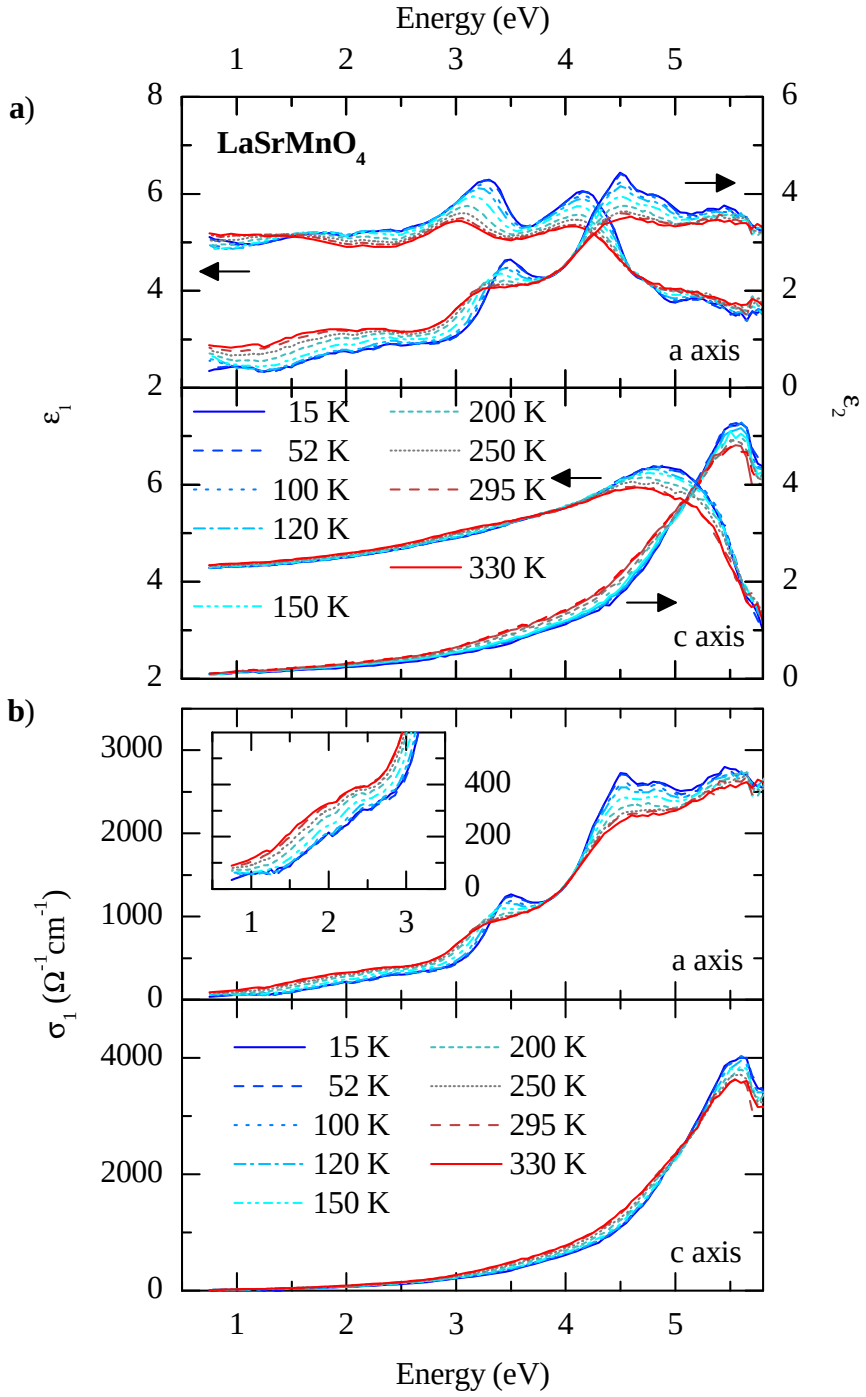

Figure 4.12: Dielectric constant a) and optical conductivity b) of $LaSrMnO_4$ for the a and c direction between 0.75 - 5.80 eV for different temperatures.

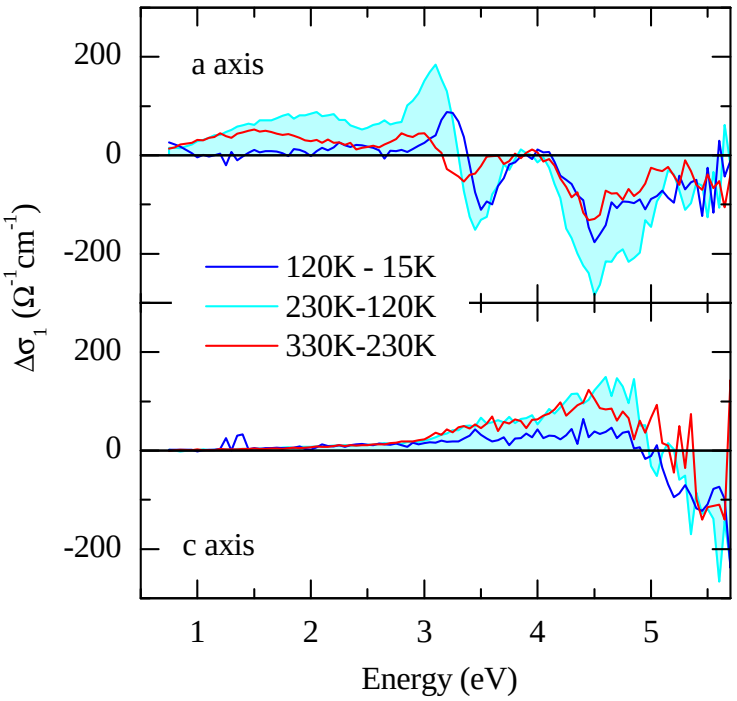

Figure 4.13: Change of the optical conductivity of $LaSrMnO_4$ in temperature intervals of approximately 100 K. $\sigma_1(120K)$-$\sigma_1(15K)$, $\sigma_1(230K)$-$\sigma_1(120K)$, $\sigma_1(330K)$-$\sigma_1(230K)$.

(SW) for different temperature ranges in Fig. 4.13. It is remarkable that in the temperature range 120 K - 230 K the changes in σ_1 are most prominent. Some shifts of the SW from high to low energies can be observed, in particular 3.5 → 3.0 eV and 4.5 → 2.0 eV in the a-axis spectra.

In order to discuss the development of the spectral weight (SW) in more detail we show in Fig. 4.14 the effective carrier concentration from the partial sum rule from Equation 4.1. We use as lower limit $\omega_{c1} = 0.75$ eV instead of $\omega_{c1} = 0.0$ eV, since the missing weight between 0 and 0.75 eV is negligibly small. Equation 4.1 translates into the f-sum rule with $\omega_{c2} \rightarrow \infty$ [93]. The overall spectral weight in the measured region ($\omega_{c2} = 5.5$) decreases (increases) with increasing T in case of the a (c) direction, as indicated in Fig. 4.14 (top panel). The overall change between 4 K and 300 K amounts to approximately 10% in the c axis and 3% in the a axis. It is striking that σ_1 in the a direction intersects at approximately $\omega_i = 4.0$ eV for all temperatures. In order to analyze the shift of SW across this energy we plotted N_{eff} for the a direction, see the middle panel of Fig. 4.14. The SW increases with increasing temperature below ω_i and increases above. It is worth noting that the change in weight sets in almost 30 K below the magnetic transition temperature of 133 K, but at approximately T_N the curves posses a point of inflection.

We go one step further and assume that the optical spectrum is composed out of a sum

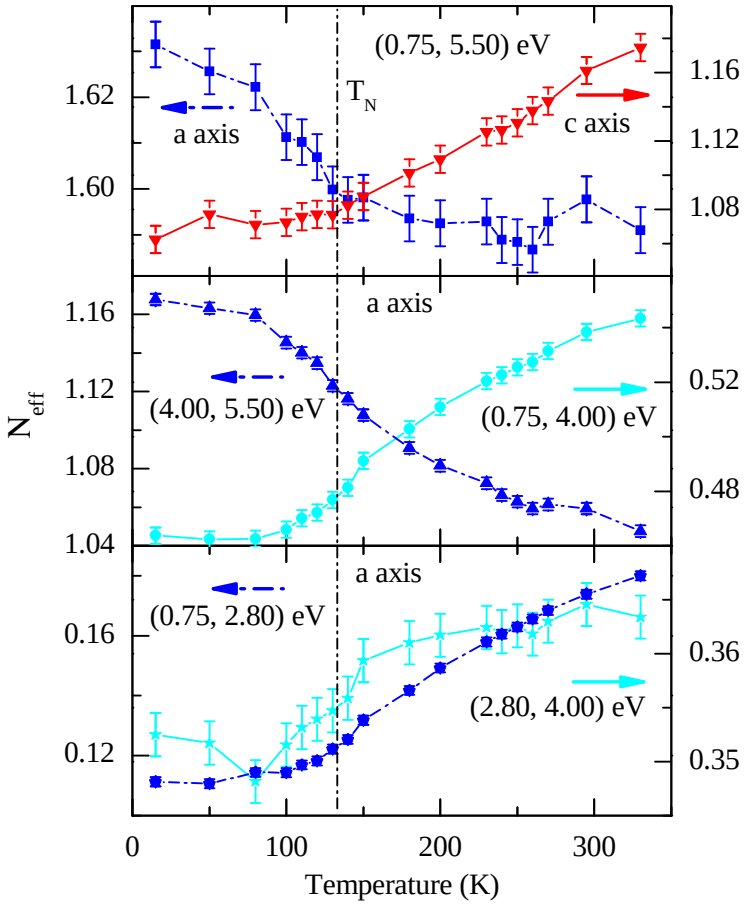

Figure 4.14: Effective carrier concentration N_{eff} for the a and c direction of $LaSrMnO_4$ as a function of temperature. Full energy range (top panel), partial energy range with an intermediate energy of ω_i=4 eV (middle panel), and below 4 eV with an intermediate energy of ω_i'=2.8 eV (bottom panel).

of Drude-Lorentz oscillators [93]:

$$\epsilon(\omega) = \epsilon_\infty + \sum_j \frac{\omega_{p,j}^2}{\omega_{0,j}^2 - \omega^2 - i\gamma_j\omega} \tag{4.2}$$

The parameters $\omega_{0,j}$, $\omega_{p,j}$, γ_j, and ϵ_∞ are the peak frequency, the plasma frequency, the damping of the jth oscillator and the dielectric constant at "infinite" frequency (outside the measured region). The great advantage of this function is its Kramers-Kronig consistency, in contrast for example to a Gauss function. The spectral weight of a single Lorentzian can be put into relation to the plasma frequency [2, 93]:

$$N_{eff} = \frac{2\,m\,V}{\pi\,e^2}\int_0^\infty \sigma_1(\omega)d\omega = \frac{m\,V\,\omega_p^2}{4\pi\,e^2} \tag{4.3}$$

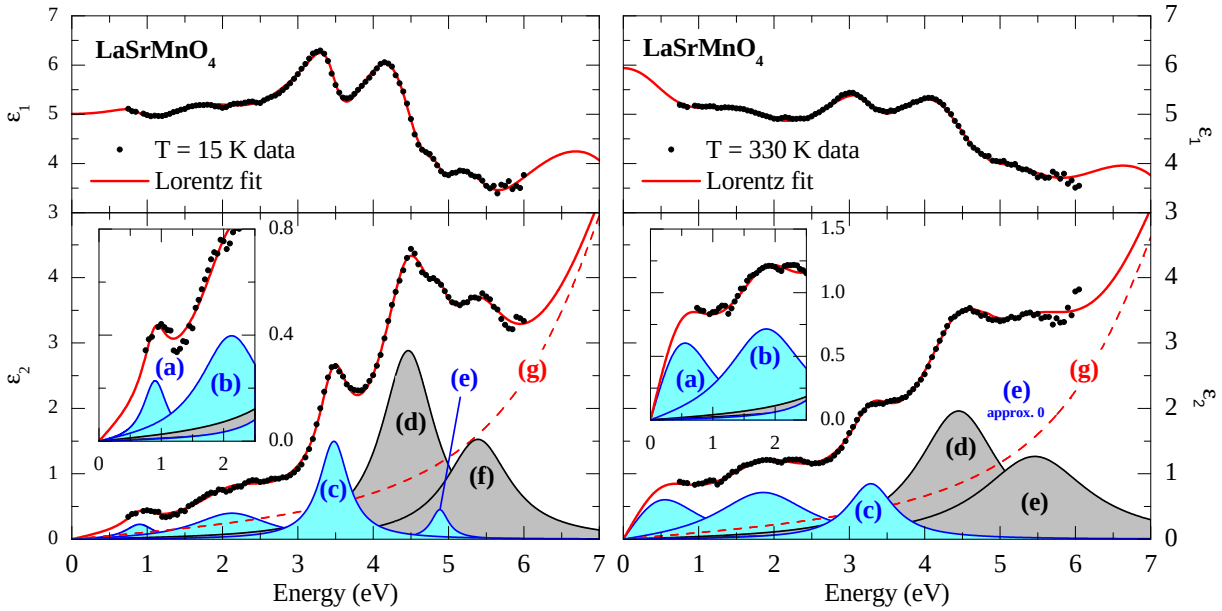

Figure 4.15: Dielectric constant along the a direction of $LaSrMnO_4$ at 15 K and 330 K (black dots). Additionally a fit using seven Drude-Lorentz oscillators is shown (solid line). The contributions of the different oscillators to ϵ_2 are also given.

The variables have the following meaning: m is the effective mass (we will set this value to the electron mass, i.e. $m = m_e$), V is the volume of the unit cell per number of ions that constitute to this particular oscillator, e is the electron charge, $\int_0^\infty \sigma_1(\omega)d\omega$ is the spectral weight (SW) , and ω_p the plasma frequency. All quantities are measured within the cgs system. For a conversion into the SI system, see Refs. [92, 166]. Figure 4.15 shows a simultaneous fit[8] to the dielectric constants ϵ_1 and ϵ_2 along the a direction using seven Drude-Lorentz oscillators (see Eq. 4.2). It is necessary to put one strong oscillator outside the measured region in order to get a good fit. The inclusion of a constant ϵ_∞ is not sufficient. This procedure is justified since one finds several strong peaks in the room-temperature optical conductivity reported by Moritomo *et al.* [158] outside our measured region. The parameters ω_0 and γ of the strong oscillator outside the measured range have assumed to be constant with temperature. The fit shows that the data obtained from ellipsometry is Kramers-Kronig consistent, otherwise a satisfactory fit with Drude-Lorentz functions would not have been possible. Since ellipsometry determines both ϵ_1 and ϵ_2 independently, the contributions of higher-lying bands to the measured region can be fixed quite accurately in comparison to, e.g., pure reflectivity measurements. We denote the oscillators (a) to (g). For the c direction we performed a corresponding fit using two oscillators at 5.5 and 8 eV; the parameters of the oscillator inside the measured region are shown in Fig. 4.17(h). The temperature dependence of these seven Drude-Lorentz oscillators, i.e. their parameters ω_0, ω_p and γ, has been plotted in Figs. 4.16 and 4.17.

[8]We used the excellent program "Reffit" by A. Kuzmenko which can be found in the web as freeware.

Note that we measured at 18 different temperatures. In Fig. 4.12 we have only shown half of them for clarity. For the fit at different temperatures along the a direction the position ω_0 and the width γ of the highest oscillator (g) as well as the value of $\epsilon_\infty = 1.22$ have been fixed. The behavior of the three lowest oscillators (a)-(c) is quite robust to the choice of starting values, because the overlap with other bands is quite small. These bands lower their peak frequency by approximately 0.2 eV and become significantly broader with increasing temperature. The bands (a) and (b) clearly gain weight while (c) slightly loses weight with increasing temperature. The peak frequencies of the higher-lying bands (d)-(f) remain almost unchanged with temperature. Only band (d) shows systematic broadening and the weight of band (e) gets suppressed to almost zero with increasing temperature. The oscillator (h) along the c direction becomes monotonically broader and more intense, while it resides almost at the same position of 5.55 eV.

In order to get an estimate of the optical gap we also performed transmittance measurements at 5-300 K using a Fourier-transform spectrometer. The sample was approximately 70 μm thick and has been prepared in the same way as briefly described in the appendix. Figure 4.18a) shows the transmittance (T) spectra and the calculated quantity $-\ln(T) \propto \sigma_1$ in the energy region from 0.10-0.90 eV. The transmittance is a very sensitive probe in order to extract the temperature dependence of the onset of the optical gap Δ_{opt}. From linear extrapolation of $-\ln(T)$ to zero we find $\Delta^a_{opt} = 0.45 - 0.50$ eV and $\Delta^c_{opt} > 0.9$ eV at $T = 5$ K. In order to monitor the temperature dependence of the gap we solve the equations $-\ln(T^a) = m_a$ and $-\ln(T^c) = m_c$ with $m_a = 5.0, 4.5$ and $m_c = 0.40, 0.35, 0.30$, respectively, where $T_{a,c}$ are transmittances along the a and c axes. The results have been normalized to the values at $T = 5$ K and are shown in Fig. 4.18b). The evolution of the gap with temperature changes its slope at $T_N = 133$ K as evident from the derivative plot in the inset of 4.18b) and from the lower panel (independent of the choice of the constant m_a and m_c).

4.3.2 $La_{1-x}Sr_{1+x}MnO_4$

We proceed with a comparison of the ellipsometric data for $x = 0.0$ to the doped samples with $x = 0.13$ and $x = 0.50$. The dielectric constant at $T = 295$ K is shown in Fig. 4.19 and the optical conductivity in Fig. 4.20 (upper panel). For the discussion we only refer to the latter figure. Also for the doped samples a strong anisotropy between the a and c direction has been found. In the a axis again a multi-peak structure has been observed similar to $x = 0.0$. One clearly observes a peak at approximately 1.5 eV, which gains weight with increasing x. Besides the band at 1.5 eV, the peak at 3.5 eV clearly gains weight in the $x = 0.5$ sample and the high energy part > 4.5 eV loses weight. The evolution of the effective carrier concentration with x is shown in Fig. 4.21. The overall spectral weight in a is almost conserved, while the low-energy peak at 1.5 eV increases in intensity with x. In the c axis the overall weight in c is increased with x, see Fig. 4.21. A new feature develops at approximately 3 eV, not being present in the $x = 0.0$ case. For the higher doped sample this feature gains weight. The peak at 5.6 eV decreases in intensity while another feature gain weight at 4.5 eV, see Fig 4.20 (lower panel).

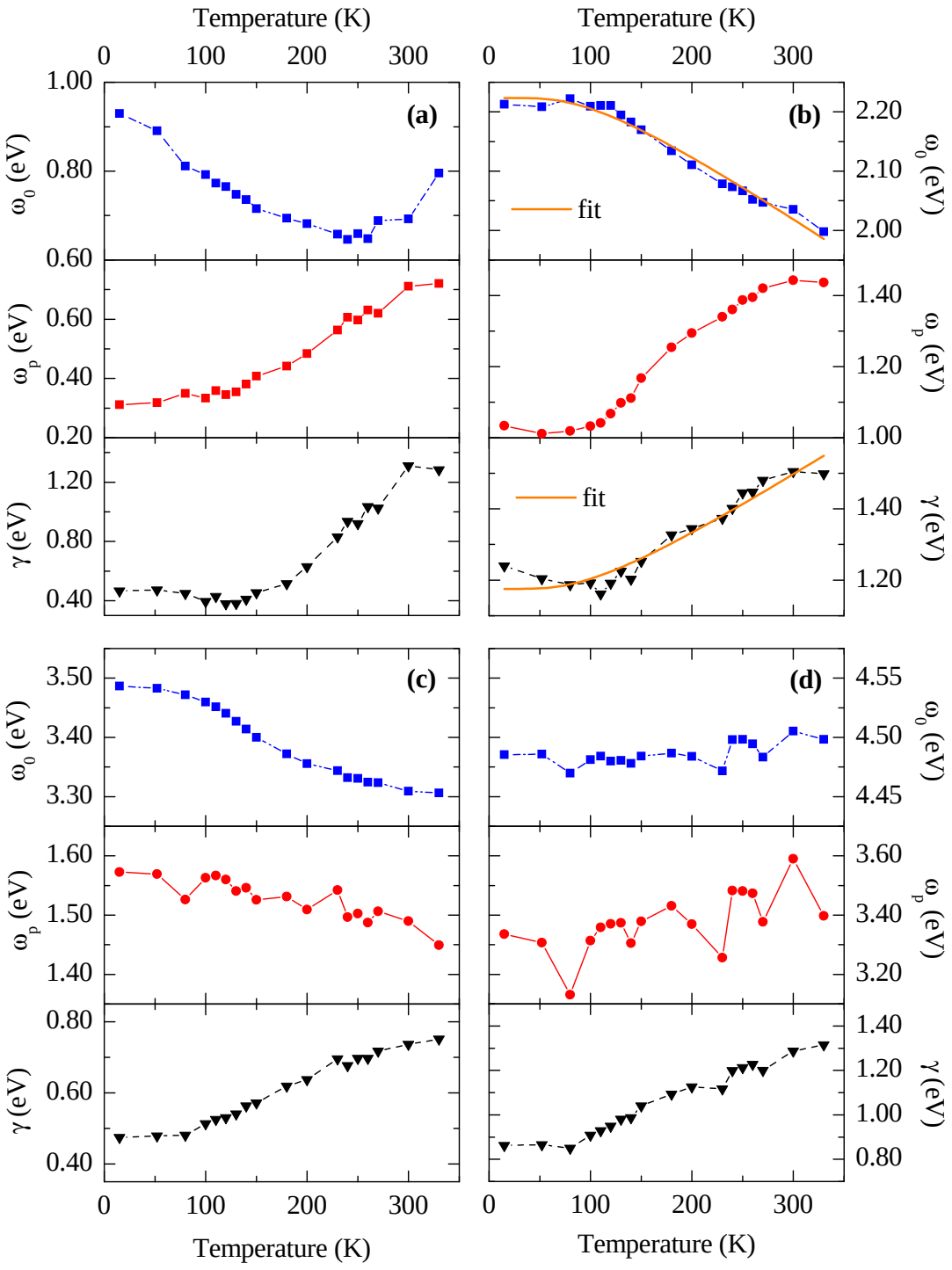

Figure 4.16: Results of a Drude-Lorentz fit to the measured data ϵ_1 and ϵ_2 of $LaSrMnO_4$. The parameters ω_0 (peak frequency), ω_p (strength), and γ (damping) are shown as a function of temperature. The panels refer to peaks (a)-(d) in Fig. 4.15. In panel (b) we show a fit using Eqs. 4.18 and 4.20 (see Sect. 4.4.2 below).

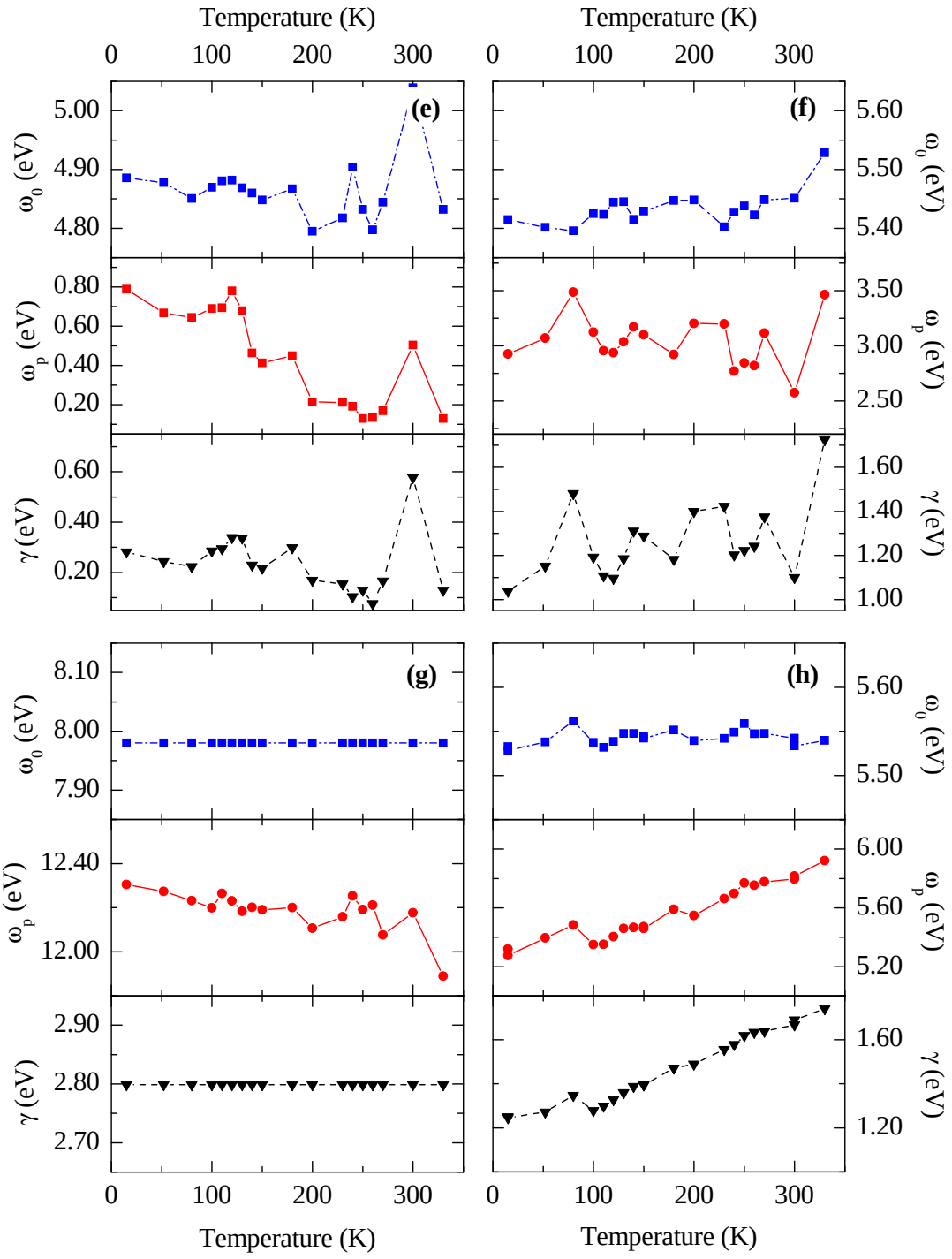

Figure 4.17: Results of a Drude-Lorentz fit to the measured data ϵ_1 and ϵ_2 of $LaSrMnO_4$. The parameters ω_0 (peak frequency), ω_p (strength), and γ (damping) are shown as a function of temperature. Panel (h) contains the parameters of the fit to the c-axis data using only two oscillators (the 2nd oscillator is placed outside the measured region and is kept fixed in ω_0 and γ; it is not shown). The panels refer to peaks (e)-(f) in Fig. 4.15.

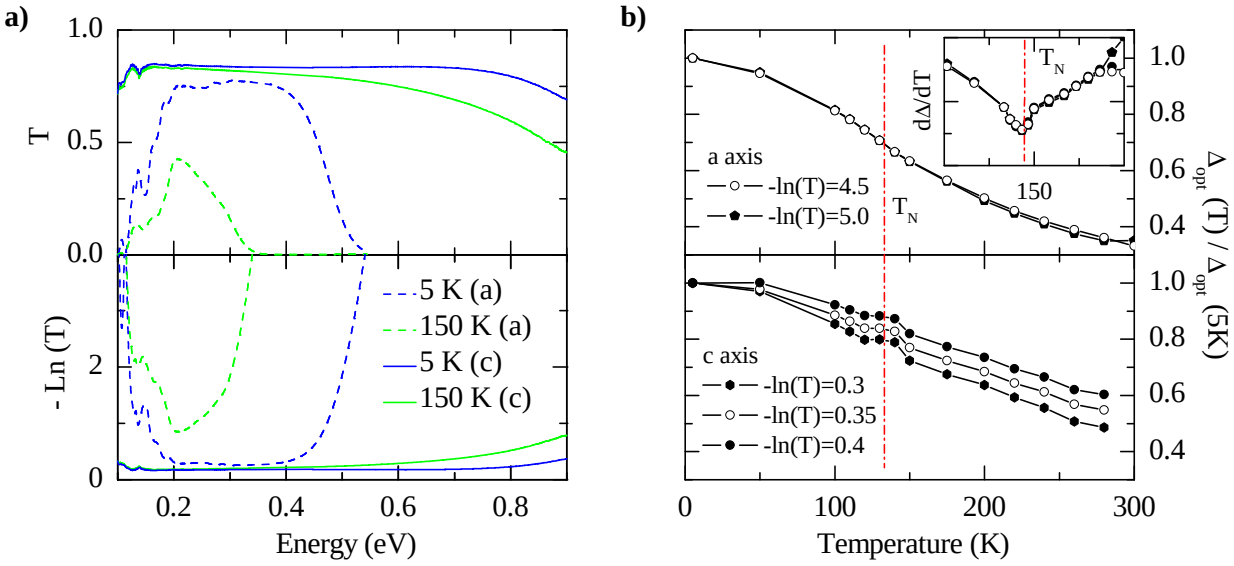

Figure 4.18: (a) Transmittance T of a thin $LaSrMnO_4$ sample (d$\sim$70μm) and -ln(T), which is proportional to σ_1, for 5 and 150 K. (b) The evolution of the optical gap as function of temperature. In order to get a measure of the gap, we take the solution of -ln(T)=m, with m_a = 5.0, 4.5 and m_c = 0.40, 0.35, 0.30 for the a and c axes, respectively.

Regarding the temperature dependence for the $x = 0.13$ compound, a similar trend as in the $x = 0.0$ case can be observed, see Fig. 4.22. Weight is shifted from the high-energy (4.5 eV) region to the low-energy region (2.0 eV). However, the dependence is weaker. It is also worth noting that the fine structure present in the $x = 0.0$ sample around 4.5 eV is washed out.

For $x = 0.5$ we have also measured the transmittance through a 9μm thick sample and the reflectivity on a thick sample with a Fourier-transform spectrometer, in order to estimate the optical gap and to track the peak at almost 1 eV to lower energies. The data is presented in Fig 4.23. The optical conductivity has been directly calculated from the measured quantities as presented in chapter 3. The oscillations in the transmittance are interference fringes from which one can determine the thickness of the sample quite accurately. The optical gap at low temperatures is approximately 0.55 eV in the a direction and roughly $>$ 1.0 eV in the c direction, similar to the results on $LaSrMnO_4$. The sample stays insulating also at room temperature.

Finally we give a comparison of our data to (to best of our knowledge) all published data for $x = 0.0$ and $x = 0.5$. Our room-temperature data agree quite well with the optical conductivity along the a axis from literature for $x = 0.0$ and $x = 0.5$ [144, 151, 153, 158], see Fig. 4.24. Differences are visible in the c direction of the $x = 0.5$ compound. We observed no peak at 1.5 eV in the c direction, in contrast to the data of Ishikawa *et al.* [144]. One may speculate whether this peak is due to a leakage from the a axis. Note

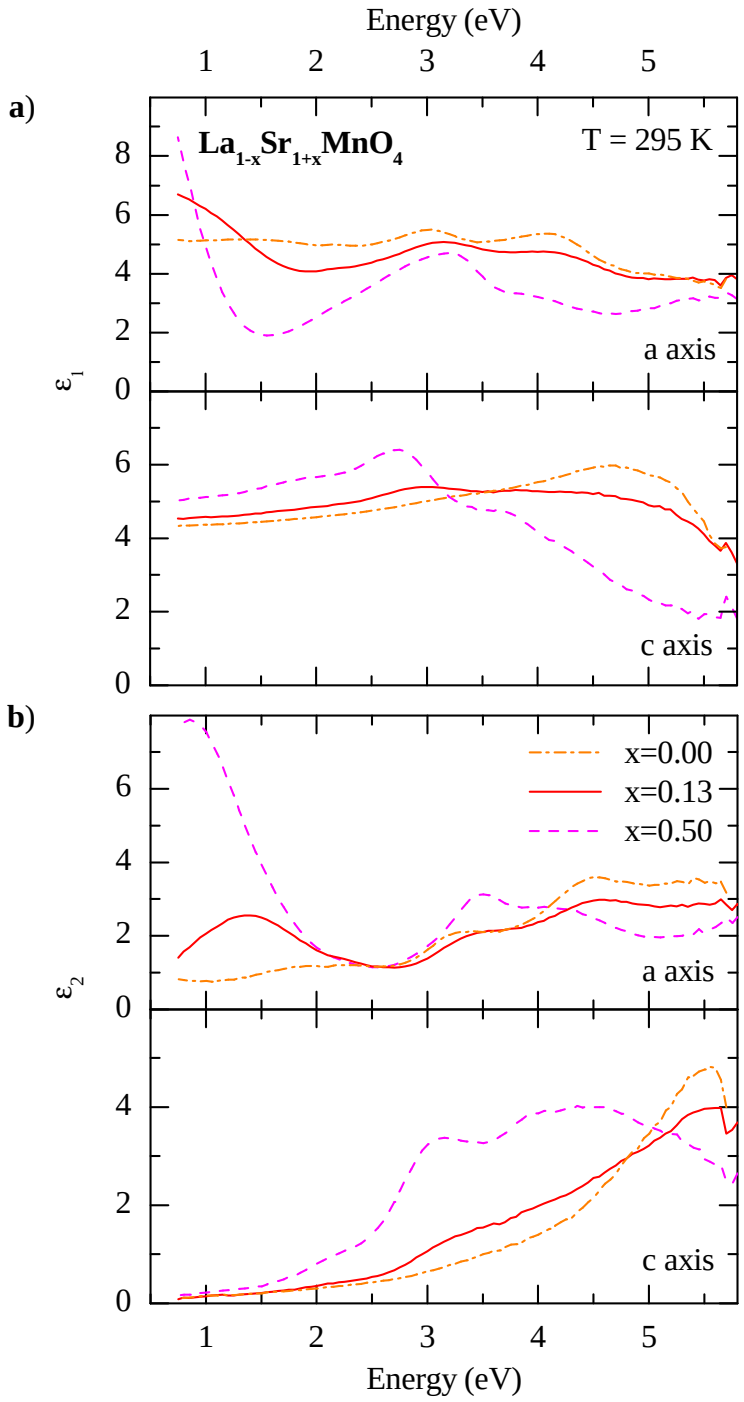

Figure 4.19: Dielectric constant $\epsilon_{1,2}$ along the a and c directions of $La_{1-x}Sr_{1+x}MnO_4$ at room temperature for different doping x.

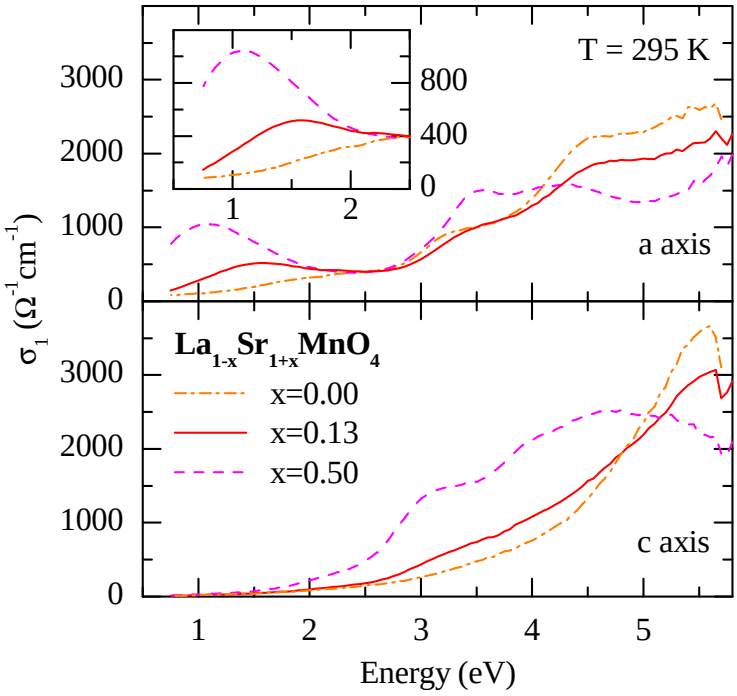

Figure 4.20: Optical conductivity σ_1 along the a and c directions of $La_{1-x}Sr_{1+x}MnO_4$ at room temperature for different doping x.

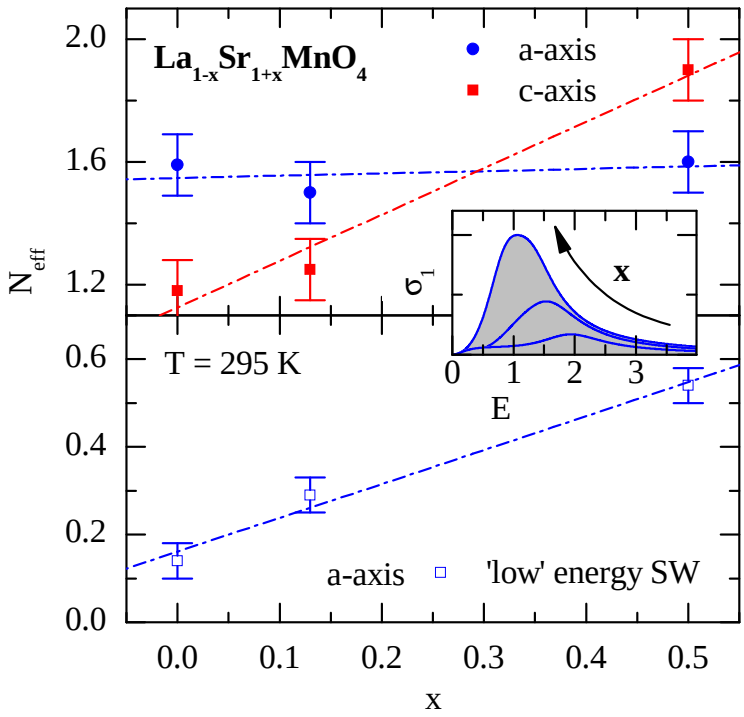

Figure 4.21: *Upper panel:* Effective carrier concentration N_{eff} between 0.75 eV - 5.5 eV of $La_{1-x}Sr_{1+x}MnO_4$ at room temperature for different doping x for a and c. *Lower panel:* N_{eff} for the features below 2.5 eV (inset). The values are obtained by a simultaneous fit to ϵ_1 and ϵ_2 with two Drude-Lorentz oscillators.

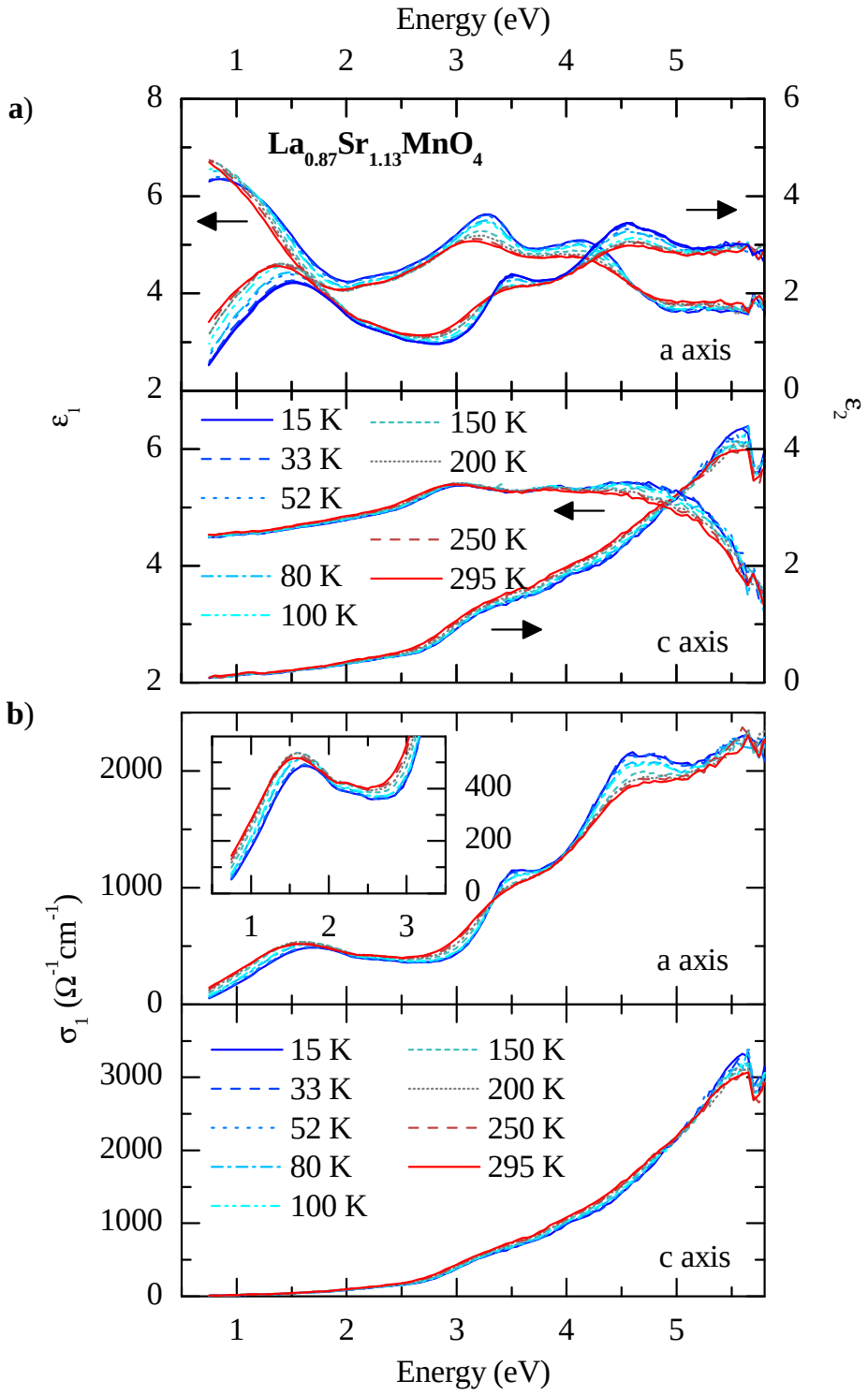

Figure 4.22: Dielectric constant (a) and optical conductivity (b) for $La_{0.87}Sr_{1.13}MnO_4$ for the a and c direction between 0.75 - 5.80 eV for different temperatures.

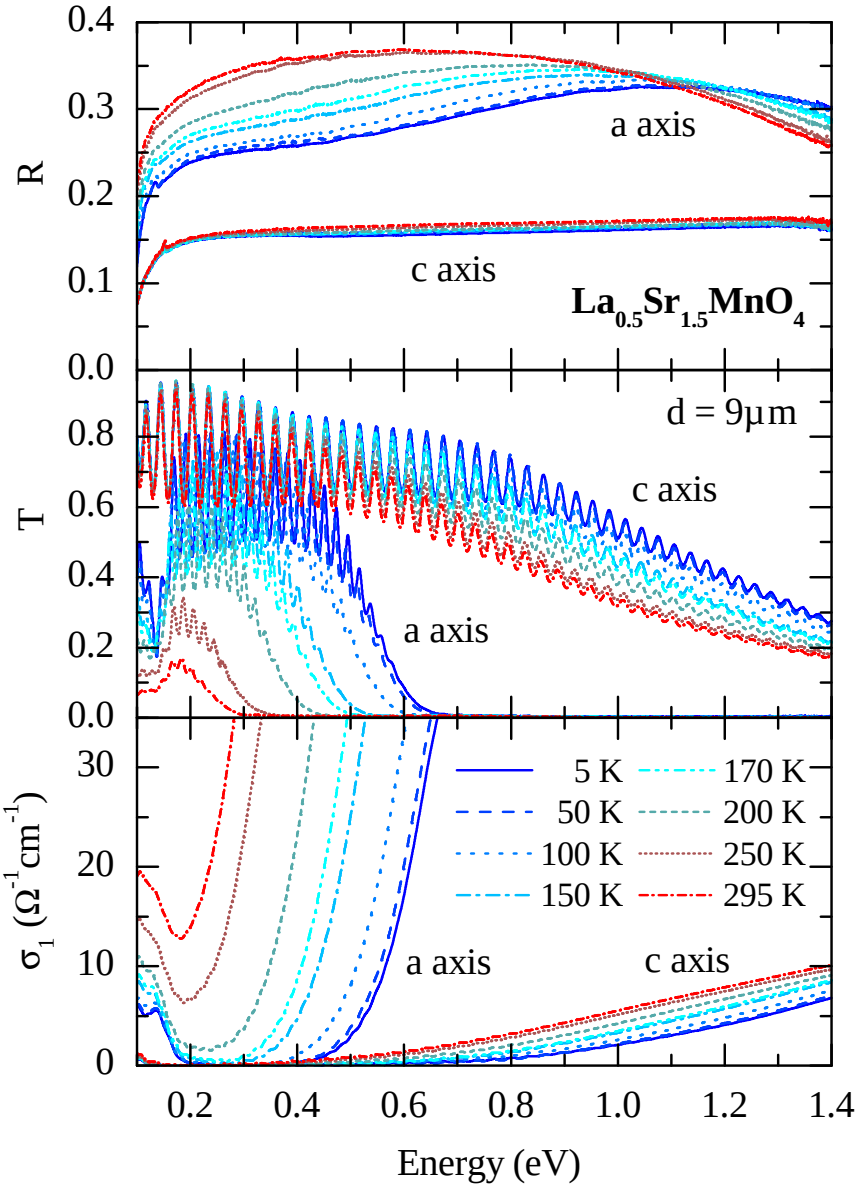

Figure 4.23: Transmittance, reflectivity and optical conductivity of $La_{0.5}Sr_{1.5}MnO_4$ as function of temperature measured with a Fourier spectrometer. For the calculation of σ_1 we averaged out the fringes of the transitions measurement.

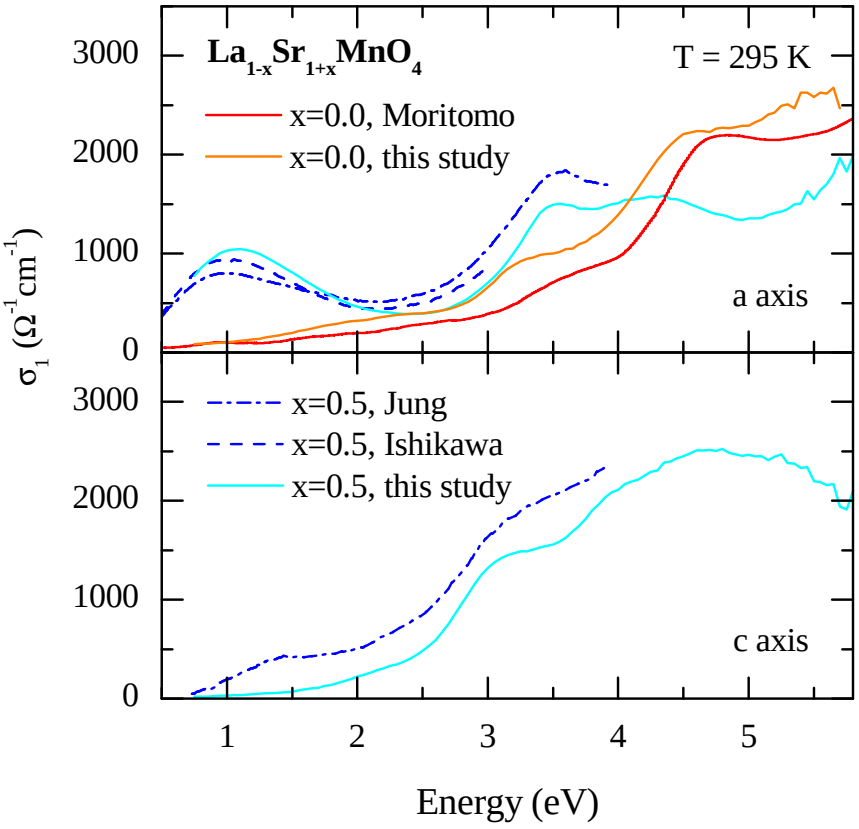

Figure 4.24: Room-temperature optical conductivities of $La_{1-x}Sr_{1+x}MnO_4$ in comparison to literature data [144, 151, 153, 158].

that no low-temperature data for $x \neq 0.5$ have been published in the literature thus far. Our combined study of the polarization, temperature, and doping dependence over a broad energy range allows us to unravel the electronic structure in great detail, e.g. to compare the weight of Mott-Hubbard and charge-transfer bands.

4.4 Discussion and analysis of $LaSrMnO_4$

4.4.1 Multiplet calculation

In order to get more insight into the electronic structure we approach the problem from the localized limit. This is justified since the bands in transition metal oxides are known to be narrow. We will only take Mn and O sites into account since these ions should be responsible for the lowest electronic transitions. As already discussed in the chapter 3, optical spectroscopy can only probe excitations with $\Delta\mathbf{k} = 0$. Interband transitions in semiconductors produce a free electron-hole pair under the restriction $\mathbf{k}_e + \mathbf{k}_h = 0$, where $\mathbf{k}_e$ is the wave vector of the electron and $\mathbf{k}_h$ the wave vector of the hole. In a correlated

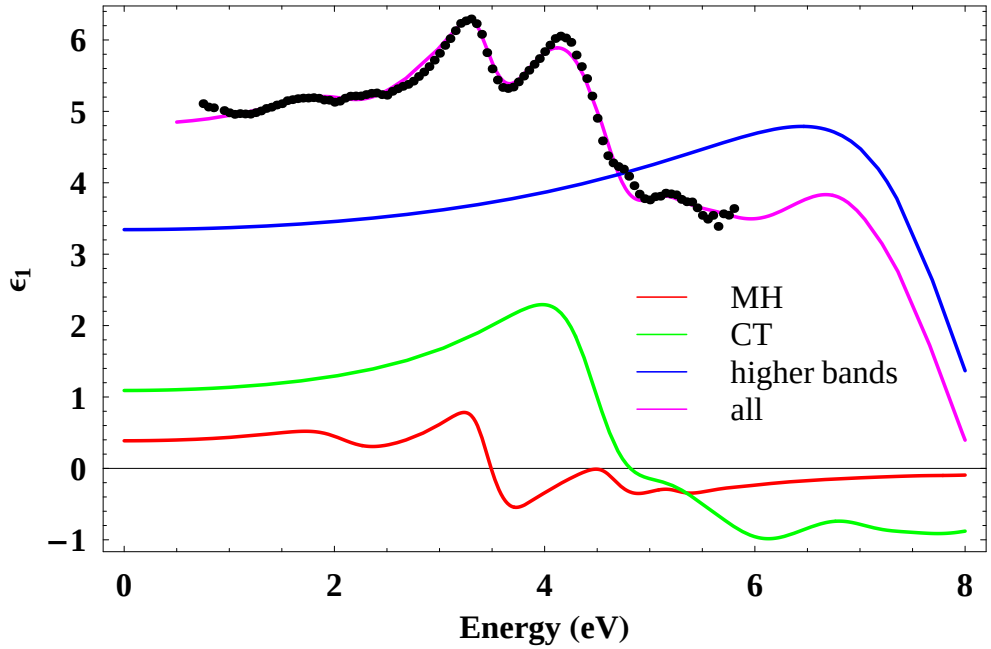

Figure 4.25: ϵ_1^a obtained from a multiplet calculation for $LaSrMnO_4$. The charge-transfer transitions (CT) have been broadened by 1.10 eV, the Mott-Hubbard transitions (MH) by 0.45 eV (the lowest MH with 0.90 eV). We used $\epsilon_\infty = 1.37$.

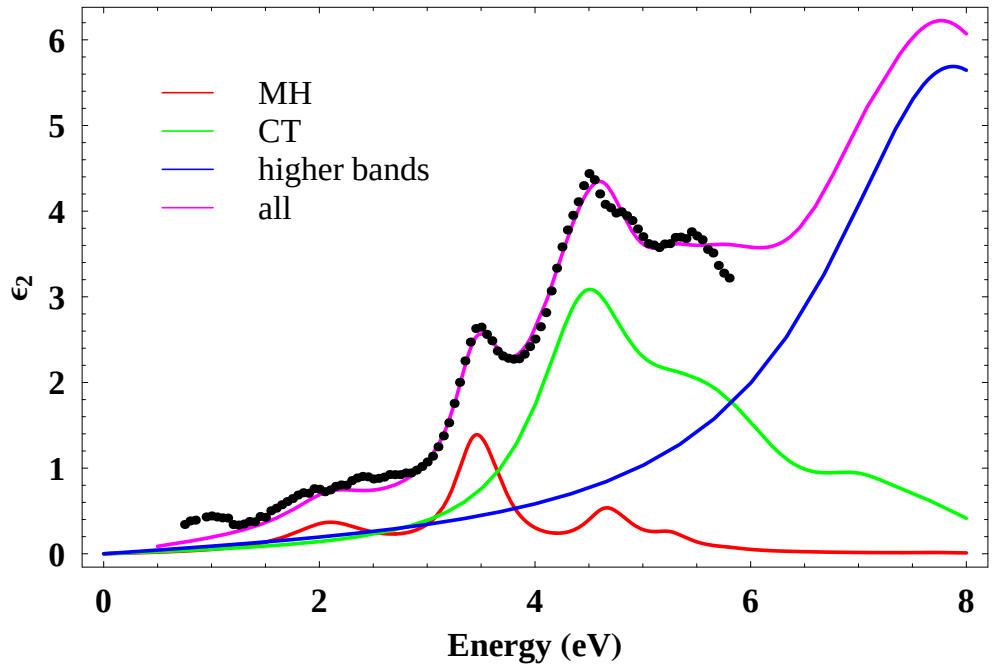

Figure 4.26: ϵ_2^a obtained from a multiplet calculation for $LaSrMnO_4$. The charge-transfer transitions (CT) have been broadened by 1.10 eV, the Mott-Hubbard transitions (MH) by 0.45 eV (the lowest MH with 0.90 eV).

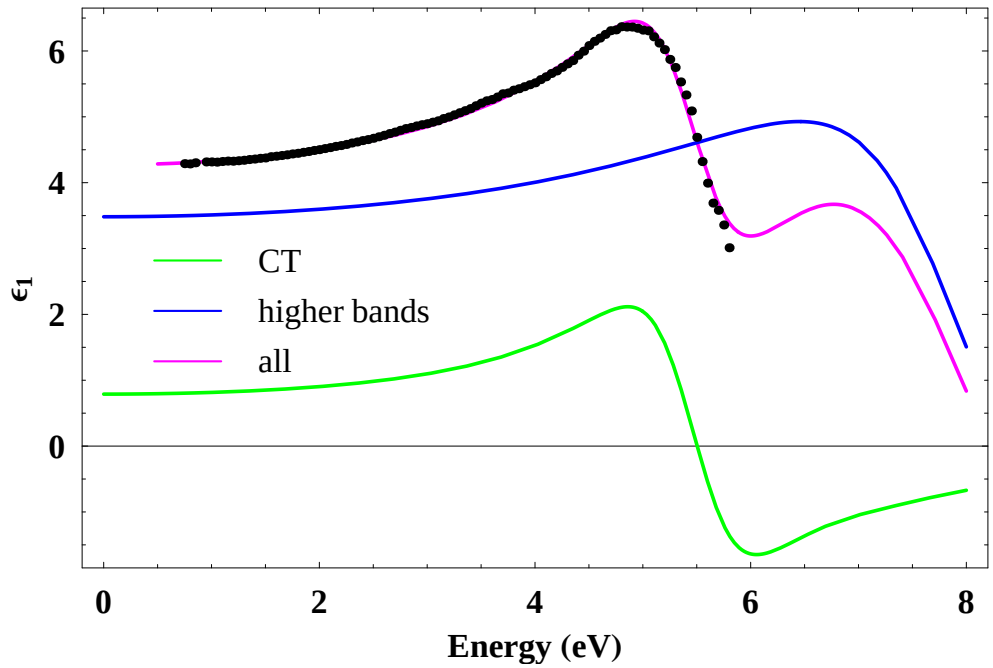

Figure 4.27: ϵ_1^c obtained from a multiplet calculation for $LaSrMnO_4$. The charge-transfer transitions (CT) have been broadened by 1.10 eV. We used $\epsilon_\infty = 1.51$.

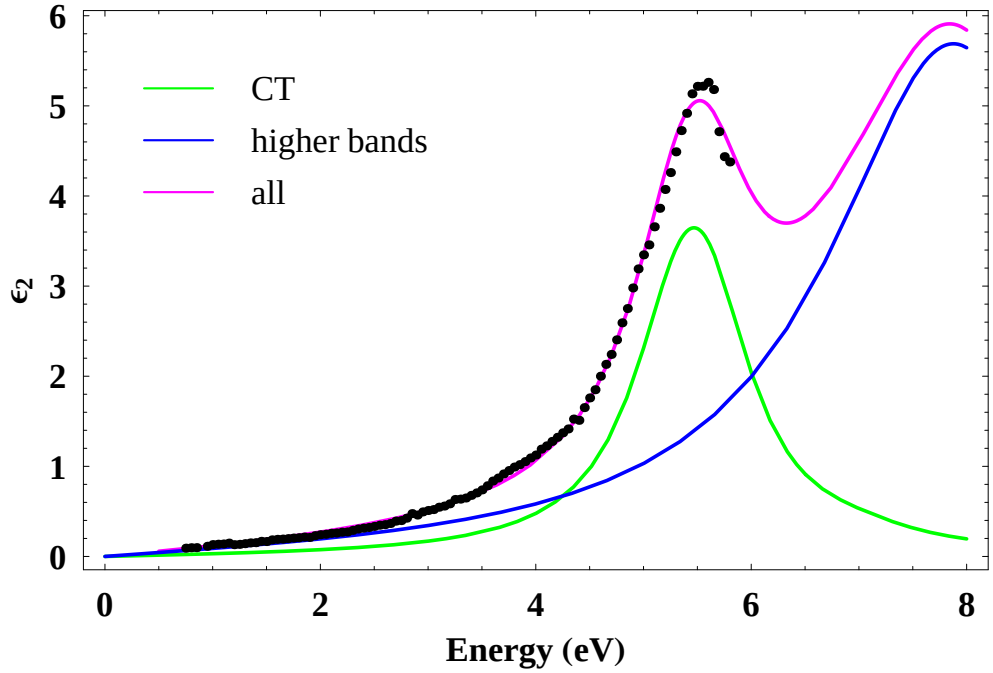

Figure 4.28: ϵ_2^c obtained from a multiplet calculation for $LaSrMnO_4$. The charge-transfer transitions (CT) have been broadened by 1.10 eV.

Table 4.2: Parameters of the crystal-field calculation adjusted to the experimental findings. F^2 and F^4 have been scaled by a global factor r with respect to the ionic values. F^0 is assumed to be equal for the different configurations. The crystal-field parameters $10Dq$, Δ_{t2g}, Δ_{eg} of the d^4 configuration have been renormalized in case of the d^3 and d^5 configurations (see text). The Slater integrals can be transferred into the commonly used Kanamori parameters [18], the onsite Coulomb repulsion $U = F^0 + 4/49\ F^2_{d4} + 36/441\ F^4_{d4} = 2.2$ eV and Hund's coupling $J_H = 2.5/49\ F^2_{d4} + 22.5/441\ F^4_{d4} = 0.6$ eV. Within the *simple* scheme $U^{simple} = F^0 = 1.2$ eV and $J_H^{simple} = 1/14\ (F^2_{d4} + F^4_{d4}) = 0.9$ eV.

Parameters	d^3	d^4	d^5
F^0 (eV)	1.20	1.20	1.20
F^2 (eV)	7.95	7.31	6.60
F^4 (eV)	5.00	4.75	4.11
r	0.64	0.64	0.64
$\langle r^2 \rangle$ (Å^2)	0.316	0.371	0.452
$\langle r^4 \rangle$ (Å^4)	0.201	0.293	0.475
$10Dq$ (eV)	0.82	1.20	1.95
Δ_{t2g} (eV)	0.25	0.20	0.05
Δ_{eg} (eV)	1.11	1.40	1.90
Δ_a (eV)	4.51	4.51	4.51
Δ_c (eV)	4.13	4.13	4.13

Table 4.3: Overview of the fixed parameters, cycled parameters, and fitted parameters for calculation the optical conductivity. The fit parameters are determined for each cycle minimizing χ^2.

fixed parameters	$\frac{F^2_{d^n}}{F^4_{d^n}} = \frac{F^{2,HF}_{d^n}}{F^{4,HF}_{d^n}}$, $\langle r^2_{d^n} \rangle$, $\langle r^4_{d^n} \rangle$, $Dq_{d^{3,5}}$, $\Delta_{e_g,d^{3,5}}$, $\Delta_{t_{2g},d^{3,5}}$,
	$\frac{pd\pi_{a,c}}{pd\sigma_{a,c}} = -\frac{1}{\sqrt{3}}$, $pd\sigma_a$, ω_0^{HB}, γ^{HB}, $\frac{\gamma_a^{MH>}}{\gamma_a^{MH<}}$, $\frac{d_c}{d_a}$
cycle parameters	r, F^0, Dq_{d^4}, Δ_{e_g,d^4}, Δ_{t_{2g},d^4}, $pd\sigma_c$
fit parameters	$\Delta_{a,c}$, $\gamma_a^{MH>}$, γ^{CT}, ω_p^{HB}, $\epsilon_\infty^{a,c}$, A

insulator electrons are more localized. For very large values of Hubbard U they are stuck at one atomic position. In the strong coupling limit ($t \ll U$) the probability to create an electron-hole pair, or better a double occupancy and a hole, on nearest-neighbor sites is $\sim t$, on next-nearest neighbor sites $\sim t^2/U \ll t$. It is thus more natural to interpret an interband transition in a correlated material as an excitation between neighboring sites. Once created the double occupancy might freely propagate in the solid. For the following discussion we will take transitions between Mn and O site (nearest-neighbor sites) and between different Mn sites (next-nearest neighbor sites) into account, i.e. the transitions $d^4p^6 \rightarrow d^5p^5$ (charge-transfer transitions) and $d^4d^4 \rightarrow d^3d^5$ (Mott-Hubbard transitions). We will further assume that the two-site states can be decomposed into d^3, d^4, d^5, p^5, and p^6 configurations on *one* Mn or O site, which equivalently means that we will not include hybridization between p_i and d_j states. For the d^n configurations we performed a crystal-field calculation in tetragonal symmetry (see below),[9] while we assume degenerate states in case of the p^5 multiplet. The p^6 state represents a full shell and does not have to be considered. In addition we calculated the optical conductivity for a transitions between a Mn and an O site and between two Mn sites in the a and c directions, by evaluating the matrix elements between all possible multiplet states.

The main parameters for the crystal-field calculations are the Slater integrals F^0, F^2 and F^4 and the crystal-field splitting (see e.g. Refs. [18, 20] for their definitions, the relations of the Slater integrals to the Hund's rule coupling J_H and Hubbard U are given in the caption of Fig.4.2). We have introduced an overall reduction factor r for the ionic Slater integrals F^2 and F^4 for all configurations, in order to account for screening of other configurations which are not explicitly considered (e.g. pd hybridization). The values of F^2 and F^4 in a crystal are only slightly reduced when comparing to their ionic values, while the parameter F^0 is strongly screened. The crystal field in tetragonal symmetry can be parameterized by Δ_{t2g}, Δ_{eg}, and $10Dq$, representing the splitting of the t_{2g}, e_g, and $t_{2g}-e_g$ levels, respectively. The parameter Δ_{t2g} and Δ_{eg} are related to the parameter scheme of Ballhausen, which is shown in Fig. 4.9, by $Dt = 1/35\,(3\Delta_{eg} - 4\Delta_{t2g})$ and $Ds = 1/7\,(\Delta_{t2g} + \Delta_{eg})$ [19]. Since we fully neglect covalency effects, we use these parameters in an effective manner. As a first estimate the crystal-field parameters can be obtained from an Ewald summation under a point-charge approximation. The underlying crystal structure was the room-temperature data of Ref. [148]. The obtained parameters are $\Delta_{t2g} = 0.45$ eV, $\Delta_{eg} = 0.81$ eV, and $10Dq = 0.60$ eV. However, we expect significantly larger values for the effective $10Dq$ and Δ_{eg} values since the e_g orbitals are more affected by the covalency [26]. For the excited states, i.e. the d^3 and d^5 configurations, we used renormalized crystal-field parameters with respect to the d^4 configuration to allow for different values of $\langle r^2 \rangle_{d^n}$ and $\langle r^4 \rangle_{d^n}$ with $\langle r^k \rangle_{d^n} = \int dr\, r^{2+k} |R_{d^n}|^2$ and R_{d^n} representing the radial part of the d^n wave function. In general $\langle r^k \rangle_{d^3} < \langle r^k \rangle_{d^4} < \langle r^k \rangle_{d^5}$ because more electrons need simply more space when filling one particular shell. The change in $\langle r^k \rangle_{d^n}$ directly translates into the a change of

[9] For the crystal-field calculations we used a Mathematica notepad which was written by Maurits. Haverkort. We would like to thank Maurits for kindly providing this software as well as his great assistance in setting up the conductivity notepad.

the parameters Dq, Ds, and Dt because $Dq \propto \langle r^4 \rangle$, $Ds \propto \langle r^2 \rangle$, and $Dt \propto \langle r^4 \rangle$ [19]. For the radial wave functions we have used values from a Hartree-Fock calculation [18]. The electronic transitions are known to be much faster than the relaxation of the lattice, thus we kept the lattice frozen in our approach.

The next step is the calculation of the optical conductivity spectrum within this multiplet-model. Here we assume that the optical conductivity consists of three parts, the charge-transfer contributions $\sigma^{l,CT}(\omega)$, the Mott-Hubbard excitations $\sigma^{l,MH}(\omega)$ and higher-lying contributions (like Mn(4s), Mn(4p), La(5d), Sr(5s)) with $l = a, c$ for the two different directions.

$$\sigma^{l}(\omega) = \sigma^{l,MH}(\omega) + \sigma^{l,CT}(\omega) + \sigma^{l,higher}(\omega) \tag{4.4}$$

The Mott-Hubbard and charge-transfer contributions are calculated separately. For simplicity we neglect charge fluctuations, i.e. the eigenfunctions have either pure d or pure p character, and the two-site wave functions are a simple product of two single-site wave functions. This has the great advantage that the two-site matrix elements decay into two independent one-site matrix elements. The prize one has to pay for neglecting the hybridization is a decrease of the transitions energies of the order of $\sim t_{pd}^2/\Delta$ in case of the charge-transfer and $\sim t_{pd}^4/(U\,\Delta^2)$ in case of the Mott-Hubbard transitions. Also the wave-functions will be modified which will lead to changes in the transitions matrices. However, the selection rules are unaffected from hybridization. This has to be kept in mind when the parameters from this study are compared to results from cluster calculations. The conductivity measured in arbitrary units is calculated by the Kubo formula [93, 120, 167, 168]. The Mott-Hubbard contributions read:

$$\sigma^{a,MH}(\omega) = \frac{4d_a^2}{N} \sum_{i,j,k,k'} \frac{\mathcal{M}_{i,j,k,k'}^{a,MH}}{E_{i,j}^{MH}}\, \delta(\omega - E_{ij}^{MH}) \tag{4.5}$$

$$\mathcal{M}_{i,j,k,k'}^{a,MH} = |< d_i^5 d_j^3 | \sum_{\tau,\tau'} t_{\tau,\tau'}^{a,MH} a_\tau^\dagger a_{\tau'} | d_k^4 d_{k'}^4 >|^2 \tag{4.6}$$

$$= |\sum_{\tau,\tau'} t_{\tau,\tau'}^{a,MH} < d_i^5 | a_\tau^\dagger | d_k^4 >< d_j^3 | a_{\tau'} | d_{k'}^4 >|^2$$

$$E_{i,j}^{MH} = E_i(d^5) + E_j(d^3) - 2E_0(d^4) \tag{4.7}$$

$$\sigma^{c,MH}(\omega) = 0 \tag{4.8}$$

For the charge-transfer contributions we obtain:

$$\sigma^{l,CT}(\omega) = \frac{d_l^2}{M}\sum_{i,j,k}\frac{\mathcal{M}_{i,j,k}^{l,CT}}{E_i^{CT}}\,\delta(\omega - E_i^{CT}) \tag{4.9}$$

$$\begin{aligned}\mathcal{M}_{i,j,k}^{l,CT} &= |< d_i^5 p_j^5|\sum_{\tau,\xi} t_{\tau,\xi}^{l,CT} a_\tau^\dagger a_\xi |d_k^4 p_1^6>|^2 \qquad (4.10)\\ &= |\sum_{\tau,\xi} t_{\tau,\xi}^{l,CT} < d_i^5|a_\tau^\dagger|d_k^4 >< p_j^5|a_\xi|p_1^6>|^2 \\ &= |\sum_{\tau,\xi} t_{\tau,\xi}^{l,CT} < d_i^5|a_\tau^\dagger|d_k^4 > \delta_{j\xi}|^2\end{aligned}$$

$$\begin{aligned}E_i^{CT} &= E_i(d^5) - E_0(d^4) + E(p^5) - E(p^6) \qquad (4.11)\\ &= E_i(d^5) - E_0(d^5) + \Delta_l\end{aligned}$$

Here, $a_{\tau,\xi}^\dagger$ ($a_{\tau',\xi}$) creates (annihilates) an electron in the orbital τ, ξ (τ') [10], $t_{\tau,\tau'}^{a,MH}$ and $t_{\tau,\xi}^{l,CT}$ are the dd and pd hopping matrices obtained from the Slater-Koster tabular [24] (see also Tab. 4.4), $N = M = 2$ represent the two different spin states in the antiferromagnetic ground state ($d_\uparrow^4 d_\downarrow^4$, $d_\downarrow^4 d_\uparrow^4$), for the paramagnetic ground state $N = 25$ and $M = 5$ (5-fold spin degeneracy of the $d^4(^5A_{1g})$ ground state), d_l is the Mn-O bond distance for the $l = a, c$ directions, the summation is carried out over all eigenstates $d_k^4 d_{k'}^4$ (see above) to the ground state eigenenergy $E_0(d^4)$ and over the excited states $d_i^5 d_j^3$ and $d_i^5 p_j^5$, respectively, with corresponding energies $E_i(d^5) + E_j(d^3)$ and $E_i(d^5) + E(p^5)$. We defined the charge-transfer energies as $\Delta_l = E_i(d^5) + E(p^5) - E_0(d^4) - E(p^6)$. Note that Mott-Hubbard transitions along a are weighted by a factor of four, because the Mn-Mn bond distance equals $d = 2d_a$ and $\sigma_1 \propto d^2$. From $\sigma^{a,MH}$ and $\sigma^{l,CT}$ we calculated $\epsilon^{a,MH}$ and $\epsilon^{l,CT}$ (in arbitrary units) in order to adjust to the measured spectrum, see Tab. 4.2. As a broadening function we used a Drude-Lorentz oscillator (see Eq. 4.2), which is intrinsically Kramers-Kronig consistent and thus directly yields ϵ_1. The explicit function can be obtained from Eq. 4.2 by normalizing to the area and with the replacement $\omega_p^2/8 = \frac{4d_a^2}{N}\sum_{i,j,k,k'}\mathcal{M}_{i,j,k,k'}^{a,MH}/E_{i,j}^{MH}$ (analogous for the charge-transfer transitions).

The term $\sigma^{l,higher}$ mimics the contributions of higher-lying bands and refers to one additional oscillator with $\omega_0^{HB} = 8$ eV and $\gamma^{HB} = 2.8$ eV. A similar oscillator has been used in the free fit discussed in the previous section. The strength of the oscillator and additionally the value of ϵ_∞ are varied to fit the experiment.

There are several parameters which are kept fixed and several other ones which are fitted or cycled in order to get a good description of the data. Tabular 4.3 gives an overview. We

[10] The two different spin contributions are included in τ, i.e. there are two different τ values for each orbital. τ is used for d orbitals, while ξ is used for p orbitals.

tried several thousand possibilities for the parameters F^0, r, $10Dq_{d^4}$, Δ_{eg,d^4}, and Δ_{t2g,d^4}, in order to describe the optical constants of the a direction. The c direction has been fitted afterwards. It can be described easily because no fine structure is present. The following parameters have not been varied: the ratios of $F^2_{d^n}/F^4_{d^n} = F^{2,HF}_{d^n}/F^{4,HF}_{d^n}$ have been obtained from ionic Hartree-Fock values [18] (see Tab. 4.2), the radial wave-functions $\langle r^k \rangle$ (Hartree-Fock values) [18], the hopping strength[11] $pd\pi_a = 0.95$ eV and $pd\sigma_a = -1.64$ eV and its ratio [169], the Mn-O bond-length ratio d_c/d_a. As discussed above the crystal field parameters of the d^4 configuration fix the parameters of the d^3 and d^5 configurations via the radial wave functions. As also discussed above the damping γ^{HB} and the energy ω_0^{HB} of the oscillator describing the higher bands has been kept constant. The following parameters have been fitted for each set of cycle parameters (F^0, r, $10Dq_{d^4}$, Δ_{eg,d^4}, Δ_{t2g,d^4}): the charge-transfer energy Δ_a, the broadening of the Mott-Hubbard transitions[12] $\gamma_a^{MH>}$, the broadening of the charge-transfer excitations γ^{CT}, the value of ω_p^{HB} of the oscillator representing the higher-lying bands, ϵ^a_∞, and a global scaling factor A since Eq. 4.5 is measured in arbitrary units.

After we obtained the minimal χ^2 for the a direction, the c direction is fitted, by varying the value of Δ_c and ϵ^c_∞. All other parameters are kept the same as in the a axis. According to the Harrison rules [169]

$$pd\sigma^{a,c} = -\frac{3\sqrt{15}}{2\pi}\frac{\hbar^2\sqrt{r_p r_d^3}}{m d^4_{a,c}},\ pd\pi^{a,c} = -\frac{1}{\sqrt{3}}\, pd\sigma^{a,c} \tag{4.12}$$

the hopping strength for the c direction is $pd\pi_c/pd\pi_a = pd\sigma_c/pd\sigma_a \sim 0.5$, i.e. $pd\pi_c \approx 0.48$ eV, because of the large anisotropy in between the Mn-O distances, namely $d_c/d_a = 1.2$ with $d_a = 1.88$ Å and $d_c = 2.28$ Å ($r_d = 0.8$ Å and $r_p = 4.41$ Å have been used for the radii of Mn and O [169]). It turned out that the overall weight in the c direction is a factor of ~ 3.2 too small when using the above value. Therefore, we also adjusted $pd\pi_c$ to fit the measured spectrum and obtained $pd\pi_c = 0.86$ eV.

The fit must reproduce the pronounced anisotropy, the relative weight of the different bands, and the peak positions. These restrictions enable us to determine a unique interpretation with a meaningful set of parameters. We would like to stress that although we have many adjustable parameters their tuning does not give arbitrary results since we have much fine structure in our data and two independent data sets, ϵ_1 and ϵ_2.

The spectra for the a and c directions obtained for the lowest χ^2 are plotted in Figs 4.25-4.28. The overall agreement is excellent. Additionally, we show the underlying multiplet energy levels for the d^3, d^4, and d^5 multiplets as a function of the crystal-field parameters in Fig 4.29. The right-most energy levels in each diagram correspond to the values used for the spectra.

[11] We do not use the term hybridization because the two sites considered are not hybridized.

[12] As a tribute to the very broad low-lying bands ("<") observed we further assumed that the Mott-Hubbard transitions below 2.6 eV get two times the broadening of higher-lying ones (">"), i.e. we set $\gamma_a^{MH<}/\gamma_a^{MH>} = 2$. A physical motivation can be found in the large band width of the upper $d_{x^2-y^2}$ band.

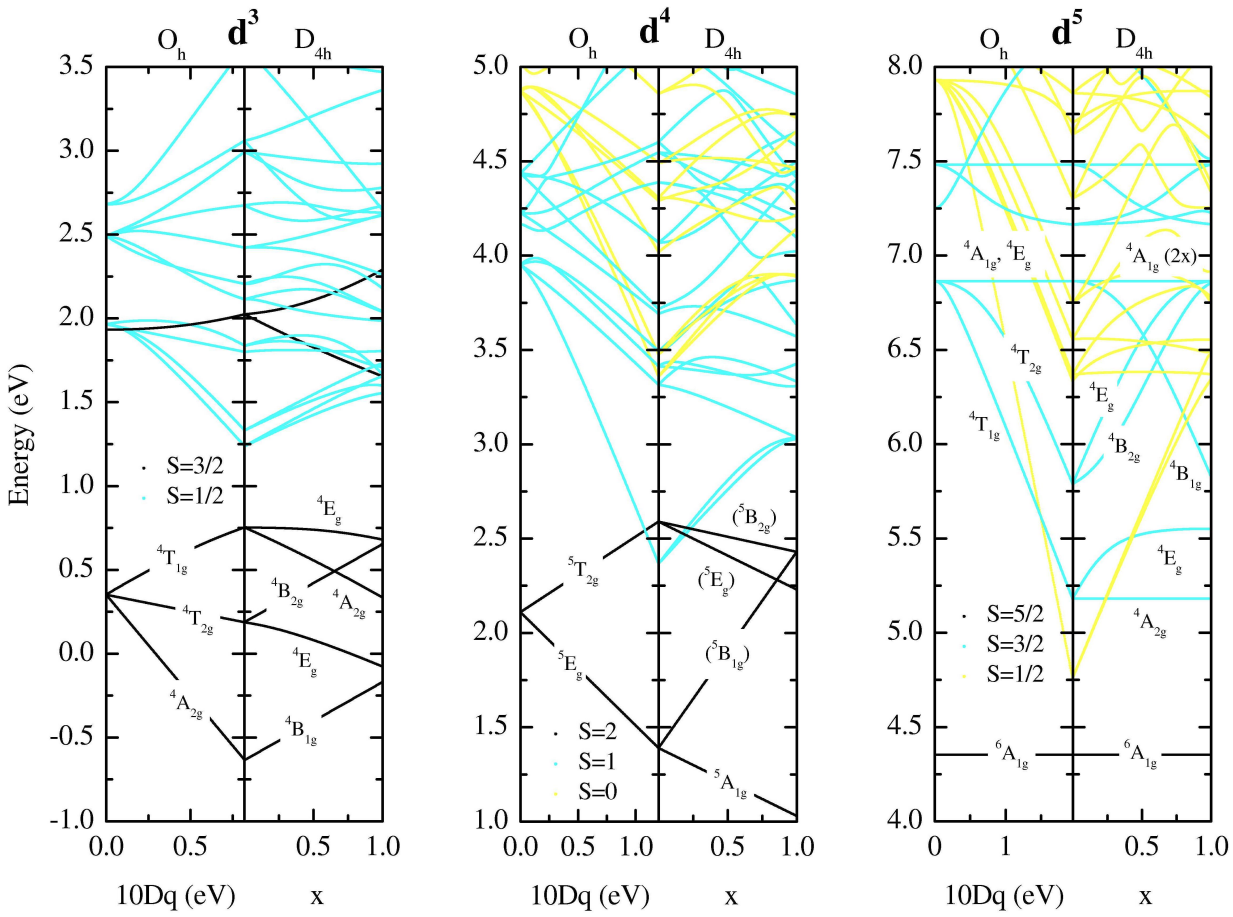

Figure 4.29: Energy-level diagrams within a multiplet calculation for the d^3, d^4, and d^5 configuration as function of $10Dq$ in O_h and as function of x in D_{4h} for a fixed value of $10Dq$. The control parameter x represents the strength of Δ_{eg} and Δ_{t2g}, unity equals the full strength. The low-lying multiples are labeled by their irreducible representations in O_h and D_{4h}, respectively, those being not relevant for the optical transitions are shown in brackets. The parameters used for the calculation are summarized in Tab. 4.2. Note that the values for the crystal-field parameters have been renormalized as given in Tab. 4.2 in order to take the different ionic radii of the d^n configurations into account.

4.4.2 Discussion

As mentioned in the previous section we will differentiate between two kinds of transitions: (i) the transitions between a ligand oxygen ion and a Mn ion, i.e. the charge-transfer excitations (CT) $Mn(d^4)O(p^6) \rightarrow Mn(d^5)O(p^5)$, and (ii) the transitions between two Mn ions, i.e. the Mott-Hubbard excitations (MH) $Mn(d^4)Mn(d^4) \rightarrow Mn(d^5)Mn(d^3)$. Note that the intensity of the latter is expected to be weaker because it can be regarded as a Mn(site1)-O and O-Mn(site2) transition, i.e., a second-order process in the Mn-O hopping, whereas the charge-transfer process is of first order. This difference in intensity can be observed very clearly in $YTiO_3$ (see chapter 5). In $LaSrMnO_4$ there is an additional way to discriminate between MH and CT excitations, namely the polarization dependence. Due to the layered structure we expect no contributions of MH bands in the c direction (for details, see below). This suggests the following scenario: the peak at $\sim$ 5.6 eV in the c direction is a CT excitation, and then the same holds true for the strong excitations in the same energy range of 5 eV in the a axis. The detailed analysis discussed below will support the assignment, that the weak features below $\sim$ 4 eV are MH excitations. But this analysis will also show that the rough argument on the polarization dependence given above is not yet sufficient, since some of the CT transitions are forbidden in the c direction.

For the following analysis we will start from a conventional picture neglecting collective Jahn-Teller phenomena, since the crystal-field splitting between the e_g levels is large ($\sim$ 1 eV). Excitations to higher-lying bands, like La($5d$), Sr($5s$), Mn($4s$) and Mn($4p$) are not considered explicitly because they are usually found outside the frequency range considered here [170]. However, for the simulation it is necessary to include the onset of these bands in order to achieve a better agreement between theory and experiment[13].

Charge-transfer transitions (CT)

Due to the layered structure of $LaSrMnO_4$, the distance between Mn ions in the plane is much smaller than perpendicular to the planes. Thus, the Mn-Mn hopping is strongly suppressed and Mott-Hubbard transitions can be neglected in the c direction. This gives rise to the pronounced anisotropy observed experimentally. We attribute the whole spectral weight (peak at 5.6 eV) in the c direction to charge-transfer and higher-energetic processes. The increase of spectral weight with temperature (see Fig. 4.14) can be understood qualitatively by the evolution of the Mn-O(2) distance d as shown in Fig. 4.10. This distance decreases from 20 K to 300 K by approximately 0.5% [148], which leads to an increased hopping and therefore to an increase of the SW. However, this decrease of d can only account for a change in SW of the order of 3%, in contrast to the observed gain of $\sim$10%, see Fig. 4.14. Here we assumed $\sigma_1 \propto d^2 \cdot t_{pd}^2 \propto d^{-6}$ (with $t_{pd} \propto d^{-4}$ [169]). Note that this is not a trivial effect of broadening. The peak frequency hardly changes as a function of temperature. Since the cut-off frequency of 5.5 eV chosen in Fig. 4.14 is very close to ω_0, the effect of thermal broadening of the peak at 5.55 eV on the SW plotted in Fig. 4.14

[13]The charge transfer-excitations are calculated up to 8 eV. We checked once that there is practically no change in weight up to 7 eV when extending the range to 15 eV.

should be very small. We checked the SW by a fit using a Lorentz profile, see Fig. 4.17(h). The change in SW is proportional to ω_p^2, which changes by $\sim 20\%$. We will come back to this point later on. In the a direction a corresponding peak is observed at approximately at 5.5 eV which we assign to the same CT origin.

To get an idea about the initial and final state of the transitions we assume that the highest occupied orbital is only of $d_{3z^2-r^2}$ type [148, 150] and the lowest unoccupied orbital is $d_{x^2-y^2}$. This assumption is supported by the tetragonally distorted MnO_6 octahedra and by our multiplet calculation. Within an intuitive two-center picture for a charge-transfer excitation (in a single-electron approximation), an electron is transferred from a ligand oxygen to the centering Mn ion. Because all oxygen orbitals p_x, p_y and p_z are occupied, the transition and its selection rules are dominated by the Mn d^5 final state. In the lowest d^5 state, electrons are in a high-spin configuration following Hund's rule. For the selection rules one has to consider the overlap between the oxygen orbitals and $d_{x^2-y^2}$ (see Tab. 4.4). This is only finite along the a direction, but zero along c. Therefore, we cannot identify the peak at 5.6 eV in the c direction with the lowest CT transition, but with the second lowest: here the oxygen electron is transferred e.g. into the two degenerate d_{xz} and d_{yz} orbitals (this is not the only possibility, see below). The overlap is finite, both in a and c direction.

This picture is strongly supported by our multiplet calculation presented in the previous section, see Figs. 4.25-4.28. In the c direction only one strong band is visible at 5.6 eV, while in the a direction another strong band at 4.5 eV is observed. Within this model the band at 4.5 eV results from a transition into a $d^5(^6A_{1g})$ final state, while the band at 5.6 eV has three multiplet contributions, namely $d^5(^4A_{2g})$, $d^5(^4E_g)$, and $d^5(^4B_{1g})$ (see Fig. 4.29). In the c-direction only transitions into a $d^5(^4E_g)$ and $d^5(^4B_{1g})$ final state are possible, the $d^5(^6A_{1g})$ and $d^5(^4A_{2g})$ final states are forbidden. The first state contains an additional electron in the $d_{x^2-y^2}$ the latter one in the d_{xy} orbital with respect to the $d^4(^5A_{1g})$ state. One can read this from the energy diagram in Fig. 4.29 of the d^5 state (right panel). The tetragonal crystal field is given in terms of fractions of the maximal tetragonal crystal field $x = \Delta_{t_{2g}}/\Delta_{t_{2g}}^{max} = \Delta_{e_g}/\Delta_{e_g}^{max}$. Starting from a cubic crystal field of $Dq_{d^5} = 0.19$ eV an increase of the tetragonal crystal field does not influence the $^6A_{1g}$ and $^4A_{2g}$ states. This indicates that the multiplet center is not influenced, which is the case for e.g. the $|e_{g\uparrow}, e_{g\uparrow}, b_{2g\uparrow}, a_{1g\uparrow}, b_{1g\uparrow}\rangle$ state (notation in D_{4h}, see Fig. 4.9). For the calculation of ϵ along c we used different values for the charge-transfer energy ($\Delta_a = 4.51$ eV and $\Delta_c = 4.13$ eV). This treatment is justified because the oxygen in the a direction resides in another crystallographic position than the one in the c direction [148, 149].

Within our assignment the distance between the two charge-transfer excitations at $E_1^{CT} = 4.5$ eV and $E_2^{CT} = 5.5$ eV can be used to get an estimate of J_H^{simple} within the simple scheme[14]: Roughly speaking the difference in energy reads $E_2^{CT} - E_1^{CT} = 4J_{H,d^5}^{simple} - (10Dq_{d^5} + \frac{1}{2}\Delta_{eg,d^5}) = 1$ eV. If one assumes now that $10Dq_{d^5} + \frac{1}{2}\Delta_{eg,d^5} = 2.9$ eV (see Tab. 4.2), one ends up with a Hund's rule coupling of $J_{H,d^5}^{simple} \sim 0.98$ eV. It translates into

[14]The simple scheme assumes the same U^{simple} for all electrons, regardless where they reside: in the same orbital or in another orbital. If two spins are parallel one gains the energy J_H^{simple}.

$J^{simple}_{H,d^4} = (F^2_{d^4} + F^4_{d^4})/(F^2_{d^5} + F^4_{d^5})\, J^{simple}_{H,d^5} \sim 1.1$ eV). The exact value from our fit to the entire spectrum is $J^{simple}_{H,d^4} = 0.9$ eV, which shows that the simple considerations have a significant error. Both values are lower than the atomic value of $J^{simple}_{H,d^4} = 1/14\ (F^2 + F^4) = 1.35$ eV obtained from a Hartree-Fock calculation [18]. However, covalency and screening from higher-lying multiples reduce the value of J^{simple}_H [163]. For Mn^{3+} values of J^{simple}_H between 0.7 and 0.9 eV have been reported [1, 2, 171]. With our value of 0.9 eV (1.1 eV) we are close to the regime reported in the literature.

Regarding only the transition energies a second assignment for the charge-transfer transitions is possible: the peak at 3.5 eV could also be assigned to the first allowed charge-transfer transition. We will argue in the following that this is not the case. Firstly, the LDA+U calculation of Park [162] shows that a peak at 3.5 eV could very well contain sizable amount of O_{2p} character. However, one may speculate (since the optical conductivity on basis of the LDA+U has not been derived) that a sharp feature can not be expected for a CT transition because of the large bandwidth of the O_{2p} bands compared to the Mn_{3d} bands (exception: the $x^2 - y^2$ band which is broad). Therefore, we assume that the sharp features in the spectrum will mainly arise from Mn to Mn transitions due to the flatness of these bands (sharp peaks in the DOS, see Fig. 4.11). Secondly, according to our multiplet model the first allowed charge-transfer transition is the strongest one. If one assigns it to the peak at 3.5 eV (which can be done by turning Δ_a to 3.5 eV), one runs into great difficulties to get sufficient weight from the CT sector into the region at 4.5 eV. From the comparison of the multiplet model with our data we see evidence that the peak at 3.5 eV can not be regarded as a CT transition, because otherwise we do not get a reasonable description.

Covalency is not included in the multiplet calculation. The band-structure calculation of Park [162] shows that the CT bands in the region of -4 eV to -2 eV have comparable contributions from the O(1) and O(2) sector. For our purpose we can therefore assume that $E(p^6)$ is constant, i.e. the Madelung potentials are almost equal on both crystallographic sites (from a pure point charge summation one finds $E^{O(1)} = -23.5$ eV and $E^{O(2)} = -19.9$ eV, i.e. a difference of 3.6 eV, this value is obviously too large). This assumption is compatible with our fit results, because we only obtained slightly different values for Δ_a and Δ_c (4.51 eV and 4.13 eV). In a molecular-orbital language a charge-transfer transition is bonding to non-bonding transitions on a MnO_6 cluster. The eigenenergies do not depend on the direction, i.e. no change in the transition energies is expected in a and c as long as the Madelung potentials are comparable.

We will briefly discuss the limits of our model. The simulation of both directions requires the assumption of an almost isotropic hopping $pd\pi^a \sim 0.9\, pd\pi^c$ eV in the a and c direction. If one strictly refers to the values obtained from Harrison's rule (see Eq. 4.12), the spectral weight in the c direction is too low. This is a result of the highly anisotropic bond length in a and c, leading to anisotropic values of $pd\pi$ and $pd\sigma$ (see Sect. 4.4.1). This shows that the bond model ends here. A way out might be the treatment of an MnO_6 cluster (see for example Ref. [172] for the case of $LaMnO_3$). However, for the Mott-Hubbard transitions one has to consider a Mn_2O_{11} cluster, increasing the computational effort tremendously.

Table 4.4: Two-center overlap integrals for $LaSrMnO_4$ using the Slater-Koster tabular [24]. The parameter space can be reduced by applying Harrison's rule $pd\pi^{a,c} = -\frac{1}{\sqrt{3}} pd\sigma^{a,c}$ [169].

	a direction (x)			a direction (y)			c direction (z)		
	p_x	p_y	p_z	p_x	p_y	p_z	p_x	p_y	p_z
d_{xy}	0	$pd\pi^a$	0	$pd\pi^a$	0	0	0	0	0
d_{zx}	0	0	$pd\pi^a$	0	0	0	$pd\pi^c$	0	0
d_{yz}	0	0	0	0	0	$V^a_{pd\pi}$	0	$pd\pi^c$	0
$d_{x^2-y^2}$	$\frac{\sqrt{3}}{2} pd\sigma^a$	0	0	0	$-\frac{\sqrt{3}}{2} pd\sigma^a$	0	0	0	0
$d_{3z^2-r^2}$	$-\frac{1}{2} pd\sigma^a$	0	0	0	$-\frac{1}{2} pd\sigma^a$	0	0	0	$pd\sigma^c$

Mott-Hubbard transitions (MH)

We turn to the transitions observed in the a direction, in particularly the band around 2 eV, a peak at 3.5 eV and some fine structure around 4.5 eV. The two strong bands at 4.5 eV and 5.5 eV already have been discussed above. They have been interpreted in terms of charge-transfer transitions. From geometrical considerations Mott-Hubbard transitions are suppressed in the c direction because the Mn ions are far apart.

First we would like to exclude local dd transitions as a source of the low-lying excitations around 2 eV: the on-site transitions would be very well compatible with the observed energy scale of approximately 1-2 eV. However, the local dd transitions are parity forbidden within a dipole approximation, thus one has to simultaneously excite a phonon. This makes these transitions very weak. Typically, their optical conductivity is of the order of a few Ωcm^{-1} or less [26]. Experimentally we found that the band at 2 eV is $\sigma_1 \sim 100\ \Omega\text{cm}^{-1}$ which make local dd transitions very unlikely as a source of the 2 eV band. We will omit the on-site transitions for the following discussion.

We now come back to the intersite $d_i d_j$ transition, i.e. the Mott-Hubbard excitations. In order to interpret the spectral features in terms of multiplets we would like to discuss some selection rules which have to be kept in mind. Optical transitions do not occur between every energy level shown in Fig. 4.29. There are basically two selection rules which have to be considered in this context, the spin and the orbital selection rule. (i) *Spin selection rule* - Within the dipole approximation for an optical transition, the spin of an electron cannot be flipped during the hopping process. The ground state of $LaSrMnO_4$ is a $d^4(^5\text{A}_{1g})d^4(^5\text{A}_{1g})$ state (see Fig. 4.29) which means $S_1 = 2$ and $S_2 = 2$ for two neighboring sites within the Mn-Mn bond model. For a ferromagnetic alignment of the two sites, only the state with $S_1 = 3/2$ and $S_2 = 5/2$ and vice versa can be reached since one electron with $S = 1/2$ is transferred. For an antiferromagnetic alignment the final states can also have $S_1 = 3/2$ and $S_2 = 3/2$. Note, that also final states with $S_1 = 3/2$ and $S_2 = 5/2$ ($S^z = 3/2$)

can be reached from an antiferromagnetic ground state[15]. Thus for the optical transitions only these two spin channels have to be taken into account. (ii) *Orbital selection rule* - The orbital selection rule is mainly determined by the matrix $t^{a,MH}_{\tau,\tau'}$ (see Eq. 4.5). It is a single-electron matrix of rank 10, where one can read whether or not there is overlap between two d levels via a bridging oxygen. This depends on the magnetic quantum numbers τ and τ' (the quantum numbers count the complex d orbitals). Note, that every second entry of this matrix is zero because of the spin selection rule. It is obvious that there is overlap between states with the same quantum numbers $\tau = \tau'$. Here one has to consider also the matrix elements $< d^5_i|a^\dagger_\tau|d^4_k >< d^3_j|a_{\tau'}|d^4_{k'} > = < d^5_i|a^\dagger_\tau|d^4_k >< d^4_{k'}|a^\dagger_{\tau'}|d^3_j >$, which will lead to another restriction: a non-vanishing matrix element is only obtained if $\Gamma_{d^5} \otimes \Gamma_{a^\dagger_\tau} \otimes \Gamma_{d^4} \supset A_{1g}$ and $\Gamma_{d^3} \otimes \Gamma_{a_{\tau'}} \otimes \Gamma_{d^4} \supset A_{1g}$. From the multiplet calculation we use $\Gamma_{d^4} = A_{1g}$ (see Fig. 4.29). For $\tau = \tau'$ the above equations simplifies to $\Gamma_{d^5} \otimes \Gamma_{a^\dagger_\tau} \supset A_{1g}$ and $\Gamma_{d^3} \otimes \Gamma_{a_\tau} \supset A_{1g}$ since A_{1g} is the identity. This is equivalent to $\Gamma_{d^3} = \Gamma_{a_\tau} = \Gamma_{a^\dagger_\tau} = \Gamma_{d^5}$. As a rule of thumb one can state the following: as long as a single e_g electron (in O_h) hops, there are two possibilities for the hopping path because the $d_{3z^2-r^2}$ on one site has overlap to both $d_{x^2-y^2}$ and $d_{3z^2-r^2}$ on the other site. In contrast if a t_{2g} electron (in O_h) hops, there is only overlap to the *same* type of t_{2g} orbital. This means as long as an e_g electron hops upon a transition, the d^3 and d^5 final state can have different symmetries, while a hop of a t_{2g} electron requires always the same symmetry for the final states. Two brief examples:

- hopping of an e_g electron into a different orbital, i.e. a transition to a $d^3(^4B_{1g})d^5(^6A_{1g})$ final state. This transition is allowed.
- hopping of an t_{2g} electron into a different orbital, i.e. a transition $d^3(^4E_g)d^5(^4A_{2g})$ to a state. This transition is forbidden.

Unfortunately things are a bit more complicated, because the eigenstates are mixed configurations. As an example we would like to discuss the configuration mixing of the cubic $d^5(^4T_{2g})$ state for the value $10Dq = 1.3$ eV. In this state, three configurations are mixed: $|1\rangle = t^4_{2g}e^1_g$, $|2\rangle = t^3_{2g}e^2_g$, and $|3\rangle = t^2_{2g}e^3_g$. For the lowest $d^5(^4T_{2g})$ eigenstate one finds $|d^5(^4T_{2g})\rangle^{(1)} = -0.95\,|1\rangle - 0.25\,|2\rangle - 0.21\,|3\rangle$, which shows that the admixture of $|2\rangle$ and $|3\rangle$ equals approximately 10% and can hence not be neglected. This means: this state might very well contribute in an e_g hopping process (if not prohibited by the spin selection rule - this is the case for $LaSrMnO_4$).

Now we finally turn to the spectra. We start from a $d^4(^5A_{1g})d^4(^5A_{1g})$ ground state. According to the multiplet calculation the lowest transition over a wide parameter range is to a $d^3(^4B_{1g})d^5(^6A_{1g})$ final state. This transition is sketched in Fig. 4.30. In an antiferromagnetic state the spectral weight of this transition is reduced, because the final d^5

[15]For a ferromagnetic alignment one forces the system to $S^z_1 = 2$ and $S^z_2 = 2$ states. Excited states from this configuration must have $S^z_1 = 5/2$ and $S^z_2 = 3/2$. With 5 and 3 electrons on site 1 and 2, respectively, this requires $S_1 = 5/2$ and $S_2 = 3/2$, i.e. the full spin polarization. For an antiferromagnetic alignment the system is in a $S^z_1 = 2$ and $S^z_2 = -2$ state. An excitation ends in a $S^z_1 = 3/2$ and $S^z_2 = -3/2$ final state. Again one needs full spin polarization for the site with 3 electrons (site 1), i.e. $S_1 = 3/2$, but for the site with 5 electrons there are now two possibilities, namely $S_2 = 3/2$ with $S^z_2 = -3/2$ and $S_3 = 5/2$ with $S^z_2 = -3/2$.

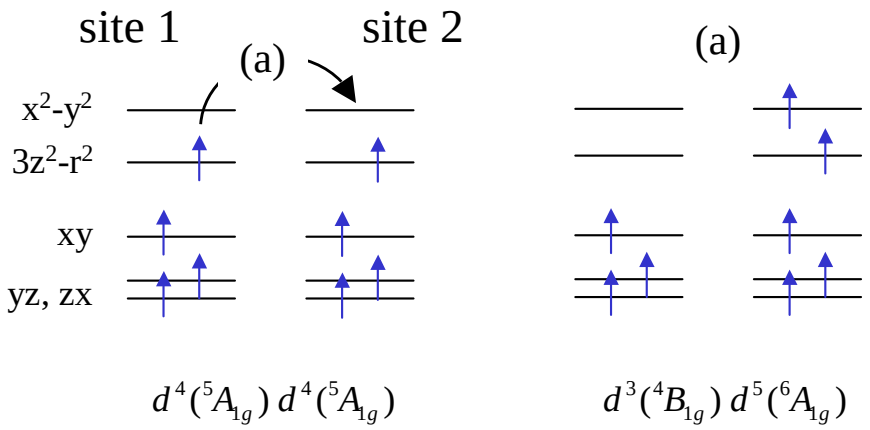

Figure 4.30: Sketch of the lowest high-spin transition in $LaSrMnO_4$ for a ferromagnetic arrangement of two neighboring sites in the strong-coupling limit, i.e. configuration mixing is neglected. The shown transition is assigned to the spectral features observed around 2 eV in the a direction.

state has $S = 5/2$. Its spectral weight increases if more neighboring spins are ferromagnetically aligned. The transition is not strictly forbidden because the antiferromagnetic state contains singlet and triplet contributions. In Figs. 4.13, 4.14, and 4.16 one can clearly see that the spectral weight increases with increasing temperature in the region around 2 eV. Below, the magnitude of the spectral weight will be compared to the kinetic energy of this process. This gives experimental evidence for our assignment. Further support comes from an LDA+U calculation [162]. The lowest occupied band consists of a Mn ($d_{3z^2-r^2}$) band hybridized with O(p) bands, and the highest unoccupied band is a Mn ($d_{x^2-y^2}$) band. Additionally, an analogous assignment for the low-lying transitions has been done for the sister compound $LaMnO_3$ [2, 125]. Our assignment is also compatible with the X-ray data of Kuepper *et al.* [165]: they identified the lowest contribution of Mn states to the lower Hubbard band at approximately -0.7 eV.

In Fig. 4.26 we show the experiential data at 15 K together with the results of our multiplet calculation. The agreement is much better above 3 eV than at lower energies. One reason is the width of the lowest band. The $d_{x^2-y^2}$ band is expected to have a large band width. However, in order to minimize the number of parameters, we used a single parameter $\gamma_a^{MH>}$ for the width of all Mott-Hubbard excitations (see Tab. 4.3) and assumed that the lowest excitation has a width of $\gamma_a^{MH<} = 2\gamma_a^{MH>}$. Obviously, a physically meaningful description of the band width cannot be obtained from a local model. What is more important is that the multiplet calculation underestimates the weight of the lowest transition. This can be attributed to (i) an underestimation of the hopping strength in our approach. An increase of $pd\pi$ and $pd\sigma$ increases the relative weight of the Mott-Hubbard transitions with respect to charge-transfer transitions. (ii) an underestimation of CT background in this energy region (see below). (iii) small amounts of Mn^{4+} which contribute to the weight in this energy region by transitions of the form $d_i^4 d_j^3 \rightarrow d_i^3 d_j^4$ (see below). As seen from the spectra of the doped compounds (see Fig. 4.20), the spectral weight at low energies

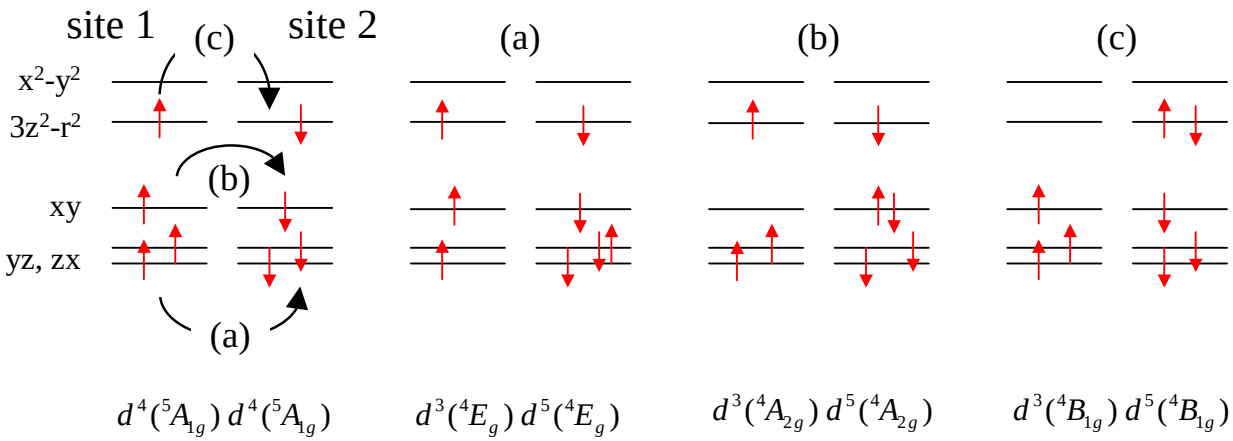

Figure 4.31: Sketch of the lowest low-spin transition in $LaSrMnO_4$ for an antiferromagnetic arrangement of two neighboring sites in the strong-coupling limit, i.e. configuration mixing is neglected. The shown transitions are all assigned to the spectral feature around 3.5 eV in the a direction.

increases with increasing doping. However, the characterization of the samples (e.g. the Neél temperature) and the comparison of the spectra for different x clearly indicates that such impurity contributions play only a minor role. (iv) an insufficiency of our model. The bond model may be at its end here, one has to consider a proper Mn_2O_{11} cluster in order to properly capture the impact of hybridization.

We continue with the higher-lying levels: as already discussed above, our assignment favors a Mott-Hubbard transition into a d^5 state with $S = 3/2$ for the peak at 3.5 eV instead of a charge-transfer process. Referring to our multiplet calculation the peak at 3.5 eV contains several multiplets, in particular $d^3(^4E_g)d^5(^4E_g)$, $d^3(^4A_{2g})d^5(^4A_{2g})$, and $d^3(^4B_{1g})d^5(^4B_{1g})$. For the first final-state multiplets an e_g electron (in D_{4h}) from the $d_{xz,yz}$ orbitals is transferred, while a b_{2g} (d_{xy}) and an a_{1g} ($d_{x^2-y^2}$) electron are transferred in the second and third process, respectively. For the strong-coupling limit the multiplet states are shown in Fig. 4.31. These transitions are favored for antiferromagnetic spin alignment, since the final d^5 state has S=3/2. As one can see in Fig.4.16 this transition indeed loses weight with increasing temperature. The loss of approximately $\omega_p^2 \sim 20\%$ over a temperature range of 300 K is not as strong as the gain of the low lying transition (see Fig. 4.16). On the basis of a change of the spin-spin correlation with temperature [38, 83] one expects a change of approximately 50% from low to high temperatures.

Our assignment is very well compatible with the results of the LDA+U. Since the corresponding bands are rather flat (the $d_{x^2-y^2}$ band is not included here), one can directly discuss the transitions within the DOS scheme. If the bands are broad this is not possible because one has to consider transitions with $\Delta\mathbf{k} = 0$ at every $\mathbf{k}$ point of the Brillouin-zone. One can read from Fig. 4.11 that the filled $d_{xy,xz,yz}$ bands with spin up can be found at approximately -2 eV, while the unoccupied $d_{xy,xz,yz}$ bands with spin down are at 1.5 eV. The

transition energy is approximately 3.5 eV (Here, we neglect excitonic effects discussed for $YTiO_3$ in chapter 5). Transitions between these bands correspond to transitions into our $d^3(^4E_g)d^5(^4E_g)$ and $d^3(^4A_{2g})d^5(^4A_{2g})$ multiplets starting from a $d^4(^5A_{1g})d^4(^5A_{1g})$ ground state. The filled $d_{3z^2-r^2}$ spin-up band is found at approximately -0.6 eV, while the unoccupied spin-down band is located around 2.6 eV, resulting in roughly 3.2 eV transition energy. If one translates this into the multiplet language a transition between these bands corresponds to a transition into the $d^3(^4B_{1g})d^5(^4B_{1g})$ multiplet. One can also read from the LDA+U DOS that CT transitions also contribute in this energy region. The background contribution of the CT transitions might be underestimated in our Lorentz fit (see above). This could explain the discrepancy between the observed change of weight with temperature and the expectations from the spin selection rules.

The next group of Mott-Hubbard transitions can be found in the region above 4.5 eV. Here the transitions are hard to separate from the charge-transfer transitions. However, we assign the sharp structures at 4.5 eV and 4.9 eV to MH bands, since CT excitations exhibit a large band width. As an example we would like to give the final state $d^3(^4B_{2g})d^5(^4A_{1g})$ multiplet, which represents the transfer of an a_{1g} ($d_{3z^2-r^2}$) electron to a b_{1g} ($d_{x^2-y^2}$) state. This energy is roughly (!) speaking Δ_{eg} higher than the transition into the $d^3(^4B_{1g})d^5(^4B_{1g})$ state. Another multiplet is the $d^3(^4B_{2g})d^5(^4B_{2g})$ final state, which only has small weight because of the contributions of the e_g^2 (in O_h) sector of the $^4T_{2g}$ cubic state are only small. We will stop the discussion at this point, because the multiplet calculation makes life easier and counts all multiplets and all spectral weights for us. The results are shown in Fig. 4.25-4.28 and show a good agreement to the experimental data.

Kinetic energy of the low-energy high-spin transition in $LaSrMnO_4$

We have calculated the kinetic energy for the low-lying high-spin excitations and compared it to the measured spectral weight. We assume that the redistribution of weight with temperature can be attributed entirely to a change of the nearest-neighbor spin-spin correlation function. We follow the lines of Refs. [2, 83]. We have assigned peaks (a) and (b) of Fig. 4.16 in the a direction to a high-spin transition into the $d^3(^4B_{1g})d^5(^6A_{1g})$ state. From the plasma frequencies of these two peaks one can calculate the effective carrier concentration N_{eff} using Eq. 4.3. The results are shown in Fig. 4.32.

Analogous to the work on the d^4 compound $LaMnO_3$ one can calculate the effective carrier concentration N_{eff} for a given transition from the kinetic energy. This has been done by evaluating the magnetic superexchange Hamiltonian, which also gives a measure of the kinetic energy. For the antiferromagnetic superexchange an electron hops into a virtual state and then hops back to its origin. The intersite excitations we probe in optical spectroscopy are the real-state counter parts of these virtual states. The hopping amplitude into both virtual and real states are the same. For the high-spin channel with a virtual d^5 state of $^6A_{1g}$ symmetry, this relation between superexchange and effective carrier concentration has been calculated [37, 83] for $LaMnO_3$. We recall equation 4.1 from the

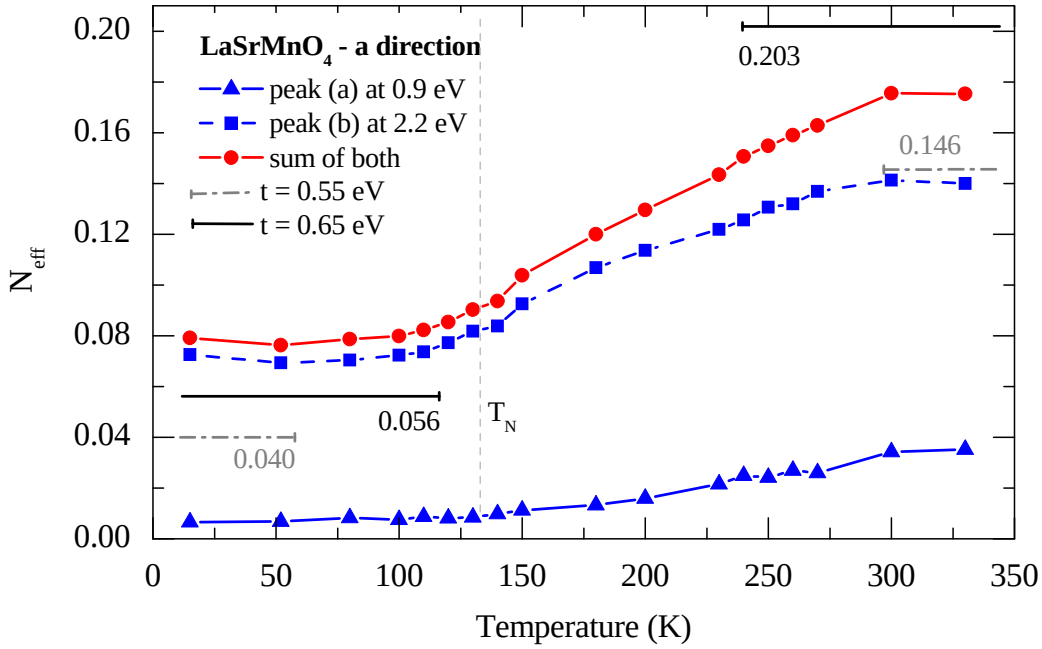

Figure 4.32: Effective carrier concentration N_{eff} of the 2 eV feature in $LaSrMnO_4$ as a function of temperature. The parameters have been taken from the Drude-Lorentz fits of peak (a) and peak (b), see Fig. 4.16 for comparison. The horizontal lines indicate N_{eff} calculated from the kinetic energy of the associated transition in the antiferromagnetic case at low temperatures and for the paramagnetic case at high temperatures (see text).

introduction between the effective carrier concentration N_{eff} and the kinetic energy K:

$$N_{eff} = \frac{ma_0^2}{\hbar^2} \cdot K \tag{4.13}$$

Here a_0 represents the Mn-Mn distance and m the free-electron mass. Since the orbital arrangement in the a direction of $LaSrMnO_4$ is similar to that of $LaMnO_3$ in the c direction, we can fully adopt the formalism applied to $LaMnO_3$. In particular the ferroorbital bond in $LaSrMnO_4$ along a with two adjacent $d_{3z^2-r^2}$ orbitals is equivalent to the ferroorbital bond in $LaMnO_3$ along c with two adjacent $d_{3x^2-r^2}$. In order to take this rotation of the coordinate system into account one has to set $\theta = 120°$ for the orbital mixing angle. Note, that orbitals with $\theta = n \cdot 120°$ fulfill the tetragonal symmetry. In the orbitally ordered state the kinetic energy is given by [2]:

$$K_a = (\tilde{J}/2)\langle \vec{S}_i \vec{S}_j + 6 \rangle \sin^2 \theta \tag{4.14}$$

$$\tilde{J} = \frac{t^2}{5(U^* - 3J_H + \Delta_{JT})} \tag{4.15}$$

where i and j denote the nearest-neighbor Mn sites, t the effective Mn-Mn hopping, $U^* = U - V$ represents Hubbard U reduced by an electron-hole binding energy V, J_H is the

Hund's rule coupling within the Kanamori scheme, and Δ_{JT} the Jahn-Teller splitting of the e_g levels. For very low temperatures in the antiferromagnetic state $T \ll T_N$, $\langle \vec{S}_i \vec{S}_j \rangle \rightarrow -4$, while for very high temperatures $\langle \vec{S}_i \vec{S}_j \rangle \rightarrow 0$. We have chosen the parameters as follows: the mixing angle is $\theta = 120°$ (see above), the Mn-Mn bond distance $a_0 = 3.786$ Å [148], for the effective hopping amplitude we assumed that $t = t_{pd}^2/E_{CT} = 0.55$ eV (and 0.65 eV), higher than the values[16] assumed for $LaMnO_3$ (we neglect the T dependence of t, the error is less than 0.05.), and $E_{CT} = 4.5$ eV from our experiment, and for $U_{eff} = U^* - 3J_H + \Delta_{JT}$ we determined the center of gravity of peak (a) and (b) by $U_{eff}(T) = (N_{eff}^{(a)}(T)\, E^{(a)} + N_{eff}^{(b)}(T)\, E^{(b)})/N_{eff}(T)$ which results in $U_{eff}^{AF}(15K) = 2.10$ eV and $U_{eff}^{para}(330K) = 1.76$ eV. Finally one derives:

$$K_a^{AF} = \frac{3}{4}\tilde{J}^{AF} = 0.021\,(0.030)\text{ eV} \Rightarrow \mathrm{N_{eff}^{AF}} = 0.040\,(0.056) \tag{4.16}$$

$$K_a^{para} = \frac{9}{4}\tilde{J}^{para} = 0.077\,(0.108)\text{ eV} \Rightarrow \mathrm{N_{eff}^{para}} = 0.146\,(0.203) \tag{4.17}$$

The calculated values for the effective carrier concentration N_{eff} are shown together with the values obtained from the experiment (see Fig. 4.32). For a hopping of $t = 0.55$ eV one generally ends up too low in the N_{eff} value. But increasing the hopping to $t = 0.65$ eV (which is still a reasonable value) leads to a good agreement with our data from experiment.

We conclude that the redistribution of spectral weight with temperature could be well described in terms of the change of the spin-spin correlation function. A one-to-one adaption of the correlation function of $LaMnO_3$ is however not possible because the dimensionality of the layered compound is more 2D, in contrast to 3D in $LaMnO_3$. Qualitatively one expects for a quasi 2D compound that nearest-neighbor correlations are still strong at temperatures above T_N [173], which means the changes across T_N are more gradual. This is in agreement with our data (Compare Fig. 4.32 with Fig. 4.7 for $E \,||\, c$).

Temperature dependence - the effect of the electron-phonon coupling

The spectra show a rather strong temperature dependence. We quantified these changes by the parameters ω_0, γ, and ω_p of the Drude-Lorentz oscillators, see Figs. 4.15 and 4.16. As pointed out in the section of the charge-transfer transitions, thermal expansion alone cannot account for the relatively large changes in spectral weight. In the previous section we have shown that for the Mott-Hubbard transitions a change in the spin-spin correlation function can explain the change of the intensity. We will now briefly discuss the impact of electron-phonon coupling on the parameters ω_0, γ, and ω_p. For this discussion it does not matter whether we assume a transitions between localized states (Franck-Condon transitions, excitons) or band-like transitions. The physics is in both cases the same and leads to similar analytic expressions.

We start with the energy shift of ω_0 with temperature. For semiconductors one has to consider a renormalization of the electron-ion potential on top of the thermal expansion.

[16] This is justified since the magnetic coupling constant J is larger in $LaSrMnO_4$ than in $LaMnO_3$ [2, 137].

The renormalization is proportional to the mean-squared amplitude $\langle u(T)^2 \rangle$ of the phonon frequencies [174–176]. Effectively this leads to an additional increase of the lattice constants and via the hybridization to an energy shift [177].

When the excitations are of localized character, i.e. a self-trapped exciton, then Franck-Condon like transitions have to be considered [161]. In this scenario the energy shift in temperature is attributed to a change of the phonon frequencies in the excited states with respect to the ground state as well as to a change of the anharmonic terms of the electron-ion potential (i.e. again a renormalization of the electron-ion potential). In fact, also the first effect is a result of the different anharmonic terms, but it enters the energy shift twice [85]. We will summarize all effects of the electron-phonon coupling including the thermal expansion causing to the energy shift in ω_0 in one particular parameter $\Delta\omega_0$. The energy shift of ω_0 with temperature reads [85, 177–179]:

$$\omega_0(T) = \omega_0(T = 0K) - \frac{\Delta\omega_0}{\exp(\frac{\hbar\Omega}{k_B T}) - 1} \tag{4.18}$$

The parameter ω_0 represents the excitation energy, and Ω denotes the frequency of an Einstein phonon. Note, that it may be necessary to include more than one Einstein mode, especially when acoustic and optical phonons have very different frequencies [175, 176]. Electron-phonon coupling will in general (for $\Delta\omega > 0$, $\Delta\omega < 0$ is also possible [175]) lead to a down-shift in energy. Thermal expansion effects alone can not explain, e.g., the magnitude of the gap closure with temperature in many semiconductors [175–177]. For our case it is important to note, that the thermal expansion can either be increased or compensated by electron-phonon interaction.

The evolution of the damping γ with temperature in an ordinary semiconductor can be attributed to life-time broadening [179–181]:

$$\gamma(T) = \gamma_1 + \gamma_0 \left(\frac{1}{\exp(\frac{\hbar\Omega}{k_B T}) - 1} + \frac{1}{2} \right) \tag{4.19}$$

γ_1 reflects the broadening due to extrinsic effects as for instance the instrumental resolution or boundary and defect scattering, and γ_0 is the quasi-particle life-time broadening, i.e. the electron-phonon coupling. In an illustrative picture, the thermal population of phonon levels leads to a delocalization of the electrons and thus to a broadening of the band or the exciton levels.

In the Franck-Condon scenario the vibronic states become more extended with temperature. For the damping of the excitations this means [84]:

$$\gamma(T) \approx \gamma_0 \sqrt{\coth\left(\frac{\hbar\Omega}{2k_B T}\right)} + \gamma_1 \tag{4.20}$$

$$\gamma_0 \approx 2\hbar\Omega\sqrt{2S} \tag{4.21}$$

The Huang-Rhys parameter S [178] quantifies the difference in the electron-phonon coupling of the ground state and the excited state (e.g. $S = 0$ means no difference) [84]. γ_1

represents extrinsic broadenings. Both, Eqs. 4.19 and 4.20, lead to an exponential increase of the broadening with temperature.

Electron-phonon interaction is expected to give much less impact on the intensity. But it allows for finite intensity in parity-forbidden transitions. The simultaneous excitation of an even-parity phonon will lead to an admixture of even-parity states to the odd-parity electronic wave functions. This admixture will scale with the thermal population of the phonons. The formally forbidden transitions becomes more and more allowed. The same argumentation holds true for indirect transitions in a band-semiconductors. The latter effect increases as the phonon occupation increases with temperature following the same coth-rule as the damping [21, 85].

As an example we fitted the parameters of the Lorentz oscillator (b) given in Fig. 4.16 using the Eqs. 4.18 and 4.20. The fit results are $\omega(T=0K) = 2.22$ eV, $\Delta\omega_0 = 0.36$ eV, $\Omega = 0.054$ eV (439 cm^{-1}), $S = 3.41$, $\gamma_1 = 0.89$ eV. For the fit of γ we fixed the Einstein-phonon frequency. The fit results are in reasonable agreement with the data. The above model function can well describe the overall trend of all peaks. However, for the peak at 3.5 eV this model is not sufficient. Two Einstein phonons with $\Delta\omega_1 > 0$ and $\Delta\omega_2 < 0$ can do the job.

Coming back to the intensity: as discussed by Biernacki *et al.* the electron-phonon interaction can be treated as an extra inter-atomic elongation [177] on top of the ordinary thermal expansion. The intensity of a transition depends on the hopping amplitude, depending itself strongly on the interatomic distance. The effect of thermal expansion on the hopping may be enhanced or compensated by electron-phonon coupling. It would be interesting to investigate how strong this effect really is and in how far it contributes to the observed redistribution of weight of the low-energy region (see previous section). However it seems unlikely that the electron-phonon coupling alone (without taking into account the effect of the spin-spin correlation function) can account for the temperature dependence of the spectral weight, in particular the different sign of the temperature dependence at high and at low energies.

Optical gap

The onset of the optical gap in the undoped compound amounts approximately 0.45 eV along the a direction and > 0.90 eV along the c direction (see Fig. 4.18). Similar values are found in the doped sample with $x = 0.5$ as one can read from Fig. 4.23. The onset of the gap should be smaller than the first onsite dd excitations. These weak transitions can be observed in optics by a simultaneous excitation of a symmetry breaking phonon. Within our multiplet calculation (see Fig.4.29) the energy of the lowest $d^4 \rightarrow d^4$ excitations is expected around 1.1 eV + the phonon energy (~ 0.08 eV). This is compatible to the finding for the $x = 0.0$ compound.

As shown in the inset of Fig. 4.18 the evolution of the gap changes its slope approximately at the magnetic ordering temperature of 130 K. This behavior can be understand because the lattice constants also shows a change in slope at this temperature (see Fig. 4.10). This change transfers to a change in transition energy via e.g. the electron-phonon coupling

(the bond length changes, phonon frequencies will change) or via a change in hybridization (Harrison rule, see Eq. 4.12).

In order to understand the observed anomalous thermal expansion Daghofer *et al.* proposed that the reduction of the c axis in $LaSrMnO_4$ can be explained by a thermal occupation of the $d_{x^2-y^2}$ orbital (they assumed a static crystal field of 0.1 eV) [159, 160]. As already pointed out in Sect. 4.2.3 the static crystal-field scenario as presented by Daghofer *et al.* sounds very unlikely since 0.20 eV (the onset of the gap value at 300 K, this is a lower boundary value) amounts to 1600 K. The thermal occupation of the $d_{x^2-y^2}$ orbital at 300 K is only 0.005.

On the other hand, one may speculate that orbitals are intermixed due to a sizable electron-phonon coupling. We see indications for a sizable electron-phonon coupling in this compound from the strong shifts in the peak frequencies of our Lorentz oscillators and their damping (see Sect. 4.4.2 and Fig. 4.16). The latter scenario is very different from the ansatz of Daghofer *et al.* because phonons are not included their orbital $t-J$ model.

4.5 Comparison with the doped compounds

Since we only investigated two different doping levels, we will be very brief in this section and discuss on a rather qualitative level. The investigation of more doping levels offers a perspective for future studies.

What are the main differences to be explained (see Figs. 4.19, 4.20, and 4.21). Firstly, there is a feature around 1.0-1.5 eV, which clearly gains weight with increasing x, while the overall spectral weight is constant in the a direction. For $x = 0.13$ an increase of this peak with increasing temperature has been observed (see Fig. 4.22). Secondly, the increase of spectral weight with increasing x in the region at 3.0-3.5 eV (a and c direction) and at 4.5 eV (c direction), and the corresponding decrease at higher energies. Thirdly, the weaker temperature dependence of the $x = 0.13$ compound when comparing to the $x = 0$ compound.

In the multiplet language one induces $Mn(d^3)$ states into the system by doping it with x holes. Besides the excitations discussed for the undoped case one expects additional excitations channels (see Fig. 4.33).

- $d_i^3 p_j^6 \rightarrow d_i^4 p_j^5$: From the results for the c direction one can read that two *new* transition channels are opened at approximately 3 eV and 4.5 eV. These results are in reasonable agreement with measurements of Matsuno *et al.* [182] on thin films of Sr_2MnO_4, i.e. $x = 1.0$. This system is a pure d^3 system, which has been measured up to 4 eV. In the c direction they found two peaks, one at approximately 3 eV and another one close to 4 eV. Our peaks are much broader which we trace back to the La/Sr disorder, but they are approximately located at the same energy positions. Thus we attribute these new transitions to charge-transfer processes of a Mn^{4+} site. What are the expectations for the a direction or more precisely what are the selection rules? This depends on the d^3 initial state. The most likely candidate is the ${}^4B_{1g}$ state according to Hund's rule (three up spins in the t_{2g} level). The d^4 final states can be read from

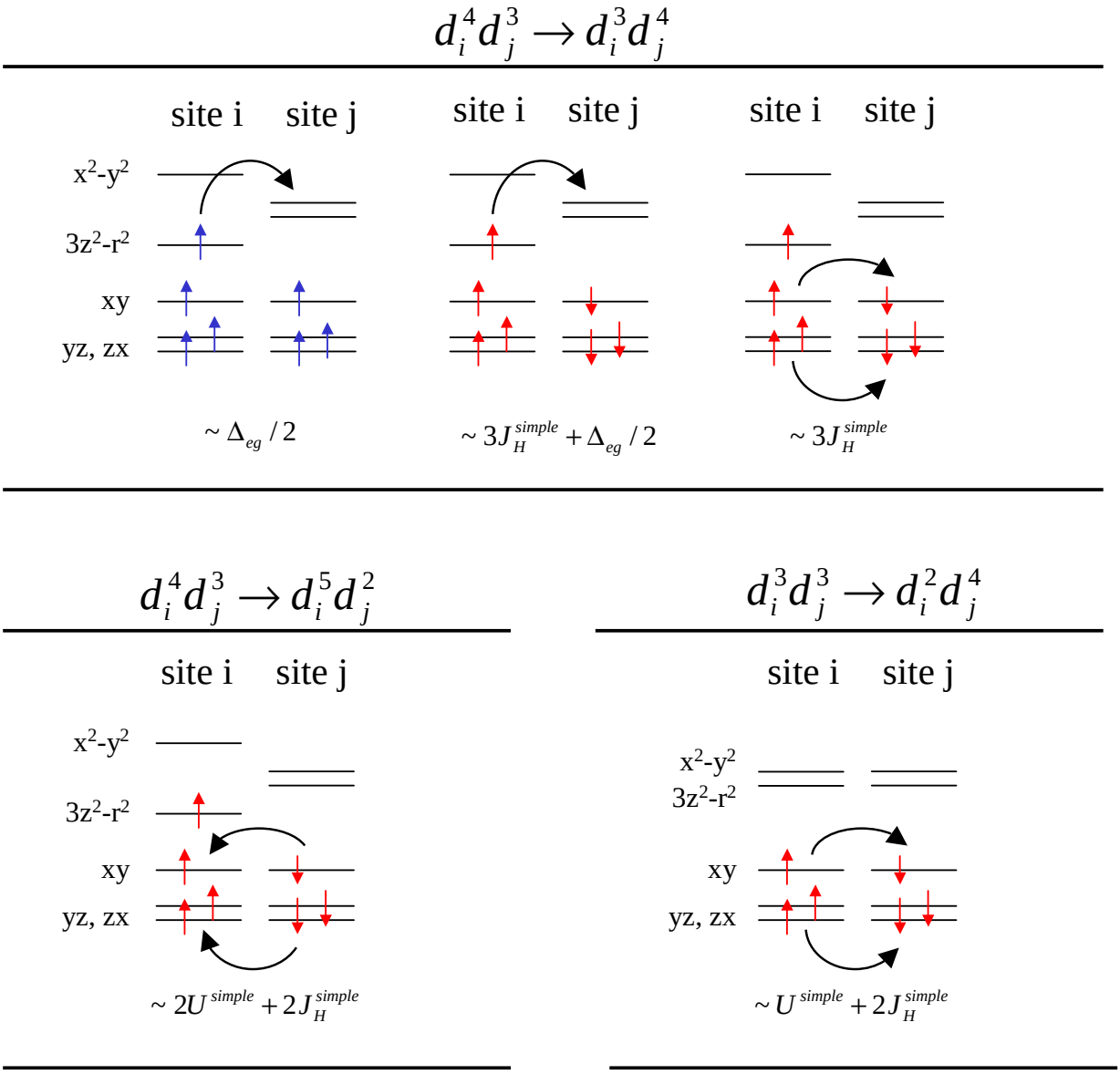

Figure 4.33: Additional multiplet excitations within the Mott-Hubbard channel for a hole-doped d^4 system. The left-most $d_i^4 d_j^3 \rightarrow d_i^3 d_j^4$ excitation has assumed to be trapped. Otherwise the excitations energy is zero.

the level diagram in Fig. 4.29: the first charge-transfer excitation is expected into a ${}^5A_{1g}$ final state, allowed in both polarizations. In contrast, starting from a ${}^4E_g$ initial state (two up spins in the d_{xz}, d_{yz}, one in the $d_{3z^2-r^2}$ levels), the lowest charge transfer is only allowed in the a direction, because the planar d_{xy} orbital has to be filled. Indeed, an anisotropy has been observed in the pure d^3 compound: a peak at 2 eV in the a direction with no counterpart in the c direction [182]. For doped 113 manganites charge-transfer transitions around 2 eV have also been reported [126]. For our feature at 1.5 eV this means that a pd charge-transfer may be a possible scenario requiring however that the d^3 ground state has ${}^4E_g$ symmetry, not ${}^4B_{2g}$. On the other hand for the $x = 0.5$ compound the spectral feature at 1 eV has been attributed to a $d_i^3 d_j^4 \rightarrow d_i^4 d_j^3$ transition [152, 153]. This will be discussed in the next paragraph. The low-lying excitation at 2 eV in the a direction in the pure d^3 system Sr_2MnO_4 could be reinterpreted in terms of a $d_i^3 d_j^3 \rightarrow d_i^2 d_j^4$ excitation. This Mott-Hubbard transition is naturally suppressed in the c direction. An estimate of the transition energy of $E(d^4({}^3E_g)) + E(d^2({}^3E_g)) - 2\,E(d^3({}^4B_{2g}))$=$U^{simple} + 2J_H^{simple} \approx 3.0$ eV[17] (using the parameters from Tab. 4.1) shows that one ends up too high in energy. The transition is sketched in Fig. 4.33. A finite crystal field and the inclusion of the full multiplet will decrease the energy to approximately 2.5 eV. Thus, a Mott-Hubbard transition cannot be excluded.

Note, that one cannot adapt the parameters of the undoped case to the doped systems. This will lead to erroneous results, since these parameters are effective, i.e. they include covalent parts. In the undoped system we formally assume that the charge is $^{3+}$ on the Mn but we did not care whether the effective charge on the Mn site is lower than $^{3+}$ (as it will be!). We hide this, e.g., in a lower value of F^0 (or U). If the system is doped, the charge is redistributed. This means that the former d^3 final-state multiplet (from a d^4 ground state) is *not* comparable to the d^3 ground state as obtained by doping because these two states may have a different electron occupation. This yields different values of F^0 due to different contributions of screening.

We will briefly show that the parameters of the undoped compound cannot directly be taken for the doped one. We consider only the c direction here: one can assume that the bands arise from charge-transfer transitions. For the undoped compound we identified the peak at 5.5 eV along c as a transition into the $d^5({}^4E_{1g})$ and $d^5({}^4B_{1g})$ multiplet. These two multiplets are found at approximately 5.7 eV, as one can read from Fig. 4.29. The ground state multiplet has the energy 1.0 eV. We assume that $E(p^5) - E(p^6) = 0.8$ eV in order to achieve an excitation energy of 5.5 eV. For the hole-doped d^4 compound a shoulder found at around 3 eV has to be attributed to the lowest charge-transfer process of the d^3 sector. Its finals state multiplet is located at 1.0 eV, the ground state $d^3({}^4B_{1g})$ at approximately -0.2 eV. The excitation energy yield 2.2 eV. Thus, the difference of the lowest CT excitation along c between the Mn^{3+} and Mn^{4+} is approximately 3.3 eV. The observed difference is only 2.5 eV. This

[17] $E(d^2) = U^{simple} - J_H^{simple}$, $E(d^3) = 3U^{simple} - 3J_H^{simple}$, $E(d^4) = 6U^{simple} - 3J_H^{simple}$

little example shows that the parameters have to be modified probably due to the change of the covalent parts of F^0. Maybe a proper adaption of the crystal field will also do the job[18]. In general the tetragonal crystal field of the d^3 sites will be smaller. Please keep in mind that the numbers given above and below have to be considered with care and on a rather qualitative level.

- $d_i^4 d_j^3 \rightarrow d_i^3 d_j^4$: If one only considerers two sites of a solid this kind of transition can be done without paying any energy. However, the d^3 ion shows no Jahn-Teller effect and has thus a smaller crystal-field splitting. We assume for simplicity that the crystal-field splitting is entirely induced by the Jahn-Teller effect, i.e. the e_g levels on the d^3 sites are degenerate. For a ferromagnetic alignment of the spins the transfer of an e_g (in O_h) electron will cost half the e_g level splitting (see Fig. 4.33). This describes the formation of a lattice (small) polaron [71]. But if one now takes the whole crystal into account the polaron can hop from site to site without any cost, giving rise to a metallic state. This is not observed in the layered manganites. If the polaron is trapped to an impurity or a precursor of a charge-ordering/orbital-ordering pattern, the material becomes insulation. The situation can then again very well be sketched within a two-site model, as shown in Fig. 4.33. There are more of such transitions but for an antiferromagnetic alignment, which are also shown in Fig. 4.33. Please note that none of these transitions costs U^{simple}, they are entirely determined by the Jahn-Teller effect and Hund's coupling. This kind of excitations has been suggested in order to explain the low-lying peak in charge-ordered/orbitally-ordered state of the $x = 0.5$ compound [152, 153], i.e. the low-lying transitions observed in our measurements at 1.0-1.5 eV. Their energies could by estimated by $\Delta_{e_g,d^4}/2 \sim 0.7$ eV, $3J_H^{simple} \sim 2.7$, and $3J_H^{simple} + \Delta_{e_g,d^4}/2 \sim 3.4$ (taking the values form Tab. 4.2). The latter two energies are too high in order to explain the peak at 1.0-1.5 eV. Regarding the temperature dependence of these peaks the first one should gain weight with increasing T, while the remaining peaks should loose weight, because ferromagnetic contributions are increased when changing from the antiferromagnetic the paramagnetic state. The overall weight has to be conserved.

- $d_i^3 d_j^4 \rightarrow d_i^2 d_j^5$: The variety of final states is very limited, because in this process only t_{2g} electrons can be moved. This is of course only valid under the assumption that the d^3 ground state is of ${}^4B_{1g}$ symmetry. Following our multiplet approach this is the case. The transitions are shown in Fig. 4.33; for the transitions from a $d^3({}^4B_{1g})d^4({}^5A_{1g})$ ground state the final states are $d^2({}^3A_{2g})d^5({}^4A_{2g})$ and $d^2({}^3E_g)d^5({}^4E_g)$. Very roughly speaking these excitations are expected around $E(d^2) + E(d^5) - E(d^3) - E(d^4) = 2U^{simple} + 2J_H^{simple} = 4.2$ eV using $U^{simple} = F_{d^4}^0 = 1.2$ eV and $J_H^{simple} = 0.9$ eV (see Tab. 4.1). These excitations are difficult to discriminate experimentally because of the other contributing multiplets in the same energy region.

[18] From a pure point charge approximation on an average crystal structure of $La_{0.87}Sr_{1.13}MnO_4$ it follows that $10Dq$ remains unaffected while the tetragonal distortion (x, see Fig. 4.29) is reduced by 0.7 with respect to the undoped compound for the d^3 configuration.

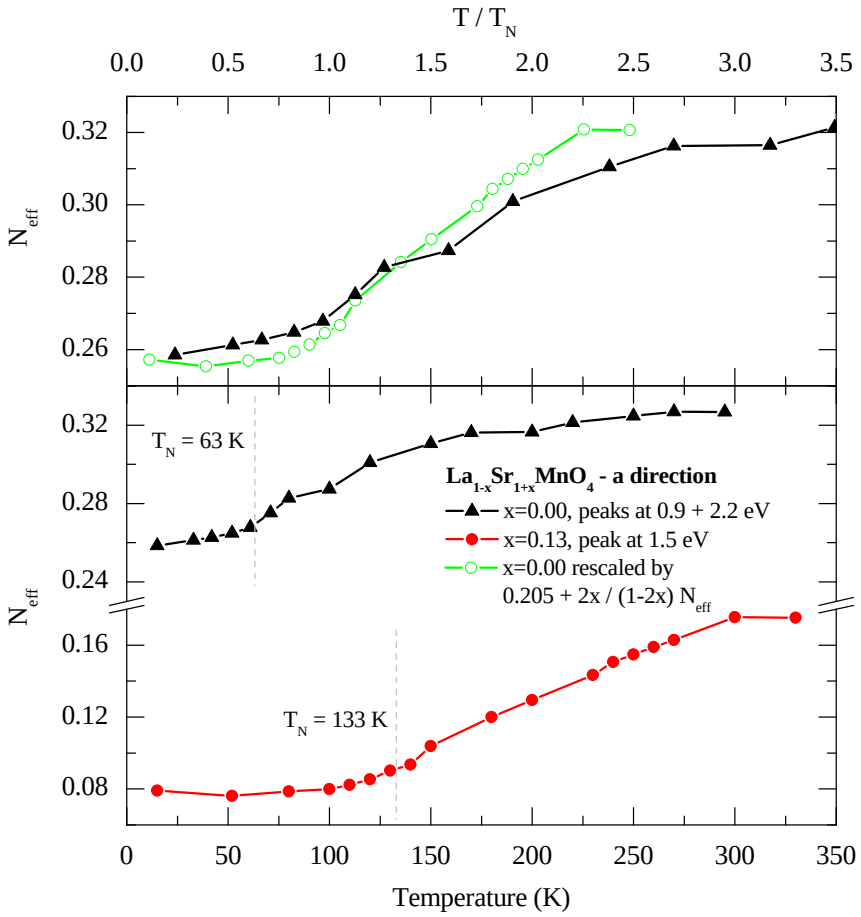

Figure 4.34: *Bottom panel:* Effective carrier concentration N_{eff} of the low-lying peak of $La_{1-x}Sr_{1+x}MnO_4$ as obtained by a Lorentzian fit as function of temperature for two different values of x. *Top panel:* the same data but with rescaled T and N_{eff} axes (only for $x = 0.0$).

- $d_i^3 d_j^3 \rightarrow d_i^2 d_j^4$: These transitions are unlikely since for $x = 0.5$ a charge-ordered pattern is established, i.e. two holes will not reside on sites next to each other. One can of course not exclude that for low doping levels the holes build clusters or bipolarons. This might be especially the case for the strong electron-phonon coupling regime. We sketched the possible multiplets in Fig. 4.33.

The feature around 1.0-1.5 eV - We would like to include the temperature dependence of this peak into the discussion; it is shown in Fig. 4.34. When comparing the $x = 0.0$ with the $x = 0.13$ compound the starting temperature for the increase of weight of the lowest excitation is smaller in the latter compound. A similar trend can be found in the evolution of the lattice constants: the inflection point in the c direction of the doped compound is found at 200 K (see Fig. 4.10) in contrast to 600 K in the undoped compound. If one assumes that the spectral weight consists of a temperature-dependent and an independent part, then the temperature-dependent part of N_{eff} for both doping levels can be scaled

on top of each other (see Fig. 4.34). The T axis has been renormalized with respect to the different antiferromagnetic ordering temperatures and $N_{eff}^{x=0.0}$ has been rescaled by $N_{eff}^{x=0.0} = 0.205 + 2x/(1-2x)\, N_{eff}^{x=0.13}$ using $x = 0.13$. The latter scaling assumes that holes are created on the Mn(d^4) site which leads to a loss of two (!) carriers in the effective carrier concentration of the $d_i^4 d_j^4 \rightarrow d_i^3 d_j^5$ channel [66]. This scaling shows that in both samples the change in spectral weight sets in at approximately T_N and one may speculate that the temperature dependence in N_{eff} is dominated by the $d_i^4 d_j^4 \rightarrow d_i^3 d_j^5$ high-spin transition also for the doped compound.

Finally two different scenarios remain: the peak at 1.0-1.5 eV is a Mott-Hubbard peak or a charge-transfer peak. From our data alone we cannot draw a final conclusion. Although we are convinced that the first excitation in the undoped compound is of Mott-Hubbard type, a broad oxygen band may lie underneath. So the new peak can be very well of charge-transfer type. From the temperature dependence one may draw the conclusion that the additional weight arising from the doping is almost temperature independent. This would favor the charge-transfer scenario. On the other hand, the most likely candidate for the d^3 ground state has $^4B_{1g}$ symmetry, in which case the lowest CT excitations can be observed in both polarization directions. The 1.5 eV band is only observed in the a direction. Furthermore, a polaronic excitation ($d_i^3 d_j^4 \rightarrow d_i^4 d_j^3$, Mott-Hubbard type) would also be temperature independent as long as the three low lying contributions have a large width and overlap strongly.

Increase of spectral weight in the region at 3.5 eV (a, c direction) and at 4.5 eV (c direction) and the corresponding decrease at higher energies - As discussed above the new features along c are new charge-transfer processes of the Mn^{4+} sites. With increasing x these new features increase in weight as clearly observed in Fig. 4.20. Corresponding peaks in a can thus be attributed to the same origin, e.g. the pronounced increase at 3.5 eV, or parts of it. On the other hand the number of Mn^{3+} sites is decreased with increasing x which leads to a decrease in weight in the strong CT excitations above 4.5 eV in the a direction and at 5.5 eV in the c direction (see Fig.4.20). As shown above several additional Mott-Hubbard transitions may also contribute to the 3.5 eV feature in the a direction (Fig. 4.20).

Weaker temperature dependence of the $x = 0.13$ compound when comparing to the $x = 0.0$ compound - In general the temperature dependence is much weaker in $La_{0.87}Sr_{1.13}MnO_4$ than in the undoped compound. This behavior is displayed for the weight of the 1.5 eV feature in Fig. 4.34. The relative change in the doped compound is only $\sim 25\%$ in contrast to $\sim 50\%$ in the undoped one. Additionally the peak shifts with temperature are not so pronounced, which can be inspected by eye in the case of the 3.5 eV feature (see Fig. 4.22). The fine structure above 4.5 eV, attributed to Mott-Hubbard excitations in the undoped case, are washed out for $x = 0.13$. A possible reason is an increase of disorder in the system. Another reason is that new excitation channels are present, which strongly overlap with the channels of the undoped compound (as suggested for the 1.5 eV feature). Thus the temperature dependence of e.g. the 3.5 eV feature along a becomes a mixture of different charge-transfer and Mott-Hubbard contributions, which cannot be separated that well as in $LaSrMnO_4$. Therefore we are not going to discuss the temperature dependence in detail.

Summary

To summarize the main points of this chapter: we have presented optical data from ellipsometry and Fourier spectroscopy on the system $LaSrMnO_4$. We find evidence that the lowest excitation observed at around 2 eV arises from an intersite $d_i d_j$ transitions. This favors a description of $LaSrMnO_4$ in terms of a Mott-Hubbard insulator. This important result challenges the wide-spread point of view that the manganites are charge-transfer insulators, but is in agreement with several recent publications [2, 125, 162, 164, 165]. Since band-structure theory fails in explaining the insulating character of $LaSrMnO_4$, we tried to understand our data in terms of local multiplets. We were able to get a good description of the spectrum by a multiplet calculation using effective parameters for the crystal field and for the Slater-integrals. We discussed the origin of each spectral feature within this model and gave a direct comparison to results from LDA+U [162]. The temperature dependence of the low-lying spectral feature around 2 eV has been explained by a change of the nearest-neighbor spin-spin correlation function with temperature. The overall evolution of the spectrum with temperature suggests that the electron-phonon coupling has to be considered. We determined the onset of the optical gap for the a and c direction with $\sim$0.45-0.50 eV and $>$0.90 eV at low temperatures. These high values for the optical gap can rule out the scenario of Daghofer *et al.* [159, 160], explaining the thermal expansion by a thermal occupation of $d_{x^2-y^2}$ in a *static* crystal field. We suggest that phonons mix the two orbital states due to electron-phonon coupling without destroying the tetragonal symmetry.

We have also shown spectra of doped compounds with $x = 0.13$ and $x = 0.50$. We found a redistribution of weight, in particulary a new peak at approximately 1.0-1.5 eV which could either be interpreted as a trapped polaronic feature or a charge-transfer excitation of the Mn^{4+} state. The redistribution of weight at higher energies could be well explained by a change in the Mn^{4+}/Mn^{3+} ratio which leads to a change in weight for the CT excitations of the d^3 and d^4 sector.

5 Ellipsometry and Raman scattering on $YTiO_3$, $SmTiO_3$, and $LaTiO_3$

5.1 Physics of titanates

The interplay of different degrees of freedom in solids, namely the charge, the spin, the orbital, and the lattice give rise to a variety of interesting phenomena in transition-metal oxides.

In the Mott-Hubbard insulators $RTiO_3$ (R - rare-earth ions) the intrinsic properties of a correlated system can be studied. For example the coupling of the spin degree of freedom to the lattice manifests in different magnetic ground states. When increasing the ionic radius from Y to La the magnetic ground state changes from ferromagnetic to antiferromagnetic [183, 184]. It has been clarified that this change is related to the raising lattice distortions [12–14, 185–187].

Incorporating spin and orbital degrees of freedom, a novel ground state termed *orbital liquid* has been proposed in order to explain the unusual properties of $LaTiO_3$ [3, 4]: an isotropic spin-wave spectrum on the one hand (suggesting a small anisotropy) and a strongly reduced magnetic moment on the other hand (suggesting a large anisotropy). However, the existence of this ground state in $LaTiO_3$ is still under debate [6–10, 15, 16, 26, 27, 41, 64, 188, 189]. The coupling of the orbital degree of freedom and the lattice can lead to orbital ordering, which was found in $YTiO_3$ [5, 189–191]. However, the orbitally-ordered ground state seems to be incompatible with the observed nearly isotropic spin wave spectrum [192]. Therefore, a dominant role of orbital fluctuations has been proposed also for $YTiO_3$ [43, 44], assuming that the ordered orbital moment is only small. Excellent reviews concerning the physics of titanates can be found in Refs. [1, 13]. In the following we focus on the electronic properties in ferromagnetic $YTiO_3$ and antiferromagnetic $SmTiO_3$ and $LaTiO_3$.

5.2 Details on titanates

We will give some further details on the titanates $YTiO_3$, $SmTiO_3$, and $LaTiO_3$. These compounds have been measured in this thesis. We focus on $YTiO_3$, which has been investigated in more detail.

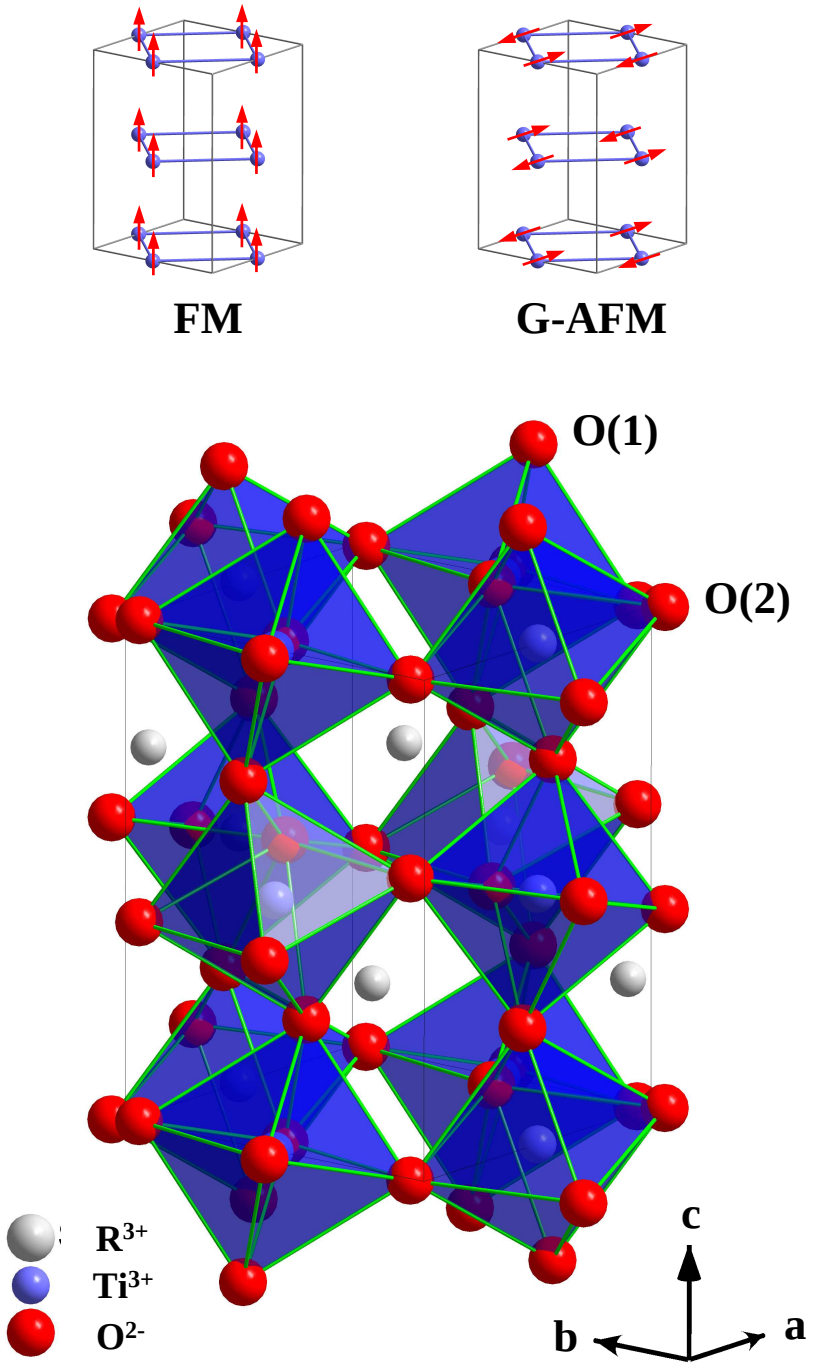

Figure 5.1: *Bottom panel:* the unit cell of $RTiO_3$ (space group *Pbnm*). It consists of TiO_6 octahedra distorted according to the $GdFeO_3$ distortion. *Upper panel:* ferromagnetic ordering as observed in $YTiO_3$ and G-type antiferromagnetic ordering as found in $LaTiO_3$ and $SmTiO_3$.

Table 5.1: Results of the single-crystal and powder neutron-diffraction experiments on $RTiO_3$ (R=Y, Sm, La). The data for La has been taken from Ref. [7] and the data for Sm and Y from Ref. [193]. The ordering temperatures have been determined by H. Roth, N. Schittner, and N. Hollmann by SQUID and thermal-expansion measurements [108, 194].

	Y (2 K)[a]	Sm (100 K)[b]	La (8 K)[a]
a (Å)	5.3226(1)	5.4651(2)	5.6435(1)
b (Å)	5.6952(1)	5.6626(2)	5.5885(1)
c (Å)	7.5962(1)	7.7133(3)	7.9006(2)
$d_{\mathrm{Ti-O(1)}}$ (Å)	2.021	2.011	2.028
$d_{\mathrm{Ti-O(2)}}$ (Å)	2.023	2.031	2.032
$d_{\mathrm{Ti-O(2)}}$ (Å)	2.078	2.069	2.053
$\alpha_{\mathrm{Ti-O(1)-Ti}}$ (°)	140.04	147.01	153.78
$\alpha_{\mathrm{Ti-O(2)-Ti}}$ (°)	143.76	147.34	152.90
	Y (290 K)[b]	Sm (290 K)[b]	La (293 K)[a]
a (Å)	5.3425(2)	5.4647(2)	5.6336(1)
b (Å)	5.6925(2)	5.6712(2)	5.6156(1)
c (Å)	7.6235(2)	7.7291(3)	7.9145(2)
$d_{\mathrm{Ti-O(1)}}$ (Å)	2.022	2.018	2.030
$d_{\mathrm{Ti-O(2)}}$ (Å)	2.027	2.032	2.031
$d_{\mathrm{Ti-O(2)}}$ (Å)	2.078	2.072	2.057
$\alpha_{\mathrm{Ti-O(1)-Ti}}$ (°)	140.90	146.48	154.24
$\alpha_{\mathrm{Ti-O(2)-Ti}}$ (°)	143.97	147.29	153.36
magnetic ordering (K)	$T_c = 27$	$T_N = 48$[c]	$T_N = 146$

[a]Refinement of powder neutron-diffraction data

[b]Refinement of single-crystal data

[c]The $SmTiO_3$ crystal used for the optical studies has $T_N = 53$ K

5.2.1 Crystal structure and magnetism

The crystal structure of $RTiO_3$ (R - rare earth) is shown in Fig. 5.1. All titanates crystallize in an orthorhombic structure with the space group *Pbnm* ($c > a, b$). The Ti ions are surrounded by distorted oxygen octahedra. The octahedra are tilted and rotated away from the cubic axes according to the $GdFeO_3$ distortion [7]. The tilting angles increase from $LaTiO_3$ to $YTiO_3$, see Tab. 5.1. The evolution of the lattice constants for $SmTiO_3$ and $YTiO_3$ with temperature is shown in Fig. 5.2. One can clearly observe an anomaly around T_N in all lattice constants and in the orthorhombic distortion in $SmTiO_3$. In $YTiO_3$ there is hardly any change across T_c.

The magnetic structure in the three compounds will now be discussed. In $YTiO_3$ ferromagnetism has been found with a magnetic moment of $0.54\mu_B$ at 10 K orientated along the c direction [192]. The structure is more complicated because in addition a G-type ordering along a ($0.08\mu_B$) and a C-type ordering along b ($0.05\mu_B$) has been found [192]. The total moment extrapolated to zero temperature yields $0.72\mu_B$. This value is small when comparing to results of $> 0.8\mu_B$ from SQUID measurements [194–196]. The ordering temperatures range from $T_c = 27 - 30$ K [108, 194, 195]. The ferromagnetic coupling constant is found to be approximately $J \approx -2.75$ meV with a very small anisotropy gap of 0.02 meV [192].

In $SmTiO_3$ antiferromagnetism has been reported with ordering temperatures of about $T_N = 50$ K [108, 197]. The ordering pattern at 10 K is G-type for the Ti spins with a magnetic moment of $0.43\mu_B$ along a and C-type for the Sm spins with a moment of $0.72\mu_B$ along c.

For $LaTiO_3$ also G-type antiferromagnetism has been found [198, 199]. The reported magnetic moment ranges from $0.45\mu_B$ [3] to $0.57\mu_B$ [7] and is orientated along the a direction. From neutron scattering an isotropic magnetic coupling of $J = 15.5$ meV together with a spin gap of $\Delta = 3.3$ meV have been found. The latter observation is indeed puzzling. An isotropic spin-wave spectrum suggests a quenched orbital moment, because otherwise the symmetry will be broken by spin-orbit coupling and the spin-wave spectrum should anisotropic. Indeed it has been found in a later study by Haverkort *et al.* [8] that the orbital moment is almost quenched. In case of a quenched orbital moment one expects only a small spin gap. Keimer *et al.* [3] suggest fluctuations in the orbital sector to be responsible for the lowering of the moment (orbital liquid, see above and chapter 2). However, in a crystal-field scenario, the spin moment is reduced from $1\mu_B$ due to spin quantum fluctuations, crystal fields, and by spin-orbit coupling to $0.72\mu_B$ [7][1]. The inclusion of covalency will lower this value further, since one transfers spin to the neighboring oxygen [7].

As pointed out in the beginning it is believed that the steric effects induced by the different ionic radii of the rare-earth ions can already account for the observed changes from ferromagnetism ($YTiO_3$) to antiferromagnetism ($LaTiO_3$) [13].

All crystals measured in this study are high-quality single crystals. They have been grown

[1] Spin fluctuations reduce the moment to $0.85\mu_B$ according to the 3D Heisenberg model [14]. A further reduction of 85% is obtained by crystal fields and spin-orbit coupling [7, 9].

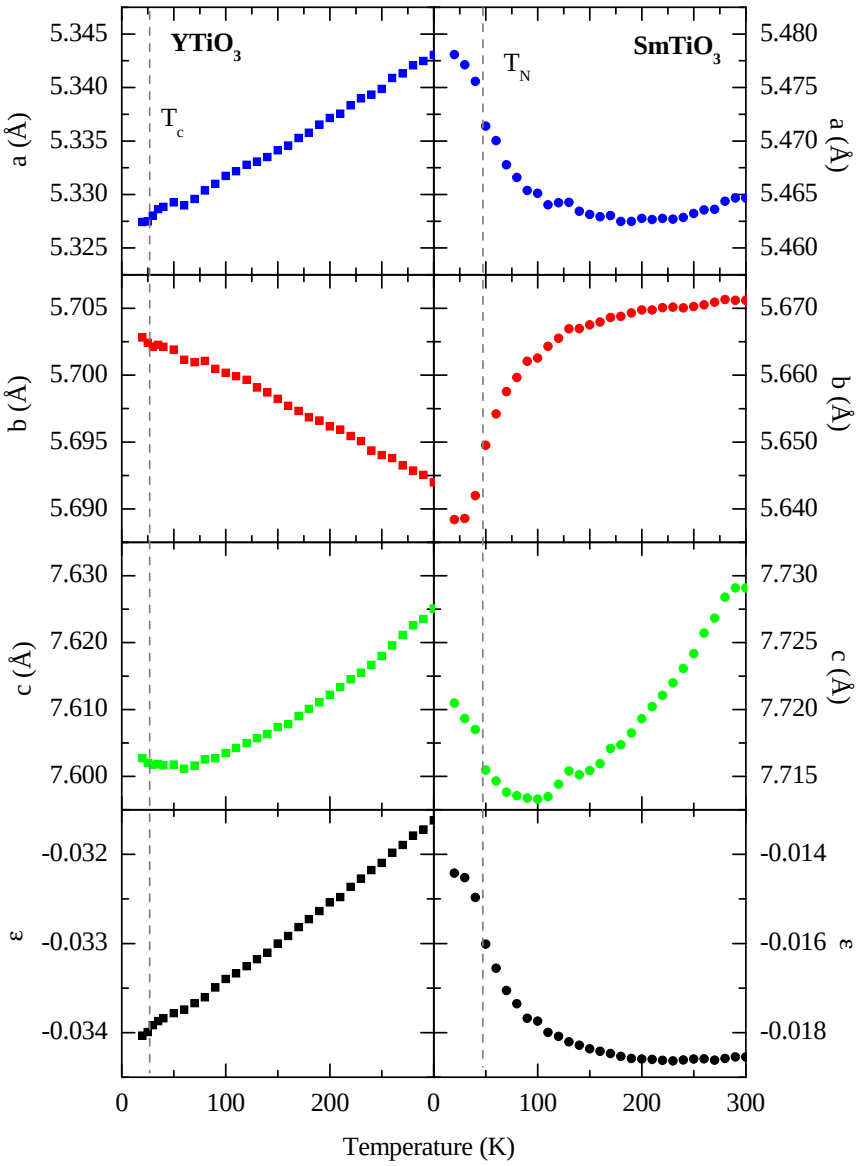

Figure 5.2: Thermal evolution of the lattice constants a, b, and c of $YTiO_3$ and $SmTiO_3$ as well as the orthorhombic distortion $\epsilon = (a-b)/(a+b)$. Reproduced from Ref. [193].

by M. Cwik ($LaTiO_3$) [7] and H. Roth ($LaTiO_3$, $YTiO_3$, $SmTiO_3$, $LaTiO_{3+\delta}$) [108, 193, 200]. The samples have been characterized by resistivity [200, 201], magnetic susceptibility [108, 194, 200], thermal expansion [200], EDX [108, 200], TGA [108, 200], and X-ray diffraction measurements [108, 193, 202] as well as by neutron scattering [193, 202]. Details on growth and characterization can be found in the references given. The most important facts are summarized in Tab. 5.1.

5.2.2 Titanium ion in an orthorhombic crystal field

The energy levels of the titanium ion in an orthorhombic crystal field are split due to the electric field of the ligands. In contrast to the tetragonal fields all d orbitals can be intermixed due to the $GdFeO_3$ distortion. The crystal-field levels are shown in Fig. 5.3. On the basis of the crystal structure the level splitting has been calculated by different methods by several research groups. The t_{2g} splitting is roughly 0.25 eV, while the $t_{2g} - e_g$ splitting is of the order of 2.0 eV. An overview is given in Tab. 5.2. The point-charge (pc) approximation assumes that every lattice site is occupied by a point-like charge (nominal valence). The crystal field is calculated by an Ewald summation [9, 26, 45]. If hybridization is switched on (cluster), the t_{2g}-e_g splitting is increased by almost a factor of two [9, 26, 45]. The intra-t_{2g} splitting stays almost unaffected. This is obvious because the hybridization to e_g levels is of σ type and thus stronger than hybridization to the t_{2g} levels which is of π type. Projections of LDA results on a local basis set yield almost the same energy levels [10, 11, 205]. An exception is the calculation of Solovyev [203, 204] which shows a significantly smaller splitting.

A large crystal-field splitting is not compatible with the orbital-liquid or fluctuating-orbital scenarios as proposed in Refs. [3, 4, 37, 43, 44]. In order to be the dominant contribution for lifting the orbital degeneracy the energy gain from an orbital flip has to be tremendous to overcome a crystal field of 250 meV. However, there is always a finite probability of such fluctuations. Pavarini *et al.* [10, 11] calculated the electron-occupation within a LDA+DMFT approach. Projecting on the crystal field basis they found that occupation of the lowest crystal-field orbital amounts 0.96 for $YTiO_3$ and 0.88 for $LaTiO_3$, i.e. the orbital ordering is almost complete in both compounds for a value of $U = 5$ eV (for $U = 0$ eV the occupation number is only 0.5 electrons). They concluded that orbital fluctuations are unlikely in $YTiO_3$ and quite weak in $LaTiO_3$. From the experimental side it has been proposed by Rückamp *et al.* [26] that the intra-t_{2g} excitations have been observed by means of infrared spectroscopy. The formally forbidden onsite-dd transitions are accessible by the simultaneous excitation of a symmetry-breaking phonon. In all three titanate compounds the peak has been found at approximately 300 meV. This energy is the sum of the orbital excitation and the medium energy of all symmetry-breaking phonons (40-80 meV). The energy of 220-260 meV is in good agrement to the calculations summarized in Tab. 5.2. Furthermore, it has been shown by Haverkort *et al.* that X-ray absorption spectra on $LaTiO_3$ could not be fitted accurately without any crystal-field splitting, but require a crystal-field splitting of the order of 0.15-0.30 eV.

We would like to mention that the above calculations have problems to get the magnetism

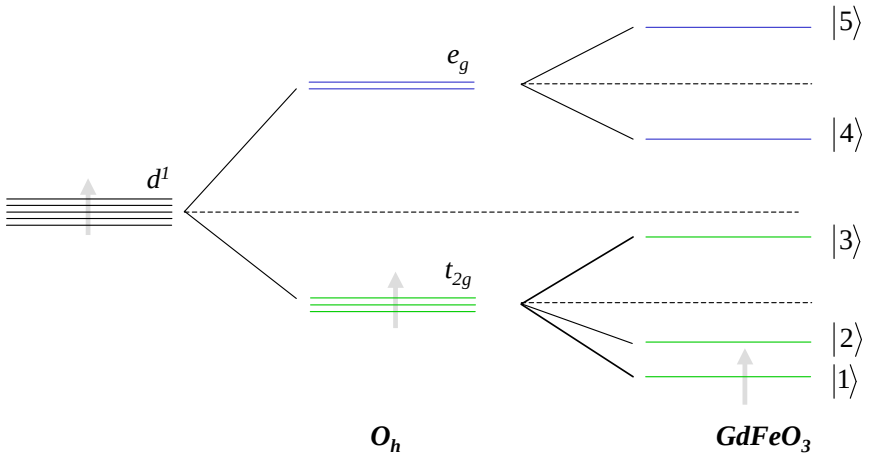

Figure 5.3: Crystal-field splitting of a d^1 electron in a $GdFeO_3$-distorted crystal.

Table 5.2: Onsite crystal-field splitting in eV of $RTiO_3$ calculated with different methods: point-charge model (pc), configuration-interaction cluster (cluster), downfolding from LDA(+U). We assume $E(|1\rangle) = 0$ eV.

Refs.	[9, 26, 45]	[9, 45]	[26]	[10, 11]	[203]	[204]	[205]
Method	pc	cluster		LDA(+U)			
			$YTiO_3$				
$E(\|2\rangle)$ (eV)	0.14	0.15	0.14	0.20	0.05	0.10	0.18
$E(\|3\rangle)$ (eV)	0.28	0.26	0.28	0.33	0.08	0.12	0.26
$E(\|4\rangle)$ (eV)	0.87	1.41	2.20				
$E(\|5\rangle)$ (eV)	1.00	1.54	2.50				
			$SmTiO_3$				
$E(\|2\rangle)$ (eV)	0.15		0.21				
$E(\|3\rangle)$ (eV)	0.26		0.31				
$E(\|4\rangle)$ (eV)	0.90		2.20				
$E(\|5\rangle)$ (eV)	1.00		2.50				
			$LaTiO_3$				
$E(\|2\rangle)$ (eV)	0.21	0.21	0.21	0.14	0.03		0.23
$E(\|3\rangle)$ (eV)	0.23	0.22	0.31	0.20	0.18		0.27
$E(\|4\rangle)$ (eV)	0.92	1.39	2.20				
$E(\|5\rangle)$ (eV)	0.98	1.45	2.40				

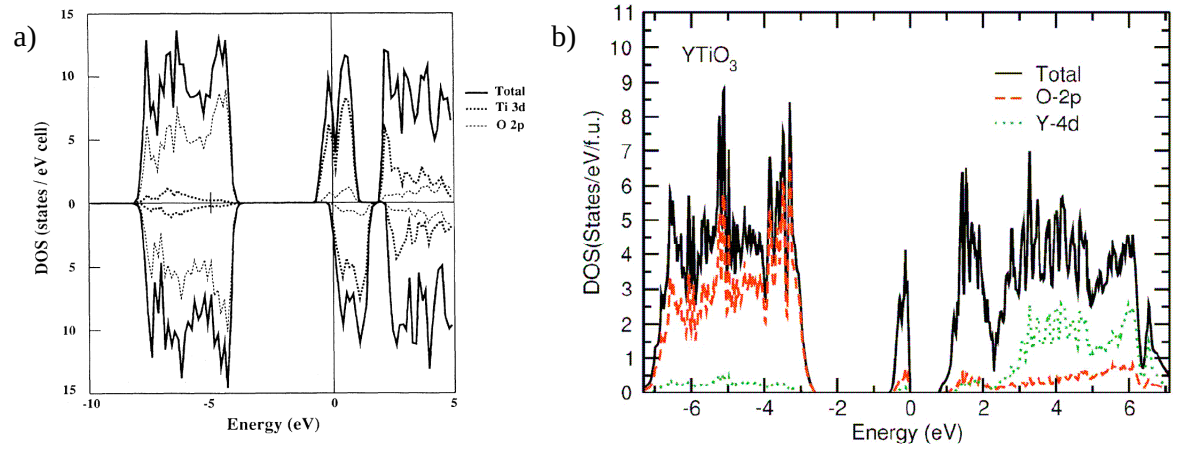

Figure 5.4: Density of states (DOS) of $YTiO_3$ obtained from a) LDA [206] and b) LDA+U [205]. As there is a finite DOS at the Fermi edge, LDA ends up in a metallic ground state. In contrast, LDA+U finds a finite gap.

quantitatively correct. Especially in $YTiO_3$ the coupling constants along c and ab are always calculated as anisotropic [11, 45]. However the magnetic ground state found in experiments has the lowest total energy in LDA+DMFT and LDA+U calculations [11, 203, 205].

Inspired by the work of Rückamp *et al.* we performed Raman measurements[2] on $LaTiO_3$ and $YTiO_3$ in order to get more insights into the low energy properties (see below). In crystals having inversion symmetry, Raman scattering is a direct probe of even-even excitations, e.g. local dd excitations will be directly allowed.

5.2.3 Electronic structure

Conventional band-structure theory fails in order to describe the insulating ground state of all titanates. Exemplarily we show results from LDA [206]. Again the inclusion of U in a LDA calculation drives the system into the insulating state [205] (see Fig. 5.4). It is consensus that all titanates are Mott-Hubbard insulators with relatively small gaps of the order of 0.2-1.0 eV ranging from $LaTiO_3$ to $YTiO_3$ [26, 106]. The titanates can be driven by doping of e.g. Sr or Ca into a metallic state, which has been nicely shown by means of optical spectroscopy [1, 106]. Lower and upper Hubbard bands in the undoped compounds and charge-transfer bands have been found in photoemission [124, 207, 208], X-ray absorption spectroscopy [8, 190, 191, 209] and optical spectroscopy [104–107]. We will give the details when discussing our data. In optical spectroscopy a multi-peak structure has been observed in unpolarized room temperature data in all titanate systems [104–107]. This multi-peak structure contains valuable information about the underlying Hubbard

[2] in collaboration with the MPI Stuttgart (C. Ulrich and B. Keimer).

bands of these compounds, i.e. the correlations present. It is our goal to give a meaningful assignment in terms of the underlying microscopic parameters like U, J_H, and Δ. In the literature the optical data of the titanates have only been analyzed in terms of a single-band Hubbard model. We will go one step further and try an assignment within a multi-orbital picture. All data presented in the literature have been measured unpolarized at room-temperature. We present a detailed study of the temperature and polarization dependence for $YTiO_3$ and $SmTiO_3$.[3] We track the evolution of the multi-peak structures with temperature. The evolution of spectral weight with temperature is a direct measure of the kinetic energy of a certain transition (see chapter 4). There are quantitative predictions for this evolution of the kinetic energy from an orbitally ordered arrangement [83].

We will start with the results from Raman scattering before entering the discussion of the ellipsometry data.

5.3 Orbital excitations in $LaTiO_3$ and $YTiO_3$: a Raman scattering study

We performed Raman scattering experiments on three different samples: pure and lightly doped $LaTiO_{3+\delta}$ and pure $YTiO_3$. Most of the results presented have been published in Ref. [64]. The ordering temperatures are $T_N = 146$ K, 120 K, and $T_c = 27$ K, respectively. The $LaTiO_{3+\delta}$ crystals were partly twinned, while the $YTiO_3$ crystal is single domain. The $YTiO_3$ (and also most likely the $LaTiO_3$) crystal was measured on a (100) or (010) surface within the *Pbnm* space group. We did not resolve the difference between a and b since we were interested in the difference between ab (approximate bond direction in the ab plane) and the c axis. The samples have been lapped and polished as described in the appendix. Raman spectra have been measured with a triple-monochromator Raman spectrometer (Dilor xy 800) at the MPI Stuttgart[4]. The setup is described in more detail in chapter 3. All spectra have been recorded with a laser power below 10 mW at the sample position in order to avoid heating. All spectra have been corrected for the spectrometer response using a calibrated white-light source (Ulbricht sphere). The experiments were performed in backscattering geometry parallel to the crystallographic b (or a) direction. The polarizations of incident and scattered photons are specified as (z, z), (x, z), etc., where $z||c$ (Ti-Ti bond direction) whereas x is along the next-nearest-neighbor Ti-Ti direction in the ab plane (i.e. the a or b direction). The z' and x' directions are rotated by 45° from z and x. In an additional experiment (which is not shown in Ref. [64]) we performed measurements on another piece of an $YTiO_3$ crystal of the same batch, in particular on a (001) and a (1-10) surface. We performed intensity measurements at a certain energy (~ 250 meV) as function of the rotation angle on this sample with respect to the laboratory coordinate system. This sample has also been measured with spectroscopic ellipsometry.

[3] Low temperature data is only presented for $SmTiO_3$ and $YTiO_3$ because our $LaTiO_3$ crystals are partly twinned.

[4] in collaboration with C. Ulrich and B. Keimer

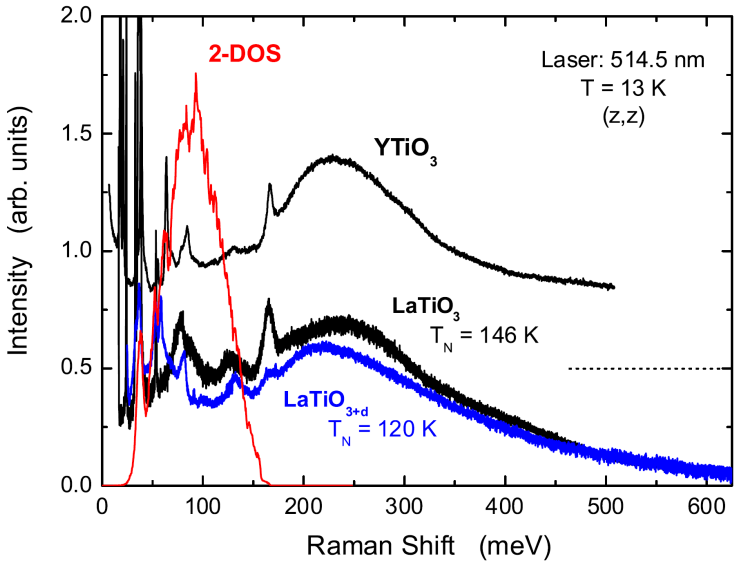

Figure 5.5: Raman spectra of $LaTiO_3$ and $YTiO_3$ measured at T = 13 K using the 514.5 nm laser line of an Ar^+/Kr^+ mixed-gas laser in (z, z) polarization. The red line shows the calculated two-phonon density of states [64].

Orbital excitations

Figure 5.5 shows the Raman spectra of $LaTiO_3$ and $YTiO_3$ over a wide energy range. Below 80 meV the spectra are dominated by one-phonon excitations (see for comparison Refs. [210, 211]). Up to approximately 170 meV some weak features can be observed which we attribute to two-phonon processes. The broad peak around 235 meV will be the main issue of this section.

We will briefly discuss whether the broad feature can be attributed to two-phonon or higher-order phonon processes. Therefore the two-phonon density of states (2-DOS) of $YTiO_3$ has been calculated [212]. It is shown together with the data in Fig. 5.5. It represents the convoluted one-phonon density of states within a shell model. The model parameters have been adapted by fitting to the observed one-phonon frequencies [212]. The 2-DOS extends to 170 meV. This is in accordance to rough estimates of one-phonon overtones from IR and Raman spectroscopy. The highest phonon in Raman is found at approximately 80 meV [211] and in infrared spectroscopy at about 70 meV [90]. Thus, one expects overtones up to about 160 meV. Therefore we can rule out two-phonon processes as a source of the 235 meV feature. Higher-order processes like three-phonon or four-phonon excitations will have less intensity than the two-phonon contributions and can therefore not account for the large intensity of the 235 meV peak. The sharp feature at 165 meV is attributed to a two-phonon excitation. A similar Raman mode is also observed in other transition-metal oxides [47, 111, 210], and has been attributed to a two-phonon excitation [59, 210].

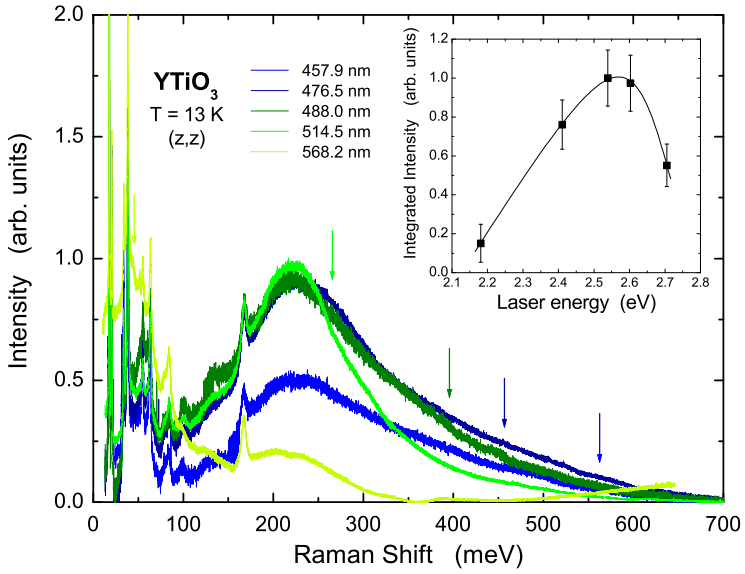

Figure 5.6: Raman spectrum of $YTiO_3$ measured at T = 13 K for different laser lines. A frequency-independent background has been subtracted from every profile. The arrows depict the position of the photoluminescence peak at 2.14 eV for the different laser lines. The inset shows the integrated intensity of the broad high-energy peak [64].

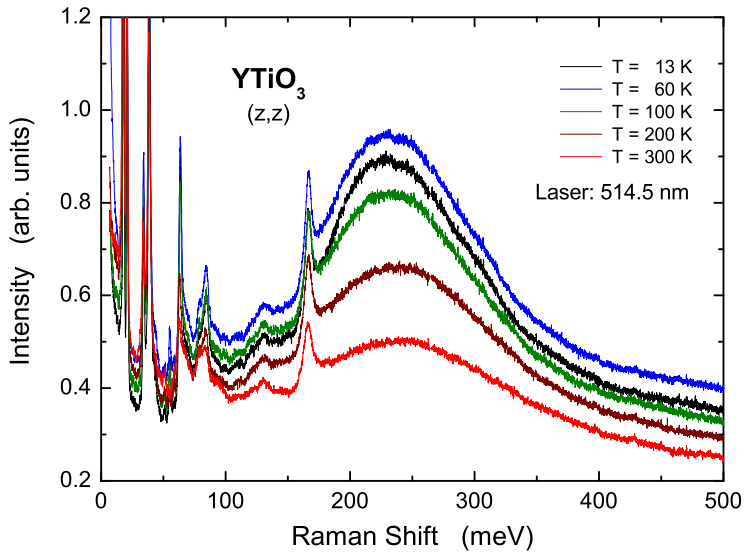

Figure 5.7: Temperature dependence of the Raman spectrum of $YTiO_3$ in (z, z) geometry, using the 514.5 nm laser line.

The Raman measurements were also performed with different excitation wavelengths ranging from 457.9 nm up to 568.2 nm. The spectra are shown in Fig. 5.6. Since the peak position is unaffected by the different excitation wavelengths, photoluminescence can be ruled out as the origin of the peak at 235 meV. Raman scattering measures the energetic difference between incident wavelength and scattered wavelength (Raman shift). A photoluminescence feature will appear shifted when changing the excitation energy. A weak photoluminescence peak at 2.14 eV with a width of 75 meV is indeed observed (indicated by arrows). It can explain the increased weight around 50 meV in the spectrum measured with 568.2 nm ($\sim$ 2.2 eV). As clearly shown the overall spectral shape of the excitation is almost unaffected by the additional photoluminescence feature. In the inset of Fig. 5.6 the integrated intensity of the 235 meV peak has been plotted. The mode is resonantly enhanced at 2.54 eV. In addition a strong temperature dependence is observed as shown in Fig. 5.7.

The effect of (oxygen) defects has also be considered as a possible source of the peak at 235 meV. We measured another sample of $LaTiO_{3+\delta}$ having an oxygen non-stoichiometry of the order of $\delta = 0.02$ with a significantly lower ordering temperature of $T_N = 120$ K. As displayed in Fig. 5.5 the feature at 235 meV stays unaffected of the different oxygen content, i.e. oxygen defects can also be ruled out as a possible explanation for this peak.

Magnons can also be observed in Raman scattering experiments and this peak shows indeed similarities to the two-magnon peaks as observed in the cuprates (see Ref. [112] as an overview). However, in the titanates the magnetic coupling constant J is tiny ($J = 3 - 15$ meV) when comparing to the cuprates ($J = 100 - 150$ meV). A two-magnon mode is expected at about $5\,J$ in a three-dimensional $S = 1/2$ system and has indeed been observed around 80 meV in $LaTiO_3$ [211]. Thus, also a magnetic origin can be excluded for the 235 meV feature.

In Fig. 5.8 the polarization dependence of the 235 meV peak is displayed. The mode strongly depends on the configuration of polarizer and analyzer, i.e. the mode is reduced when turning the crystal from (z, z) to (x, x). The Raman intensities for crossed and parallel polarizations can be expressed by the entries of the Raman tensors of a cubic point group (O_h), i.e. A_{1g}, E_g and T_{2g}. The relations for this particular geometry read:

$$\begin{aligned} I_{parallel} &= (\frac{2}{3} - a_\theta - b_\theta)E_g + (a_\theta + b_\theta)T_{2g} + \frac{1}{3}A_{1g}, \\ I_{crossed} &= b_\theta E_g + (\frac{1}{2} - b_\theta)T_{2g}, \end{aligned} \tag{5.1}$$

where θ is the angle between the incident electric-field vector and the c (z) axis, $\theta = 90°$ corresponds to the a or b (x) axis, and $a_\theta = \frac{1}{2}\sin^2\theta$, $b_\theta = \frac{3}{8}\sin^2 2\theta$. This relation can describe the observed polarization dependence.

We have also measured the maximum intensity of the 235 meV feature and of the two-phonon peak at 165 meV on a different piece of sample. The data is displayed in Figs. 5.9 and 5.10. If the sample is rotated from one Ti-Ti bond to another Ti-Ti bond around c and around b^* (one of the Ti-Ti bond directions in the ab plane), the uncorrected data (see below) show roughly cubic behavior. This can be seen by eye since the intensity for

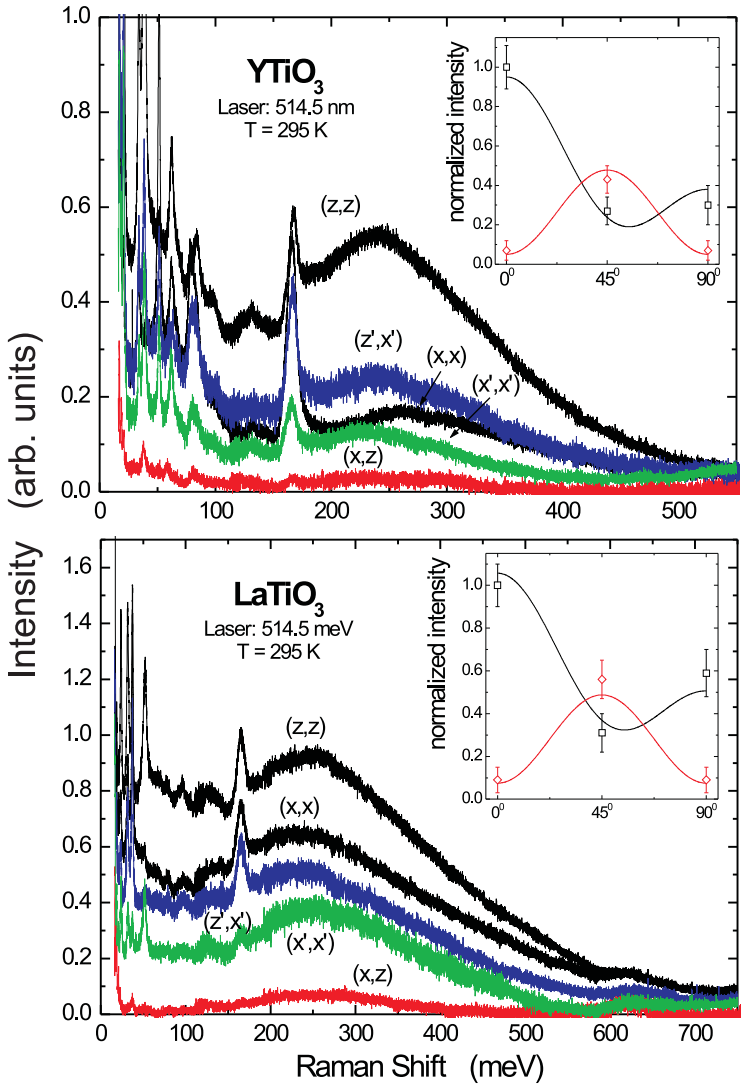

Figure 5.8: Polarization dependence of the Raman spectra of $YTiO_3$ and $LaTiO_3$ at room temperature. The intensity is symmetric with respect to $(\alpha, \beta) \rightarrow (\beta, \alpha)$. A frequency-independent background has been subtracted. Insets: relative scattering intensities for the parallel ($\square$) and crossed ($\Diamond$) polarizations as a function of the angle θ (see Eq. 5.1). The experimental intensities are scaled with respect to the value at $\theta = 0°$. Solid and dashed lines are obtained from Eq. 5.1, with relative intensities $E_g : A_{1g} : T_{2g} \approx 1 : 0.3 : 0.1$ $(1 : 0.5 : 0.1)$ in $YTiO_3$ ($LaTiO_3$). Note, that $\theta = 0°$ corresponds to a Ti-Ti bond direction while $\theta = 90°$ does not (an isotropy is not expected).

all bond directions is approximately the same at $\theta = 90°$ and $\theta = 180°$. Note, that we assume that the width of the excitations does not change under rotating the sample and that the height is a measure of the peak area. One can observe especially in Fig. 5.9 that there are clear deviations from the cubic symmetry (compare the blue curve and the red curve). These deviations reflect the rotated and tilted octahedra.

Several scenarios for the peak at 235 meV have clearly been ruled out above. What is now the origin of this peak? We attribute this feature to an orbital excitation. A corresponding feature has been observed by Rückamp *et al.* in IR spectroscopy, but it is shifted by the energy of a symmetry-breaking phonon, see Fig. 5.11. From the maximum-maximum distance between infrared and Raman spectra one can read a difference of 65 meV. This is a very reasonable value for an average phonon frequency. We conclude that the symmetry of the excitation has to be even, i.e. ground state and excited states have the same parity. From the resonating behavior of the excitation at 2.5 eV we can conclude that the intermediate state for the Raman process lies inside the upper Hubbard band (see Ref. [107] and our data below). This means that the excitation process has to involve two Ti sites. The electron on one Ti site is transferred to another Ti site which yields a double occupancy (i.e. an intermediate state in the upper Hubbard band). One of the two electrons of the double occupancy hops back to the initial site, resulting in either one or two flipped orbitals.

The question is now how large is the dispersion of these excitations or in other words: can this excitation propagate? For the further interpretation we will discuss two scenarios (i) a propagating excitation (orbiton, orbital wave) and (ii) a local crystal-field excitation.

(i) a local crystal-field excitation - The point-charge, cluster, and LDA($+U$) calculations presented above suggest a crystal-field splitting of 250 meV on the titanium site. This is in excellent agreement with the observed 235 meV and also compatible with the data from IR spectroscopy [26]. In order to address the polarization dependence of such a transition, we will discuss the probability of the two-site process mentioned above for a final state with a single orbital flipped. A double flip would be energetically too high in energy for explaining our feature at 235 meV and will not be considered. Note, that in a recent Raman study of Sugai *et al.* [57] a second peak has been found in $YTiO_3$ at about 0.5 eV for crossed polarizations. This feature is not present in our data. We will focus on $YTiO_3$ since this crystal is single domain. We do not know the degree of twinning in the $LaTiO_3$ system[5]. Consider two Ti sites i and j, each occupied with one electron. For resonant Raman scattering there are now three processes which yield a single orbital excitation on site i from the ground state to the 1st and 2nd crystal field levels [214] (see Fig. 5.12): $c^\dagger_{i,2}c_{j,2}c^\dagger_{j,2}c_{i,1}$, $c^\dagger_{i,2}c_{j,3}c^\dagger_{j,3}c_{i,1}$, and $c^\dagger_{j,1}c_{i,1}c^\dagger_{i,2}c_{j,1}$, where $c^\dagger_{j,m}$ ($c_{j,m}$) creates (annihilates) an electron on site j in the orbital m. As one can see, the first two contributions yield the final state $c^\dagger_{i,2}c_{i,1}|0\rangle$ while the latter one results in $c_{i,1}c^\dagger_{i,2}|0\rangle$. One has to commute once which gives the second process a minus sign due to the commutator relations of fermions. The processes are sketched in Fig. 5.12 for excitations on site i (site j has to be calculated in an analogous fashion). The intensity for the transition into the first crystal-field level (1st CF) can be

[5]Assume the crystal would be fully twinned, then the Raman spectra will be perfectly cubic.

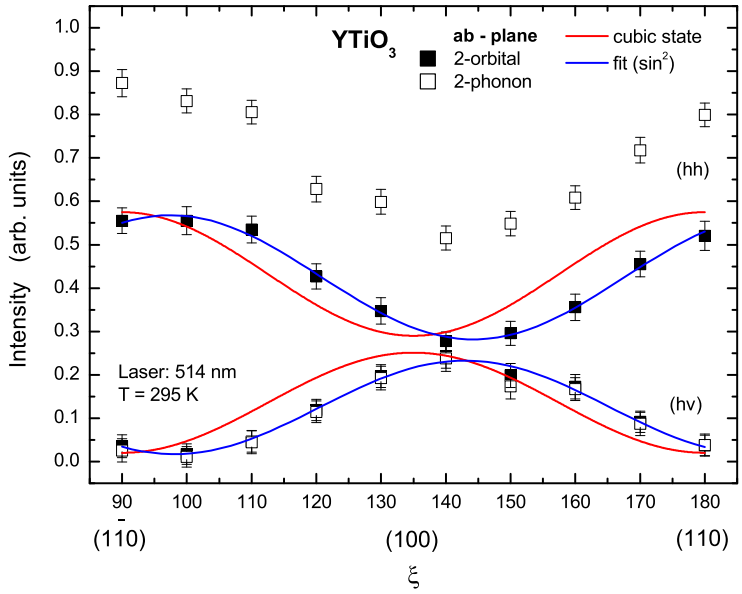

Figure 5.9: Polarization dependence of the Raman spectra of $YTiO_3$ at room temperature measured on the *ab* surface (hh - parallel polarization, hv - crossed polarization). The intensity at 235 meV (2-orbital) and at 165 meV (2-phonon) is plotted as a function of the sample rotation angle ξ.

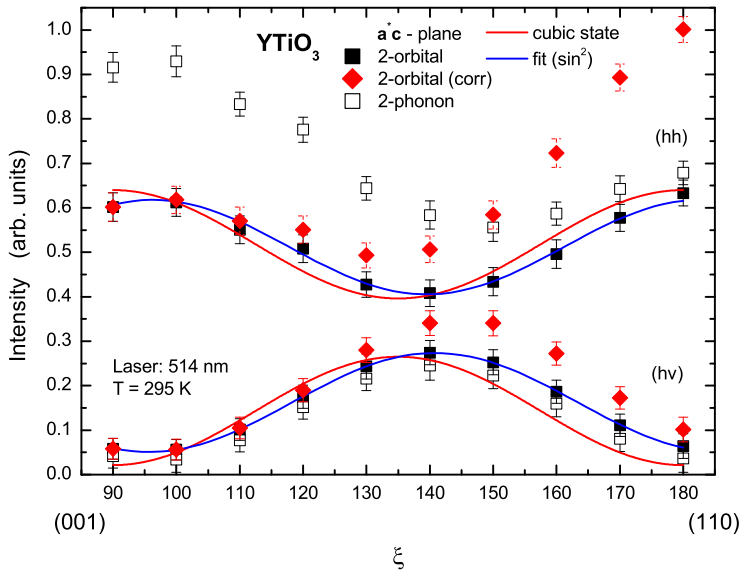

Figure 5.10: Polarization dependencies of the Raman spectra of $YTiO_3$ at room temperature measured on the a^*c surface (hh - parallel polarization, hv - crossed polarization). The intensity at 235 meV (2-orbital) and at 165 meV (2-phonon) is plotted as a function of the sample rotation angle ξ.

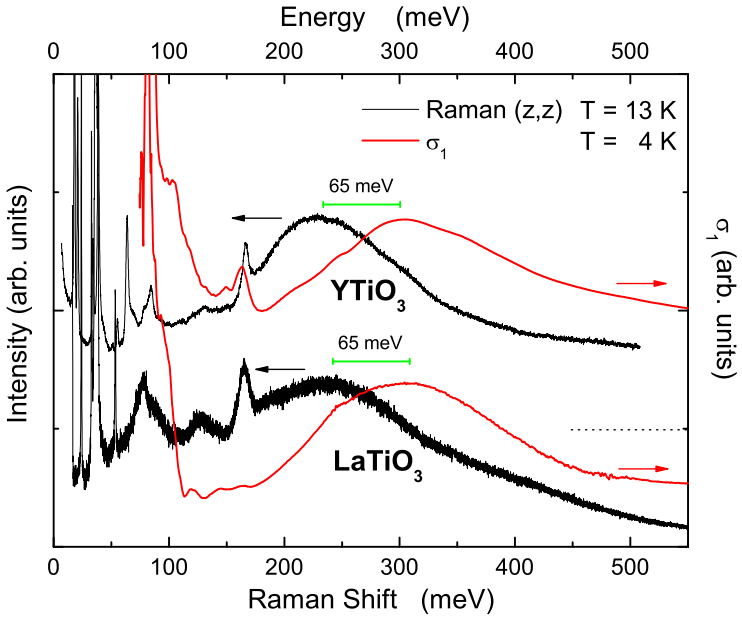

Figure 5.11: Comparison of Raman spectra of $YTiO_3$ and $LaTiO_3$ at low temperatures [64] with optical conductivity spectra [26]. A power-law background has been subtracted from σ_1 and the spectra have been rescaled and shifted for clarity.

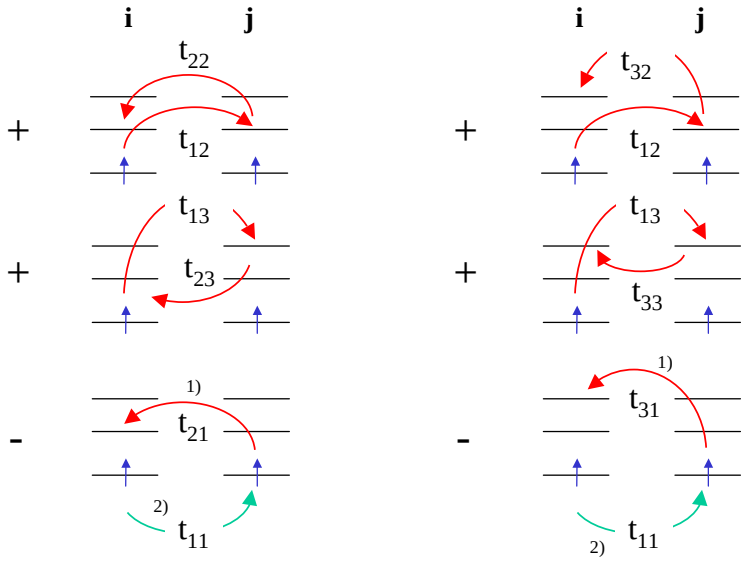

Figure 5.12: Sketch of the different hopping processes contributing to a single orbital excitation on site i in resonant Raman scattering. Note, that $t^{ij}_{nm} = t^{ji}_{mn}$.

Table 5.3: Matrix elements for resonant Raman scattering.

t matrices from Refs.	[45]		[11]		[204]		[213]		[54]	
	ab	c	ab	c	ab	c	ab	c	ab	c
1st CF ($\times 10^{-4}$ eV^2)	5.38	0.27	1.02	0.07	3.16	0.96	1.36	0.37	-	-
2nd CF ($\times 10^{-4}$ eV^2)	5.92	0.17	4.23	7.08	2.32	0.42	2.05	0.10	-	-
$I(ab) : I(c)$	25:1		0.6:1		4:1		6:1		∞:1	

calculated by $|A_{ij}|^2 + |A_{ji}|^2$ with $A_{ij} = t_{12}t_{22} + t_{13}t_{23} - t_{21}t_{11}$ (A_{ji} analogous). We assume that the two crystal-field levels are degenerate, or that their splitting cannot be resolved. Thus we will only discuss the total intensity of both excitations. We obtained the results presented in Tab. 5.3: the matrix elements for the ab and c directions are anisotropic and depend strongly on the underlying hopping matrices. From the data of Pavarini *et al.* [11] we obtain a ratio $I(ab)/I(c) = 0.6$, while we found $I(ab)/I(c) = 25$ using the hopping matrices of Schmitz *et al.* [45]. Note, that very recently an erratum of the data of Schmitz *et al.* has been submitted [213] in which the hopping matrices have been revised. With the revised matrices[6] the ratio reduces to $I(ab)/I(c) = 6$. This anisotropy (especially in the old data of Schmitz *et al.* [45]) seems to be incompatible with the observed isotropy.

However, recently we also measured the optical conductivity of $YTiO_3$ (see below) and found a sizable anisotropy between the ab and c direction (the in-plane and out-of plane Ti-Ti bond). In other words, the absorption coefficient is different in ab and c which leads to a different penetration depth for the light wave. We neglect the anisotropy between a and b, since it is "only" 1.2. For the Raman experiment the difference in the penetration depth yields a different scattering volume along ab and c. One has to correct for this difference since the Raman cross section (see chapter 3) is proportional to the scattering volume [115]. We found that the ratio of the penetration depth at 514 nm is approximately $d_c/d_{ab}(2.41\text{eV}) \approx 1.55$, i.e. the data along ab has to be multiplied by this factor. The modified data is also displayed in Fig. 5.10; figure 5.9 has not been modified because the values at 90° and 180° will change by the same amount, since both directions contain equal contributions of the a and b directions. The isotropy between the Ti-Ti bond in c direction and between the bond in ab is lost. Therefore it is not possible anymore to regard the data as cubic, in contrast to the statement of our earlier publication [64]. While the uncorrected spectra yield a ratio between ab and c of 1:1, the correction induces an anisotropy of 1.55:1. None of the calculated matrix elements can explain the observed ratio in a *quantitative* manner. However, with the corrected result of Schmitz *et al.* [213] the discrepancy between theory and experiment has become (much) smaller. Originally, these seemed to be a factor of 25, large enough to rule out the crystal-field scenario. Now the this discrepancy is only a factor of 6, i.e. the crystal-field scenario is a plausible option again.

[6] We thank for the kind provision before publication.

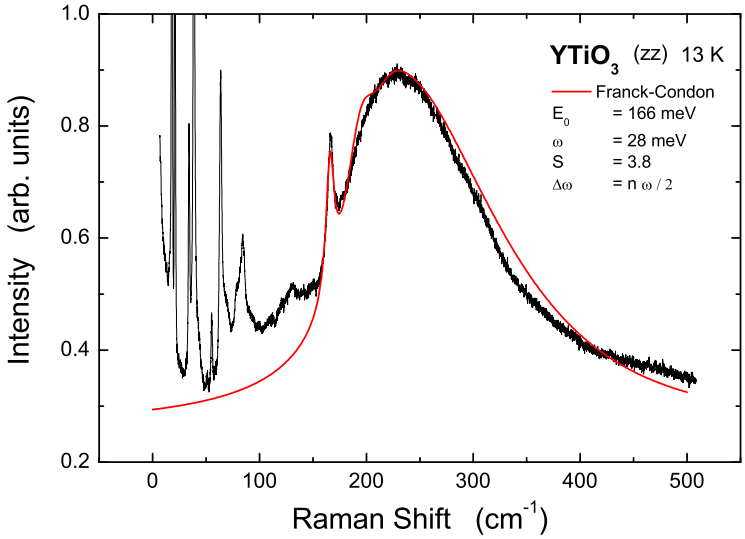

Figure 5.13: Franck-Condon line shape in comparison to the measured Raman spectrum of $YTiO_3$.

Finally we would like to suggest that the electron-phonon coupling has to be considered explicitly in order to understand the observed polarization dependence. The admixture of phonons to the initial and final states will change the transition probabilities. The line shape and temperature dependence of the Raman response in $YTiO_3$ are typical for a vibronic transition [84]. We have plotted a Franck-Condon line shape [84] together with the measured data at low temperatures and got a reasonable agreement (see Fig. 5.13). Due to phonon-phonon interaction the phonon modes in $YTiO_3$ lose intensity with increasing temperature. This can explain the intensity loss of the orbital excitation observed in $YTiO_3$. As an aside the two-phonon mode at 165 meV may be reinterpreted as the zero-phonon line of the orbital excitation, i.e. the bare electronic excitation.

(ii) A propagating excitation (orbiton) - For a very low splitting of the t_{2g} manifold (Jahn-Teller effect, 27 meV) Ishihara proposed the existence of orbital waves in $YTiO_3$ [54]. He calculated the Raman response for a spin-orbital Hamiltonian with isotropic hopping amplitudes also including a small contribution from the Jahn-Teller effect. For a four-sublattice pattern of the form $(xz \pm xy)/\sqrt{2}$, $(yz \pm xy)/\sqrt{2}$ a single orbital flip is predicted for the *ab* direction, but a two-orbital flip for the *c* direction. This selection rule is in clear contradiction to our findings, where no change of the peak position has been observed upon a change of the polarization (see Fig. 5.8). However this approach has been used to describe Raman data similar to ours [57], claiming a good agreement to the above theory. The selection rule proposed by Ishihara has been ignored. The theory of Ishihara disregards the steric crystal fields, i.e. the $GdFeO_3$ distortions which lead to a strong increase of the t_{2g} level splitting. The Jahn-Teller effect has been shown to play a minor role in the titanates [11].

Another scenario for a dispersing excitation is given in the orbital-liquid model. It

naturally predicts an isotropic Raman response, i.e. a ratio $I(ab) : I(c) = 1 : 1$ can be understood, because no orbital direction is favored. As shown above the Raman data should be corrected in order to take the anisotropic scattering volumes into account before entering the discussion. Note, that the conductivity data has not been known when the Raman study [64] has been carried out. It has been implicitly assumed that the response is isotropic. Later, it turned out that this is not the case. Thus the orbital liquid picture predicts an isotropic behavior (1 : 1), the crystal field scenario varies between 0.6 : 1 and 6 : 1, and the experiment gives 1.5:1.

The observed energy of 235 meV is in reasonable agreement with the orbital-liquid model. It predicts a two-orbiton excitation with an energy of 180 meV [43, 44, 64]. The analogy to the two-magnon scattering has been pointed out. For a quenched orbital moment the spin has to be conserved in Raman scattering with linearly polarized light. This is the reason why only two-magnon scattering is observed in many transition-metal compounds. For the spin-orbital Hamiltonian one can only flip two orbitals when the excitation process involves two sites, i.e. one has pseudo-spin conservation. To see this we start from an orbital dimer with an antiferro-orbital arrangement: one electron resides in the d_{xz} orbital on site 1 and another one in the d_{yz} orbital on site 2. Since t_{2g} electrons in cubic symmetry can only hop between t_{2g} orbitals of the same type, one can only induce a two-orbital flip with an excitation process involving two sites. In IR absorption a single orbital flip (plus phonon) should be allowed.

To conclude, we observed a peak at 235 meV in $LaTiO_3$ and $YTiO_3$. We see strong evidence that this peak is an orbital excitation and that the excitation process involves two Ti sites. In the light of the most recent experimental and theoretical results, i.e. the "not so cubic" data and "not so anisotropic" results within the crystal-field scenario, it is not possible to unravel the nature of the ground state, orbitally ordered or orbitally fluctuating, on the basis of this data alone.

5.4 Electronic structure of $YTiO_3$ probed by ellipsometry

In this section we study optical excitations from the lower to the upper Hubbard band in $YTiO_3$. Peaks in the optical conductivity at 2.55 and 4.15 eV reflect the existence of multiple upper Hubbard bands in a multi-orbital system. A temperature-dependent peak at 1.95 eV is interpreted in terms of a Hubbard exciton, i.e. a charge-neutral (quasi-)bound state of a hole in the lower Hubbard band and a double occupancy in the upper one. We suggest that the binding to such a Hubbard exciton may arise both due to Coulomb attraction between nearest-neighbor sites and due to a lowering of the kinetic energy in an orbitally-ordered state.

In general, the competition between Coulomb and kinetic energy governs the formation of bound states. In BCS theory, Cooper pairs are formed due to a reduction of Coulomb energy, which overcompensates an *increase* in kinetic energy. The Coulomb energy also drives the binding of particles and holes to excitons in conventional semiconductors. However, the physics may be very different in strongly correlated systems. One interesting scenario

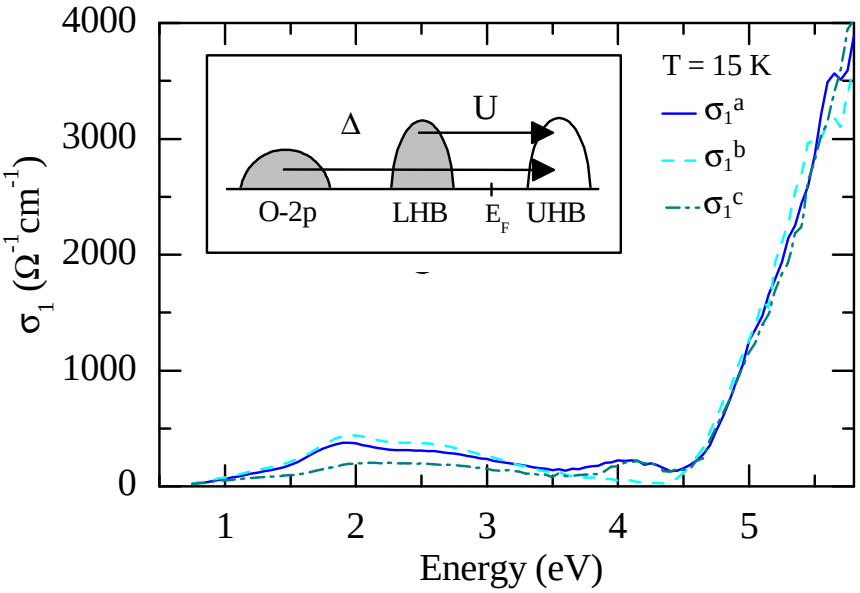

Figure 5.14: Optical conductivity of $YTiO_3$ at 15 K. *Inset:* sketch of the optical excitations from the lower Hubbard band (LHB) and the oxygen $2p$ band into the upper Hubbard band (UHB) in case of a single, half-filled orbital at the transition-metal site.

for high-T_c superconductivity in the cuprates assumes that the formation of Cooper pairs is based on a reduction of the *kinetic* energy [215–217]. For the case of a two-dimensional (2D) antiferromagnetic Hubbard system relevant for the cuprates, Wrobel and Eder [77] pointed out that the Coulomb energy may neither be crucial for excitons. Instead, the formation of a Hubbard exciton may be dominated by the kinetic energy and interactions with the antiferromagnetic spin background, bearing much resemblance to the binding of holes to Cooper pairs [77].

We report on the observation of an excitonic resonance in the optical conductivity $\sigma(\omega)$ of the undoped, *orbitally* ordered Mott-Hubbard insulator $YTiO_3$. Due to the orbital multiplicity in this d^1 spin $S = 1/2$ compound, the upper Hubbard band (UHB) consists of a series of multiplets. A peak at 2.55 eV is identified with the lowest multiplet (i.e., the 'lowest UHB'), whereas a strongly temperature-dependent peak at 1.95 eV is attributed to an excitonic resonance. We point out that the exciton formation in *orbitally*-ordered compounds may be similar to the case of a 2D antiferromagnet discussed by Wrobel and Eder [77]. Our result provides the experimental basis to disentangle the role of Coulomb and kinetic energy.

5.4.1 Experimental

A single crystal of $YTiO_3$ was grown using the floating-zone technique. The crystal quality and stoichiometry were checked by X-ray diffraction, EDX, and polarization microscopy. From SQUID measurements we find that the sample becomes ferromagnetic below $T_c \approx 27$

K. Details of the growth and the characterization can be found in the Diploma thesis of H. Roth [108]. Four-sublattice orbital order has been reported up to room temperature [5, 190]. However, no anomaly in the evolution of the lattice constants up to 700 K has been observed [202] pointing towards an orbital-ordering transition, i.e. $YTiO_3$ may be orbitally ordered up to the melting temperature.

Generalized ellipsometric data [218] was obtained using a rotating-analyzer ellipsometer (Woollam VASE) with an angle of incidence of 70°. Immediately after polishing, the sample was kept in an UHV cryostat with a pressure $< 10^{-9}$ mbar. Window effects have been corrected using a standard Si wafer.

In orthorhombic $YTiO_3$, only the diagonal elements σ^a, σ^b and σ^c of the complex optical conductivity tensor $\sigma(\omega) = \sigma_1 + i\sigma_2$ are finite. We have determined $\sigma(\omega)$ from measurements with 4 different orientations, namely with the p-polarized light parallel to the crystallographic a and b (a^* and c) axes on the ab (a^*c) surface, where $a^* = (110)$ within the $Pbnm$ space group. A non-absorbing cover layer ($d \leq 2$ nm) has been assumed in order to achieve a consistent description of the data of the two distinct surfaces (see chapter 3 for more details). In Fig. 5.14 we plot an overview spectrum of σ_1^a, σ_1^b, and σ_1^c from 0.75 to 5.8 eV at 15 K.

5.4.2 Results and Discussion

Undoped $YTiO_3$ is a Mott-Hubbard insulator. In the ground state there is a single electron in the $3d$ shell at each Ti site. It is well accepted that the absorption above the gap corresponds to excitations from the LHB to the UHB, i.e. to the creation of an empty and a doubly occupied site, $|d^1d^1\rangle \rightarrow |d^0d^2\rangle$. The strong increase of $\sigma_1(\omega)$ above ≈ 4.5 eV reflects the onset of charge-transfer excitations from the O_{2p} band to the UHB ($|d^1p^6\rangle \rightarrow |d^2p^5\rangle$). The charge-transfer excitations are of first order in the Ti-O hopping t_{pd}, whereas the Mott-Hubbard excitations are of second order in t_{pd}, which explains the difference in spectral weight.

Photoemission spectroscopy [124, 207, 208] yields a charge-transfer energy $\Delta \cong 6$ eV and an on-site Coulomb interaction $U \gtrsim 5$ eV. Here, U denotes the Coulomb repulsion if both electrons occupy the *same* orbital[7] (Kanamori scheme). In a single-band Hubbard model, the splitting between LHB and UHB is given by U (cf. inset of Fig. 5.14). However, for a quantitative description of $\sigma(\omega)$ one has to take all five $3d$ orbitals into account [219].

Figure 5.15 focuses on the inter-Hubbard-band excitations below 4.5 eV. Three peaks are observed at 1.95 (A), 2.55 (B), and 4.15 eV (C). First we address the peak assignment, the temperature dependence will be discussed below. The excited $|d^0d^2\rangle$ states can be distinguished according to the d^2 sector, because d^0 is an empty shell. The d^2 sector is

[7] For a comparison of different results one needs to distinguish between $U \equiv U^{Kanamori} = F^0 + \frac{4}{49}F^2 + \frac{36}{441}F^4$ (both electrons occupy the *same* orbital) and $U_{av} = F^0 - \frac{14}{441}(F^2 + F^4)$ (averaged over all multiplets) with the Slater integrals F^0, F^2, and F^4 (see chapter 2 for further details). The value of $U_{av} \cong 4$ eV reported in Ref. [124] corresponds to $U^{Kanamori} \approx 5.3$ eV. However, this value is based on a TiO_6 configuration-interaction cluster model including covalency. Due to screening effects by O_{2p} orbitals, the effective value of U is somewhat smaller, in good agreement with U=4.5 eV chosen in Fig. 5.18.

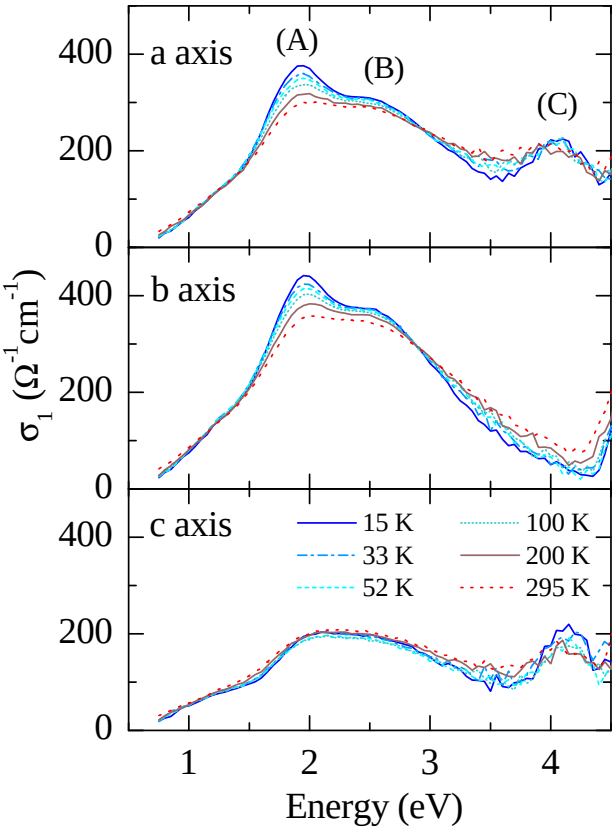

Figure 5.15: Optical conductivity of $YTiO_3$.

split into a series of multiplets by the electron-electron interaction, the crystal field, and the hybridization with the ligands [20]. We start from cubic symmetry, in which case the crystal field and the hybridization give rise to a splitting of the $3d$ orbitals into a triply degenerate t_{2g} level and a doubly degenerate e_g level at higher energy. The splitting is denoted by 10 Dq, which roughly can be estimated as 2 ± 0.5 eV [26, 45, 190] (see also Tab. 5.2). The electron-electron interaction within the $3d$ shell can be parameterized by the three Slater integrals F^0, F^2 and F^4. Here, $F^4/F^2 \approx 5/8$ is determined by an atomic Hartree-Fock (HF) study and F^2=6.75 eV is characteristic for Ti^{2+} ions in a crystal [20]. The only parameter that can be adapted is F^0. It drastically deviates from the HF value due to screening effects.

For $F^0 = 3.60$ eV (or $U \approx 4.5$ eV)[7] (see footnote on p. 145) the excitation energies are given in Fig. 5.18, focusing on the four multiplets lowest in energy: the triplet $^3T_1$, the singlets $^1T_2$ and ^1E, and the triplet $^3T_2$. For an intuitive picture we consider the crystal-field limit ($10\,\mathrm{Dq} \gg U$), in which there is one electron in the t_{2g} level and one in the e_g level in the $^3T_2$ state, whereas both electrons occupy the t_{2g} level in the three other states. It is common to consider the simplified Kanamori scheme [219] with the Hund on-site exchange coupling $J_H \equiv J_H^{Kanamori} = \frac{2.5}{49}F^2 + \frac{22.5}{441}F^4$. For Ti^{2+} one finds $J_H = 0.6 \pm 0.1$ eV. For

$U \equiv U^{Kanamori} \cong 4-5\,\mathrm{eV}$, the Kanamori scheme predicts the lowest excitation into the $^3T_1$ triplet at $U - 3J_H \approx 2-3\,\mathrm{eV}$, separated from the singlets by $2J_H \approx 1.2\,\mathrm{eV}$ (reflecting Hund's rule) and from the $^3T_2$ state by $10\,\mathrm{Dq} \approx 2\,\mathrm{eV}$, in qualitative agreement with the result of the rigorous calculation shown in Fig. 5.18.

The inclusion of the full crystal structure (i.e. deviations from cubic symmetry) as well as covalency effects do not change our considerations above. In Fig. 5.16 we show the results of a configuration interaction calculation performed on a TiO_6 cluster[8]. In order to obtain the Mott-Hubbard transition energies one has to calculate the d^0, d^1, and d^2 configurations. The energy of the Mott-Hubbard transitions reads $E_{MH} = E(d^2) + E(d^0) - 2E(d^1)$. We adapted the Slater integrals and the ionic radii of the different configurations according to the atomic Hartree-Fock values [18]. The energy-level diagram is shown as function of $U_{dd}\,(= U_{av})$. The red horizonal lines indicate our peaks positions. The dotted line represents the region at 3.5 eV where weight is clearly gained with increasing temperature. We assign this region to transitions into low spin states (This line should meet the S=0 excitations). It is difficult to get all lines simultaneously intersecting at one value of U_{dd}. Nevertheless a reasonable agreement is obtained for 4-4.5 eV, which again is a reasonable value. For the calculation we have strictly used the Harrison rules [169] for the spatial dependence of the hybridization. The results for the d^1 sector have to reproduce a t_{2g}-level splitting of 0.25 eV (see above) and a charge-transfer transition at 5.5 eV. Our calculations yield 10% reduced values for the t_{2g}-e_g splitting (see Tab. 5.2). Regarding the d^2 sector the *average* multiplet splitting between the $^3T_1$ (lowest three $S = 1$ levels) and $^1E/^1T_2$ (lowest five $S = 0$ levels, one higher level) as well as between the $^3T_1$ and $^3T_2$ (higher $S = 1$ levels) states are approximately 1 eV and 1.7 eV and are thus comparable to the multiplet splittings discussed within the cubic scenario. We can therefore restrict ourselves to the cubic scenario for the following discussion.

Figures 5.18 clearly shows that the $^3T_1$ state is more about 1.0-1.2 eV below the next multiplet for any reasonable choice of 10 Dq. Thus the small splitting of 0.6 eV between peaks A and B can not be identified with the difference between the $^3T_1$ state and any other multiplet. We conclude that both peak A and B are related to excitations into the $^3T_1$ state. Peak C can be attributed to the $^3T_2$ state, since only excitations into triplet states are allowed from a fully polarized ferromagnetic ground state within an electric dipole approximation. Excitations to the singlet states $^1T_2$ and ^1E require a spin flip and thus are suppressed, at least at low temperatures. This assignment is supported by the observed temperature dependence. We display in Fig. 5.17 the integrated spectral weight (effective carrier concentration - N_{eff}, see chapter 4 for details) of certain regions of the spectrum. Note that the changes are very small, but we think that the values are reliable with an accuracy of 0.001. Between 1.6-2.6 eV one can clearly observe an anomaly in the a and b direction approximately (!) at T_c, i.e. an additional increase of weight with decreasing temperature. Additionally, one finds an anomalous decrease of weight with decreasing temperature again in a and b in the region between 2.6-3.9 eV. Furthermore, most clearly observed in c, there is again an increase at approximately T_c between 3.9-4.3 eV. Starting

[8]We thank A. Tanaka for the kind provision of his configuration-interaction software.

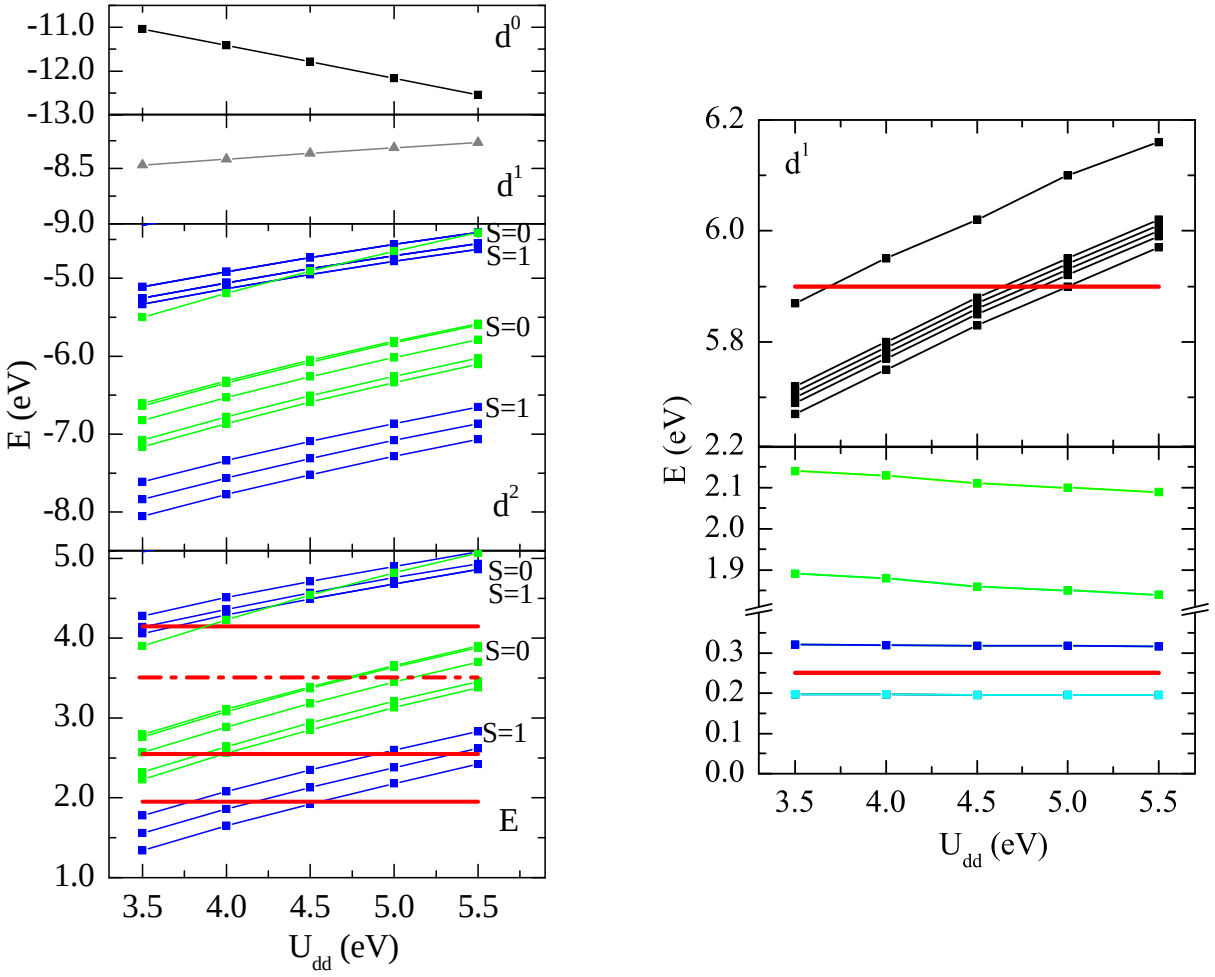

Figure 5.16: Configuration-interaction calculation for a d^0, d^1 and d^2 configuration for $YTiO_3$. We calculated the Mott-Hubbard excitation energies by $E(d^2)+E(d^0)-2E(d^1)+U_{dd}$ (left panel). The value of U_{dd} has to be added since there is no unique zero for the three different configurations in the calculation. The plots show the dependence on Hubbard U_{dd}. The horizontal red lines indicate the bands observed by ellipsometry. The charge-transfer transition energy and the transition energy within the t_g multiplet (Raman) are shown in the right panel together with the calculated d^1 excitation spectrum.

from a ferromagnetic ground state, transitions can only occur into a high-spin state ($S = 1$), i.e. into the ^3T states. Cooling down from a paramagnetic state the latter transitions gain weight below T_c. In contrast, excitations into a low-spin state ($S = 0$) will loose weight at T_c when cooling down. We observe changes in the spectral weight up to temperatures of roughly $10\,T_c$ and indeed smaller changes at approximately $2\,T_c$. The deviation of the anomaly in spectral weight away from T_c cannot be explained by an uncertainty of the sample temperature, because it amounts only several K in that temperature region. We calibrated the sample temperature once with an additional sensor at the sample position (see appendix). Another, more plausible explanation is that we keep some short-range ordering above T_c in the same manner as in $LaSrMnO_4$ and $LaMnO_3$ [2]. It has been proposed by Oles *et al.* [83] that the change in spectral weight between the paramagnetic and the ferromagnetic state amounts to 25% in $YTiO_3$ in the *ab* and *c* directions. This can be understood by the evolution of the nearest-neighbor spin-spin correlation function $\langle \mathbf{S}_i \cdot \mathbf{S}_j + 3/4 \rangle$. Assuming classical vectors with $S = 1/2$ one finds $\langle \mathbf{S}_i \cdot \mathbf{S}_j + 3/4 \rangle = 1$ in the ferromagnetic state and $\langle \mathbf{S}_i \cdot \mathbf{S}_j + 3/4 \rangle = 3/4$ in the paramagnetic state sector, i.e. a redistribution of 25%. A redistribution of weight of this magnitude is clearly not observed, especially not in the *c* direction. The effect described furthermore cannot explain the change of peak A up to at least $300\,\mathrm{K} \gtrsim 10 \cdot T_c$ (see Fig. 5.15).

In the following, we discuss three scenarios for the splitting between peak A and B: deviations from cubic symmetry, band structure effects, and an excitonic resonance.

The deviation from cubic symmetry lifts the degeneracy of the t_{2g} orbitals and thereby also of the $^3T_1$ state. In infrared transmittance [26] and in our Raman measurements this t_{2g} splitting was found to be $\approx 0.25\,\mathrm{eV}$. This is more than a factor of two too small to explain the splitting[9] between peaks A and B. Also from LDA+U [205] and from our configuration-interaction calculations (see above), the t_{2g} splitting of the d^2 sector is at most 0.4 eV.

Now we address possible band-structure effects. A LDA+DMFT study of $YTiO_3$, based on the actual crystal structure, does not show a splitting of the lowest peak in $\sigma_1(\omega)$ [11], see Fig. 5.19. Assuming U=5 eV, this peak in $\sigma_1(\omega)$ is found at 3.3 eV. Reasonable agreement with our data, in particular with the energy of 2.55 eV of peak B and with the onset of absorption below 1 eV, is obtained by assuming $U \approx 4.3\,\mathrm{eV}$. Note that this calculation finds a metallic state for U=3.5 eV, thus it is unreasonable to identify peak A at 1.95 eV with the calculated peak. Furthermore, in photoemission (PES) data of $YTiO_3$ the LHB is a single peak $\approx 1.3\,\mathrm{eV}$ below the Fermi level [207, 208], see Fig. 5.21. In inverse PES on $Y_{1-x}Ca_xTiO_3$ (x=0.4 - 0.8) the UHB can be identified with the lowest peak or shoulder $\approx$ 1.5-2 eV above the Fermi level [208], see Fig. 5.22 . Both PES and inverse PES agree with the LDA+DMFT result [11] for $U = 4$ - 5 eV. Finally, $U \approx 5.3\,\mathrm{eV}$[7] (see footnote on p. 145 for a comparison of the different values of U) has been derived from $2p$ core-level PES [124]. Altogether, these results support our interpretation that the splitting between

[9] The t_{2g} splitting Δ_{t2g} is relevant for a precise determination of U, since the lowest non-excitonic excitation (peak B) is expected at about $U - 3J_H + \Delta_{t2g}$. However, we will neglect this refinement in the following discussion.

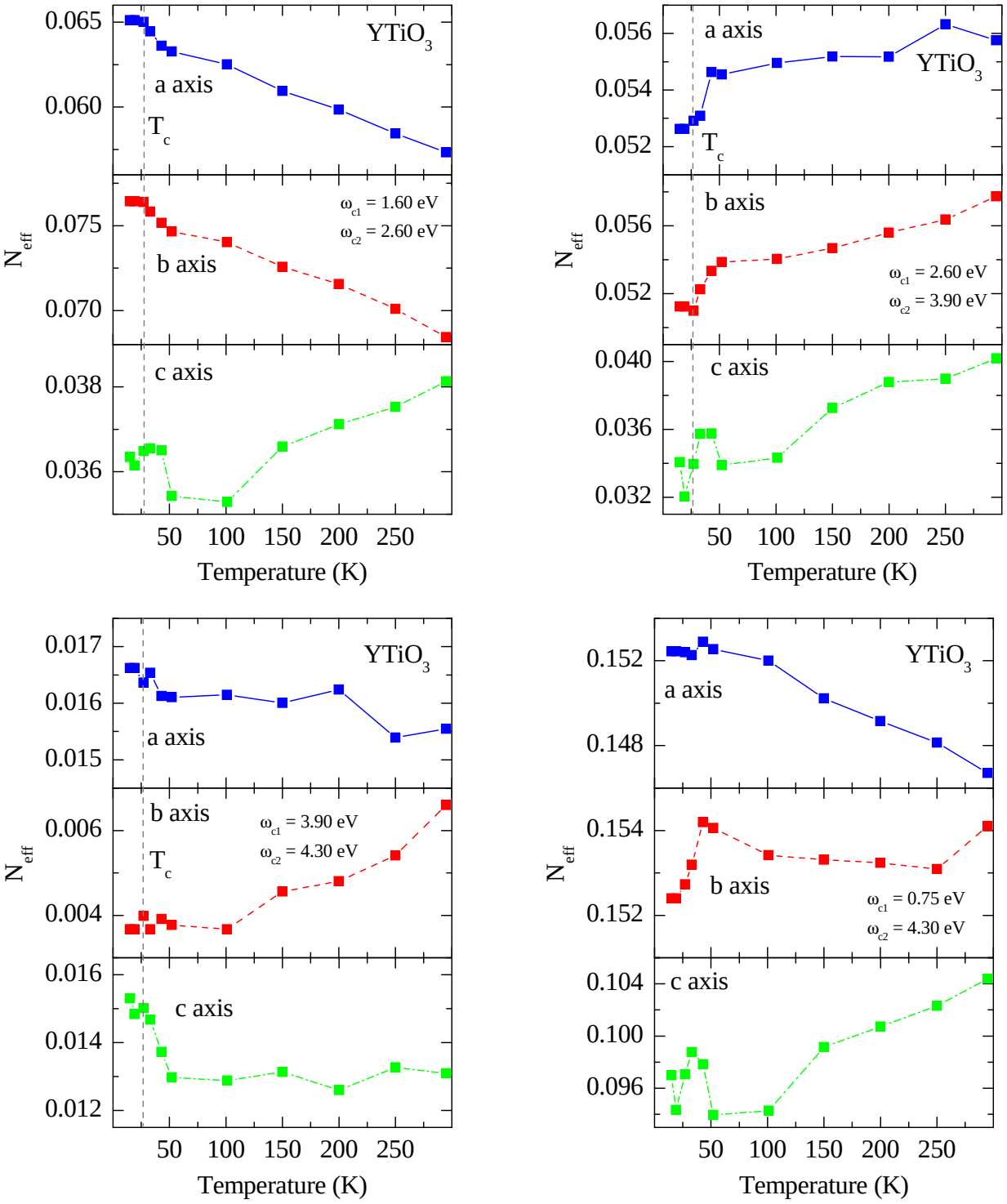

Figure 5.17: Effective carrier concentration of $YTiO_3$ for different cut-off frequencies (lower limit ω_{c1}, upper limit ω_{c2}). The unit-cell volume has been kept fixed to the 290 K value (see Tab. 5.1).

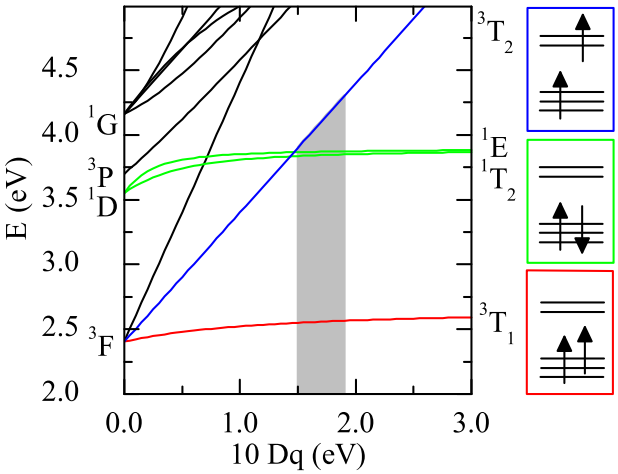

Figure 5.18: Left: Calculated energies for a $|d^1d^1\rangle \rightarrow |d^0d^2\rangle$ excitation with different d^2 final states in a cubic crystal field [20]. The Slater integrals were chosen as $F^0 = 3.60\,\text{eV}$, F^2=6.75 eV, and F^4=4.55 eV, corresponding to $U = 4.5\,\text{eV}$[7] (see footnote on p. 145). For $10\,\text{Dq} = 0$ the ionic multiplet structure is obtained. For $10\,\text{Dq} \approx 1.5$ - 1.9 eV (grey) the energy of peak C is well described by excitations into the $^3T_2$ state. Right: sketch of the orbital occupation in the crystal-field limit.

peaks A and B does not result from the band structure and that peak B at 2.55 eV is the dominant excitation. A LDA+U band-structure calculation [205] finds some fine structure in the $^3T_1$ band. However this splitting is only 0.4 eV. Furthermore the energetic distances do not fit our experiment. For the t_{2g} splitting of the d^2 sector we also find a value of 0.4 eV (see above).

In contrast to (inverse) PES, the optical conductivity reflects particle-hole excitations and thus is sensitive to interactions between the particle in the UHB (i.e. a double occupancy) and the hole in the LHB. These interactions are also neglected in the LDA+DMFT calculation of $\sigma(\omega)$ of Ref. [11]. We therefore identify peak B as a particle-hole excitation in which the particle and the hole are well separated, whereas peak A is interpreted as an excitonic resonance, where the particle and the hole remain close to each other. Note that peak A is not lying below the gap, i.e. it is not a truly bound exciton, but a resonance within the continuum (see chapter 2). Just as in conventional semiconductors, a Hubbard exciton may arise due to the attractive Coulomb interaction between the particle and the hole. The nearest-neighbor[10] particle-particle repulsion V of the extended Hubbard model [48] is equivalent to a particle-hole attraction $-V$. We will give a very rough estimate for the value of V. It is the energetic distance to the Hubbard-band maximum at 2.55 eV, i.e. roughly $\sim$ 0.6 eV. We can not decide whether this is a realistic value for $YTiO_3$. More

[10]In Mott-Hubbard insulators, the particle and the hole may reside on the *same* site, albeit with different spin or orbital quantum numbers. Such a very strongly bound 'exciton' corresponds to a magnon or an orbiton, excitations within the spin or orbital channel. There is no doubly occupied site and one does not have to pay U, in contrast to the excitations discussed here.

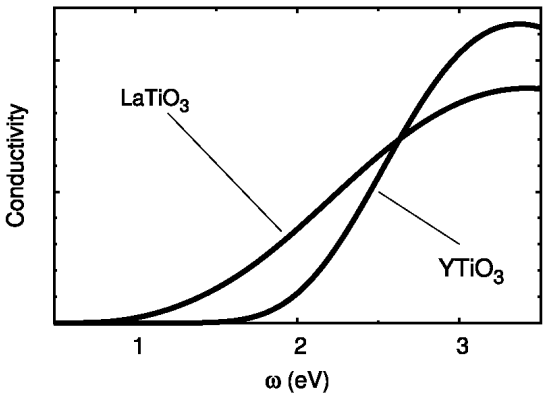

Figure 5.19: Optical conductivity of $YTiO_3$ from LDA+DMFT with the parameters $U = 5$ eV at $kT = 0.1$ eV. Note that all matrix elements are set to unity [11].

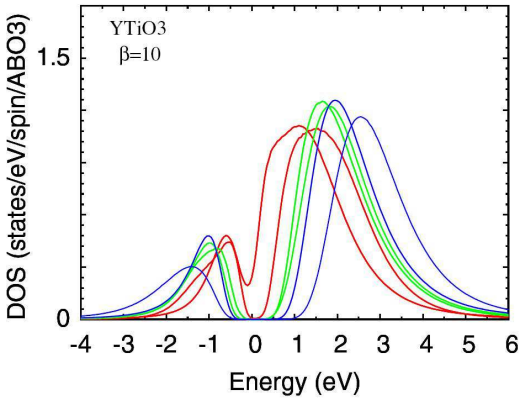

Figure 5.20: DOS of $YTiO_3$ from LDA+DMFT with the parameters $U = 3.5$ (red), 4.0 (red), 4.5 (green), 4.75 (green), 5.0 (blue), 6.0 (blue) eV at $kT = 0.1$ eV [11].

detailed theoretical studies are required to decide whether a realistic value of V is sufficient to explain the splitting of 0.6 eV observed between peaks A and B.

For a 2D Mott-Hubbard insulator with antiferromagnetic (AF) exchange J on a square lattice, Wrobel and Eder pointed out that exciton formation may be governed by the interplay between the *kinetic* energy and the interaction with the AF background [77]. The motion of a single hole doped into the LHB (or equivalently of a double occupancy in the UHB) is hindered by the interaction of the spin of the hole with the AF background. This can be described in terms of a spin polaron. Hopping of the bare hole on the energy scale t results in a trace of misaligned spins. Coherent motion of the dressed polaronic quasiparticle requires the emission of magnons; i.e. the bare hole band width $\sim t$ is reduced to the polaronic band width $\sim J$. In this case, the kinetic energy may be lowered by the formation of spinless excitons below the Mott-Hubbard gap. Interestingly, this mechanism for exciton formation may be relevant for the formation of Cooper pairs in the case of superconductivity [77]. One may speculate that a similar mechanism is at work in the case of antiferro-*orbital* (AFO) order (see Fig. 5.23). The orbital ordering pattern in $YTiO_3$ is more complex than simple AFO [5, 190, 191]. Still Fig. 5.23 may be relevant for the ab plane, since hopping from the lowest orbital on one site to the lowest orbital on a neighboring site is 2-3 times smaller than hopping to the excited states [11, 45].

Finally we address the observed anisotropy between the ab plane and the c direction. From the matrix elements from Refs. [11, 204, 213] one can estimate the transition probability by considering that $(N^a_{eff} + N^b_{eff})/(2N^c_{eff}) \propto (t_{ab}/t_c)^2 = 1.1$ [204], 3.5 [11], and 5.1 [213]. Experimentally we find $(N^a_{eff} + N^b_{eff})/(2N^c_{eff}) \approx 2$ in the region 1.6-2.6 eV (see Fig. 5.1), which is in reasonable agreement to the data of Pavarini *et al.* [11]. Also the peak at 4.2 eV exhibits an anisotropy between ab and c, and even more pronounced between

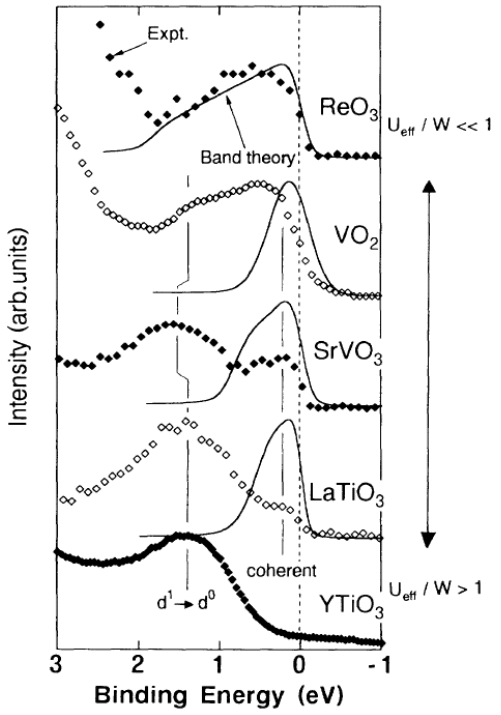

Figure 5.21: PES of $YTiO_3$ [207]. The maximum of the LHB is approximately located at 1.3 eV.

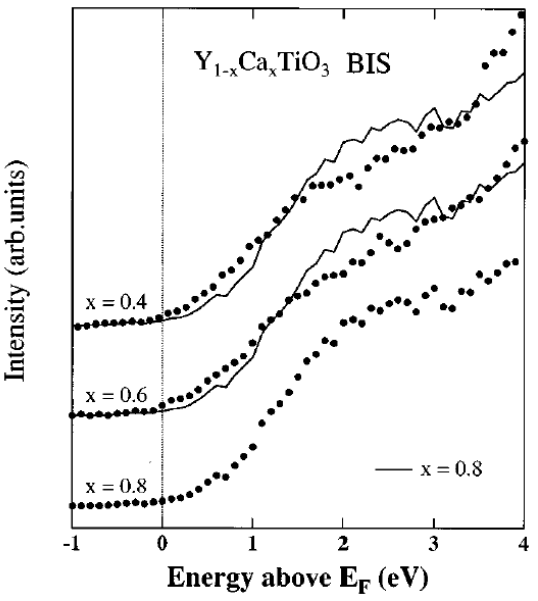

Figure 5.22: IPES of $Y_{1-x}Ca_xTiO_3$ [208]. The maximum of the UHB is located at 1.5-2.0 eV. Note that the resolution is only 0.7 eV.

a and b. By using the hopping matrices the anisotropy can be understood qualitatively: $(N^a_{eff}+N^b_{eff})/(2N^c_{eff}) \approx 0.7$ (experiment) and ≈ 0.4 (theory [213]). The difference between a and b direction is unclear and must be related to a strong orbital selection rule.

In summary, we report on $\sigma(\omega)$ of the inter-Hubbard-band excitations in $YTiO_3$. Taking into account all $3d$ orbitals, the peak positions and the anisotropy of σ can be understood in a local scenario using $U \approx 4.5\,\text{eV}$. The peak assignments are in agreement with photoemission and LDA+DMFT results. Peak B at 2.55 eV is attributed to excitations into the lowest d^2 multiplet ($^3T_1$ in cubic symmetry) with an energy of roughly $U - 3J_H$ (see footnote [9] on p. 149). Peak A at 1.95 eV is interpreted as an excitonic resonance. We suggest that this Hubbard exciton may result both from Coulomb interaction and from a lowering of the kinetic energy in an orbitally ordered state. A quantitative description of this binding phenomenon is essential for a consistent explanation of optical and photoemission data and will allow us to extract important information on electronic correlations in Hubbard systems.

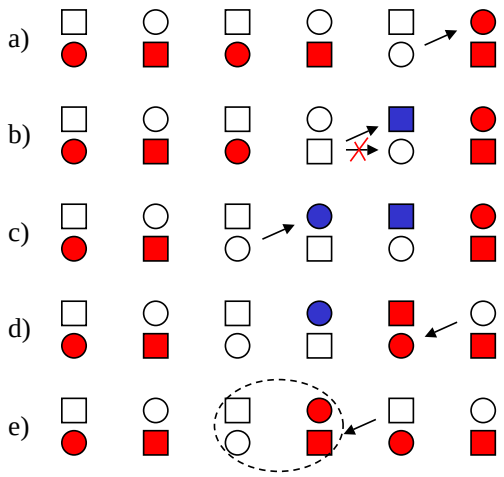

Figure 5.23: Sketch of the suggested formation of a Hubbard exciton (dashed circle) due to lowering of the *kinetic* energy in a state with antiferro-orbital order. Circles and squares denote two distinct orbitals per site. We assume that hopping is finite only between orbitals of the same type. Full (open) symbols refer to occupied (empty) orbitals. (a) Excitation from the LHB to the UHB, $|d^1d^1\rangle \rightarrow |d^0d^2\rangle$. (b) and (c): Propagation of the hole, i.e. the $|d^0\rangle$ site. Since the hopping between circles and squares is zero, this creates a trace of misaligned orbitals (blue), suppressing the hole motion. (d) and (e): This can be repaired if the doubly occupied site accompanies the hole, forming a bound state.

5.5 Comparison to $SmTiO_3$ and $LaTiO_3$

In this section we will present ellipsometric data of the *antiferromagnetic* compounds $SmTiO_3$ and $LaTiO_3$ and compare them to our measured data of the *ferromagnetic* compound $YTiO_3$. Ellipsometric measurements have been performed on a (001) surface and a (100) surface of two $SmTiO_3$ crystals of the same batch (see above). Here we give a detailed study of the temperature and polarization dependence. The $LaTiO_3$ crystals have only been investigated at room temperature without any polarization analysis because they were partly twinned. We also found that the surfaces of $LaTiO_3$ are not stable in time when comparing e.g. $LaSrMnO_4$ (see appendix). Note that only unpolarized room temperature data are available in the literature [104, 106, 107]

We start with a comparison of all three titanates at room temperature. Their spectra are displayed in Fig. 5.24. The onset of the charge-transfer excitations can be found in all compounds at approximately 4.5 eV. We focus on the Mott-Hubbard bands below 4.5 eV [104, 107]. Two different spectra of $LaTiO_3$ are shown. They both have nominally a T_N of approximately 150 K. There are significant differences especially in the region around 4.5 eV, which we trace back to the unstable surfaces of $LaTiO_3$. The line shape of both compounds is similar and also comparable to the optical conductivity (averaged over all directions) of $SmTiO_3$. $YTiO_3$ differs in line shape, since one can clearly observe three peaks instead of two in the other compounds. The bandwidth decreases from roughly 3.1

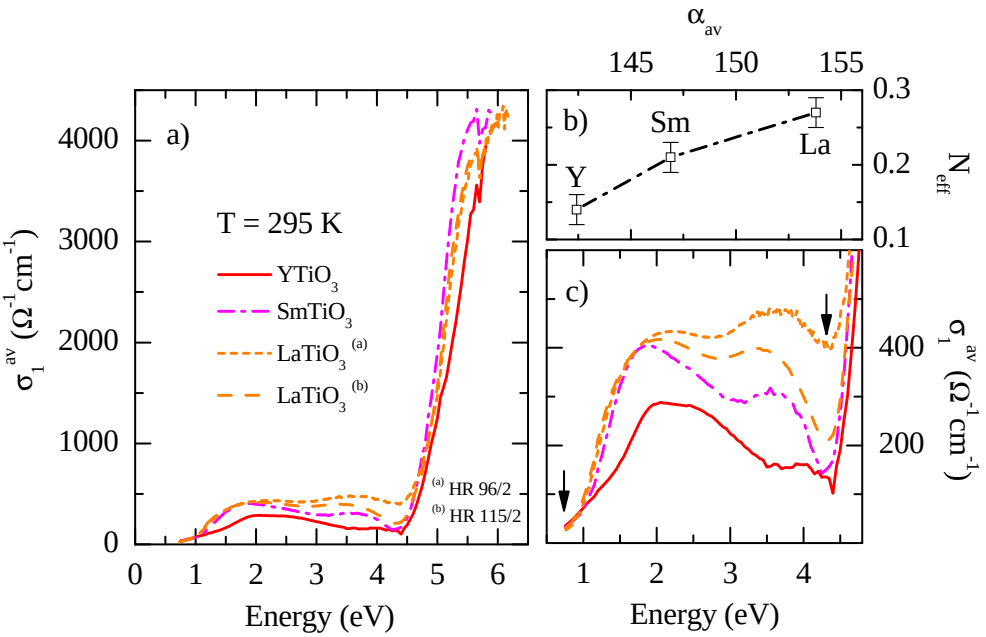

Figure 5.24: a,c) Comparison of $RTiO_3$ optical conductivity spectra at room temperature. The two different $LaTiO_3$ spectra are measured on two different crystals which have nominally almost the same Neél temperature of about 150 K. The $SmTiO_3$ and $YTiO_3$ spectra have been averaged over all three directions of σ_1, because $LaTiO_3$ is (partly) twinned and thus all directions are measured simultaneously. b) The overall spectral weight of the Mott-Hubbard bands as function of the averaged Ti-O-Ti bond angle α.

eV ($LaTiO_3$) to 2.8 eV ($YTiO_3$). This behavior can be qualitatively understood because the hopping in $SmTiO_3$ and $LaTiO_3$ should be larger due to the increased Ti-O-Ti bond angle α (see Tab. 5.1). However, this is not the full truth because the ground-state orbitals, presuming orbital ordering, in $LaTiO_3$ and $YTiO_3$ are very different. Considering only t_{2g} orbitals of the form $d_1|xy\rangle+d_2|yz\rangle+d_3|zx\rangle$ a ground state wavefunction with $d_1^2 = 0.6$, $d_2^2 = 0.0$ and $d_3^2 = 0.4$ has been reported for $YTiO_3$ [5, 190, 191] and $d_1^2 = 0.36$, $d_2^2 = 0.15$ and $d_3^2 = 0.49$ for $LaTiO_3$ [13, 14, 220] ($SmTiO_3$ lies in between [13, 14]). The different ground states will have further influence on the hopping matrices, in particular the reduction of the prefactor d_2 from La to Y gives the major impact on the changes, since the other prefactors are found to be almost independent on the Ti-O-Ti bond angle [13, 14]. In addition to the increase in bandwidth we find an increase of the overall spectral weight from Y to La. The (averaged) effective carrier concentration amounts to roughly 0.14 ± 0.02 ($YTiO_3$), 0.21 ± 0.02 ($SmTiO_3$), and 0.27 ± 0.02 ($LaTiO_3$), see Fig. 5.24(b). Qualitatively this behavior agrees with the magnetic exchange constant obtained from neutron scattering which decreases from $LaTiO_3$ ($|J| = 15.5$ meV [3]) to $YTiO_3$ ($|J| = 3$ meV [192]).

We now discuss the temperature dependence of the optical conductivity of $SmTiO_3$. The spectra are shown in Fig. 5.25. A multi-peak structure can be clearly observed, one hump at 1.7 eV and another one at 3.7 eV. The a and c direction are almost identical, but the b

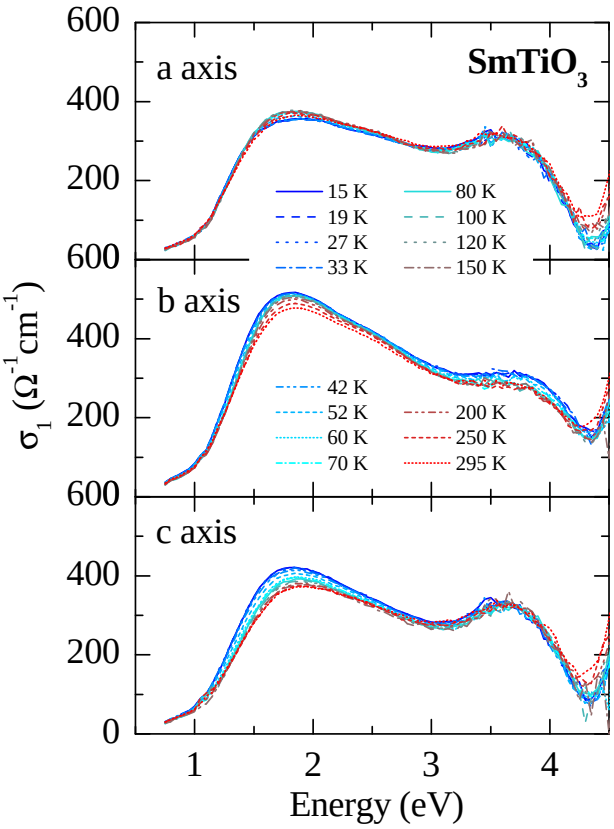

Figure 5.25: Optical conductivity of $SmTiO_3$.

direction significantly differs. A two-peak structure like in $YTiO_3$ can not be resolved, i.e. we see no direct experimental evidence of an excitonic resonance in $SmTiO_3$ (and also $LaTiO_3$). One may speculate that the excitonic resonance is washed out in the latter compounds because the hopping in ab and c are comparable while they are anisotropic by a factor of 2-3 in $YTiO_3$ [11, 213]. This yields a more two-dimensional orbital character in $YTiO_3$. A reduction of the dimensionality will generally sharpen a bound state (this can e.g. be seen in spatially confined semiconductors [71]).

We have also calculated the spectral weight, i.e. the effective carrier concentration, in certain regions of the spectrum between the energies ω_{c1} and ω_{c2} as a function of temperature. This is displayed in Fig. 5.26. We found a pronounced change exactly at the magnetic ordering temperature of 53 K. This may give evidence for the Mott-Hubbard character of these bands. The anomalies observed in the lattice constants at T_N can only account for a change of the order of 1% in spectral weight when applying the Harrison rules [169] (see also chapter 4), whereas we observe changes of about 5%. It seems that the weight of the a and c directions predominately changes in the energy region 0.75-3.1 eV, while it changes in the b direction over the entire energy region 0.75-4.3 eV of the Mott-Hubbard excitations. The temperature dependence is puzzling to us since it con-

tradicts our expectations in two ways: firstly one would expect a *reversed* temperature dependence when comparing to $YTiO_3$ because the magnetic ground states are different, and secondly one would naively expect changes of the order of 25 % due to the changes in nearest-neighbor spin-spin correlation function[11]. An antiferromagnetic ground state contains singlet and triplet states. This allows for transitions into high-spin (S=2) and low-spin states (S=0). As already shown in $YTiO_3$ this simple picture can only explain the temperature changes across T_c but not the overall (stronger) changes in weight above T_c. For the transitions into a high-spin state ($^3T_1$ in cubic symmetry), which should be the first Mott-Hubbard transition observed, we expect an increase in weight when increasing the temperature above T_N (in contrast to $YTiO_3$ where a decrease is expected above T_c and also observed.). This increase is only observed for the a direction, the b and c directions lose weight, in disagreement with our expectations (see Fig. 5.26).

So far we have completely omitted the Sm ion. In contrast to La and Y it does not have a closed shell and is thus magnetic. It may be that the magnetism of the Sm ion has some impact on the evolution of the spectral weight with temperature. Note however that a hopping between Sm and Ti sites can be omitted to good approximation because the f electrons a very localized when comparing to d electrons.

To conclude this section, we reported on ellipsometric measurements on $LaTiO_3$ and $SmTiO_3$. We focussed on the $SmTiO_3$ crystal since it is single domain. We found a pronounced redistribution of weight across the magnetic ordering temperature of $T_N = 53$ K in all three crystallographic directions up to 3.1 eV. This points towards the Mott-Hubbard character of these bands. However, the sign of the change and the magnitude contradict the expectations of a "spin-controlled" Mott-Hubbard transition in the fashion of $LaMnO_3$ [2]. Definitely more theoretical and experimental work on this compound is needed to get a more quantitative understanding.

Summary

To summarize the main points of this chapter: we have presented a Raman-scattering study on $LaTiO_3$ and $YTiO_3$, and an ellipsometric study on the compounds $LaTiO_3$, $SmTiO_3$, and $YTiO_3$.

From the Raman experiment we see strong evidence for an orbital excitation at 235 meV in both compounds. The excitation is resonantly enhanced at an excitation energy of 2.5 eV, which we trace back to a resonance with the upper Hubbard-band, i.e. the excitation process for a single or double orbital flip involves two sites.

In $YTiO_3$ we observed a multi-peak structure in the optical conductivity which reflects multiple-orbital Hubbard bands. We see evidence that the peak observed at 1.95 eV can be interpreted as a Mott-Hubbard excitonic resonance, i.e. a quasi-bound state inside the continuum. Furthermore we observed a significant anisotropy between ab and c direction of $YTiO_3$, which can be understood by the orbital ordering pattern found in the literature [5, 11, 45, 190, 191, 213]. Regarding the temperature dependence of the spectral weight

[11] For a transition from an antiferromagnetic state into a high-spin states one finds: $\langle \mathbf{S_i S_j} + 3/4 \rangle \rightarrow 1/2$ ($T \ll T_N$) and $\langle \mathbf{S_i S_j} + 3/4 \rangle \rightarrow 3/4$ ($T \gg T_N$) for classical spins with $S = 1/2$.

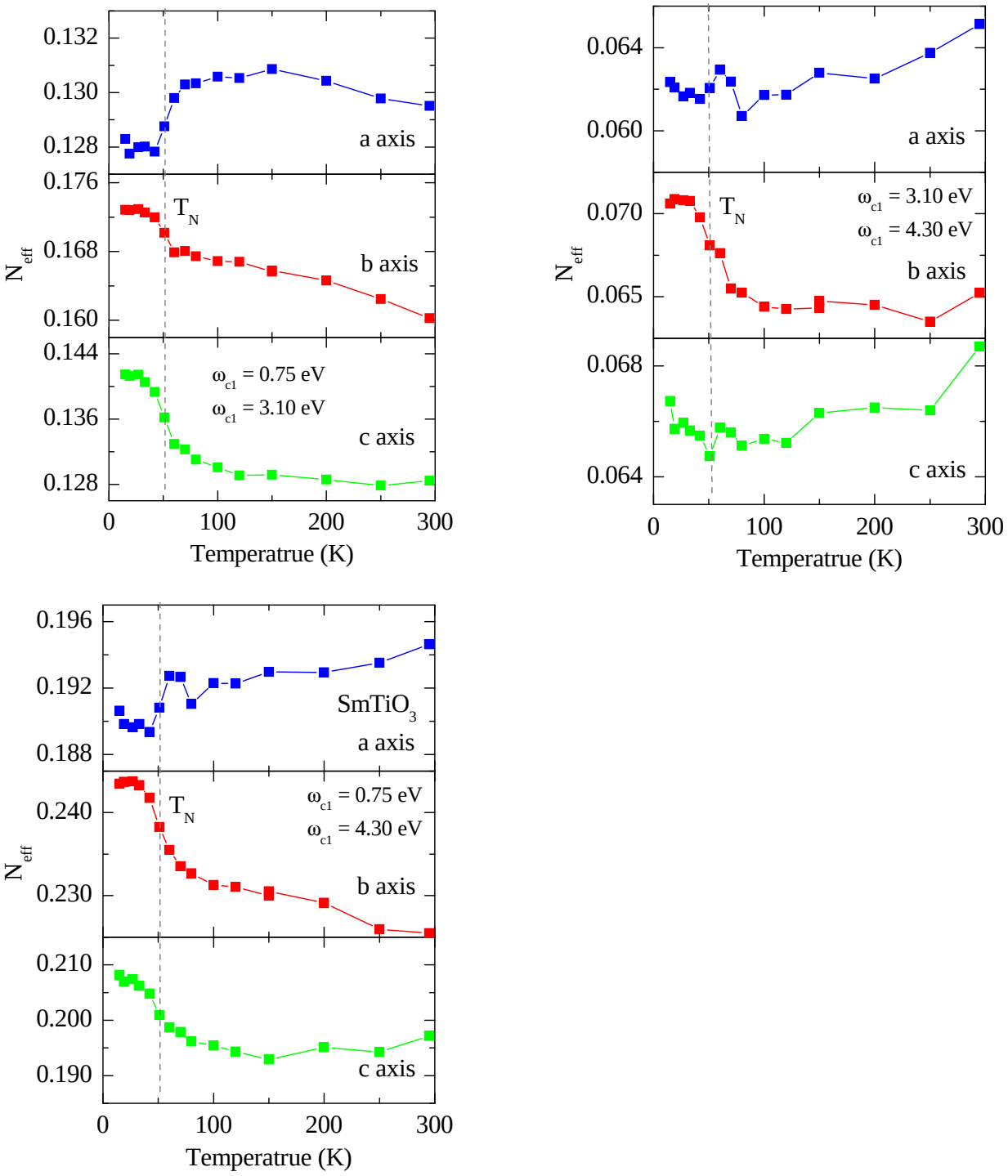

Figure 5.26: Effective carrier concentration of $SmTiO_3$ for different cut-off frequencies (lower limit ω_{c1}, upper limit ω_{c2}). The unit-cell volume has been kept fixed to the 290 K value (see Tab. 5.1).

we found small changes across a temperature of $\sim T_c$ and larger changes up to $T > 10\,T_c$. However, the magnitude of the changes contradicts the expectations from the nearest-neighbor spin-spin correlation function.

Finally we compare the data of ferromagnetic $YTiO_3$ to those of the antiferromagnetic compounds $SmTiO_3$ and $LaTiO_3$. The evolution of weight with increasing ionic rare-earth radius can be qualitatively understood by the evolution of the Ti-O-Ti bond angle and the change in the (orbitally-ordered) ground states. The spectral weight in $SmTiO_3$ shows significant changes at T_N. Here the expectations from the spin-selection rules completely fail to describe the observed sign of the change and the magnitude.

6 Conclusions

Within the scope of this thesis the electronic structure of different transition-metal compounds with open d shells has been investigated. The focus is on Mott-Hubbard insulators in particular on excitations from the lower to the upper Hubbard band, on the effect of spin and orbital correlations of these transitions, and on orbital excitations. We used three different optical techniques for this study, in particular Fourier-transform spectroscopy (for an energy range of 0.1-1 eV), spectroscopic ellipsometry (0.75-6 eV) and Raman scattering (0.01-0.6 eV). The spectra have been recorded as a function of temperature and polarization. For the ellipsometry results the spectral features have been analyzed in terms of multiplets, which reflect multi-orbital Hubbard bands. We check our assignments by testing the selection rules and by tracking the evolution of these features with temperature.

Ellipsometry setup

An ellipsometer has been put into operation by C. Hilgers and myself. Low-temperature measurements down to liquid-He temperatures are now possible and well established. A bake-out procedure is necessary to avoid the formation of ice layers. We were able to determine the full dielectric (or conductivity) tensor of an orthorhombic sample by measuring the Müller matrix for at least three different orientations of the sample. All data sets have been analyzed simultaneously. The determination of the Müller matrix allows for additional model parameters like depolarization, surface roughness, cover layers, etc.

Ellipsometry and Fourier spectroscopy on $La_{1-x}Sr_{1+x}MnO_4$

We measured the single-layered manganites $La_{1-x}Sr_{1+x}MnO_4$ for the compositions $x = 0.0$, 0.13, and 0.50. In the $x = 0.0$ compound a multi-peak structure has been found by ellipsometry in the energy range between 0.75-5.8 eV in the a direction while there is only a single peak in the c direction. This reflects the strong anisotropy between the inter- and intra-layer directions. We were able to identify different charge-transfer and Mott-Hubbard excitations by comparing the data directly to the optical conductivity obtained from a multiplet calculation, which is shown to give a good description of the data. The lowest multiplet around 2 eV is found to be a transition between two manganese sites, i.e. a Mott-Hubbard transition. We get further evidence for this assignment from the evolution of the spectral weight with temperature: the spectral weight of this transition increases with increasing temperature, in contrast to higher-lying excitations which lose spectral weight. This behavior reflects the change of magnetism from antiferromagnetic to paramagnetic. We were able to understand the evolution of the spectral weight by

the evolution of the nearest-neighbor spin-spin correlation. Therefore we conclude that this compound is predominantly a Mott-Hubbard insulator. This result challenges the widespread opinion that manganese compounds are always of charge-transfer type, but it is in agrement with recent studies on the compound $LaMnO_3$ [2, 125, 164, 165]. We also measured the onset of the optical gap by means of Fourier-transform spectroscopy. No (onsite) orbital excitation has been found up to 0.55 eV in the *ab* direction. This shows that the intra-e_g splitting has to be larger than this value.

In the doped compounds we found a redistribution of spectral weight which can be qualitatively understood by inducing d^3 states into the d^4 host. A new feature develops at 1.0-1.5 eV which can be assigned to either a polaron or a charge-transfer excitation of the d^3 sector.

Raman scattering on $YTiO_3$ and $LaTiO_3$

We performed Raman scattering experiments[1] on the Mott-Hubbard insulators $YTiO_3$ and $LaTiO_3$. We found a broad feature at 235 meV which we interpreted as an orbital excitation. The intensity of this peak is resonantly enhanced at a laser energy of 2.5 eV. Since this energy lies inside the upper Hubbard band, we believe that the excitation involves two Ti sites. In the light of the most recent experimental and theoretical results, it is not possible to unravel the nature of the ground state, orbitally ordered or orbitally fluctuating on basis of this data alone.

Ellipsometry on $YTiO_3$, $SmTiO_3$ and $LaTiO_3$

In $YTiO_3$ we observed a multi-peak structure in the optical conductivity which reflects multiple-orbital Hubbard bands. We find evidence that the peak observed at 1.95 eV can be interpreted as a Mott-Hubbard excitonic resonance, i.e. a quasi-bound state inside the continuum. Furthermore we observed a significant anisotropy between the *ab* and *c* direction of $YTiO_3$, which can be understood by the orbital ordering pattern reported in the literature [5, 11, 45, 190, 191, 213]. Regarding the temperature dependence of the spectral weight we found small changes across a temperature of $\sim T_c$ and larger changes up to $T \gg T_c$. However, the magnitude of the change contradicts the expectations from the nearest-neighbor spin-spin correlation function. In contrast, in the manganite system $LaSrMnO_4$ the observed changes follow the expectations based on the spin-spin correlation function almost on a quantitative level.

Finally we compare the data of ferromagnetic $YTiO_3$ to those of the antiferromagnetic compounds $SmTiO_3$ and $LaTiO_3$. The increase of spectral weight with increasing ionic rare-earth radius can be qualitatively understood by the increase of the Ti-O-Ti bond angle and the change in the (orbitally-ordered) ground state. The spectral weight in $SmTiO_3$ shows significant changes at T_N. Here the expectations from the spin-selection rules completely fail to describe the observed sign of the change and the magnitude.

[1] in collaboration with C. Ulrich and B. Keimer from the Max-Planck institute Stuttgart.

Comparison of t_{2g}^1 and e_g^1 systems

If we finally compare the evolution of spectral weight of the lowest electronic excitation in the prototypical t_{2g}^1- ($YTiO_3$, $SmTiO_3$) and e_g^1-electron ($LaSrMnO_4$) systems with temperature, one finds that the relative changes of the spectral weight are more pronounced in case of the e_g^1 systems. This reflects firstly the larger spin value (S=2 compared to S=1/2) for the e_g^1 system and secondly a stronger hybridization in the e_g^1 systems. Both effects yield a stronger temperature dependence in the e_g^1 case. As already pointed out the change of spectral weight in the titanates is lower then the predicted change based on the spin-spin correlation function. This may indicate that spin and orbital degree of freedom can not be regarded as decoupled in these systems as it was the case for $LaSrMnO_4$.

A Appendix

Measurement overview

Table A.1: Measurement overview: ellipsometry (E), Raman scattering (R), and Fourier-transform spectroscopy (FT).

$La_{1-x}Sr_{1+x}MnO_4$	name	surface	measurements
$x = 0.00$[a]	MB10	(010) or (100)	E, FT
$x = 0.125$[b]	Zd05	(010) or (100)	E
$x = 0.50$[a]	MB04	(010) or (100)	E, FT
$RTiO_{3+\delta}$	name	surface	measurements
Y[c] ($\delta < 0.02$)	HR28/2/3(a)	(100) or (010)	R
Y[c] ($\delta < 0.02$)	HR28/2/3(b)	(001) and (1-10)	E, R
Sm[c] ($\delta \approx 0.005$)	HR160/3/3	(-100)	E
Sm[c] ($\delta \approx 0.005$)	HR160/3	(001)	E
La[d] ($\delta = -0.01$)	MC33B	twinned	R
La[c] ($\delta \approx -0.005$)	HR96/2	twinned	E
La[c] ($\delta \approx -0.005$)	HR115/2	twinned	E
La[c] ($\delta = 0.04$)	HR104/3/4	twinned[e]	R
La[c] ($\delta = 0.03$)	HR104/3/1	twinned	E

[a] Crystal growth by M. Benomar [143].

[b] Crystal growth by P. Reutler [156, 221].

[c] Crystal growth by H. Roth [108, 200].

[d] Crystal growth by M. Cwik [7].

[e] orientated within the cubic space group.

Sample preparation

All samples were first orientated by means of Laue X-ray diffraction (see Fig. A.1). Afterwards they were sawed by an inside-hole saw. Then the surfaces were first lapped, then polished, and finally cleaned.

Lapping

- The sample is heated up to 100°C and glued with Gatan wax onto the sample holder.
- The sample is lapped for 20 minutes on a Logitech polishing machine (PM2) with a suspension of Al_2O_3 (3 μm graining) in distilled water.
- The sample is cleaned with distilled water and ethanol.

Polishing

- Cleaning of the polishing disc.
- The sample is polished for 20 minutes on the Logitech PM2 with the Logitech polishing suspension SF1.
- If the surface does show any contaminations of SF1 or is not smooth enough the polishing is continued.

Cleaning

- The sample is removed from the polishing plate by acetone.
- Ultrasonic bath for 3 minutes in fresh acetone.
- Ultrasonic bath for 3 minutes in distilled water.
- Ultrasonic bath for 3 minutes in ethanol.
- Ultrasonic bath for 3 minutes in distilled water.
- The sample is dried in air.

Finally, the sample is glued onto a Cu plate with silver paint and mounted on the cold finger of a cryostat.

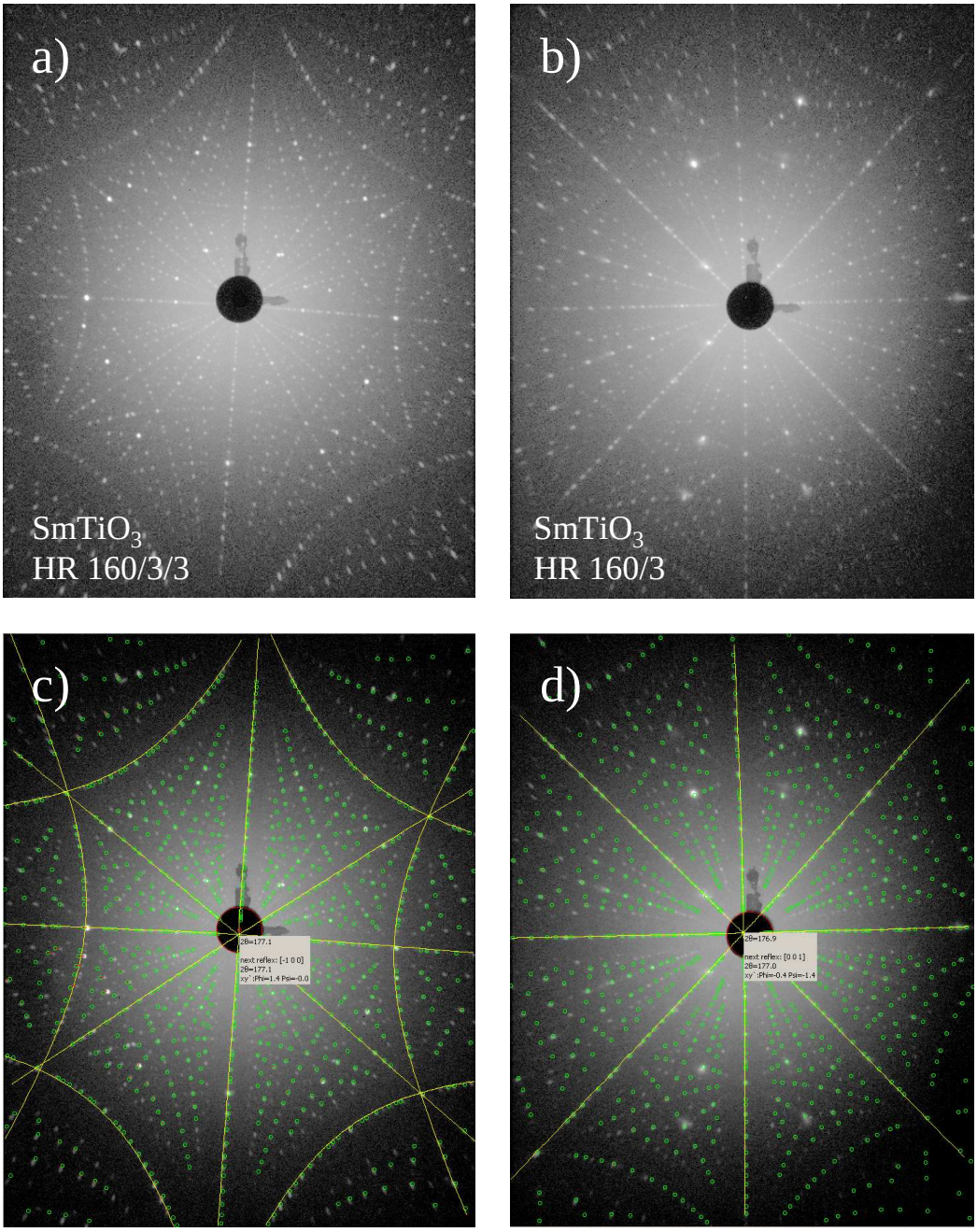

Figure A.1: a,b) Exemplarily Laue picture of $SmTiO_3$ (HR160/3) taken with the $U = 30$ kV, $I = 20$ mA, $T = 160$ s. c,d) The data has been fitted with *Clip*[1] in order to check to orientation. The orientation along the crystallographic axes is within 3°.

Temperature at the sample position

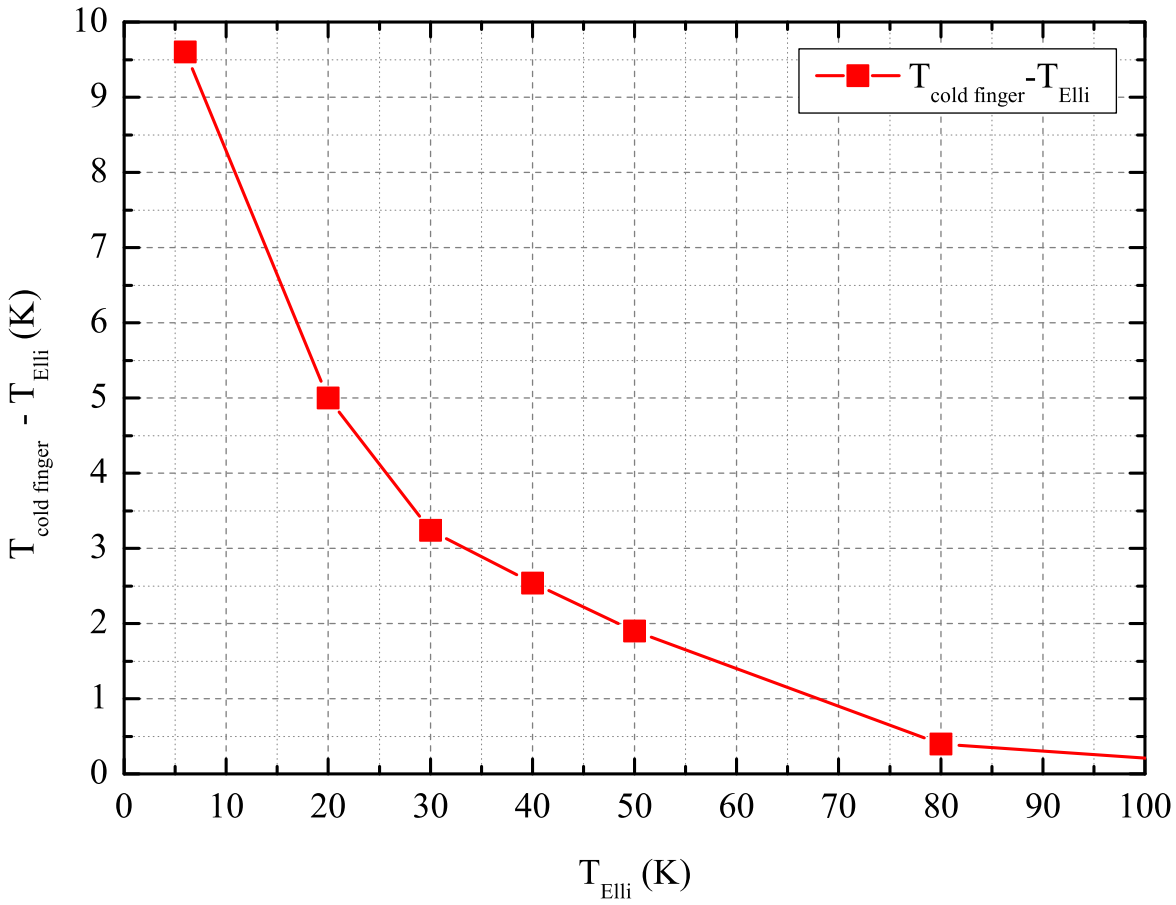

Figure A.2: The temperature at the sample position on the cold finger $T_{cold\ finger}$ deviates from the temperature at the cooling unit T_{Elli}. A calibrated Cernox thermometer has been glued with GE-kit directly next to the sample ($YTiO_3$ in this case). The maximum difference is 9.5 K at a nominal temperature of $T_{Elli} = 5$ K.

Madelung potentials

We give the Madelung potentials [18]

$$V(r,\theta,\phi) = \sum_{k=0}^{\infty} \sum_{m=-k}^{k} A_{k,m} r^k \sqrt{\frac{4\pi}{2k+1}} Y_k^m(\theta,\phi) \tag{A.1}$$

of $YTiO_3$ and $LaSrMnO_4$ as calculated by the program $A_{k,m}$ by M. Haverkort [18]. The Madelung potential has been expanded in spherical harmonics $Y_k^m(\theta,\phi)$ with the quantum numbers k and l; r^k represents the radial part of the wavefunction. The coefficients $A_{k,m}$ have been calculated by an Ewald summation under a point-charge approximation. It is only necessary to determine the coefficients up to $k = 4$ [222]. Note that $A_{k,m} = (-1)^m A_{k,-m}$ due to the hermicity of the crystal-field Hamiltonian. For $YTiO_3$ and $LaSrMnO_4$ we used the room-temperature structural data of Refs. [148, 223].

Table A.2: Madelung potentials for $YTiO_3$ and $LaSrMnO_4$.

$A_{k,m}$	$YTiO_3$	$LaSrMnO_4$
$A_{0,0}$	(35.11444487, 0.00000000)	(36.40609517, 0.00000000)
$A_{1,0}$	(0.00000000, 0.00000000)	(0.00000000, 0.00000000)
$A_{1,1}$	(0.00000000, 0.00000000)	(0.00000000, 0.00000000)
$A_{2,0}$	(-0.17991136, 0.00000000)	(-3.43002758, 0.00000000)
$A_{2,1}$	(-0.57458390, 0.12648298)	(0.00000000, 0.00000000)
$A_{2,2}$	(0.06304254, -0.16055590)	(0.00000000, 0.00000000)
$A_{3,0}$	(0.00000000, 0.00000000)	(0.00000000, 0.00000000)
$A_{3,1}$	(0.00000000, 0.00000000)	(0.00000000, 0.00000000)
$A_{3,2}$	(0.00000000, 0.00000000)	(0.00000000, 0.00000000)
$A_{3,3}$	(0.00000000, 0.00000000)	(0.00000000, 0.00000000)
$A_{4,0}$	(1.64039522, 0.00000000)	(2.93828254, 0.00000000)
$A_{4,1}$	(-1.53545785, -0.43486220)	(0.00000000, 0.00000000)
$A_{4,2}$	(0.31484023, 0.31204117)	(0.00000000, 0.00000000)
$A_{4,3}$	(-0.55439916, -0.74602701)	(0.00000000, 0.00000000)
$A_{4,4}$	(-1.01435714, -1.16156142)	(2.55753592, 0.00000000)

Unstable surface

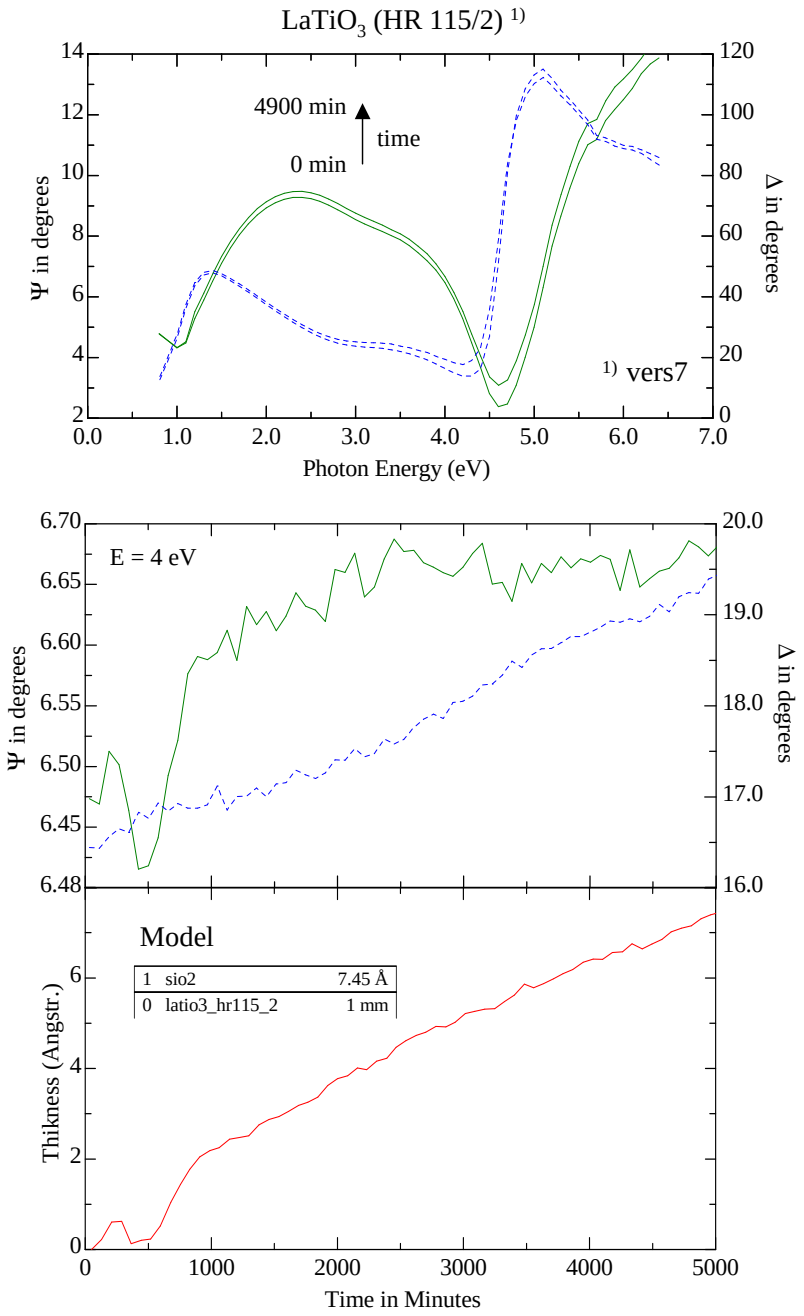

Figure A.3: Unstable surface of $LaTiO_3$. The sample has been placed inside a cryostat immediately after polishing. The spectra change in time. The change can be modeled by a growing non-absorbing cover layer (we have chosen SiO_2).

Ice layer

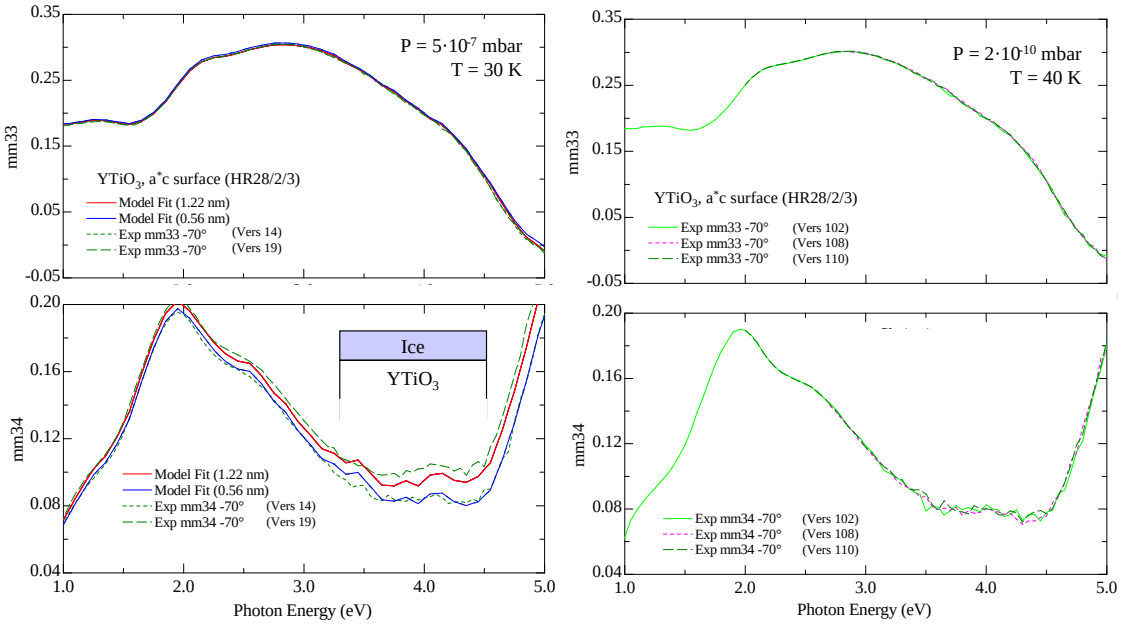

Figure A.4: *Left panels:* At a pressure of 10^{-7} mbar the measured spectra (i.e. the Müller-matrix elements m_{33} and m_{34}) are not reproducible. The second spectrum (vers 19) has been measured after a heating-cooling cycle (300 K) and does not lie on top of the first spectrum (vers14). We believe that an ice layer is formed on top of the sample. We modeled the formation of this ice layer using the optical constants of $YTiO_3$ from the low-pressure measurements (right panel) as presented in chapter 5 and the optical constants of ice from Ref. [224]. Both data sets can be described by only varying the thickness of the ice layer. *Right panels:* At a pressure of 10^{-10} mbar all spectra fall on top of each other. The spectra do not change after a heating-cooling cycle (300 K). We conclude that no ice layers are formed.

Fit of additional data sets of $YTiO_3$

Table A.3: Using the optical constants obtained from the measurements presented in chapter 3 and 5 we are able to model a large number of additional measurements on the same sample of $YTiO_3$ by only varying the thickness d of the cover layer (Cauchy). We present here a selection of fit results at room temperature. All spectra can be described by our final set of optical constants. The abbreviations "AOI", "mm", and "iso" denote angle of incidence, "Müller-matrix" and "isotropic" measurement.

Measurement	AOI (°)	surface	Euler angles (ϕ, θ, ψ) (°)	d (nm)	Kryo?	MSE
vers2^{mm}	65, 70	ab	(45, 0, 0)	0.530	y	10.18
vers4a^{mm}	65, 70	ab	(0, 0, 0)	0.808	y	3.85
vers4b^{mm}	65, 70	ab	(-45, 0, 0)	0.788	y	2.63
vers5^{mm}	65, 70	a^*c	(0, 90, -45)	1.292	y	7.14
vers7^{iso}	65, 70	a^*c	(90, 90, -45)	0.879	y	0.92
vers7^{mm}	65, 70	a^*c	(90, 90, -45)	0.758	y	3.79
vers10^{iso}	70	a^*c	(0, 90, -45)	1.946	y	0.86
vers17^{mm}	70	a^*c	(0, 90, -45)	1.844	y	2.80
vers35^{mm}	70	a^*c	(90, 90, -45)	1.829	y	2.07
vers39^{mm}	70, 75	a^*c	(90, 90, -45)	2.016	y	2.60
vers43^{mm}	70	a^*c	(90, 90, -45)	2.380	y	3.89
vers65^{mm}	70	a^*c	(90, 90, -45)	2.637	y	7.33
vers130^{mm}	70	ab	(45, 0, 0)	0.931	y	2.75
vers132^{mm}	70	ab	(-45, 0, 0)	0.287	y	1.63
vers135^{mm}	70	a^*c	(0, 90, -45)	2.208	y	2.68
vers182^{mm}	20, 45, 70	ab	(0, 0, 0)	0.789	n	3.24
vers183^{mm}	20, 45, 70	ab	(0, 0, 0)	0.789	n	3.24
vers185^{mm}	20, 45, 70	ab	(90, 0, 0)	0.782	n	2.53
vers186^{mm}	20, 45, 70	ab	(90, 0, 0)	0.782	n	2.53
vers187^{mm}	20, 45, 70	ab	(90, 0, 0)	0.782	n	2.53
vers188^{mm}	20, 45, 70	ab	(-45, 0, 0)	0.983	n	3.04
vers189^{mm}	20, 45, 70	ab	(-45, 0, 0)	0.983	n	3.04

Bibliography

[1] M. Imada, A. Fujimori, and Y. Tokura, Rev. Mod. Phys. **70**, 1039 (1998).

[2] N. N. Kovaleva et al., Phys. Rev. Lett. **93**, 147204 (2004).

[3] B. Keimer et al., Phys. Rev. Lett. **85**, 3946 (2000).

[4] G. Khaliullin and S. Maekawa, Phys. Rev. Lett. **85**, 3950 (2000).

[5] J. Akimitsu et al., J. Phys. Soc. Japan **70**, 3475 (2001).

[6] J. Hemberger et al., Phys. Rev. Lett. **91**, 066403 (2003).

[7] M. Cwik et al., Phys. Rev. B **68**, 060401(R) (2003).

[8] M. W. Haverkort et al., Phys. Rev. Lett. **94**, 056401 (2005).

[9] R. Schmitz, O. Entin-Wohlman, A. Aharony, A. B. Harris, and E. Müller-Hartmann, Phys. Rev. B **71**, 144412 (2005).

[10] E. Pavarini et al., Phys. Rev. Lett. **92**, 176403 (2004).

[11] E. Pavarini, A. Yamasaki, J. Nuss, and O. K. Andersen, New J. Phys. **7**, 188 (2005).

[12] M. Mochizuki and M. Imada, Phys. Rev. Lett. **91**, 167203 (2003).

[13] M. Mochizuki and M. Imada, New J. Phys. **6**, 154 (2004).

[14] M. Mochizuki and M. Imada, J. Phys. Soc. Japan **73**, 1833 (2004).

[15] T. Kiyama and M. Itoh, Phys. Rev. Lett. **91**, 167202 (2003).

[16] T. Kiyama et al., J. Phys. Soc. Japan **74**, 1123 (2005).

[17] H. A. Jahn and E. Teller, Proc. roy. Soc. **161**, 220 (1937).

[18] M. Haverkort, *Spin and orbital degrees of freedom in transition metal oxides and oxide thin films studied by soft x-ray absorption spectroscopy*, PhD thesis, University of Cologne, 2005.

[19] C. J. Ballhausen, *Introduction to Ligand Field Theory*, McGraw-Hill, 1962.

[20] S. Sugano, Y. Tanabe, and H. Kaminura, *Multiplets of transition-metal Ions in crystals*, volume 33 of *Pure and Applied Physics*, Academic Press, 1970.

[21] B. N. Figgis and M. A. Hitchman, *Ligand Field Theory and Its Applications*, Wiley-VCH, 2000.

[22] D. Senff et al., Phys. Rev. Lett. **96**, 257201 (2006).

[23] M. Merz et al., The European Phys. J. B **51**, 315 (2006).

[24] J. C. Slater and G. F. Koster, Phys. Rev. **94**, 1498 (1954).

[25] A. Podolskiy and P. Vogl, Phys. Rev. B **69**, 233101 (2004).

[26] R. Rückamp et al., New J. Phys. **7**, 144 (2005).

[27] R. Schmitz, O. Entin-Wohlman, A. Aharony, A. B. Harris, and E. Müller-Hartmann, Phys. Rev. B **71**, 214438 (2005).

[28] J. Hubbard, Proc. roy. Soc. A **276**, 238 (1963).

[29] J. Zaanen, G. A. Sawatzky, and J. W. Allen, Phys. Rev. Lett. **55**, 418 (1985).

[30] V. J. Emery, Phys. Rev. Lett. **58**, 2794 (1987).

[31] K. I. Kugel and D. I. Khomskii, Sov. Phys. Usp. **25**, 231 (1982).

[32] J. van den Brink, W. Stekelenburg, D. I. Khomskii, and G. A. Sawatzky, Phys. Rev. B **58**, 10276 (1998).

[33] G. Kotliar and D. Vollhardt, Physics Today **57**, 53 (2004).

[34] C. Knecht, N. Blümer, and P. van Dongen, Phys. Rev. B **72**, 081103(R) (2005).

[35] K. I. Kugel and D. I. Khomskii, Sov. Phys. JETP **37**, 725 (1973).

[36] L. M. Roth, Phys. Rev. **149**, 306 (1966).

[37] G. Khaliullin, Prog. Theor. Phys. Suppl. **160**, 155 (2005).

[38] L. F. Feiner and A. M. Oleś, Phys. Rev. B **59**, 3295 (1999).

[39] D. I. Khomskii and M. V. Mostovoy, J. Phys. A **36**, 9197 (2003).

[40] M. Mostovoy, private communication.

[41] G. Khaliullin, Phys. Rev. B **64**, 212405 (2001).

[42] A. M. Oleś, P. Horsch, L. F. Feiner, and G. Khaliullin, Phys. Rev. Lett. **96**, 147205 (2006).

[43] G. Khaliullin and S. Okamoto, Phys. Rev. Lett. **89**, 167201 (2002).

[44] G. Khaliullin and S. Okamoto, Phys. Rev. B **68**, 205109 (2003).

[45] R. Schmitz, O. Entin-Wohlman, A. Aharony, and E. Müller-Hartmann, Annalen der Physik **14**, 626 (2005).

[46] W.-G. Yin, D. Volja, and W. Ku, Phys. Rev. Lett. **96**, 116405 (2006).

[47] E. Saitoh et al., Nature **410**, 180 (2001).

[48] J. van den Brink, M. Meinders, J. Lorenzana, R. Eder, and G. Sawatzky, Phys. Rev. Lett. **75**, 4658 (1995).

[49] D. L. Dexter and R. S. Knox, *Excitons*, John Wiley and Sons, 1965.

[50] E. R. Chalbaud and J.-P. Gallinar, J. Phys.: Condens. Matter **1**, 3325 (1989).

[51] J. Franck, Trans. Faraday Society **21**, 536 (1925).

[52] E. Condon, Phys. Rev. **28**, 1182 (1926).

[53] V. Perebeinos and P. B. Allen, phys. stat. sol (b) **215**, 607 (1999).

[54] S. Ishihara, Phys. Rev. B **69**, 075118 (2004).

[55] S. Miyasaka et al., Phys. Rev. Lett. **94**, 076405 (2005).

[56] S. Miyasaka, J. Fujioka, M. Iwama, Y. Okimoto, and Y. Tokura, Phys. Rev. B **73**, 224436 (2006).

[57] S. Sugai, A. Kikuchi, and Y. Mori, Phys. Rev. B **73**, 161101(R) (2006).

[58] S. Sugai and K. Hirota, Phys. Rev. B **73**, 020409(R) (2006).

[59] M. Grüninger et al., Nature **418**, 39 (2001).

[60] J. van den Brink, Phys. Rev. Lett. **87**, 217202 (2001).

[61] K. Schmidt, M. Grüninger, and G. Uhrig, arXiv:cond-mat/0603766 (2006).

[62] Y. Wang et al., Phys. Rev. Lett. **77**, 1809 (1996).

[63] Y. Kim et al., Phys. Rev. Lett. **89**, 177003 (2002).

[64] C. Ulrich, A. Gössling et al., Phys. Rev. Lett. **97**, 157401 (2006).

[65] P. A. Fleury and R. Loudon, Phys. Rev. **166**, 514 (1968).

[66] H. Eskes, M. B. J. Meinders, and G. A. Sawatzky, Phys. Rev. Lett. **67**, 1035 (1991).

[67] H. Eskes, A. M. Oleś, M. B. J. Meinders, and W. Stephan, Phys. Rev. B **50**, 17980 (1994).

[68] H. Eskes and A. M. Oleś, Phys. Rev. Lett. **73**, 1279 (1994).

[69] K. Tobe, T. Kimura, Y. Okimoto, and Y. Tokura, Phys. Rev. B **64**, 184421 (2001).

[70] H. Matsueda, T. Tohyama, and S. Maekawa, Phys. Rev. B **71**, 153106 (2005).

[71] M. Fox, *Optical Properties of Solids*, Oxford University Press, 2001.

[72] P. Y. Yu and M. Cardona, *Fundamentals of Semiconductors*, Spinger, 2001.

[73] E. Jeckelmann, Phys. Rev. B **67**, 075106 (2003).

[74] E. Hanamura, N. T. Dan, and Y. Tanabe, Phys. Rev. B **62**, 7033 (2000).

[75] F. H. L. Essler, F. Gebhard, and E. Jeckelmann, Phys. Rev. B **64**, 125119 (2001).

[76] J. E. Hirsch, Phys. Rev. Lett. **53**, 2327 (1984).

[77] P. Wróbel and R. Eder, Phys. Rev. B **66**, 035111 (2002).

[78] M. J. Rozenberg et al., Phys. Rev. Lett. **75**, 105 (1995).

[79] F. B. Gallagher and S. Mazumdar, Phys. Rev. B **56**, 15025 (1997).

[80] E. Jeckelmann, F. Gebhard, and F. H. L. Essler, Phys. Rev. Lett. **85**, 3910 (2000).

[81] E. Dagotto, A. Moreo, F. Ortolani, J. Riera, and D. J. Scalapino, Phys. Rev. B **45**, 10107 (1992).

[82] H. Itoh, A. Takahashi, and M. Aihara, Phys. Rev. B **73**, 075110 (2006).

[83] A. M. Oleś, G. Khaliullin, P. Horsch, and L. F. Feiner, Phys. Rev. B **72**, 214431 (2005).

[84] B. Henderson and G. F. Imbusch, *Optical Spectroscopy of Inorganic Solids*, Oxford University Press, 1989.

[85] R. Englmann, Molecular Physics **3**, 23 (1960).

[86] G. Khaliullin, P. Horsch, and A. M. Oleś, Phys. Rev. B **70**, 195103 (2004).

[87] J. Rodríguez-Carvajal et al., Phys. Rev. B **57**, 3189(R) (1998).

[88] M. Kim et al., Phys. Rev. Lett. **96**, 247205 (2006).

[89] M. Windt, *Optical Spectroscopy of Spin Ladders*, PhD thesis, Universität zu Köln, 2002.

[90] R. Rückamp, *Orbital excitations of transition-metal oxides in optical spectroscopy*, PhD thesis, Universität zu Köln, 2006.

[91] L. D. Landau and E. M. Lifschitz, *Electrodynamics of Continous Media*, chapter 60, page 251, Pergamon Press, 1960.

[92] H. Kuzmany, *Solid-State Spectroscopy*, Springer, 1998.

[93] M. Dressel and G. Grüner, *Elektrodynamics of Solids: Optical Properties of Electrons in Matter*, Cambridge University Press, 2002.

[94] J. Lorenzana and G. A. Sawatzky, Phys. Rev. Lett. **74**, 1867 (1995).

[95] M. Windt et al., Phys. Rev. Lett. **87**, 127002 (2001).

[96] J. Gronholz and W. Herres, *Understanding FT-IR Data Processing*, Dr. Alfred Huething Publishers, 1985.

[97] M. Schubert, Ann. Phys. **15**, 480 (2006).

[98] R. M. A. Azzam and N. M. Bashara, *Ellipsometry and Polarized Light*, Elsevier, 1987.

[99] D. E. Aspnes, J. Opt. Soc. Am. **70**, 1275 (1980).

[100] F. Bréhat and B. Wyncke, J. Phys. D: Appl. Phys. **24**, 2055 (1991).

[101] M. Born, *Optik - Ein Lehrbuch der elektromagnetischen Lichttherorie*, Springer, 1972.

[102] W. S. Bickel and W. M. Bailey, Am. J. Phys. **53**, 468 (1985).

[103] C. M. Herzinger, B. Johs, W. A. McGahan, J. A. Woollam, and W. Paulson, J. Appl. Phys. **83**, 3323 (1998).

[104] T. Arima, Y. Tokura, and J. B. Torrance, Phys. Rev. B **48**, 17006 (1993).

[105] Y. Taguchi, Y. Tokura, T. Arima, and F. Inaba, Phys. Rev. B **48**, 511 (1993).

[106] T. Katsufuji, Y. Okimoto, and Y. Tokura, Phys. Rev. Lett. **75**, 3497 (1995).

[107] Y. Okimoto, T. Katsufuji, Y. Okada, T. Arima, and Y. Tokura, Phys. Rev. B **51**, 9581 (1995).

[108] H. Roth, *Präparation und Charakterisierung von Titanaten*, Diplomarbeit, Universtät zu Köln, 2003.

[109] C. V. Raman and K. S. Krishnan, Nature **121**, 501 (1928).

[110] M. G. Cottam and D. J. Lockwood, *Light Scattering in Magnetic Solids*, J. Wiley and Sons, 1986.

[111] A. Gößling et al., Phys. Rev. B **67**, 052403 (2003).

[112] K. P. Schmidt, A. Gössling et al., Phys. Rev. B **72**, 094419 (2005).

[113] A. Pinczuk and E. Burstein, *Light Scattering in Solids*, chapter 2, Springer, 1975.

[114] R. M. Martin and L. M. Falicov, *Light Scattering in Solids*, chapter 3, Springer, 1975.

[115] M. Cardona, *Light Scattering in Solids II: Resonance Phenomena*, chapter 2, Springer, 1982.

[116] R. Loudon, Proc. Roy. Soc. A **275**, 218 (1963).

[117] D. L. Rousseau, R. P. Baumann, and S. P. S. Porto, J. Raman Spectrosc. **10**, 253 (1981).

[118] Y. Tokura and N. Nagaosa, Science **288**, 462 (2000).

[119] E. Dagotto, T. Hotta, and A. Moreo, Phys. Rep. **344**, 1 (2001).

[120] E. Dagotto, *Nanoscale Phase Separation and Colossal Magnetoresistance*, Springer, 2003.

[121] E. Dagotto, New J. Phys. **7**, 67 (2005).

[122] N. Mannella et al., Phys. Rev. Lett. **92**, 166401 (2004).

[123] Y. Murakami et al., Phys. Rev. Lett. **81**, 582 (1998).

[124] A. E. Bocquet et al., Phys. Rev. B **53**, 1161 (1996).

[125] S. Grenier et al., Phys. Rev. Lett. **94**, 047203 (2005).

[126] R. Rauer, M. Rübhausen, and K. Dörr, Phys. Rev. B **73**, 092402 (2006).

[127] M. B. Salamon and M. Jaime, Rev. Mod. Phys. **73**, 583 (2001).

[128] B. J. Sternlieb et al., Phys. Rev. Lett. **76**, 2169 (1996).

[129] Y. Murakami et al., Phys. Rev. Lett. **80**, 1932 (1998).

[130] S. S. Dhesi et al., Phys. Rev. Lett. **92**, 056403 (2004).

[131] S. B. Wilkins et al., Phys. Rev. Lett. **91**, 167205 (2003).

[132] D. J. Huang et al., Phys. Rev. Lett. **92**, 087202 (2004).

[133] S. B. Wilkins et al., Phys. Rev. B **71**, 245102 (2005).

[134] S. B. Wilkins et al., Phys. Rev. B **74**, 049902(E) (2006).

[135] A. Daoud-Aladine, J. Rodríguez-Carvajal, L. Pinsard-Gaudart, M. T. Fernández-Díaz, and A. Revcolevschi, Phys. Rev. Lett. **89**, 097205 (2002).

[136] J. van den Brink, G. Khaliullin, and D. Khomskii, Phys. Rev. Lett. **83**, 5118 (1999).

[137] S. Larochelle et al., Phys. Rev. B **71**, 024435 (2005).

[138] J.-C. Bouloux, J.-L. Soubeyroux, G. L. Flem, and P. Hagenguller, J. Solid Sate Chem. **38**, 34 (1981).

[139] Y. Moritomo, Y. Tomioka, A. Asamitsu, Y. Tokura, and Y. Matsui, Phys. Rev. B **51**, 3297 (1995).

[140] C. Baumann et al., Physica B **326**, 505 (2003).

[141] W. Norimatsu and Y. Koyama, Phys. Rev. B **74**, 085113 (2006).

[142] D. Senff, PhD thesis, University of Cologne, 2007.

[143] M. Benomar, PhD thesis, University of Cologne, 2007.

[144] T. Ishikawa, K. Ookura, and Y. Tokura, Phys. Rev. B **59**, 8367 (1999).

[145] K. Yamamoto, T. Kimura, T. Ishikawa, T.Katsufuji, and Y. Tokura, Phys. Rev. B **61**, 14706 (2000).

[146] S. Larochelle et al., Phys. Rev. Lett. **87**, 095502 (2001).

[147] J. Herrero-Martín, J. García, G. Subías, J. Blasco, and M. C. Sánchez, Phys. Rev. B **72**, 085106 (2005).

[148] D. Senff et al., Phys. Rev. B **71**, 024425 (2005).

[149] M. Merz et al., Phys. Rev. B **74**, 184414 (2006).

[150] W. B. Wu et al., J. Elec. Spec. **137-140**, 641 (2004).

[151] J. H. Jung, H. J. Lee, T. W. Noh, and Y. Moritomo, J. Phys. – Condens. Matter **12**, 9799 (2000).

[152] Y. S. Lee et al., Phys. Rev. Lett. **97**, 077203 (2006).

[153] J. H. Jung et al., Phys. Rev. B **61**, 6902 (2000).

[154] Y. Okimoto et al., Phys. Rev. Lett. **75**, 109 (1995).

[155] Y. Okimoto and Y. Tokura, Journal of Superconductivity **13**, 271 (2000).

[156] P. Reutler, *Korrelierte Orbitale in $La_{1-x}Sr_{1+x}MnO_4$*, PhD thesis, RWTH Aachen, 2003.

[157] D. Senff, *Magnetische und orbitale Korrelationen in einfach geschichteten Manganaten der Reihe $La_{1-x}Sr_{1+x}MnO_4$*, Universität zu Köln, Diplomarbeit, 2005.

[158] Y. Moritomo, T. Arima, and Y. Tokura, J. Phys. Soc. Japan **11**, 4117 (1995).

[159] M. Daghofer, A. M. Oleś, D. R. Neuber, and W. von der Linden, Phys. Rev. B **73**, 104451 (2006).

[160] M. Daghofer, D. R. Neuber, A. M. Oleś, and W. von der Linden, phys. stat. sol. (b) **243**, 277 (2006).

[161] P. B. Allen and I. B. Bischofs, Phys. Rev. B **65**, 115113 (2002).

[162] K. T. Park, J. Phys. – Condens. Matter **13**, 9231 (2001).

[163] J. van Elp et al., J. Phys. Soc. Japan **69**, 2391 (2000).

[164] K. Kuepper, R. Klingeler, P. Reutler, B. Büchner, and M. Neumann, J. Appl. Phys. **99**, 08Q308 (2006).

[165] K. Kuepper, R. Klingeler, P. Reutler, B. Büchner, and M. Neumann, Phys. Rev. B **74**, 115103 (2006).

[166] A. Kuzmenko, *Guide to RefFIT - software to fit optical spectra*, 2006.

[167] M. Cuoco, P. Horsch, and F. Mack, Phys. Rev. B **60**, 8438(R) (1999).

[168] D. van der Marel, *Strong interactions in low dimensions*, volume 25 of *Physics and Chemistry of Materials with Low-Dimensional Structures*, chapter 1, page 1, Kluwer, 2005.

[169] W. A. Harrison, *Elementary Electronic Structure*, World Scientific, 1999.

[170] J. H. Jung et al., Phys. Rev. B **55**, 15489 (1997).

[171] F. Bridges, C. H. Booth, G. H. Kwei, J. J. Neumeier, and G. A. Sawatzky, Phys. Rev. B **61**, 9237(R) (2000).

[172] A. S. Moskvin, Phys. Rev. B **65**, 205113 (2002).

[173] P. A. Fleury and H. J. Guggenheim, Phys. Rev. Lett. **24**, 1346 (1970).

[174] M. Cardona, phys. stat. sol. (a) **188**, 1209 (2001).

[175] M. Cardona, Solid State Communications **133**, 3 (2005).

[176] M. Cardona and M. L. W. Thewalt, Rev. Mod. Phys. **77**, 1173 (2005).

[177] S. Biernacki, U. Scherz, and B. K. Meyer, Phys. Rev. B **49**, 4501 (1994).

[178] K. Huang and A. Rhys, Proc. roy. Soc. A **204**, 406 (1950).

[179] P. Lautenschlager, P. B. Allen, and M. Cardona, Phys. Rev. B **33**, 5501 (1986).

[180] L. Viña, S. Logothetidis, and M. Cardona, Phys. Rev. B **30**, 1979 (1984).

[181] S. Logothetidis, M. Cardona, P. Lautenschlager, and M. Garriga, Phys. Rev. B **34**, 2458 (1986).

[182] J. Matsuno, Y. Okimoto, M. Kawasaki, and Y. Tokura, Phys. Rev. Lett. **95**, 176404 (2005).

[183] J. E. Greedan, J. Less Common Metals **111**, 335 (1985).

[184] T. Katsufuji, Y. Taguchi, and Y. Tokura, Phys. Rev. B **56**, 10145 (1997).

[185] T. Mizokawa and A. Fujimori, Phys. Rev. B **51**, 12880(R) (1995).

[186] T. Mizokawa and A. Fujimori, Phys. Rev. B **54**, 5368 (1996).

[187] M. Mochizuki, J. Phys. Soc. Japan **71**, 2039 (2002).

[188] V. Fritsch et al., Phys. Rev. B **65**, 212405 (2002).

[189] M. Kubota et al., Phys. Rev. B **70**, 245125 (2004).

[190] F. Iga et al., Phys. Rev. Lett. **93**, 257207 (2004).

[191] F. Iga et al., Phys. Rev. Lett. **97**, 139901(E) (2006).

[192] C. Ulrich et al., Phys. Rev. Lett. **89**, 167202 (2002).

[193] A. Komarek et al., arXiv:cond-mat/0701452 (2007).

[194] N. Schittner, *Magnetisierung von Lanthanoid-Titanaten*, Diplomarbeit, Universtät zu Köln, 2003.

[195] J. D. Garret, J. E. Greedan, and D. A. MacLean, Mater. Res. Bull. **16**, 145 (1981).

[196] H. D. Zhou and J. B. Goodenough, Phys. Rev. B **71**, 184431 (2005).

[197] G. Amow, J. E. Greedan, and C. Ritter, J. of Solid State Chem. **141**, 262 (1998).

[198] J. P. Goral and J. E. Greedan, J. Magn. Matter **37**, 315 (1983).

[199] G. I. Meijer et al., Phys. Rev. B **59**, 11832 (1999).

[200] H. Roth, PhD thesis, University of Cologne, 2007.

[201] A. E. Filali, *Elektrischer Widerstand von dotierten Titanaten*, Diplomarbeit, Universtät zu Köln, 2004.

[202] A. Komarek, *Strukturuntersuchungen an Titanaten*, Diplomarbeit, Universtät zu Köln, 2005.

[203] I. V. Solovyev, Phys. Rev. B **69**, 134403 (2004).

[204] I. V. Solovyev, Phys. Rev. B **73**, 155117 (2006).

[205] S. V. Streltsov et al., Phys. Rev. B **71**, 245114 (2005).

[206] H. Fujitani and S. Asano, Phys. Rev. B **51**, 2098 (1995).

[207] A. Fujimori et al., Phys. Rev. Lett. **69**, 1796 (1992).

[208] K. Morikawa, T. Mizokawa, A. Fujimori, Y. Taguchi, and Y. Tokura, Phys. Rev. B **54**, 8446 (1996).

[209] H. Nakao et al., Phys. Rev. B **66**, 184419 (2002).

[210] M. Reedyk, D. A. Crandles, M. Cardona, J. D. Garrett, and J. E. Greedan, Phys. Rev. B **55**, 1442 (1997).

[211] M. N. Iliev et al., Phys. Rev. B **69**, 172301 (2004).

[212] C. Ulrich, to be published.

[213] A. Aharony, private communication, 2007.

[214] G. Khaliullin, private communication, 2007.

[215] J. E. Hirsch, Phys. Rev. Lett. **59**, 228 (1987).

[216] J. E. Hirsch, Science **295**, 2226 (2002).

[217] H. J. A. Molegraaf, C. Presura, D. van der Marel, P. H. Kes, and M. Li, Science **295**, 2239 (2002).

[218] M. Schubert, Phys. Rev. B **53**, 4265 (1996).

[219] J. S. Lee, M. W. Kim, and T. W. Noh, New J. Phys. **7**, 147 (2005).

[220] M. Mochizuki and M. Imada, J. Phys. Soc. Japan **70**, 2872 (2001).

[221] P. Reutler, O. Friedt, B. Büchner, M. Braden, and A. Revcolevschi, J. Cryst. Growth. **249**, 222 (2003).

[222] S. L. Altmann and P. Herzig, *Point-Group Theory Tables*, Clarendon Press, Oxford, 1994.

[223] V. G. Zubkov, I. F. Berger, A. M. Artamonova, and G. V. Bazuev, Sov. Phys. Crystallogr. **29**, 296 (1984).

[224] S. G. Warren, Appl. Opt. **23**, 1206.

Publications

1. **Spectral weight transfer in the optical conductivity of $LaSrMnO_4$**
   A. Gössling, M. Haverkort, M. Benomar, H. Wu, T. Möller, D. Senff, M. Braden, J.A. Mydosh, and M. Grüninger
   submitted

2. **Mott-Hubbard exciton in $YTiO_3$ probed by ellipsometry**
   A. Gössling, R. Schmitz, H. Roth, M.W. Haverkort, T. Lorenz, J.A. Mydosh, E. Müller-Hartmann, and M. Grüninger
   submitted

3. **Orbital excitations in titanates**
   C. Ulrich, A. Gössling, M. Grüninger, M. Guennou, H. Roth, M. Cwik, G. Khaliullin, and B. Keimer
   Physical Review Letters **97**, 157491 (2006)

4. **Phonon modes of monoclinic BiB_3O_6**
   A. Gössling, T. Möller, W.-D. Stein, P. Becker, L. Bohatý, and M. Grüninger, physica status solidi (b) **242**, R85 (2005)

5. **Raman Response of Magnetic Excitations in Cuprate Ladders and Planes**
   K.P. Schmidt, A. Gössling, U. Kuhlmann, C. Thomsen, A. Löffert, C. Gross, and W. Assmus
   Physical Review B **72**, 094419 (2005)

6. **Magnetic excitations in $SrCu_2O_3$: a Raman scattering study**
   A. Gößling, U. Kuhlmann, C. Thomsen, A. Löffert, C. Gross, and W. Assmus
   Physical Review B **67**, 052403 (2003)

Danksagung

Dankeschön ...

- Herrn Prof. Dr. A. Freimuth, der mir die Möglichkeit gegeben hat, meine Promotion in Köln durchzuführen und seinem Lehrstuhlvertreter Herrn Prof. Dr. J.A. Mydosh, dem Zweitgutachter dieser Arbeit, für sein Engagement.

- meinem Doktorvater Prof. Dr. M. Grüninger für die Betreuung dieser Arbeit, die wertvollen Korrektur-Vorschläge zu diesem Manuskript und für die zahlreichen Diskussion über Physik. Markus, es hat Spaß gemacht.

- den Optikern Eva Benckiser, Christina Hilgers, Thomas Möller und Dr. Reinhard Rückamp für Zusammenhalt, Einarbeitung, viele Diskussionen, Rat und Tat bei "Soft-" und "Hardware" und vieles mehr. Christina, danke für die Zusammenarbeit beim Aufbau des Ellipsometers und für das Korrekturlesen einiger Teile dieser Arbeit. Thomas, danke für die Zusammenarbeit im BiBO-Projekt, die Einführung in Fortran und ständige Tipps und Tricks zu Mathematica. Eva, danke u.a. für das Korrekturlesen der Zusammenfassung.

- Wolf Dieter Stein, Frau Dr. P. Becker und Prof. Dr. L. Bohatý für die Zusammenarbeit im BiBO-Projekt. Prof. Dr. L. Bohatý ein zusätzlicher Dank für die Übernahme des Vorsitzes der Prüfungskommission.

- Holger Roth, Mohammed Benomar und Matthias Cwik sowie (unbekannter Weise) Pascal Reutler für die schönen Einkristalle und deren Charakterisierung. Holger, danke für die Zusammenarbeit bei den Titanaten.

- Dr. Maurits Haverkort für Hilfe bei Clustern, Punktladungen, für die Nutzung seiner Mathematica-Notepads, die Zusammenarbeit beim den Schichtmanganat und beim "Tag der offenen Tür".

- Dr. A. Tanaka für die Nutzung des Programms zur Clusterrechnung.

- Dr. Hua Wu für die LDA+U Rechnung für das Schichtmanganat.

- Dr. Clemens Ulrich, Prof. Dr. B. Keimer und Dr. G. Khaliullin für die Zusammenarbeit bei der Ramanspektroskopie an den Titanaten.

- Dr. Robert Schmitz und Prof. Dr. E. Müller-Hartmann für die Zusammenarbeit bei den Titanten.

- den Mitarbeitern der Werkstätten unter Leitung von Herrn Külzer (Feinmechanik) und Herrn Menz (Elektronik), für stete Hilfsbereitschaft und zuverlässige Arbeitsausführung.

- den technischen Mitarbeiterinnen Lucie Hamdan, Inge Simons und Susanne Heijligen für ihre Hilfsbereitschaft.

- Dr. Jörg Baier für die Zusammenarbeit beim "Tag der offenen Tür".

- Dr. Thomas Lorentz, Prof. Dr. D. Khomskii, M. Mostovoy für eine stets offene Tür bei Fragen aller Art.

- Dr. Harald Kierspel für die Zusammenarbeit im AP und seine Hilfe bei allen organisatorischen Fragestellungen.

- Herrn Dr. Roden und Herrn Dommel für das flüssige Helium.

- Dr. Ralf Müller für zuverlässige Versorgung mit Kaffee, Wasser, Ostereiern und sonstigen Chemikalien.

- meinen ehemaligen und aktuellen Zimmerkollegen Dr. Markus Kriener, Kostas Kordonis, Dr. Alexandr Sologubenko und Thomas Möller für die gesellige Runde und das Schwätzchen zwischendurch.

- Olaf Schumann und Jonas Weinen für die Hilfe bei Computerproblemen aller Art.

- Daniel Senff für die Zusammenarbeit bei den Schichtmanganaten.

- Kai Berggold für das Löten kleinster Verdrahtungen.

- Carmen Handels für ein freundliches Lächeln am Morgen und Büroartikel aller Art.

- allen Mitgliedern des Institutes für eine angenehme Atmosphäre und ihre Hilfsbereitschaft.

- Dr. Alexander Reischl, Dr. Kai. P. Schmidt und Dr. Sebastien Dusuel für die netten Espressopausen im Theorie-Institut und die Diskussionen über Leitern und Ketten. Dr. Kai. P. Schmidt danke ich für die Zusammenarbeit im daraus entstandene Raman-Projekt über Spinleitern.

- meinen Eltern und meiner Schwester.

- meiner Freundin Kerstin, dass sie so viel Rücksicht auf mich genommen hat und meiner Tochter Hannah-Marie, dass sie mich nach der Abgabe wiedererkannt hat.

- der Deutschen Forschungsgemeinschaft (DFG) für die Finanzierung meiner Doktorandenstelle durch den SFB 608.

Offizielle Erklärung

Ich versichere, dass ich die von mir vorgelegte Dissertation selbständig angefertigt, die benutzten Quellen und Hilfsmittel vollständig angegeben und die Stellen der Arbeit - einschließlich Tabellen, Karten und Abbildungen -, die anderen Werken im Wortlaut oder dem Sinn nach entnommen sind, in jedem Einzelfall als Entlehnung kenntlich gemacht habe, dass diese Dissertation noch keiner anderen Fakultät oder Universität zur Prüfung vorgelegen hat, dass sie - abgesehen von den in der Publikationsliste angegebenen Teilpublikationen - noch nicht veröffentlicht worden ist sowie, dass ich eine solche Veröffentlichung vor Abschluss des Promotionsverfahrens nicht vornehmen werde. Die Bestimmungen dieser Promotionsordnung sind mir bekannt. Die von mir vorgelegte Dissertation ist von Prof. Dr. M. Grüninger betreut worden.

Köln, den 19. April 2007

Alexander Gößling

Abstract

Within the scope of this thesis the electronic structure of different transition-metal compounds with open d shells has been investigated by three optical techniques. We used Fourier-transform spectroscopy (energy range: 0.1-1 eV), spectroscopic ellipsometry (0.75-6 eV) and Raman scattering (0.01-0.6 eV). The focus is on Mott-Hubbard insulators, on excitations from the lower to the upper Hubbard band, on the effect of spin and orbital correlations of these transitions, and on orbital excitations. For the ellipsometry results the spectral features have been analyzed in terms of multiplets, which reflect multi-orbital Hubbard bands.

The single-layered manganite $LaSrMnO_4$ (d^4) has been investigated by spectroscopic ellipsometry and Fourier-transform spectroscopy. We find a multi-peak structure which strongly depends on the polarization. We could unravel charge-transfer and Mott-Hubbard excitations by analyzing both, polarization and temperature dependence, and by comparing the spectra to a multiplet calculation. We find evidence that the first peak observed at around 2 eV is a Mott-Hubbard transition. The temperature dependence of this peak fulfills the expectations based on the nearest-neighbor spin-spin correlation function. We further investigated the hole-doped $La_{1-x}Sr_{1+x}MnO_4$ for $x = 0.13$ and 0.50. We found a redistribution of weight induced by the new d^3 states in a d^4 host.

The titanates (d^1) $LaTiO_3$ and $YTiO_3$ have been examined by means of Raman spectroscopy[1]. We found an orbital excitation in both compounds at 235 meV. From the resonant enhancement of this excitation for a laser energy of 2.5 eV we concluded that the excitation has to proceed via the upper Hubbard band, i.e. it has to involve two Ti sites.

The compounds $YTiO_3$, $SmTiO_3$, and $LaTiO_3$ have also been investigated by means of ellipsometry. In $YTiO_3$ we find evidence for the existence of a Mott-Hubbard excitonic resonance, i.e. a quasi-bound state inside the continuum of the Hubbard bands. We observed small changes of the spectral weight around T_c but larger changes up to at least $10\,T_c$. The relative change in spectral weight with temperature is too small when comparing to the spin-spin correlation function. Finally we compared the data of ferromagnetic $YTiO_3$ to those of the antiferromagnetic compounds $SmTiO_3$ and $LaTiO_3$. The evolution of spectral weight with increasing ionic rare-earth radius can be qualitatively understood by the evolution of the Ti-O-Ti bond angle and the change in the (orbitally-ordered) ground state. The spectral weight in $SmTiO_3$ shows significant changes at T_N. Here the expectations from the spin-selection rules completely fail to describe the observed sign of the change and the magnitude. The latter results may indicate the spin-degree of freedom can not discussed separately without considering the orbital degree of freedom.

[1] in collaboration with C. Ulrich and B. Keimer (Max-Planck institute, Stuttgart).

Kurzzusammenfassung

Im Rahmen dieser Doktorarbeit wurde die elektronische Struktur von Übergangsmetalloxiden mit offenen d-Schalen untersucht. Der Schwerpunkt liegt auf den Mott-Hubbard Isolatoren, die Anregungen zwischen unterem und oberem Hubbard Band, dem Effekt von Spin-Orbital-Korrelationen und orbitalen Anregungen. Hierzu wurden drei spektroskopische Techniken eingesetzt: die Fourier-Spektroskopie (Energiebereich: 0.1-1 eV), die spektroskopische Ellipsometrie (0.75-6 eV) und die Raman-Streuung (0.01-0.5 eV). Die Ergebnisse der Ellipsometrie wurden mit Hilfe von Multipletts analysiert, wodurch wir multiorbitale Hubbard Bänder identifizieren können.

Das Schichtmanganat $LaSrMnO_4$ (d^4) wurde mit Hilfe der Ellipsometrie und der Fourier-Spektroskopie untersucht, wobei stark anisotrope optische Eigenschaften beobachtet werden. Diese können direkt auf die anisotrope Kristallstruktur zurückgeführt werden. Aus dem Temperatur- und Polarisationsverhalten sowie dem direkten Vergleich zu theoretischen Spektren, konnten wir Ladungs-Transfer- und Mott-Hubbard-Übergänge unterscheiden. Wir identifizieren den ersten Peak bei etwa 2 eV mit einem Mott-Hubbard-Übergang. Weiterhin haben wir lochdotiertes $La_{1-x}Sr_{1+x}MnO_4$ mit $x = 0.13$ und 0.5 untersucht. Mit steigender Dotierung erfolgt eine Umverteilung des spektralen Gewichtes, die den d^3 Zuständen zugesprochen werden kann.

Die Titanate (d^1) $LaTiO_3$ und $YTiO_3$ wurden mittels Raman-Streuung untersucht[1]. Eine Anregung bei 235 meV konnte in beiden Systemen beobachtet werden und wird als orbitale Anregung interpretiert. Da diese Anregung bei einer Laserenergie von etwa 2.5 eV resonant verstärkt wird, muss der Anregungsprozess über das obere Hubbard-Band verlaufen, d.h. zwei Ti-Plätze sind beteiligt.

Ellipsometrische Messungen sind an den oben genannten Titanaten und an $SmTiO_3$ durchgeführt worden. In ferromagnetischem $YTiO_3$ interpretieren wir eine Anregung bei 1.95 eV als ein Mott-Hubbard Exziton, ein quasi-gebundener Zustand innerhalb des Kontinuums. Die Temperaturabhängigkeit des spektralen Gewichtes folgt nicht oder nur teilweise den Erwartungen, die sich aus der der Spin-Spin Korrelationsfunktion ergeben. Dasselbe gilt für das ebenfalls untersuchte antiferromagnetische $SmTiO_3$. Dieses könnte darauf hindeuten, dass der orbitale und der Spin-Freiheitsgrad nicht mehr als entkoppelt angesehen werden können, wie im Fall des Schichtmanganats $LaSrMnO_4$.

[1] in Kooperation mit C. Ulrich und B. Keimer (Max-Planck Institut, Stuttgart).